Structural Plasticity in Intermetallic Compounds:

Interpreting Complexity as a Structural Response to Chemical Pressure

By

Veronica M. Berns

A dissertation submitted in partial fulfillment of the requirements for the degree of

Doctor of Philosophy

(Chemistry)

at the

UNIVERSITY OF WISCONSIN-MADISON

2014

Date of final oral examination: 5/30/2014

This dissertation is approved by the following members of the Final Oral Committee:

Daniel C. Fredrickson, Assistant Professor, Chemistry
Robert Hamers, Professor, Chemistry
Song Jin, Professor, Chemistry
Clark R. Landis, Professor, Chemistry
Paul Voyles, Associate Professor, Materials Science and Engineering

Abstract

Several parameters are known to influence the structural chemistry of intermetallic compounds, but our overall understanding of the forces that shape these structures is incommensurately poor relative to the extensive array of intermetallic structure types we know to exist. Close examination of the diversity of intermetallic compounds reveals a possible foothold in the overwhelming variety of crystal structures: large, complex unit cells often have close relationships to compounds with simpler structures. For example, unit cells of over a thousand atoms such as $NaCd_2$ can be broken down into the sum of fragments of more easily understood compounds, plus any new coordination occurring at the interfaces between fragments. Beginning to organize these compounds into structural progressions inspired the hypothesis of *structural plasticity*, the centerpiece of this work: The possibility that fragmented nature of complex intermetallic phases arises in response to the stress inherent in otherwise simple materials.

The source of this stress, proposed to be intrinsic to the compound, is *chemical pressure*; a strain created in a structure when a stoichiometry incompatible with the geometry of a simple structure experiences mismatch in atomic size or electron count. The rearrangement of atoms that occurs in response to this strain results in a related compound, related to the first by structural plasticity. We obtain the nomenclature from a similar phenomenon seen in elemental metals: on application of an external stress, dislocations or defects appear in a simple metallic lattice to alleviate the strain. On a structural level in intermetallic compounds, plasticity manifests itself in

relation to the stress of suboptimal local interactions. This can be examined computationally using Density Functional Theory-based chemical pressure analysis (DFT-CP).

This document outlines the elucidation of the idea of structural plasticity, from experimental endeavors to computational applications of the DFT-CP method. We begin with experimentally synthesized compounds whose complex unit cells exhibit fragmented versions of related phases. After synthesizing several new compounds, the stage of development of the CP tools available inspired work on this project to turn to testing new chemical pressure methods. We show several examples of structural plasticity along with the development of the tool of DFT-CP.

To conclude, we offer an illustration of the structural plasticity of the $CaCu_5$-type in the form of a family of three related compounds: Ca_2Ag_7, $Ca_{14}Cd_{51}$, and $CaCd_6$. Using DFT-CP analysis, we identify the mechanisms by which each compound copes with the strain caused by negative pressure on the calcium site. The insertion of a defect plane in Ca_2Ag_7 resolves excess negative pressure observed in the hypothetical $CaCu_5$-type $CaAg_5$. While Ca_2Ag_7 retains 2-dimensional slabs of the $CaCu_5$-type, $Ca_{14}Cd_{51}$ exhibits columns of $CaCu_5$-like environments. The final family member, $CaCd_6$, alleviates the negative pressure by compressing each individual calcium coordination environment, resulting in five-fold local coordination, and the beginnings of the icosahedral Tsai-type cluster, seen both in this 1/1 quasicrystalline approximant and the Tsai-type quasicrystal, $CaCd_{5.7}$. The diversity of all of these phases can be traced back to structural adaptations in response to chemical pressure.

To my family. All of you.

Acknowledgements

There are so many people I want to thank, for all of the big things of course, but also for little things they've done to support me in carrying out this dream of mine.

I came to Wisconsin certain that I wanted to research complex intermetallic crystal structures, but I did not know that the group I already had my scientific heart set on joining would become the research family that I so needed. Danny, through your ever-present positivity and contagious enthusiasm, you have cultivated a strong team of supportive and brilliant people. You've done your job of pushing me to become a better scientist, but working with you makes me strive to be a better person as well. I am honored to have been a part of the beginning of your group. I admire you for so many reasons scientifically, but the kindness and empathy you have shown me at the darkest times is what makes you, without exaggeration, the best advisor I could have asked for.

Rie, you have not only been a great source of crystallographic knowledge and know-how, but you have also done so much to create a warm, inviting place to live and work in our laboratories. Dr. Steven Girard has also been a great mentor to me. We met sharing the unique lab equipment involved in solid state chemistry, but you've shared your experience and wisdom too.

Dr. John Fournelle, Phil Gopon, Dr. Hiromi Konishi, and Professor Huifang Xu of the UW Geology Department have all been immensely generous with conveying a tiny slice of their expertise in EDS, WDS, SEM, and powder diffraction.

The gentlemen of the Chemistry Department's machine shop—Jerry Stamn, Matt Martin, Eddie Vasiukevicius, Jim Mullarkey, and Steve Myers—have always entertained my "how does it work" questions, even if there's no problem to be solved.

The Chemical Pressure crew could not have made it to shore without everyone rowing their hardest. Kale and Yiming, your programming talents are truly exceptional, and I'm an even bigger fan of your patience and willingness to walk me through your code line by line as I learn to program myself. Working closely on the Chemical Pressure project with you two and Brandon has given me such scientific satisfaction; I'm glad I can always share my excitement over good data with you.

To you three and the rest of the merry band of scientists in the Fredrickson Group—Tim, Amelia, Vince, Anastasiya, Katie, Nick, Mike, Mariana, Alex, and Arthur—you have been the best group of coworkers. You've challenged, taught, and inspired me over these past five years, and I'm so excited to see where you go in this world; wherever it is, I know you will make it a better place.

On several occasions over the past five years, I have had cause to step back and realize just how much I've learned. Most often the lessons I noticed were academic in nature, but I am lucky to have people around me who can point out other sorts of important lessons as well. To my parents, Ashlan, and Max: I'm the reason I came here, but you're the reason I stayed. The best things are always the hardest things to do, and they are only ever possible because of the support of the great people that surround me. Love to all of you.

It is rather fitting that the work I have done in graduate school culminates with a paper about the structural family of $CaCu_5$-type phases. What we thought would be a linear progression of phase deformation actually looks quite different, incorporating branches like a family tree. My own family looks different than I ever thought it would too. Thank you, all of you.

Table of Contents

List of Figures

List of Tables

Chapter 1.

Introduction

1.1 Diversity in intermetallic compounds

The overwhelming diversity of intermetallic compounds is a great source of wonder among those familiar with the structures of solid state materials. While elemental metals most often form simple close packings of spheres, binary mixtures vary wildly from the colored variants of face-centered cubic packing such as $AuCu_3$ ($cP4$),[1] to the family of Laves phases including $MgCu_2$ ($cF24$),[2] to the icosahedral Tsai-type quasicrystal $CaCd_{5.7}$ and its approximant, $CaCd_6$ (Figure 1.1).[3,4] Despite significant advancements

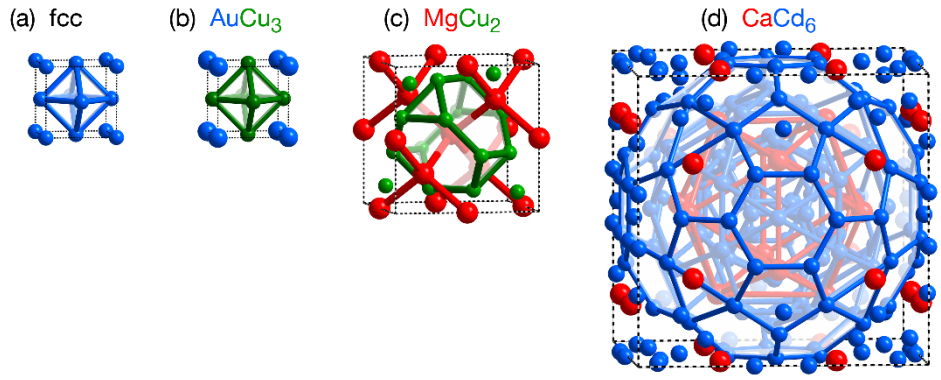

Figure 1.1. Structural complexity in intermetallic systems. While most elemental metals adopt a simple packing of spheres such as (a) a face centered cubic (fcc) arrangement, binary intermetallics exhibit a vast range of structures as shown for (b) $AuCu_3$, (c) $MgCu_2$, and (d) $CaCd_6$, a 1/1 Tsai-type quasicrystalline approximant.

in crystallographic characterization of these structures, the driving forces behind the formation of one structure over another remain enigmatic. In fact, many complex compounds have similar local coordination environments to simpler ones, making differentiation between structural choices all the more mysterious. Why should a compound attain stability in a complex structure when a simpler alternative exists?

Over the course of this thesis, we will see that it is these connections between simple and complex compounds that provide a route to answering this question. Often, a complex compound can be interpreted as fragments of one or more similar structures. For example, within a unit cell of $Mg_{17}Al_{12}$, seen in Figure 1.2a, we find a body-centered arrangement $MgCu_2$-type clusters (Figure 1.2b).[5,6] In $MgCu_2$, this unit is part of an infinite diamond network of these clusters (Figure 1.2c), while in $Mg_{17}Al_{12}$, they are separated by planar interfaces. Structural fragmentations such as this concretize our question about the source of complexity; we can now ask a more specific question about the structural advantages of the cluster itself, and what is gained in the interfaces between clusters in each structure.

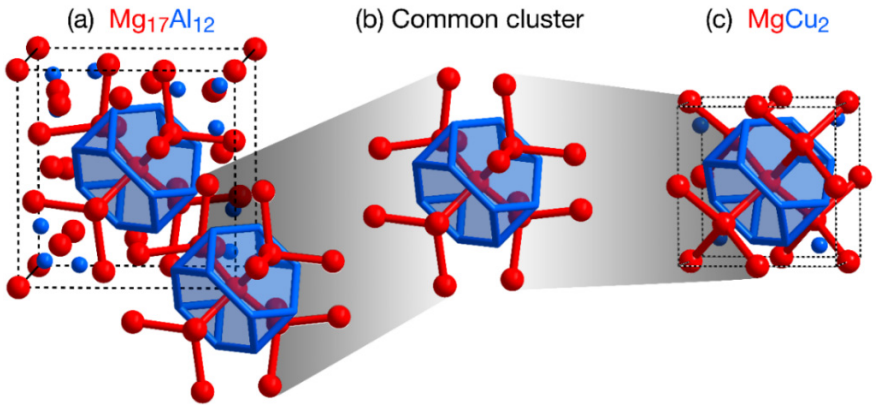

Figure 1.2. Many complex structure types are rearrangements of structural motifs seen in simpler compounds. (a) $Mg_{17}Al_{12}$ is a body-centered cubic arrangement of the 29-atom clusters pictured in (b). This cluster derives from (c) $MgCu_2$, which is a continuous diamond network of Mg atoms, each surrounded by 12 Cu atoms arranged in a truncated tetrahedron.

These structural relationships emphasize the robust nature of certain coordination environments within a compound. As we will see, when local strain is inflicted (in the form of altering the stoichiometry, for example), portions of the structure remain unchanged, while other portions rearrange in response to the stress. This ability to respond and adapt under stress can be likened to the plastic deformation of pure metals, and so we term it *structural plasticity*. Through the lens of structural plasticity, we can begin to identify families of related compounds, pinpointing structural flexibilities. With this perspective, we eventually achieve the ability to predict how structures will deform in response to applied chemical stresses, such as a change in atomic size or electron count, in a manner analogous to a material's response to physical stress.

This thesis develops the idea of structural plasticity through both experimental exploration and theoretical calculations. Offered here are targeted synthetic methods that yielded the discovery of new compounds whose complex crystal structures exemplify the fragmentation of simpler phases. DFT-CP computations serve to flesh out the motivation for the structural relationships observed in the laboratory, creating a story of structural progression that connects a family of similar compounds. The original idea of structural plasticity envisioned a structure's response to chemical pressure (CP) as a linear structural progression, where incremental increases in structural stress further deform the original compound's features in a continuous progression. The major result of this work illustrates that CP-driven phase transitions can find relief in more than one manner, creating a branching family tree of related structure types. The DFT-CP method was central to this conclusion.

1.2 Utility and execution of Chemical Pressure Analysis

Up until this point, we have assumed that there are internal stresses inherent to solid state compounds. These have their origins in principles intuitive to chemists, such as electron count or atomic size. These concepts are appealing, as they draw from deep-seated concepts proven useful throughout different fields of chemistry.[7–9] However, these rationalizations prove difficult to test in a controlled manner. Though we understand the ratio of atomic radii to have some effect on structure, there is some difficulty in visualizing and mapping the full effects of such an argument.

This led to the development of the DFT-based chemical pressure analysis (DFT-CP), a theoretical technique which allows us to examine the ideality of the bond lengths in a given compound. For any given interaction between two atoms, the energy is dependent on the distance between the species involved in the form of a Lennard-Jones-type potential. In an isolated molecule, a bond length is able to attain the most energetically favorable distance—unless sterically hindered. In an extended solid network, bond lengths experience more restrictions, as lengthening one distance inherently means shortening another. Because of this intertwined nature, a bond may be electronically favorable, but unable to form due to steric hindrance, a concept referred to as electronic packing frustration (EPF).[10] Ultimately the interactions in an extended solid represent an energetic compromise, where some atomic contacts are shorter than the ideal length, and some are longer.

This idea is graphically represented in the two dimensional case in Figure 1.3, where a close packed layer of large light grey atoms is interrupted by a smaller, dark grey atom. We anticipate the favorable heteroatomic interaction between the small and large atoms (A) should draw the large atoms inwards. As

the six contacts shorten, so does the distance between the large atom and its homoatomic neighbors (B), which are already at the optimal distance for a close packed layer of large atoms. The observed distances that result should represent the compromise we spoke of above; the observed A distance will be longer than its energetic minimum, and the observed B distance will be shorter.

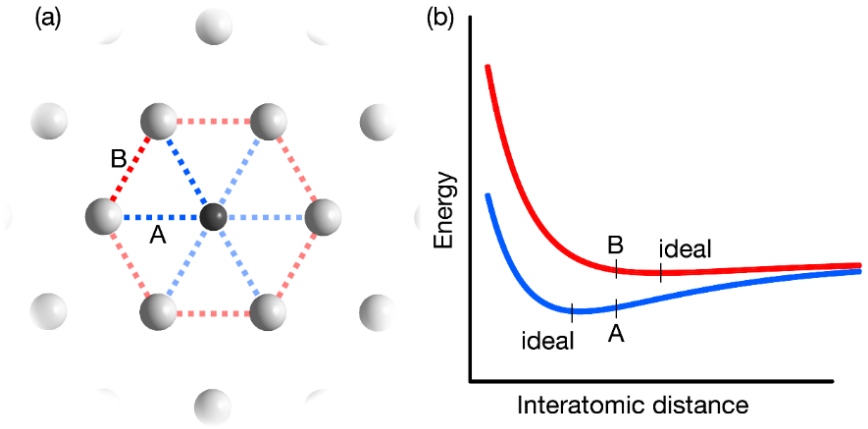

Figure 1.3. Schematic representation of chemical pressure in a 2-dimensional system. (a) In a sheet of close packed uniform atoms (light grey), one is replaced with a smaller atom (dark grey). The heteroatomic interaction is expected to shorten the blue bond distances, but this rearrangement requires shortening the distance between neighboring large atoms (red). The observed distances are expected to lie somewhere between the ideal distance for the heteroatomic interaction and that for the homoatomic interaction. This scenario corresponds to Lennard-Jones potentials illustrated in (b), the blue line representing the curve for the blue contacts and the red line for the red contacts. Ideal bond distances for the individual curves are shown, as are "observed" distances, indicated by "A" and "B" which optimize the overall energy of the system.

A cartoon of the corresponding Lennard-Jones-like potential is offered in Figure 1.3b, with the blue curve representing the blue contacts, and the red curve representing the red contacts.[11] The energetic minimum on the blue curve lies at a significantly shorter distance than that for the red curve. Because the

system is geometrically constrained, we expect the observed distance to lie somewhere in the middle, here labeled "A" and "B". Chemical pressure is the stress that remains in the structure as bond distances are held at non-ideal lengths, and is quantified as the slope of bond energy versus volume curve for a system at the observed geometry:

$$P = -\frac{dE}{dV} \tag{1.1}$$

In practice, this is computed as

$$P = -\frac{E_2 - E_1}{V_2 - V_1} \tag{1.2}$$

where "1" and "2" indicate the energy and volume for datasets of a slightly deflated unit cell, and a slightly inflated unit cell, respectively. From the spatially resolved output of a DFT-calculation, we are able to obtain an energy map for every point on a grid superimposed on the unit cell, from which we can compute a smooth map of the pressure. This map holds significant information about the interactions in the structure, but it is often more useful when the pressures are integrated and projected onto the nearest atomic contacts, allowing for a 3-dimensional model of interatomic interactions. Development of the mapping and integration procedures can be found in chapters 4 and 6.

The results of a chemical pressure analysis have proven quite useful in explaining structural phenomena of the solid state. Using CP, we are able to elevate a comparison of a complex compound to the simpler type that precedes it in a structural progression, providing information beyond atomic positions; we can obtain some indication of the stress inherent in the current configuration, and with

careful interpretation, this enhanced insight into the structure suggests solutions to alleviate the highest pressures present. Chemical pressure highlights the idea of structural plasticity in the system: structural alterations appear in response to the local stresses revealed through CP analysis. In the next section, we introduce a model system through which these concepts can be illustrated and developed: the relationship between the $CaCu_5$ type and the Yb_2Ag_7-type phase Ca_2Ag_7.

1.3 Chemical Pressure in practice: the $CaCu_5$- and Yb_2Ag_7-types

$CaCu_5$ is a common intermetallic structure type, defined by alternating honeycomb and Kagome layers of copper atoms (blue and green in Figure 4a), with calcium atoms stuffing the center of each hexagonal hole in the honeycomb layer. This structure type is common for combinations of electropositive alkaline or rare earth metals and late transition metals, forming for example when Ca is paired with Ni, Cu, Zn, Pd, or Pt in a 1:5 ratio. However, when Ca is paired with a larger transition metal atom such as silver, no 1:5 compound forms. In this case, we observe instead the Yb_2Ag_7–type Ca_2Ag_7: here similar layers of Kagome and honeycomb nets exist, but every other Kagome net is removed. In its place, we find a shift in the layers (Figure 1.4b). As was shown earlier with more preliminary versions of the CP analysis, this layer deletion and planar shift is the major deviation from the $CaCu_5$ type.[10,12] We can begin to discern why Ca_2Ag_7 is more favorable than a hypothetical $CaCu_5$-type compound using the results of a chemical pressure analysis of both phases. Such a comparison (updated to with the latest version of the DFT-CP analysis) is given in Figure 1.5.

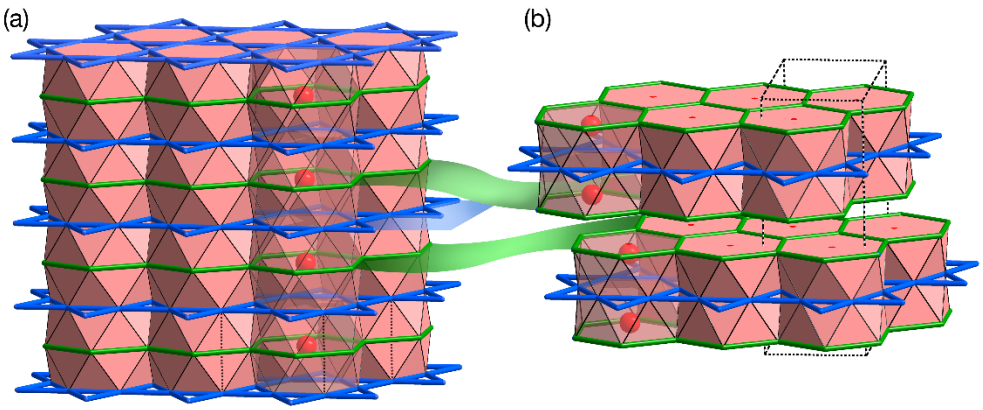

Figure 1.4. The $CaCu_5$ type as compared to Ca_2Ag_7, with several unit cells shown. (a) The $CaCu_5$ type consists of alternating layers of Cu Kagome (blue) and honeycomb nets (green), with calcium atoms (red) filling the voids, centered in the honeycomb layer. (b) Ca_2Ag_7 exhibits the same Kagome (blue) and honeycomb (green) layers, but half of the Kagome nets are removed. The structure incorporates a shift to compensate, and the calcium atoms (red) move slightly out of the plane of the honeycomb layer.

Chemical pressure is represented in Figure 5 as black and white lobes overlayed on the structural picture. Black lobes represent negative pressure, and occur between atoms whose ideal distance is shorter than the observed distance. White lobes indicate a positive pressure between atoms where it would be energetically favorable for contacts to lengthen. The size of the lobe corresponds to the magnitude of the pressure, so that a large white lobe would indicate a distance that is much too short for the size of the atoms involved. These conventions have an astronomical mnemonic: Black indicates areas of the structure that would condense if unopposed, pulling inwards much like a black hole pulls on its surroundings. White lobes push outwards, similar to the ever-outward radiation of light from white-hot stars. Returning to our example of $CaCu_5$-type $CaAg_5$ in Figure 5a will help solidify this notation.

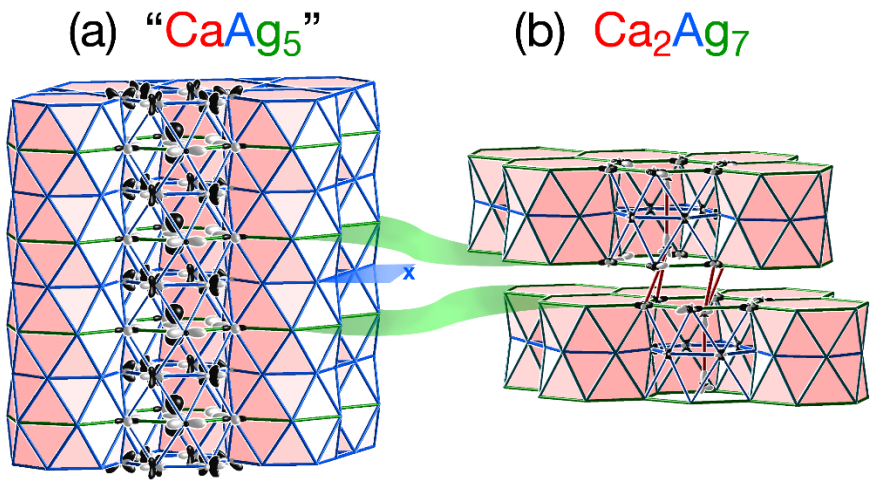

Figure 1.5. Comparison of (a) hypothetical $CaCu_5$-type $CaAg_5$ and (b) observed Ca_2Ag_7, with overlaid chemical pressure results. The black and white lobes shown indicate the directionality of the pressure, and their size corresponds to the magnitude. Black lobes signify negative pressure, where the bond distances are longer than ideal, and white, positive pressure for distances shorter than ideal.

The most striking feature of the chemical pressure in the hypothetical $CaAg_5$ compound is perhaps the large black lobes on the calcium atoms, pointing to the silver on the Kagome net (blue). This distance is longer than it would like to be, but contraction is prevented by the white, positive pressure appearing between the silver atoms of the Kagome net. We can see that this portion of the structure is locked in opposition, but we can also see the overall benefit of obtaining closer silver neighbors for the calcium atom.

If we look to the structure of Ca_2Ag_7 in Figure 1.5b, we immediately notice that the structural shift occurs where we would expect: every other Kagome net is removed, and the structure shifts to align calcium with two silver atoms of the neighboring honeycomb net (red contacts). Along this Ca-Ag contact, chemical pressure is nearly zero. The strongest pressures (much weaker than those seen in

$CaAg_5$) now lie between calcium atoms; as each calcium has moved out of the plane of the honeycomb layer, we see a positive pressure interaction between them.

On the whole, we see that the chemical pressure analysis highlights the regions of greatest stress in our hypothetical $CaAg_5$ compound. This provides motivation for a structural transformation to occur, while also preserving relatively optimal regions of the parent compound. Through this example, we are able to see structural plasticity at work as it sculpts the arrangement of the atoms to fit the requirements of the local interactions involved and create more favorable interfaces between fragments.

In this thesis, we will see several examples of structural plasticity in intermetallic compounds, most often offered as relationships between one simple and one complex structure. It was not until the work with the $CaCu_5$-type related compounds in Ca-late TM binary systems that we began to understand the extent to which this concept can unite entire structural families. Figure 1.6 offers a hint at the direction of this work: a structural response to chemical pressure can take more than one possible path, creating a beautiful family tree of related structure types under the parent compound—in this case, the $CaCu_5$-type.

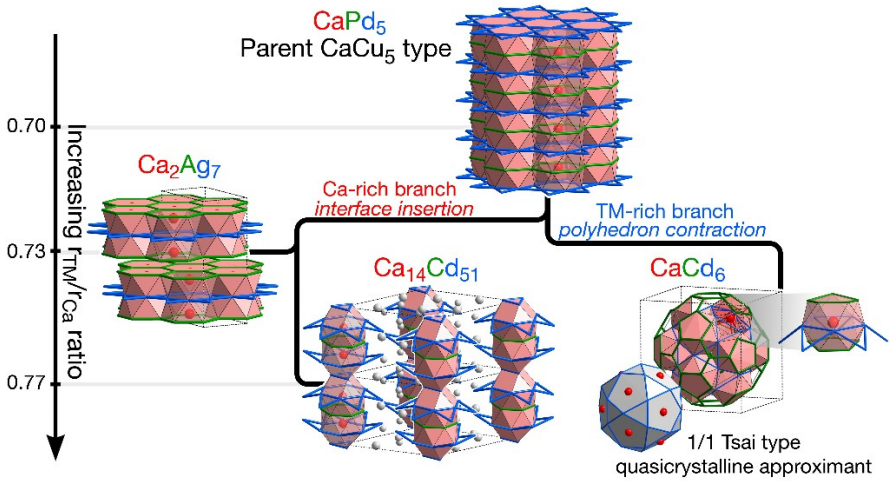

Figure 1.6. The structural plasticity of the $CaCu_5$ type, as observed in Ca-TM phases for TM = Pd, Ag, and Cd.

1.4 Outline of thesis—progression of structural plasticity through various intermetallic systems

In this work, we trace the evolution of the concept of structural plasticity along with the development of the DFT-CP analysis. The examination of this idea begins in the laboratory, with the aim to synthesize compounds targeted to exhibit complex fragmentations of simpler phases. Syntheses were developed based on ternary phase diagrams whose binary subsystems exhibit similar, compatible structural trends. The goal was to seed intergrowth phases, new arrangements with familiar structural motifs, which may exhibit novel adaptations in their chemical bonding.

With this inspiration, we looked to the Mg-Cu-Al ternary system; Mg and Cu form a simple and common Laves phase, $MgCu_2$ (*cF*24), while the Mg and Al binary of similar stoichiometry forms β-Mg_2Al_3 (*cF*1227)[13]. Though very different in their overall complexity, these two compounds are both based on packings of Friauf polyhedra (Figure 1.2b). From our investigation in this system, we obtained a new ternary example of the $K_{17}In_{41}$-type compound, itself a structural rearrangement of Friauf-based building blocks. Further investigation of this compound continued with a Mulliken Population Analysis, yielding geometrically-derived electronegativities and justification for specific site coloration. This lead to unexpected connections beyond the Laves phase, to the Clathrate II framework.

Chapter 3 continues with further synthetic work, collecting together several unpublished crystal structures synthesized while targeting structural progressions in families related to dodecagonal quasicrystals. Included here are the structures of $Fe_7Mo_4Si_8$ and Mn_{24} $Co_{14}Si_{14}$. This wealth of new structural compounds came at a time when the chemical pressure theory was still in its infancy, and full analysis and understanding of such complex phases was not yet possible.

The remainder of this thesis moves away from synthetic results to focus on the development and utility of the chemical pressure technique in investigating similarly fragmented compounds. This led to testing and reevaluating the DFT-CP methods with colleagues in the Fredrickson Group, resulting in the work presented in Chapter 4. This chapter improves upon the first version of the DFT-CP programs, illustrating the need to compensate for the strong core pressures in the CP maps with an averaging procedure. Taking $Ca_{36}Sn_{23}$ as a case study, we also introduce a new integration method based on distributing pressure to pairs of atoms instead of dividing space into single atomic domains.

Chapter 5 illustrates the power of this new version of the DFT-CP method to elucidate structural chemistry. Similar to the example seen for calcium and silver in section 1.3, calcium and cadmium do not form a 1:5 $CaCu_5$-type compound. Because cadmium is even larger than silver, the negative chemical pressure between Ca-Cd contacts increases even further, and we might anticipate the need for a more drastic transformation to relieve the negative chemical pressure in a hypothetical $CaCu_5$-type $CaCd_5$ compound. Shrinking calcium's coordination environment and shortening Ca-Cd distances would alleviate this pressure. Here, pressure reduction is achieved by breaking the hexagonal symmetry of the $CaCu_5$ type, replacing the 6-membered rings with 5-membered rings. The newfound pentagonal symmetry inspires the creation of the Tsai cluster, the building block of the Tsai-type icosahedral quasicrystal, implying the origins of icosahedral quasicrystallinity may lie in the effects of chemical pressure.

Further method development continues in Chapter 6, where we improve upon the core averaging procedure, creating a new version of *CPmap* which better handles the alignment of grid points in the separate single-point DFT calculations. The integration procedure is also updated, employing electron

density-based Hirshfeld-style[14] criteria for determining borders of the contact volumes, over the former geometric criteria. This work also details how these improvements yield interpretable data for formerly troublesome compounds in the $MgCu_2$ type, as well as the $AuBe_5$ type. We use DFT-CP analysis to compare the advantages of two common AB_5 structure types, the $AuBe_5$ type and the $CaCu_5$ type, ultimately breathing life into the radius ratio arguments of earlier empirical structural studies.

In Chapter 7, we see that the structural plasticity of the $CaCu_5$-type is not limited to Ca_2Ag_7 and $CaCd_6$. Here we examine the multiple paths for destruction of a $CaCu_5$-type lattice as larger atoms on the transition metal site makes Ca-TM distances too long, and we are able to draw conclusions about the plasticity of the system as a whole. The rearrangements seen in Ca_2Ag_7, $Ca_{14}Cd_{51}$, and $CaCd_6$ represent three different responses to the negative chemical pressure on calcium; Ca_2Ag_7 preserves 2-dimensional slabs of the original structure, $Ca_{14}Cd_{51}$ maintains 1-dimensional columns, and $CaCd_6$ isolates the calcium-centered polyhedra with the addition of extra cadmium atoms. We revisit the quasicrystalline approximant phase to complete our investigation of the structural plasticity of the $CaCu_5$-type, with all of the variants mentioned motivated by response to the negative chemical pressure on the calcium atom. The progression of structural destruction that we find here is not linear as expected; rather, these three compounds branch the progression into a family tree, reflecting the rich diversity of possibilities for structural rearrangements in response to chemical pressure.

The final chapter of this thesis intends to speak to a broader audience. The importance of fundamental scientific studies is not often presented to the general public. Most newsworthy science is couched in connections to everyday applications, but those works are ultimately based on the fundamental investigations of predecessors in the field. The invisibility of this foundation of fundamental

science to the general public perpetuates the difficulty of funding basic research, endangering the integrity of the network that enables our innovation and discovery. Chapter 8 presents a summary of the contents of this thesis work, written in common language for a non-scientist in comic book format, with hand-drawn illustrations. It is the hope that this chapter will inspire the respect, joy, and wonder that is essential to the pursuit of fundamental science.

1.5 References

(1) Blanc, M. L.; Richter, K.; Schiebold, E. *Ann. der Phys.* **1928**, *391*, 929–1005.

(2) Friauf, J. B. *J. Am. Chem. Soc.* **1927**, *49*, 3107–3114.

(3) Takakura, H.; Gómez, C. P.; Yamamoto, A.; De Boissieu, M.; Tsai, A. P. *Nat. Mater.* **2007**, *6*, 58–63.

(4) Tsai, A. P.; Guo, J. Q.; Abe, E.; Takakura, H.; Sato, T. J. *Nature* **2000**, *408*, 537–538.

(5) Marakov, E. S. *Dokl. Akad. Nauk. SSSR* **1950**, *74*, 935–938.

(6) Berns, V. M.; Stacey, T. E.; Sapiro, M.; Fredrickson, D. C. *Eur. J. Inorg. Chem* **2011**, *2011*, 3936–3949.

(7) Pauling, L. *J. Am. Chem. Soc.* **1927**, *49*, 765.

(8) Smith, M.; March, J. *March's Advanced Organic Chemistry: Reactions, Mechanisms, and Structure*; Wiley-Interscience: Hoboken, NJ, 2007.

(9) Van der Waals, J. D. *Nobel Lectures, Physics 1901-1921*; Elsevier Publishing Company: New York, NY, 1967.

(10) Fredrickson, D. C. *J. Am. Chem. Soc.* **2011**, *133*, 10070–10073.

(11) Engelkemier, J.; Berns, V. M.; Fredrickson, D. C. *J. Chem. Theory Comput.* **2013**, *9*, 3170–3180.

(12) Fredrickson, D. C. *J. Am. Chem. Soc* **2012**, *134*, 5991–5999.

(13) Samson, S. *Acta Cryst* **1965**, *220*, 401–413.

(14) Hirshfeld, F. L. *Theor. Chim. Acta* **1977**, *44*, 129–138.

Chapter 2.

$Mg_{11}Cu_6Al_{12}$, A New Link in the Structural Chemistry of $MgCu_2$-type Clusters

This chapter has been published: Berns, V.M.; Stacey, T.E.; Sapiro, M.; Fredrickson, D.C. *Eur. J. Inorg. Chem.* **2011**, *26*, 3936-3949.

2.1. Abstract

We report the synthesis and crystal structure of a new phase in the Mg-Cu-Al system: $Mg_{11}Cu_6Al_{12}$. This compound crystallizes in the $K_{17}In_{41}$ structure type. When written as $Mg_{17-x}Cu_xAl_{12}$, x=6, the composition of this phase foretells a connection to $Mg_{17}Al_{12}$ (α-Mn type). The structures of both can be constructed from 29-atom fragments of the $MgCu_2$ structure type. They differ in the orientations of these fragments: the $Mg_{11}Cu_6Al_{12}$ structure is obtained when half of the $MgCu_2$-type clusters of $Mg_{17}Al_{12}$ are rotated by 90°. Electronic structure calculations using density functional theory (DFT) and the extended Hückel (eH) method point to driving forces for this structural transformation. Density of states (DOS) curves calculated for $Mg_{11}Cu_6Al_{12}$ in the two structure types indicate that both are stabilized by DOS minima close to the Fermi energy, with the pseudogap being deeper for the observed structure. An eH relative Mulliken population analysis reveals that cluster rotation also changes the electronic character of the outermost sites of the $MgCu_2$-type fragments: six atoms per formula unit go from being ambiguous to anionic, and thus suitable to occupation by relatively electronegative elements.

These are the positions occupied by Cu in $Mg_{11}Cu_6Al_{12}$. The creation of these six anionic sites adapted to occupation by Cu provides an impetus for cluster rotation. The removal of ambiguity of the outermost sites of the $MgCu_2$-type fragments creates extended networks of anionic and cationic sites in $Mg_{11}Cu_6Al_{12}$. The cationic sites trace out the clathrate II framework noted by Corbett and coworkers in the $K_{17}In_{41}$-type, while the anionic sites ensheathe this framework to complete Friauf polyhedra around the framework atoms.

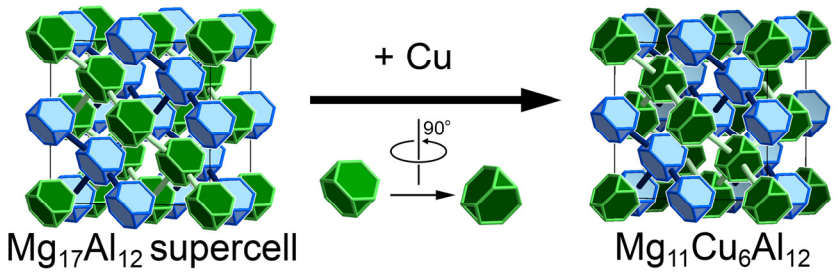

Figure 2.0. The substitution of magnesium with copper atoms in $Mg_{17}Al_{12}$ creates a 2×2×2 supercell adopted by $Mg_{11}Cu_6Al_{12}$, in which half of the $MgCu_2$-type clusters of the former are rotated by 90°. Relating the structures of these phases to the simple, ubiquitous Laves phases through structural and quantum mechanical analysis leads to an explanation of the driving force for this structural transformation, and shows that complex structures can have simple origins.

2.2. Introduction

Perhaps the first indication of the diversity in the field of intermetallic phases is found in Linus Pauling's X-ray diffraction investigations of $NaCd_2$ in 1923.[1] It would be almost 40 years of developing experience with intermetallics before Linus Pauling's associate Sten Samson would solve the structure of this phase, revealing a giant F-centered cubic unit cell of 30.56 Å containing more than one thousand atoms.[2,3] Since then, the theme of giant cubic unit cells has continued to expand. $NaCd_2$ has been joined by not only the closely related structures of β-Mg_2Al_3[4] and Cd_3Cu_4,[5] but also by the exponentially more

complex structures of $Al_{56.5}Cu_{3.9}Ta_{39.5}$ (*cF*5908) and $Al_{55.4}Cu_{5.4}Ta_{39.1}$ (*cF*23134).[6,7] Our ability to solve the complex crystal structures of these phases has greatly improved since Pauling's original experiments on $NaCd_2$, but the chemical bonding factors underlying the formation of these incredible structures remain mysterious.

In this paper, we describe an attempt to probe their origins experimentally. This attempt is based on the observation of a shared feature of these phases: they all contain large blocks of the cubic Laves phase structure type, the $MgCu_2$ type. We wondered how tunable these blocks might be, and whether it is possible to enlarge or shrink them through, say, elemental substitution. A simple way to approach this would be to examine ternary systems which contain both Laves phases and one of these complex cubic structures. For instance, the Mg-Cu-Al system contains both the classic Laves phase $MgCu_2$ and the monumental β-Mg_2Al_3 compound, as well as other phases based on Laves structure fragments, such as $Mg_{17}Al_{12}$ (ordered variant of the α-Mn type),[8,9] $Mg_{23}Al_{30}$,[10] and the low temperature rhombohedral form of Mg_2Al_3, the β' phase.[11] Mg atoms and Cu/Al atoms play similar roles in all of these phases: the Mg atoms form the vertices of diamondoid (D) networks, while the Al/Cu atoms trace out networks including truncated tetrahedra (TT). Could partial replacement of Cu for Al in the Mg-Al phases enlarge their $MgCu_2$-type fragments?

After asking this question, we were excited to find that the Mg-Cu-Al phase diagram exhibits a phase with an unknown crystal structure, $Mg_6Cu_3Al_7$,[12-14] and we set out to synthesize it and solve its structure. As we will describe below, this endeavor resulted in crystals of the new phase $Mg_{11}Cu_6Al_{12}$, a ternary variant of the $K_{17}In_{41}$ structure type[15-17] as shown in Figure 2.1. In our examination of its crystal structure, we realized that we had, in the words of Prof. John Corbett, done the right experiment for the wrong reasons. We will see that, rather than leading to a path between the Laves phases and Samson's giant

cubic phase β-Mg_2Al_3, $Mg_{11}Cu_6Al_{12}$ reveals an intimate link between two structures based on $MgCu_2$-type fragments: the $K_{17}In_{41}$ and the α-Mn structure types. In doing so, this phase will show us one mechanism by which complex intermetallic superstructures can have simple origins.

2.3. Synthetic results: Identification of $Mg_{11}Cu_6Al_{12}$

As we described above, our original synthetic target was the $Mg_6Cu_3Al_7$ phase indicated by the Al-Mg-Cu phase diagram,[12-14] whose 12.09 Å body-centered cubic unit cell was originally assigned from X-ray diffraction data by Mirgalovskaya in 1951,[18] and was more recently observed in electron diffraction data.[19,20] The results of our synthetic work (described in detail in the Technical Procedures section at the end of this paper) could be readily understood from the position of the $Mg_6Cu_3Al_7$ composition being under the primary phase-field of Laves phase structures. Syntheses involving slow cooling from a molten mixture of the elements resulted in multi-phase samples, from which crystals for single crystal X-ray diffraction work could be obtained. Quenching from the melt followed by annealing below the liquidus provided samples with much greater phase purity, with the principle impurity being a $MgZn_2$-type phase which presumably crystallized out as the sample passed through the liquidus during the quench. The only crystals observed under these synthetic conditions were of the $MgZn_2$-type phase.

The powder X-ray diffraction patterns exhibited peaks which matched some of the low angle peaks reported for the $Mg_6Cu_3Al_7$ phase in the ICDD Powder Diffraction File. However, in our single crystal X-ray diffraction analysis of numerous crystals we never obtained this cell. Instead, we repeatedly encountered a 20.1 Å cubic unit cell, as well as a 5.6 Å×5.6 Å×8.4 Å hexagonal unit cell. After collecting full data sets and carrying out structure solutions and refinements (see experimental procedures) on

crystals of these phases, the cubic cell was revealed to belong to a phase whose atomic positions matched the $K_{17}In_{41}$ type. The hexagonal cell was found to belong to a $MgZn_2$-type structure. WDS measurements gave approximant compositions for these phases as respectively $Mg_{11.30(11)}Cu_{6.00(9)}Al_{12.86(11)}$ and $Mg_{32(2)}Cu_{38(4)}Al_{30(6)}$. Virtually all peaks in the experimental powder patterns for our highest purity samples could be assigned to one of these phases.

One interpretation of these results can be found by comparing our synthetic conditions with the original conditions used by Mirgalovskaya in the preparation of $Mg_6Cu_3Al_7$.[18] Mirgalovskaya's synthesis involved annealing at 400 °C for 45 days, whereas the minimum annealing temperature in our syntheses so far has been 450 °C. It seems possible that Mirgalovskaya's $Mg_6Cu_3Al_7$ compound is a lower temperature phase occurring below the liquidus.

2.4. The crystal structure of $Mg_{11}Cu_6Al_{12}$ by comparison with $Mg_{17}Al_{12}$

While our initial goal was to investigate $Mg_6Cu_3Al_7$, our focus shifted to the new $Mg_{11}Cu_6Al_{12}$ phase we encountered. This phase crystallizes in the $K_{17}In_{41}$ type, a structure type that has been described in a variety of ways: in terms of Bergman clusters,[21] as a framework of deltahedral clusters connected via exo-bonds,[22] as being built from $MgCu_2$-type fragments,[23] and in terms of a clathrate II framework.[24] Our original interest in the Mg-Cu-Al ternary system was due to its potential to bridge the Laves phase fragments in the Al-Mg system and the classic $MgCu_2$ Laves phase in the Mg-Cu system. This leads us to seek structural connections between $Mg_{11}Cu_6Al_{12}$ and these known compounds. Looking through the list of Al-Mg phases reveals a compound with a close compositional relationship to the new $Mg_{11}Cu_6Al_{12}$ phase: $Mg_{17}Al_{12}$. The $Mg_{11}Cu_6Al_{12}$ stoichiometry can be obtained from $Mg_{17}Al_{12}$ by simply replacing six

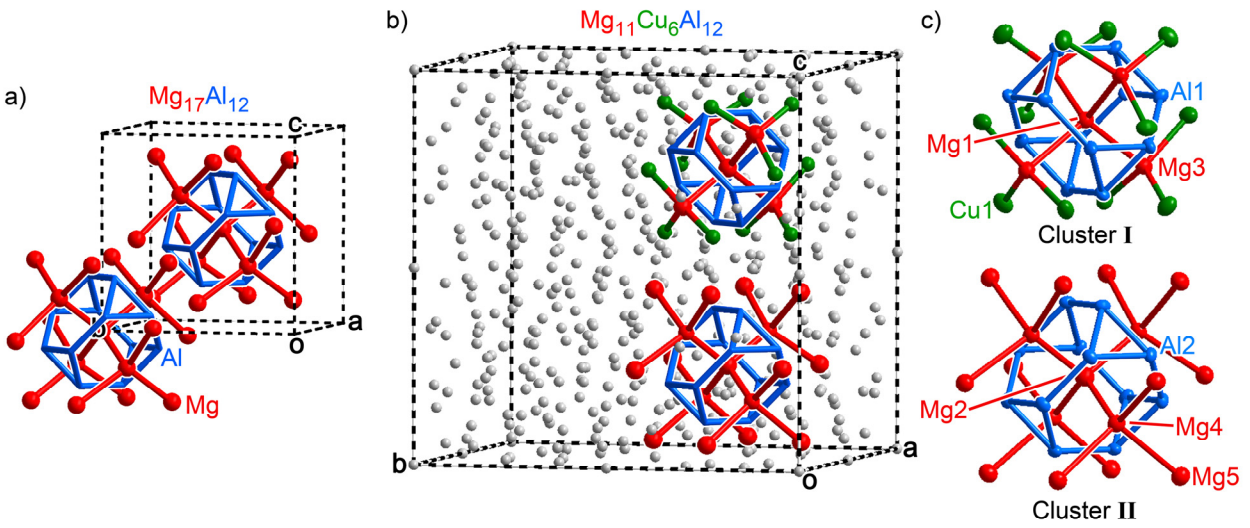

Figure 2.1. $MgCu_2$-type fragments in the $Mg_{17}Al_{12}$ (α-Mn-type) and $Mg_{11}Cu_6Al_{12}$ structures. (a) The crystal structure of $Mg_{17}Al_{12}$, with the $MgCu_2$-type fragments at one unit cell corner and the cell center drawn. Red spheres indicate Mg atoms corresponding to Mg-occupied positions in the $MgCu_2$ type, and blue bars trace out trace out connections between Al atoms, which correspond to Cu-occupied positions in the $MgCu_2$ type. (b) The two symmetry distinct $MgCu_2$-type fragments in $Mg_{11}Cu_6Al_{12}$, presented in the context of the full unit cell. Both are closely analogous to the fragments in (a). (c) The $MgCu_2$-type fragments of $Mg_{11}Cu_6Al_{12}$ drawn individually, with site labels, and thermal ellipsoids plotted at the 99% probability level. Each symmetry inequivalent site belongs to one of these two fragments.

Mg atoms with Cu.

This similarity in stoichiometry stems from a deeper structural relationship between these two phases. Let's start by reviewing the structure of $Mg_{17}Al_{12}$. This phase forms an ordered binary variant of the α-Mn structure. A simple, quantum mechanically derived way of viewing this structure has previously been presented.[23] In this view, the structure is constructed from fragments of the simple $MgCu_2$ type (Figure 2.1a). These fragments can be decomposed into two networks: truncated tetrahedra (TT) corresponding to Cu-occupied sites in the $MgCu_2$-type (blue), and diamondoid (D) networks (red) interpenetrating the TT network corresponding to Mg-occupied sites in the $MgCu_2$ type.

Each fragment contains 12 Al atoms on the TT sites, and 17 Mg atoms on the Mg sites to give the phase's $Mg_{17}Al_{12}$ stoichiometry. This model accounts for all atoms in the unit cell uniquely.

Analogous 29-atom $MgCu_2$-type fragments can be identified in the $Mg_{11}Cu_6Al_{12}$ phase. Two symmetry inequivalent fragments occur, labeled as clusters **I** and **II**. These are shown in the context of the full unit cell in Figure 1b, and separately with thermal ellipsoids in Figure 1c. Just as in $Mg_{17}Al_{12}$, all symmetry inequivalent sites of the structure can be mapped to these 29-atom $MgCu_2$-type fragments. It then becomes natural to discuss $Mg_{11}Cu_6Al_{12}$ in terms of its differences from the structure of $Mg_{17}Al_{12}$. These can be expected to be of two kinds: (1) differences in the details of the $MgCu_2$ fragments, and (2) differences in their packing to form the full unit cell of the structure. Differences of the first kind are readily apparent in Figure 2.1.

Whereas cluster **II** shows a close correspondence to the $Mg_{17}Al_{12}$ cluster, with all TT sites being occupied by Al and all the D sites with Mg, cluster **I** shows a somewhat different site-coloring. All TT sites are still occupied by Al, and in the innermost D sites are still filled by Mg, but now the outermost D sites are occupied by Cu. This distribution of both Mg and Cu over the D sites and the exclusive occupation of TT sites by Al leads to the $(Mg/Cu)_{17}Al_{12}$ stoichiometry noted above.

The differences in the packing of these clusters are shown in Figure 2.2. These differences can be simply derived with the following construction: We begin with a 2×2×2 supercell of $Mg_{17}Al_{12}$, as shown in Figure 2.2a. Here we've taken a simplified view in which the $MgCu_2$-fragments are abbreviated as truncated tetrahedra. We then resolve the body-centered packing of fragments into two interpenetrating diamond networks, one drawn in blue, the other in green. These two networks are drawn separately in Figures 2.2b and 2.2c. Next, we rotate each of the clusters in the network in green 90° about the *c*-axis,

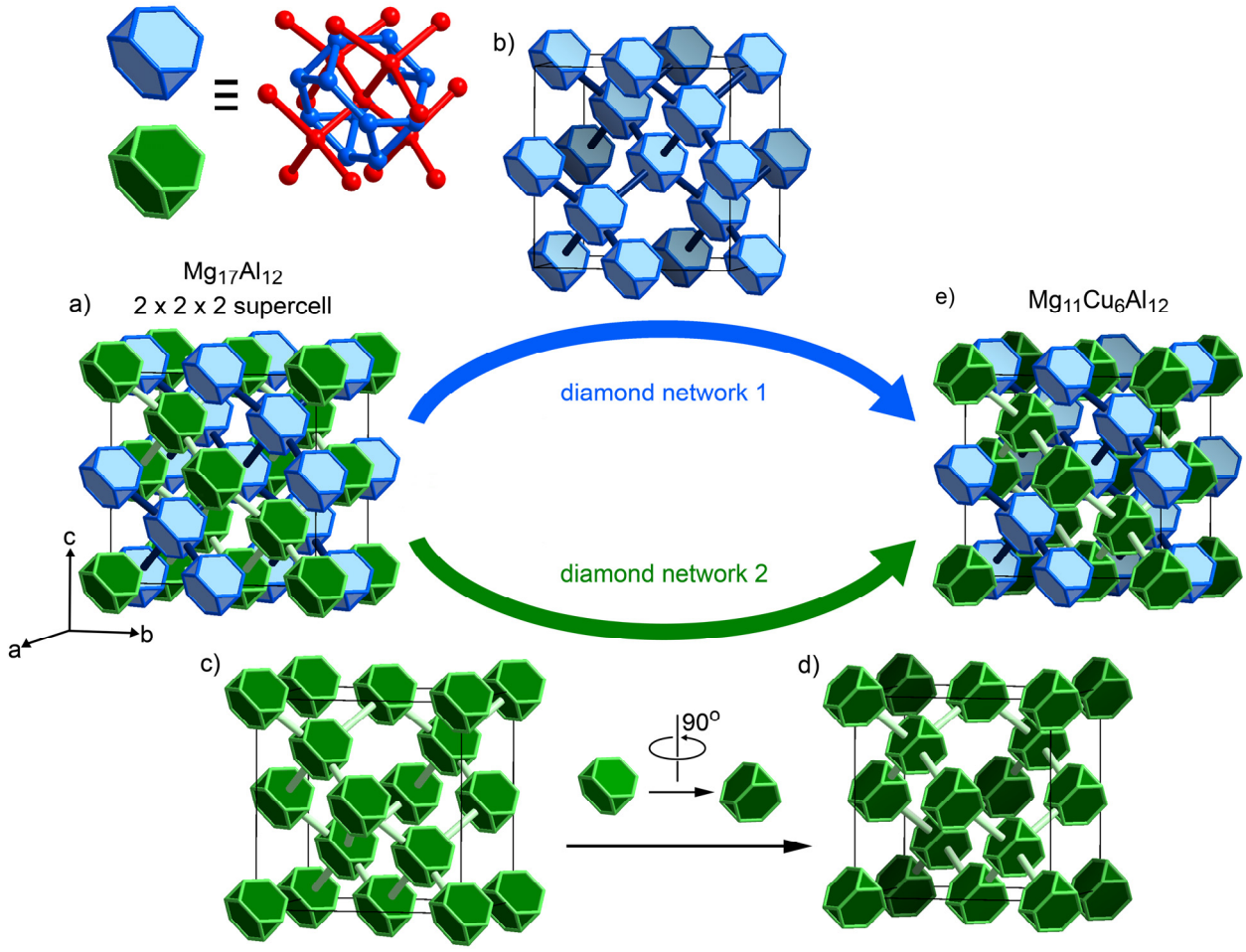

Figure 2.2. The structural transformation connecting $Mg_{17}Al_{12}$ (α-Mn-type) to $Mg_{11}Cu_6Al_{12}$. (a) A 2×2×2 supercell of $Mg_{17}Al_{12}$, with two diamond networks of $MgCu_2$-type clusters (abbreviated here as truncated tetrahedra) differentiated with blue (diamond network 1) and green (diamond network 2). (b) Diamond network 1 remains unchanged during the transformation. (c) The $MgCu_2$-type clusters of the diamond network 2 are rotated 90° about the *c*-axis to produce (d) a new diamond network with its $MgCu_2$-type clusters in a new orientation. (e) Recombining the unchanged network 1 with the transformed network 2 results in the $MgCu_2$-type cluster packing of $Mg_{11}Cu_6Al_{12}$ structure.

creating a new diamond network with the fragments in a new orientation (Figure 2.2d). Finally, we remerge the two diamond networks—one unchanged, one with rotated fragments—into a double diamond framework to arrive at the fragment packing of $Mg_{11}Cu_6Al_{12}$ (Figure 2.2e).

This transformation has consequences for the symmetry of the structure. In $Mg_{17}Al_{12}$, the networks drawn in blue and green are made equivalent by the lattice translations of the crystal. Cluster rotation to produce $Mg_{11}Cu_6Al_{12}$ breaks this translational symmetry, generating a $2 \times 2 \times 2$ supercell. The blue and green networks are no longer translationally equivalent. Instead, they are now related through the *d*-glides of the $Fd\bar{3}m$ space group.

What is accomplished in terms of increased stability through the transformation? In the next sections, we will begin to see clues to the answer of this question, as we investigate the electronic structure of $Mg_{11}Cu_6Al_{12}$ through theoretical calculations using both Density Functional Theory (DFT) and the semi-empirical extended Hückel method.

2.5. Pseudogap stabilization of $Mg_{11}Cu_6Al_{12}$

In the above structure analysis, we uncovered a simple relationship between the crystal structure of the newly determined $K_{17}In_{41}$-type phase $Mg_{11}Cu_6Al_{12}$ and that of $Mg_{17}Al_{12}$. The atomic positions for the former may be obtained from the latter by a rotation of half of its $MgCu_2$-type clusters by 90° about the *c*-axis. By comparing the stoichiometries of the two compounds, it appears that this rotation is driven by the substitution of 6 Mg atoms/formula unit with Cu. How does such a substitution drive this structural change? Previous work on the $K_{17}In_{41}$ structure type suggests that electron count may be playing a role here. In their analysis of the isostructural phase $Mg_{35}Cu_{24}Ga_{53}$, Lin and Corbett found that this structure can be viewed as a network of deltahedral clusters interconnected by exo-bonds, with spectator atoms occupying the interstitial spaces of this network.[22] This suggested that the Zintl approach, employing the Wade-Mingos rules to the expected electron counts of the deltahedral clusters, should be applicable.

The valence electron count was indeed very close to that predicted from the Zintl model, with the mismatch in electron counts being only 0.22 or 0.54 %, depending on the sample.

As Mg is substituted with Cu to go from $Mg_{17}Al_{12}$ to $Mg_{11}Cu_6Al_{12}$, each atom replaced lowers the valence electron count by one (viewing Mg and Cu as respectively $3s^2$ and $4s^1$ metals). One hypothesis for the origin of the structural transformation is that this lowering of the electron count tunes the E_F to match a pseudogap for the electronic density of states (DOS) curve for the $K_{17}In_{41}$-type structure. To explore this possibility, we performed GGA-DFT calculations on a series of structures connecting $Mg_{17}Al_{12}$ to $Mg_{11}Cu_6Al_{12}$: (1) $Mg_{17}Al_{12}$, (2) a phase with the composition $Mg_{11}Cu_6Al_{12}$ but the α-Mn-type structure of $Mg_{17}Al_{12}$, with Cu atoms placed on the outermost D sites of one of the two $MgCu_2$-type fragments in the body-centered unit cell, and (3) the $Mg_{11}Cu_6Al_{12}$ structure. Calculation of DOS curves was performed for each phase on structures energy-minimized with GGA-DFT (the details of the calculations are provided in the Appendix).

The DOS curves from the DFT-optimized structures are presented in Figure 2.3. Perhaps the most notable differences occurring among these curves is the presence of a sharp DOS peak at ca. -9 eV for those structures containing Cu, and its absence in those structures without Cu. This peak corresponds to the Cu 3*d* orbitals, whose narrow distribution along the energy axis suggests that they may be considered as largely core-like.

When the presence or absence of the Cu 3*d* peak is disregarded, the DOS curves display some similarity. Each of them shows a largely parabolic distribution, characteristic of nearly-free-electron *sp* states. Each curve also shows a DOS depression near the E_F at about -5.5 eV, suggestive of a special stability at these electron counts. The deeper pseudogap afforded by $Mg_{11}Cu_6Al_{12}$ in the $K_{17}In_{41}$-type

would be expected to provide a driving force for the structural transition.

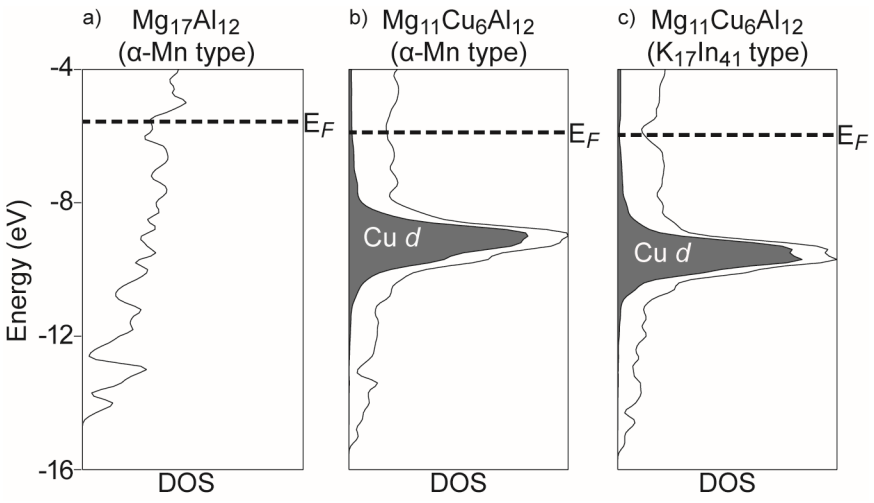

Figure 2.3. Density of states (DOS) curves calculated at the GGA-DFT level for (a) $Mg_{17}Al_{12}$ in its α-Mn-type structure, (b) $Mg_{11}Cu_6Al_{12}$ in the α-Mn type, and (c) $Mg_{11}Cu_6Al_{12}$ in the experimentally observed $K_{17}In_{41}$ type. The Fermi energy (E_F) for each is represented with a dashed line. Note that in all three DOS curves, the E_F lies in a depression of the DOS. This pseudogap is optimized for $Mg_{11}Cu_6Al_{12}$ in the $K_{17}In_{41}$ type (c). In (b) and (d), the shaded areas give the projected density of states for the Cu *d* states. In order to bring out the overarching features of the DOS distributions, the presented curves have been treated with Gaussian broadening.

2.6. Relative Mulliken population analysis of the $MgCu_2$-type clusters in $Mg_{11}Cu_6Al_{12}$

A much simpler quantum mechanical approach—the relative Mulliken population analysis—can lead us to a more dramatic driving force for the structural transition. In this approach, one uses quantum mechanical calculations (usually of the extended Hückel type) on an elemental model of a phase to probe the impetus for elemental substitution in its structure. This technique was pioneered in the field of

organic chemistry,[25,26] where it was noted that carbon atoms appearing as (slightly) anionic in an elemental calculation were found to be most easily substituted by more electronegative heteroatoms, while those showing cationic charges were most easily replaced by more electropositive elements. This observation was termed Topological Charge Stabilization (TCS). Later, this approach was applied to intermetallic phases, providing insights into and predictions of site-preferences,[27,28] and guidance for those navigating the multitude of possible descriptions of complex crystal structures.[23,29,30]

Let's start with a review of what this type of analysis tells us about the $Mg_{17}Al_{12}$ structure,[23] for contrast with the results we will find for $Mg_{11}Cu_6Al_{12}$. For this analysis, we first perform an extended Hückel (eH) calculation on an elemental model of $Mg_{17}Al_{12}$, with the valence electron concentration adjusted to match that of $Mg_{17}Al_{12}$, i.e. $(2\times17+3\times12)/(17+12) = 2.41$ electrons/atom. This is envisioned as representing a version of this phase without Al/Mg ordering, but in practice is achieved by beginning with Al eH parameters and tuning them to achieve a qualitative match with a band structure calculated with DFT. After the eH calculation is carried out, Mulliken populations are extracted, and charges are calculated relative to the average electron count, yielding relative Mulliken populations.

The result for $Mg_{17}Al_{12}$ is plotted in Figure 2.4a, where following earlier conventions, the relative Mulliken populations are represented with spheres. White spheres indicate sites that are more anionic than the average electron count, while black spheres indicate those that are more cationic that the average. The volumes of the spheres are proportional to the magnitudes of the charges. In this plot, the differences in electronic character between the atoms of the TT sites and the D sites are readily apparent. The TT sites are exclusively decorated by white spheres, indicating that these are relatively anionic. The D sites, on the other hand, are decorated with black spheres; these are relatively cationic.

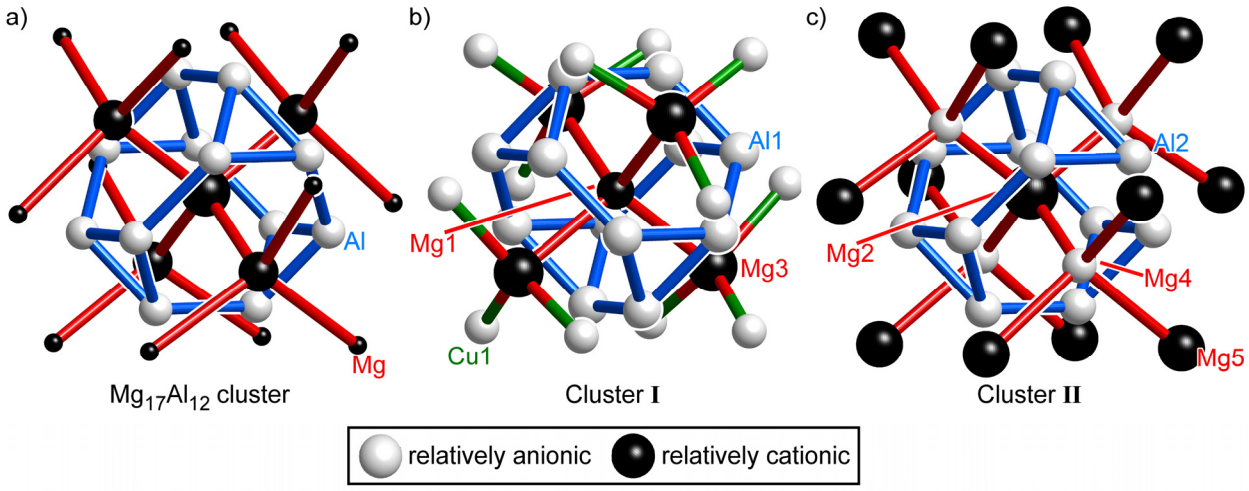

Figure 2.4. Relative Mulliken population distributions over the $MgCu_2$-type fragments occurring in (a) $Mg_{17}Al_{12}$ and $Mg_{11}Cu_6Al_{12}$ at the (b) cluster **I** and (c) cluster **II** positions. Mulliken populations were extracted from extended Hückel calculations on elemental models of the $Mg_{17}Al_{12}$ and $Mg_{11}Cu_6Al_{12}$ structures (see text for details). Sites that are anionic relative to the average electron count are indicated with white spheres, while relatively cationic sites are shown with black spheres. The magnitude of the relative charge is proportional to the sizes of the spheres. In general, the TT networks are drawn in blue, while D networks are shown in red. Due to the importance that Cu occupation will take in the story to come, Cu positions are indicated with green regardless of their assignment to TT or D networks. These conventions will be used throughout this chapter.

From this plot, several things can be learned about the electronic structure of this phase. First are the affinities of the sites for relatively electronegative vs. electropositive atoms. Following the logic of TCS, the most electronegative atoms are expected to go to the most electron-rich sites in an elemental calculation. This is indeed the case: of Al and Mg, Al is the more electronegative, and this element is observed to occupy the relatively anionic sites, while Mg is relegated to the remaining relatively cationic sites.

We also gain insights into structural connections between intermetallic structure types. The cationic D network interpenetrating an anionic TT network is also seen in the much simpler and more common $MgCu_2$ structure, where the D network extends throughout the structure as a full diamond lattice, and the TT network forms an infinite network of vertex-sharing tetrahedra. These networks appear in truncated form not only in $Mg_{17}Al_{12}$, but also in Mulliken population analyses of the more complex $NaCd_2$, and β-Mg_2Al_3 structures. Relative Mulliken population analysis places these phases into a structural series based on Laves phase fragments.

Finally, relative Mulliken population analysis provides us with a sense of the texture of the crystal structure. Near the centers of the $MgCu_2$-type fragments, the spheres representing relative charges are comparatively large, indicating that these sites show a strong preference for either Al or Mg. Toward the boundaries of the fragment, however, this preference becomes much weaker: the outermost atoms now exhibit tiny black spheres. This weaker preference can be traced to the geometry at the interfaces between clusters. While these sites are drawn connected to the D networks of their $MgCu_2$-type fragments, they can also be viewed as continuing the TT networks of the neighboring clusters (Figure 2.5a). This ambiguity leads to a difference in bonding character between the more central atoms of the cluster, where sites are relatively polar (relative Mulliken populations larger in magnitude, whether positive or negative), and the outer atoms of the cluster, where sites are relatively nonpolar (relative Mulliken populations smaller in magnitude).

To what extent do these conclusions also apply to $Mg_{11}Cu_6Al_{12}$? In Figures 2.4b and 2.4c, we overlay spheres corresponding to relative Mulliken populations on the sites of clusters **I** and **II** of this phase, respectively. For both clusters, similarities and differences are seen when compared to the fragments in $Mg_{17}Al_{12}$ and to each other. In all three clusters, the central D atom appears as cationic, and the

surrounding TT sites are relatively anionic. The main differences are seen in the charges of the sites further from the fragment centers. While the D sites immediately adjacent to the central site are cationic as expected in cluster **I**, the corresponding sites in cluster **II** now appear as anionic. The outermost sites show differences that are just as significant: the small black spheres at the fringes of the fragment in $Mg_{17}Al_{12}$ have given rise in $Mg_{11}Cu_6Al_{12}$ to large black spheres for cluster **II** and large white spheres for cluster **I**. The nonpolar cluster exterior sites of $Mg_{17}Al_{12}$ have split into two types of polar sites in $Mg_{11}Cu_6Al_{12}$ with opposite charges. During the transformation between these two structure types presented in Figure 2.2, the ambiguities in the assignments of these sites seem to have been resolved.

2.7. New connectivities at the interfaces between $MgCu_2$-type clusters

Evidently, quantum mechanics is directing us to reevaluate our descriptions of the atoms at the fragment exteriors in $Mg_{11}Cu_6Al_{12}$. To do this, we now change our focus from individual clusters to the interfaces between them. In $Mg_{17}Al_{12}$, only one type of interface occurs: each triangular face of the TT of one cluster lies opposite to a hexagonal face of the TT network of a neighboring cluster (Figure 2.5a). In $Mg_{11}Cu_6Al_{12}$, by contrast, several different types of interfaces are present. As we saw in Figure 2.2, the packing of $MgCu_2$ clusters in this phase can be represented by two interpenetrating diamond networks, related by *d*-glide symmetry. Within each of these networks the interfaces remain closely analogous to those in $Mg_{17}Al_{12}$: TT triangles face TT hexagons with Friauf polyhedra occurring at the interface. Between the clusters of different networks, on the other hand, new interfaces arise. At half of these interfaces, TT triangles face TT triangles; at the other half TT hexagons meet TT hexagons. We will designate these interface types as respectively triangle-facing-hexagon (TfH), triangle-facing-triangle (TfT), and hexagon-facing-hexagon (HfH).

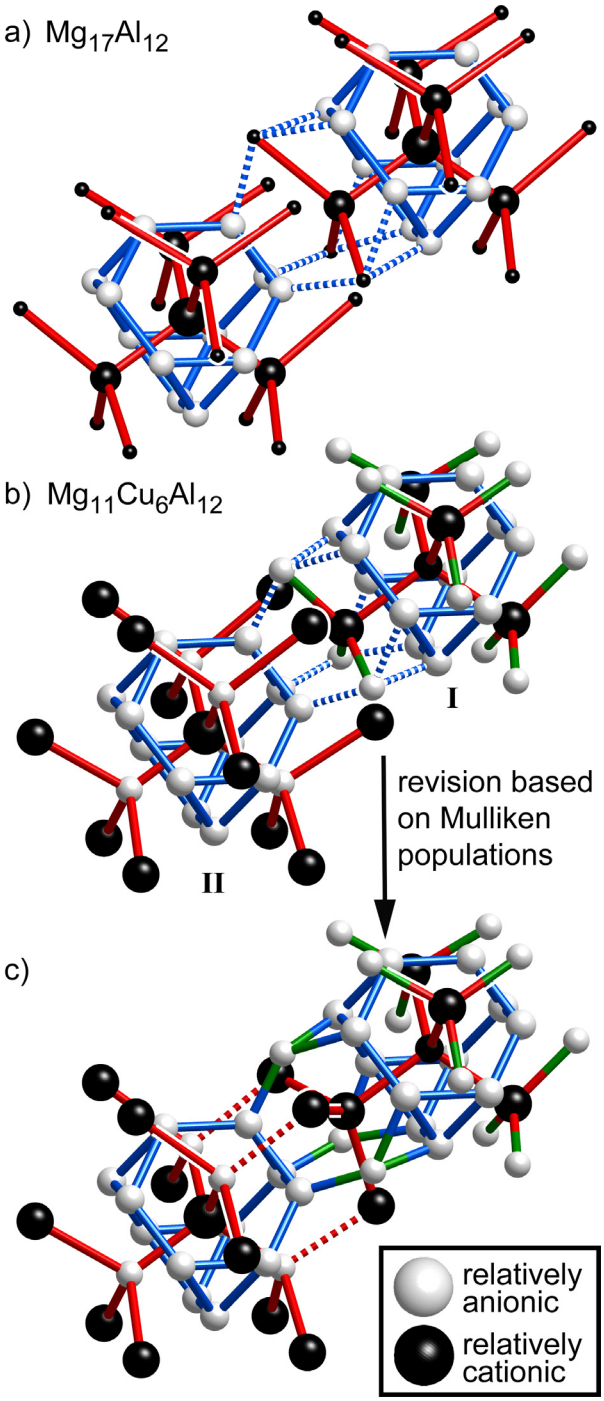

Figure 2.5. The triangle-facing-hexagon (TfH) interfaces between $MgCu_2$-type fragments in $Mg_{17}Al_{12}$ and $Mg_{11}Cu_6Al_{12}$. (a) Mulliken population analysis of TfH interfacial regions in $Mg_{17}Al_{12}$. (b) Mulliken population analysis of the $MgCu_2$-type clusters meeting at a TfH interface in $Mg_{11}Cu_6Al_{12}$, and (c) revised site network assignments based on the signs of the relative Mulliken populations. See caption to Figure 2.4 for plotting conventions.

Let's begin with the interface type shared with the $Mg_{17}Al_{12}$ structure, the TfH interface. In Figure 2.5, we show two clusters meeting at one of these interfaces for both the $Mg_{17}Al_{12}$ (Figure 2.5a) and the $Mg_{11}Cu_6Al_{12}$ (Figure 2.5b) structures. In both structures, the outermost D sites of the clusters coming from the left and right play different roles at this interface. Those from the right cluster form contacts that bridge the TT networks of the two clusters, as is shown with dashed blue lines. These complete a new TT at the interface. The outermost D sites of the left cluster belong to a D network that threads through the interfacial TT network. Together these features form a Friauf polyhedron at the cluster interface in both structures.

Despite these geometrical similarities, the relative Mulliken populations at the TfH interfaces show significant differences between $Mg_{17}Al_{12}$ and $Mg_{11}Cu_6Al_{12}$. In $Mg_{17}Al_{12}$ (Figure 2.5a), the symmetry equivalence of the outermost D sites means that they are not well-adapted to their roles in either the D network or the TT network. This is seen in their relative Mulliken populations, which appear here as tiny black spheres, with their small size indicating small magnitudes of relative charge. In $Mg_{11}Cu_6Al_{12}$ (Figure 2.5b), the clusters coming from the right and left are symmetry inequivalent. The one coming from the left is an instance of cluster **II**, while that from the right is an instance of cluster **I**. As these clusters are not related by symmetry, neither are their outermost D sites. This has a profound effect on the Mulliken populations. The sites contributing to the interfacial TT network from cluster **I** now show strong anionic character, while those contributing to the D network of the interfacial Friauf polyhedron show clear cationic character. Both changes are consistent with the assignment of these sites to the networks of the interfacial Friauf polyhedron.

From this analysis, we are led to revise our assignments of these interfacial sites in $Mg_{11}Cu_6Al_{12}$, as shown in Figure 5c. In this new view of the structure, the outermost D sites of cluster **II** remain assigned

as D sites, but are now viewed as unambiguously belonging to the D network connecting clusters **I** and **II**. The corresponding sites of Cluster **I** are now viewed as TT sites bridging the TT networks of the two clusters.

2.8. Another driving force for adopting the structure of $Mg_{11}Cu_6Al_{12}$

This is far from the last word that the Mulliken populations will have to tell us about the optimal description of this structure, but at this point we can already understand why this structure might be preferred over that of $Mg_{17}Al_{12}$ for the composition $Mg_{11}Cu_6Al_{12}$. Consider the creation of this phase beginning with $Mg_{17}Al_{12}$ and then substituting some of its Mg sites with Cu to attain the $Mg_{11}Cu_6Al_{12}$ stoichiometry. Cu is of greater electronegativity than both Al and Mg. If Cu is constrained to substitute for Mg as per the stoichiometry, it would be expected to substitute for the most electron-rich of the Mg-sites. These are the outermost D sites of the $MgCu_2$-type clusters. If the $Mg_{17}Al_{12}$ structure were to be retained, however, the structure would offer no differentiation between those sites to be occupied by Cu and those to remain Mg. Upon moving to the $Mg_{11}Cu_6Al_{12}$ structure type, this issue is solved with the resolution of the outermost D positions into two sets, one set more appropriate for relatively electronegative elements, the other set better suited to more electropositive elements.

This is indeed seen in the site occupancies. In $Mg_{11}Cu_6Al_{12}$, those outermost D sites that are now firmly established as electropositive D network atoms continue to be occupied by Mg. The sites that we have reassigned to interfacial TT networks, based on their clear anionic character in the Mulliken populations, are occupied by Cu atoms. The stability thus seems to be related to the removal of the ambiguity in the site identities of the outermost D atoms on going from the $Mg_{17}Al_{12}$ structure to that of $Mg_{11}Cu_6Al_{12}$.

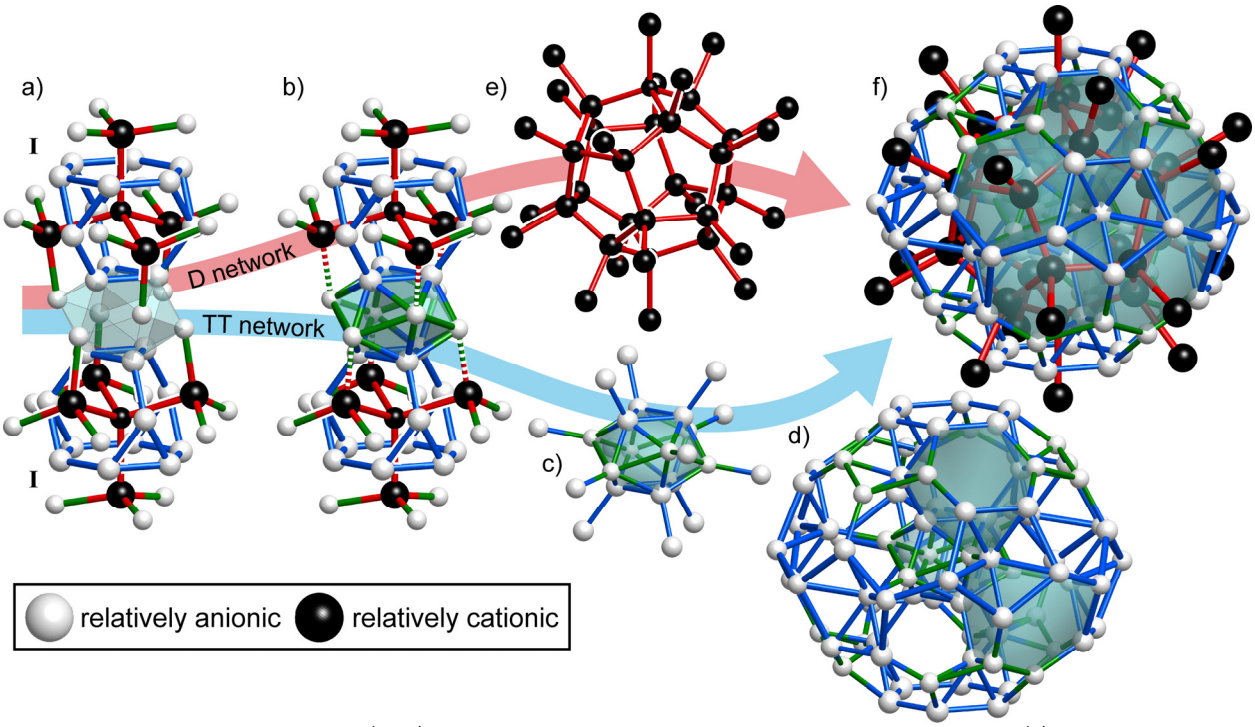

Figure 2.6. Triangle-facing-triangle (TfT) interfaces between $MgCu_2$-type fragments in $Mg_{11}Cu_6Al_{12}$. (a) TfT interfaces occur between two instances of cluster **I**. (b) Drawing connections between relatively anionic sites at the interface yields an empty icosahedron. (c)-(d) Following connections from this icosahedron to other anionic sites reveals a TT network consisting of a central icosahedron sharing all of its faces with truncated tetrahedra. The outer shell of this network is the familiar fullerene cage. (e) Tracing out the contacts between cationic sites surrounding the icosahedron in (b) creates a D network based on dodecahedra. (f) Combining the D and TT networks from (c)-(e) yields a Bergman cluster. Plotting conventions are given in the caption to Figure 2.4.

2.9. More interfaces, more new connectivities

What are the changes in the environments of these sites that have removed their ambiguous identities? To answer this question, we now turn to the remaining interface types in this structure: the HfH and TfT interfaces. These interfaces are shown, along with their Mulliken populations, in Figures 2.6 and 2.7, respectively. From looking at the identities of the clusters involved in the interfaces,

an important difference from the TfH interfaces becomes apparent. Whereas the clusters on opposites sides of the TfH interfaces were symmetry inequivalent—one being of the cluster **I** type, the other of the cluster **II** type—the clusters meeting at the HfH and TfT are now related by symmetry. At the TfT interfaces two type **I** clusters meet, while at the HfH interfaces two type **II** clusters face each other.

At the TfT interface, the Cu1 sites interdigitate and connect the triangular faces of their clusters to create an empty icosahedron (Figures 2.6a-b). This icosahedron forms the center of the Bergman clusters that have been noted previously in this structure type.[21] In fact, tracing out connections between anionic sites starting from this interface polyhedron leads to an icosahedron of truncated tetrahedra, each sharing a triangular face with this central icosahedron (Figures 2.6c-d). This is the TT network of a Bergman cluster. For the Cu1 sites, rather than have their TT character at the TfH interface deconstructively interfere with a D network at another interface as in the original $Mg_{17}Al_{12}$ structure, the TT character is reinforced by the larger structural context. In fact, their positions at the central icosahedron of a Bergman cluster means that each Cu1 site participates in not one but five truncated tetrahedra, one for each of the triangular faces of the icosahedron sharing that site.

The exclusive decoration of the Bergman cluster TT network by anionic sites in Figures 6c-d indicates that this cluster is an electronically important feature of the $Mg_{11}Cu_6Al_{12}$ structure. This is confirmed by a look at the Bergman cluster's D network (Figure 2.6e); all of the sites of this D network are relatively cationic. In Figure 2.6f, we show the full Bergman cluster with the relative Mulliken populations for each site. Again a clear segregation of the charges for the cluster is seen between a cationic D network and an anionic TT network.

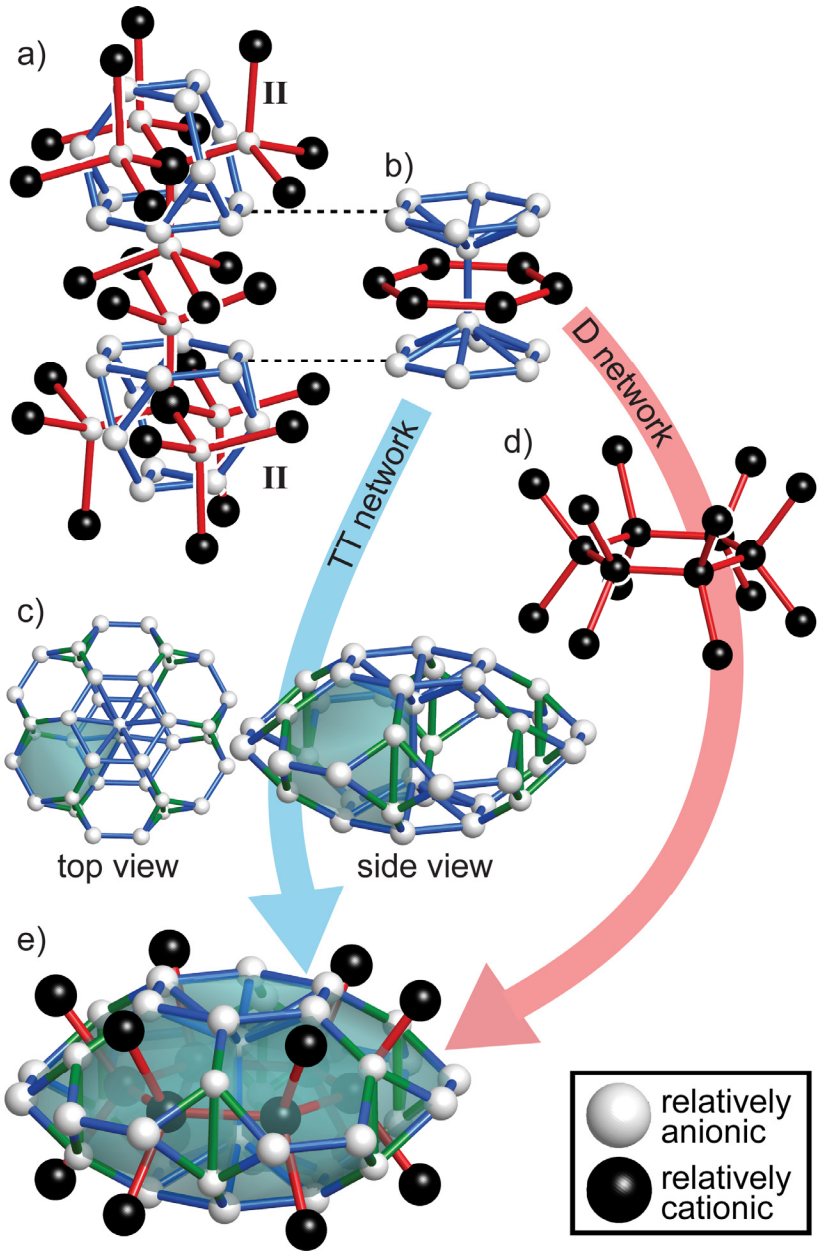

Figure 2.7. Hexagon-facing-hexagon (HfH) interfaces between $MgCu_2$-type fragments in $Mg_{11}Cu_6Al_{12}$. (a) Two instances of cluster II meeting at the HfH interface. (b) Assigning atoms at the interface to anionic and cationic networks constants reveals a grooved anionic hexagonal "car wheel," encircled by a cationic "tire." (c) Extending the TT contacts outward yields a hexagon of face-sharing truncated tetrahedra. (d) The D network that results from including further contains between cationic sites. (e) Merging the TT and D networks of (c) and (d) respectively creates a hexagonal ring of Friauf polyhedra. Conventions used in the plots are described in the caption to Figure 2.4.

From our analysis of the TfT interface, we have seen that the rotation of half of the $MgCu_2$-type clusters of the $Mg_{17}Al_{12}$ structure to create $Mg_{11}Cu_6Al_{12}$ has yielded a host of new Friauf polyhedra. The same theme is also observed at the HfH interface. The joining of the two $MgCu_2$-type clusters at the HfH interface is shown in Figure 2.7. Here, the D networks of the two clusters interdigitate in a similar way to the interface between symmetrically inequivalent $MgCu_2$ type clusters in $NaCd_2$.[23] In $NaCd_2$, this type of interface was noted to form a fragment of the Al_3Zr_4 structure type. This description applies geometrically here as well, but in following the Mulliken populations, a quite different view emerges.

We begin by noting that the Mg4 sites just above and below the TT hexagonal faces at the interfaces exhibit relative Mulliken populations uncharacteristic of D network sites. Sites assigned to D networks usually appear as cationic in these calculations, but here the Mg4 sites show clear anionic character, suggesting that they should be reassigned as TT sites. In doing so, we seek out connections to other nearby TT sites, as shown in Figure 2.7b. The Mg4 sites become connected to each other and to the hexagonal faces of the TT networks above and below, effectively becoming the axle between a pair of hexagonal wheels. Upon making this change, the remaining D atoms at the interface are left unconnected, unless we search for other possible D-D connectivities. The interdigitation of the two D networks stemming from the two $MgCu_2$-type clusters allows for such new connections (Figure 2.7b); these trace out a hexagon around the pair of Mg4 sites.

From this close-up view, it is difficult to see how these patterns of relatively anionic and cationic sites should be interpreted. In Figures 2.7c-e, we zoom out to show the HfH interface sites in their larger structural context. Figure 2.7c displays contacts between the anionic interfacial sites and other nearby anionic sites between the two $MgCu_2$-type clusters. The double hexagonal wheel of Figure 2.7b manifests here as the intersection of six truncated tetrahedra arranged, via the sharing of hexagonal faces,

into a sixfold ring. Seeking out contacts from the interfacial cationic sites also yields familiar features. In Figure 2.7d, we trace out connections from these sites to their nearest cationic neighbors in the immediate surroundings. The new contacts complete tetrahedral coordination of the interfacial cationic sites by other cationic sites. This result is a hexagonal array of tetrahedra corresponding to a new D network.

When these anionic TT and cationic D networks are superimposed, the D network threads through the hexagonal faces of the TT network, creating Friauf polyhedra. The HfH interface thus serves at the meeting point of six Friauf polyhedra arranged in a ring. The Mulliken populations at this interface reflect their placement on either the TT (anionic) or D (cationic) networks of this ring of polyhedra.

From this conclusion, we can understand the somewhat puzzling appearance of Mg4 as an electron-rich site, despite its placement on the D network of one of the $MgCu_2$-type clusters originally identified in $Mg_{11}Cu_6Al_{12}$. The D network extending from the center of the $MgCu_2$-type cluster is just one network that the site takes part in. It also participates in the six truncated tetrahedra encircling the HfH interface. This TT network character dominates in the Mulliken population analysis. However, the partial D-character, while not apparent in the Mulliken population for the Mg4 site, may help explain why Mg occupies this site when the relative Mulliken population analysis predicts it to have an affinity for more electronegative atoms. Placement of Mg atoms at only the sites calculated as relatively cationic gives the stoichiometry $Mg_9(Cu/Al)_{20}$, quite Mg-deficient relative to the crystal structure's composition of $Mg_{11}(Cu/Al)_{18}$. The partial D-character of this site can be evoked to rationalize the placement of the excess Mg atoms on the Mg4 sites.

2.10. A quantum mechanically-derived view of $Mg_{11}Cu_6Al_{12}$, featuring a clathrate framework

Now that we have examined all of the interface types occurring in $Mg_{11}Cu_6Al_{12}$, we would like to make an observation. Unlike $Mg_{17}Al_{12}$, where the blurred identities of the outermost D sites of the $MgCu_2$ clusters creates the impression of isolated clusters, no clear boundaries have been found so far to the TT and D networks identified by relative Mulliken populations in $Mg_{11}Cu_6Al_{12}$. In fact, these networks extend throughout the whole crystal, as shown in Figure 8. In Figure 8a, we show first the D network formed from the cations. This forms a space-filling arrangement of pentagonal dodecahedra and hexakaidecahedra, the two polyhedra that make up the clathrate II structure. Indeed, this network is the very clathrate II framework of cations that Corbett and coworkers identified previously in the $K_{17}In_{41}$ type.[24,22]

The relatively anionic sites ensheathe this cationic clathrate network, providing each cationic site with truncated tetrahedral coordination by anions. The D-D contacts of the clathrate network then pass through the hexagonal faces of the TT network. With this view in hand, many features already noted in this structure become easily interpretable (Figure 2.8b). The Bergman clusters appearing at the TfT interfaces arise from the decoration of the dodecahedra of the clathrate framework with Friauf polyhedra. Similarly, the hexagonal rings of Friauf polyhedra identified at the HfH are created by the decoration of the hexagonal faces of the hexakaidecahedra.

Only one symmetry inequivalent site is yet to be accounted for in this clathrate framework description: the Mg2 site that forms the center of cluster **II**. In the D network of Figure 8b, these sites are represented by the isolated black spheres at the centers of the hexakaidecahedra. Recall that all of the Mg2 site's neighbors are anionic (Figure 2.4c). As such, it exhibits no connectivity with the other D network atoms.

As this site centers a $MgCu_2$-type cluster, its coordination environment is a Friauf polyhedron. All of

the other Friauf polyhedra in this structure can be described as decorating the clathrate framework. The presence of this one can also be explained from this point of view as follows: in the process of building the TT network around the D atom dodecahedron and hexakaidecahedra, each TT presents triangular faces toward centers of the clathrate cages that it straddles. In the case of the dodecahedron, the TT triangles meet at the center to produce the central icosahedron of the Bergman cluster. In the case of the hexakaidecahedra, however, the TT triangles meet to create a Friauf polyhedron. This can explained in a different way: the Bergman cluster can be created by beginning with a central icosahedron and fusing each of its faces with the triangular face of the TT of Friauf polyhedra (allowing, of course, for the Friauf polyhedra to interpenetrate). The cluster of Friauf polyhedra surrounding the hexakaidecahedron can be constructed in a similar way, only this time the nucleus of the cluster is a Friauf polyhedron. The Mg2 site lies at the core of this central Friauf polyhedron.

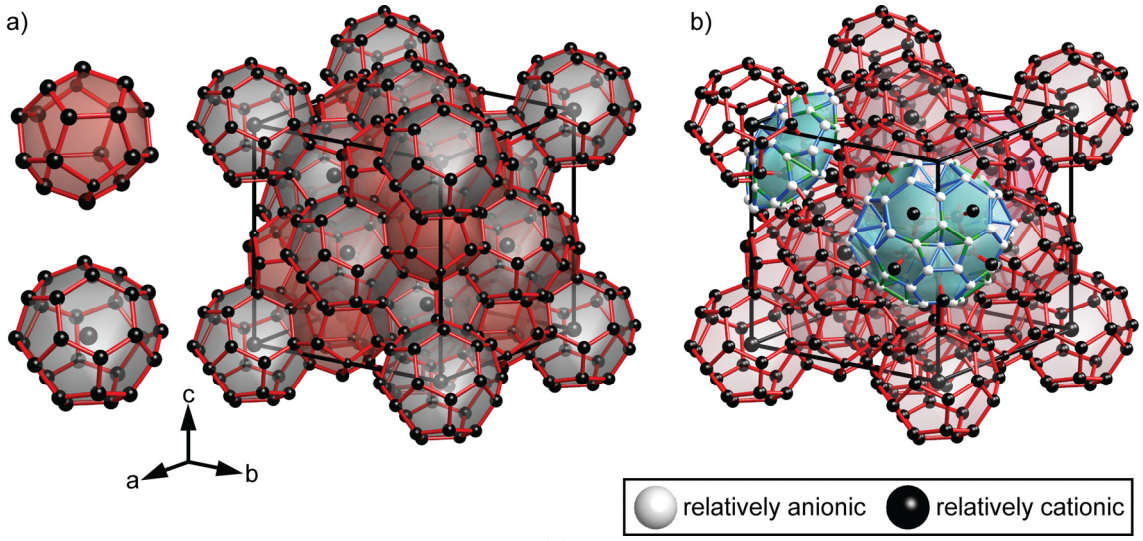

Figure 2.8. Extended D and TT networks in $Mg_{11}Cu_6Al_{12}$. (a) The relatively cationic D network of $Mg_{11}Cu_6Al_{12}$ forms a clathrate II framework, built from dodecahedra (red faces) and hexakaidecahedra (gray faces). (b) The relatively anionic TT network completes Friauf polyhedra around the D atoms. For clarity only a single Bergman cluster and hexagonal wheel of Friauf polyhedra are shown. See the caption to Figure 2.4 for plotting conventions.

We thus arrive at a simple quantum mechanically-derived view of the structural transition between the crystal structures of $Mg_{17}Al_{12}$ and $Mg_{11}Cu_6Al_{12}$. Upon the rotation of half of the $MgCu_2$-type clusters in $Mg_{17}Al_{12}$ as shown in Figure 2.2, the ambiguous atoms at the cluster interfaces snap into clear D and TT identities. The result is a structure that consists of D and TT networks extending throughout the crystal, as in Laves structures such as the $MgCu_2$- and $MgZn_2$-types. The difference lies in the way these networks are arranged. Whereas the D networks of the $MgCu_2$- and $MgZn_2$-types trace out the simple cubic diamond and hexagonal diamond structures, the D network of $Mg_{11}Cu_6Al_{12}$ traces out a more complex array of tetrahedra: the same clathrate network noted by Lin and Corbett in the nearly analogous structure of $Mg_{35}Cu_{24}Ga_{53}$.[22] The TT networks grow around this clathrate scaffold, providing each D site with a truncated tetrahedron. This process forms the polyhedra at the centers of the clathrate cavities: an icosahedron and a Friauf polyhedron of TT atoms at the cores of the dodecahedral and hexakaidecahedral cavities, respectively. The latter has space for hosting one additional D atom.

In the course of the $Mg_{17}Al_{12}$ to $Mg_{11}Cu_6Al_{12}$ transformation, six ambiguous positions/formula units develop TT character with relatively anionic relative Mulliken populations. This is the just the number of sites needed to host the the six Cu atoms that substitute for Mg on going from $Mg_{17}Al_{12}$ to $Mg_{11}Cu_6Al_{12}$. When we recall that the GGA-DFT results presented in the last section suggest that both structure types meet the stability criterion of a pseudogap close to the E_F for the $Mg_{11}Cu_6Al_{12}$ composition, the emergence of new sites sites with affinity for the relatively electronegative Cu atoms in the $Mg_{11}Cu_6Al_{12}$ composition presents itself as an important driving force for the structural transformation.

2.11. Conclusions

In this paper, we have taken a long structural journey in tracing the connections between two phases with great structural and geometrical similarities, $Mg_{17}Al_{12}$ and the newly determined phase $Mg_{11}Cu_6Al_{12}$. The structures were of such similarity, differing only in the relative orientation of their clusters and the site occupancies of some sites, that we felt compelled to explore why $Mg_{11}Cu_6Al_{12}$ adopted its structure rather than the considerably simpler $Mg_{17}Al_{12}$. GGA-DFT calculations revealed that for the stoichiometry in question both structures offer a pseudo-gap at the Fermi energy. This is suggestive of an electronic origin to the stability of $Mg_{11}Cu_6Al_{12}$, but offers little in terms of explaining what features of its crystal structure make it preferable to that of $Mg_{17}Al_{12}$.

A clearer picture was found in relative Mulliken population analyses of elemental models of these structures. In examining the patterns of relatively anionic and cationic sites resulting from these calculations, a startling picture surfaced. The simplest of geometrical permutations—a 90° rotation of half of the $Mg_{17}Al_{12}$ structure's $MgCu_2$-type clusters—leads to profound electronic consequences: constructive interference between network types at the cluster interfaces leads to a new patterning of cationic and anionic sites. Now rather than $MgCu_2$-type clusters, with polar cores isolated from each other by non-polar interfaces, a continuous D network of cationic sites extends through the whole crystal. This is the very clathrate II network of cations identified by Lin and Corbett in their structural analysis of the nearly isostructural $Mg_{35}Cu_{24}Ga_{53}$.[22] The anionic sites also now make an extended network, built from face-sharing truncated tetrahedra, each of which surrounds a D site. Together, the TT and D neworks create an extended array of Friauf polyhedra that includes Bergman clusters and hexagonal wheels.

In the process of this electronic metamorphosis between the structures of $Mg_{17}Al_{12}$ and $Mg_{11}Cu_6Al_{12}$, the Mg sites with blurred identities in the former take on clear roles in the latter. Half of these sites

become strongly cationic, with a clear affinity for relatively electropositive atoms. The other half now register as clearly anionic, to be preferred by more electronegative atoms. The nascent anionic sites accommodate the relatively electronegative Cu atoms as the Mg atoms of $Mg_{17}Al_{12}$ are replaced with Cu to attain the $Mg_{17-x}Cu_xAl_{12}$ (x=6) composition of $Mg_{11}Cu_6Al_{12}$.

In this way, Mulliken population analysis reveals one driving force that may be at work in the formation of this 2×2×2 superstructure of $Mg_{17}Al_{12}$. These results contribute to an emerging theme in the structural chemistry of complex intermetallics: while the complete bonding picture for individual phases may be complicated and subtle, the formation of superstructures from them often has simple, traceable origins.[31] We hypothesize that a similar mechanism of breaking site ambiguities to accommodate changes in the balance of relatively electropositive and electronegative atoms may play a role in the structural preferences of other intermetallic systems. Indeed, elemental substitution in intermetallic structures exhibiting ambiguous sites (as revealed in a Mulliken population analysis) may be one approach to the synthesis of new complex structures.

Acknowledgements

We thank Drs. John Fournelle and Hiromi Konishi at UW-Madison Dept. of Geosciences for their assistance with, respectively, the EDS/WDS measurements, and powder X-ray diffraction measurements. We also gratefully acknowledge the financial support of the US DOE Office of Science Early Career Program (DE-SC0003947) through the Office of Basic Energy Sciences, and the University of Wisconsin through start-up funds.

2.12. Technical Procedures

2.12.1. Synthesis

The synthesis of $Mg_{11}Cu_6Al_{12}$ evolved from our pursuit of the $Mg_6Cu_3Al_7$ phase reported in the phase diagrams of the Al-Mg-Cu system.[12-14] The phase diagrams suggested that the preparation of $Mg_6Cu_3Al_7$ would be challenging, as this composition lies beneath the primary phase field for either a $MgCu_2$-type phase, or more a complex Laves phase, depending on the phase diagram. Stoichiometric preparations are then expected to create substantial amounts of Laves phases in addition to the phase of interest. Two synthetic approaches were then taken, one aiming for optimal crystallinity, the other for phase purity. Both approaches involving direct reaction of elements (aluminum, Alfa Aesar, 99.97 % metals basis, powder -100+325 mesh; copper, Alfa Aesar, 99.5 % metals basis, powder -150 mesh; magnesium, Sigma-Aldrich, 99.98 % trace metals basis, chips 4-30 mesh; all used as received). The elements were weighed out in an Ar-filled glovebox into 0.876 cm diameter tantalum vessels, which were then welded shut with an arc-melting furnace and sealed into evacuated fused silica ampoules.

The two synthetic approaches differed in their nominal compositions and temperature profiles. Approach 1 aimed for crystals for single crystal studies, and involved slow cooling from a melt in the primary phase field of $Mg_6Cu_3Al_7$. The samples were placed in a muffle furnace, and the temperature was raised to 550°C and held there for 24 hours. The furnace was then cooled at a rate of 1 C° per hour to 450°C, where the samples were annealed for 165 hours. Approach 2 aimed for phase pure samples to confirm stoichiometry. In this approach near-stoichiometric mixtures were heated in a muffle furnace to 1000°C to melt all components and held there for 5 hours. The sealed quartz ampoules were then transferred directly to an ice water bath. The samples were resealed in new evacuated fused silica ampoules, and returned to the furnace at 500°C to anneal for 357 hours.

Both approaches resulted in shiny grey ingots. These were brittle, crushing easily in an agate mortar and pestle to yield shards for single crystal analysis. Further grinding resulted in fine powders for analysis with powder X-ray diffraction. No oxidation was evident after weeks in air, suggesting that the samples contain no substantial quantities of air sensitive phases.

2.12.2. Powder X-ray Diffraction

Powder X-ray diffraction data for phase purity assessment and unit cell parameter refinement were collected on a Scintag Pad V diffractometer with Cu $K_{\alpha 1}$ radiation (λ=1.54051 Å). Diffraction intensities were collected as a function of the diffraction angle (2Θ) in steps of 0.02 degrees, with dwell times of 4.0 sec. Peaks were fit with Pearson VII profiles using the program *XFIT*,[32] and unit cell parameters were refined with the program *UNITCELL*.[33]

2.12.3. Elemental Analysis using Energy Dispersive X-ray Spectroscopy (EDS)

For determination of the elemental compositions of the phases synthesized, portions of the crushed samples were suspended in non-conductive epoxy, hand-polished against silicon carbide and diamond papers to create a flat surface, and coated with 250 nm of graphitic carbon. The polished samples were then inspected with a Hitachi S-3100N scanning electron microscope fitted with an EDS probe (Voltage = 15 kV). Measurements at several points revealed the presence of only the three elements expected. Two phases were observed, but further analysis was necessary for certainty in elemental quantification.

2.12.4. Elemental Analysis using Wavelength Dispersive X-ray Spectroscopy (WDS)

The same polished samples were used for both EDS and WDS. Prior to WDS analysis, the samples were repolished to further reduce the amount of surface scratching. To ensure conductivity, carbon paint (graphite in isopropanol) was applied to the epoxy immediately surrounding exposed grains. The samples were then inspected with a Cameca SX-51 electron microprobe (Voltage = 15 kV). Several choices of standards were tested. The Mg:Al ratio was consistent for all of these choices, but sums of the percentages were closest to 100% when the following standards were employed: $MgAl_2O_4$ for Mg, Cu metal for Cu, and a 50:50 Al-Ni alloy for Al. Measurements at several points again revealed the presence of two phases, with the compositions $Mg_{32(2)}Cu_{38(4)}Al_{30(6)}$ (average of 5 measurements), and $Mg11.30(11)Cu_{6.00(9)}Al_{12.86(11)}$ (average of 7 measurements).

2.12.5. Single crystal X-ray Diffraction Measurements

A plate-shaped crystal was selected for single-crystal studies with dimensions 0.14 mm×0.05 mm×0.02 mm (see Table 1 for further details on the crystal). X-ray diffraction intensities were collected on an Oxford Diffraction XCalibur E Diffractometer with a Mo K_α sealed-tube X-ray source (λ=0.71069 Å). ω-scans were used to collect nearly a quadrant of reciprocal space out to 0.6 Å resolution. Run list optimization, as well as all steps of the data processing to create a list of integrated peak intensities, including the peak search, unit cell determination and refinement, the creation of reciprocal reconstructions, absorption correction, and frame scaling were carried out with the program *CrysalisPro Ver. 171*.[34] Structure solution was performed using the charge-flipping algorithm[35,36] with the program *SUPERFLIP*,[37] and the subsequent refinement of the crystal structure was carried out with the program *JANA2006*.[38]

Table 2.1. Crystal data, and details of data collection and structure refinement[39]

Chemical formula	$Mg_{11}Cu_6Al_{12}$
WDS composition	$Mg_{11.30(11)}Cu_{6.00(9)}Al_{12.86(11)}$
Space group/setting	*Fd*3*m* (No. 227)
a (Å)	20.1416(13)
Cell volume (Å^3)	8171.1(9)
Z	16
Calculated density (g/cm^3)	3.1608
Crystal dimensions (mm)	0.14 × 0.05 × 0.02
Crystal color	Metallic grey
Data Collection Temperature	Room temperature
Radiation Source, λ (Å)	Mo Kα, 0.7107
F(000)	7392
Absorption coefficient(mm^{-1})	6.979
Absorption correction	Analytical (method of Clark and Reid[40])
Minimum, Maximum Transmission	0.427, 0.887
Θ_{min}, Θ_{max}	3.35, 37.27
Number of Reflections	15132
Unique Reflections (all, I>3σ)	1044, 627
R_{int} (all, I>3σ)	4.25, 5.01
Number of parameters	34
R(I>3σ), R_w(I>3σ)	2.26, 5.38
R(all), R_w(all)	5.17, 5.63
S(I>3σ), S(all)	1.38, 1.11
$\Delta\varrho_{max}$ (electrons/Å^3)	0.61
$\Delta\varrho_{min}$ (electrons/Å^3)	-1.71

2.12.6. Initial inspection of single crystal data

Single crystal peak positions were fit well with a 20.1 Å metrically cubic unit cell (90.09% of reflections indexed). Analysis of both reciprocal lattice reconstructions of frame data, and R_{int} values for integrated intensities confirmed the cubic symmetry of the crystal, and offered good agreement with the Laue symmetry group *m*3*m*. Inspection of systematic absences suggested *F*-centering, the presence of *d*-glides

perpendicular to <100>, and *n*-glides perpendicular to <110>. All of these observations point to the space group $Fd\bar{3}m$ (no. 227). This choice was confirmed by the results of the structure solution and refinement.

2.12.7. Structure solution and refinement

Application of the charge-flipping algorithm to integrated intensities quickly converged to a sharp electron density map consistent with *Fd*3*m* symmetry. Peak positions corresponded to the $K_{17}In_{41}$ structure type (Figure 1). From the electron densities at the peaks, a moderately clear separation of the three elements Cu, Al and Mg was evident: one large peak with density ϱ = 148.96 electrons/$Å^3$ was assigned to Cu, two smaller peaks with densities in the range ϱ=68.95-66.86 were tentatively assigned to Al, and five peaks distributed in the range in ϱ from 60.62 to 48.17 were then attributed to Mg. An isotropic refinement was then carried out on F^2 leading to R(I>3σ) = 5.00 and reasonably consistent atomic displacement parameters (ADPs). Upon moving to an anisotropic refinement and adding an extinction correction, the R(I>3σ) decreased to 2.26. No outstanding peaks were seen in the Fourier difference map. The resulting atomic coordinates and ADPs are listed in Table 2.2.

Table 2.2. Refined atomic coordinates and atomic displacement parameters for $Mg_{11}Cu_6Al_{12}$

Site	Wyckoff Position	*x*	*y*	*z*	U_{eff}	Occupancy
Al1	96*g*	0.04592(3)	0.63883(4)	0.04592(3)	0.00896(16)	1.0
Al2	96*g*	0.04709(3)	0.85708(4)	0.04709(3)	0.00877(16)	1.0
Cu1	96*g*	0.164130(11)	0.664131(11)	0.002660(17)	0.01253(7)	1.0
Mg1	8*b*	0	0.5	0	0.0104(3)	1.0
Mg2	8*a*	0	0	0	0.0147(4)	1.0
Mg3	32*e*	0.09325(5)	0.40675(5)	0.09325(5)	0.01040(17)	1.0
Mg4	32*e*	0.08508(5)	0.08508(5)	0.08508(5)	0.01156(18)	1.0
Mg5	96*g*	0.19059(3)	0.80941(3)	0.00491(5)	0.01275(19)	1.0

Site	U_{11}	U_{22}	U_{33}	U_{12}	U_{13}	U_{23}
Al1	0.0093(2)	0.0082(4)	0.0093(2)	0.0021(2)	0.0012(3)	0.0021(2)
Al2	0.0094(2)	0.0074(4)	0.0094(2)	-0.00020(19)	-0.0018(3)	-0.00020(19)
Cu1	0.01389(11)	0.01389(11)	0.00980(16)	-0.00382(12)	0.00026(9)	0.00026(9)
Mg1	0.0104(6)	0.0104(6)	0.0104(6)	0	0	0
Mg2	0.0147(6)	0.0147(6)	0.0147(6)	0	0	0
Mg3	0.0104(3)	0.0104(3)	0.0104(3)	-0.0007(4)	0.0007(4)	-0.0007(4)
Mg4	0.0116(3)	0.0116(3)	0.0116(3)	-0.0010(3)	-0.0010(3)	-0.0010(3)
Mg5	0.0130(3)	0.0130(3)	0.0122(4)	0.0009(3)	0.0001(3)	-0.0001(3)

Having obtained the atomic positions, we then turned to finalization of the assignment of elements to sites. The electron counts of Al and Mg differ by only one (about 8%), so these are expected to be difficult to distinguish using X-ray diffraction data. Analysis of the interatomic distances (Table 2.3) was used to assess the plausibility of our initial assignments. Common Al-Al, Mg-Mg, Al-Mg, Al-Cu, and Mg-Cu contact lengths were analyzed with histograms generated by the Inorganic Crystal Structure Database (ICSD).[41-43] The common ranges for these contacts are found to be 2.6-3.1 Å for Al-Al, 2.9-3.3 Å for Mg-Mg, 3.0-3.3 for Al-Mg, 2.4-2.8 Å for Al-Cu, and 2.6-3.0 Å for Mg-Cu. All of the distances in Table 4 fall within these expected ranges, with the exception of those involving Mg4. This site exhibits coordination by six Al2 sites at distances of 3.00 Å, one Mg2 site at 2.97 Å and one Mg4 site at 2.785.

The Mg4-Al2 distances could be consistent with either rather short Mg-Al contacts or long Al-Al contacts. The Mg2-Mg4 distance, likewise could be interpreted as either a short Mg-Mg or an average Mg-Al contact. The Mg4-Mg4 contact distance is similarly ambiguous: 2.785 Å lies in the near the peak of Al-Al distances in the ICSD histograms, but is very short for a Mg-Mg contact. However, such short Mg-Mg distances have been observed previously in intermetallics,[44-47] and 2.6083 Å in MgIr.[46]

Table 2.3. Selected interatomic distances for $Mg_{11}Cu_6Al_{12}$

Site	Neighbor	Distance (Å)
Al1	Al1	2.6160(8)
	Al1(×2)	2.6464(10)
	Cu1(×2)	2.5861(7)
	Cu1	2.4641(8)
	Mg1	3.0870(8)
	Mg3(×2)	3.0998(12)
	Mg5(×2)	3.0258(11)
Al2	Al2	2.6827(8)
	Al2(×2)	2.7297(10)
	Cu1	2.4710(9)
	Mg2	3.1758(8)
	Mg3	3.1360(11)
	Mg4(×2)	3.0049(11)
	Mg5(×2)	3.1619(10)
	Mg5(×2)	3.1226(11)
Cu1	Al2	2.4710(9)
	Al1(×2)	2.5861(7)
	Al1	2.4641(8)
	Mg3	2.7943(10)
	Mg5(×2)	2.9746(8)
	Mg5(×2)	2.9447(9)
Mg1	Al1(×12)	3.0870(8)
	Mg3(×4)	3.2532(10)
Mg2	Al2 (×12)	3.1758(8)
	Mg4(×4)	2.9682(10)
Mg3	Al1(×6)	3.0998(12)
	Al2(×3)	3.1359(11)

	Cu1(×3)	2.7943(10)
	Mg1	3.2532(10)
	Mg5(×3)	3.2066(14)
Mg4	Al2(×6)	3.0049(11)
	Mg2	2.9682(10)
	Mg4	2.7852(13)
Mg5	Al1(×2)	3.0258(11)
	Al2(×2)	3.1619(10)
	Al2(×2)	3.1226(11)
	Cu1(×2)	2.9746(8)
	Cu1(×2)	2.9446(9)
	Mg3	3.2066(14)
	Mg5(×2)	3.2152(11)

For resolution of the assignment of Mg4, we turned to other experimental information. The assignment of Mg4 as Mg or Al leads to different overall compositions: $Mg_{11}Cu_6Al_{12}$ and $Mg_9Cu_6Al_{14}$, respectively. These numbers can be compared to the composition from WDS as $Mg_{11.30(11)}Cu_{6.00(9)}Al_{12.86(11)}$, whose Mg/Al ratio favors the former stoichiometry. Further evidence can be found from the single crystal data; refinement of the structure with Mg4 occupied by Al leads to a U_{eff} value nearly 2.5 times that of the other Al sites with little change in the R-factor relative to the original model. The large U_{eff} suggests that model's electron density on that site is too high when Al is placed on that site, consistent with the site being occupied by Mg. Final confirmation of the assignment of Mg4 as Mg comes from the powder X-ray diffraction patterns of samples with nominal compositions of $Mg_{11}Cu_6Al_{12}$ and $Mg_9Cu_6Al_{14}$, both of which were first heated to 1000° for 5 hours, followed by quenching in cold water, and then annealing at 500° for 357 hours. While both showed the presence of impurity phases, particularly a $MgZn_2$-type Laves phases (see above), the qualitative yield of the target phase was higher for the $Mg_{11}Cu_6Al_{12}$ composition. For these reasons, the Mg4 site was concluded to indeed be occupied by Mg. From the data available, however, we cannot rule out the possibility of some mixed occupancy with Al on this site.

2.12.8. Electronic structure calculations

All structure optimizations and the calculation of DOS curves were performed with the Vienna Ab Initio Simulation Package, at the GGA-DFT level with Projected Augmented Wave (PAW) potentials provided with the package.[48-53] The electronic structure calculations for $Mg_{11}Cu_6Al_{12}$ ($K_{17}In_{41}$-type), $Mg_{17}Al_{12}$ (α-Mn-type) with half of the outermost D sites exchanged for Cu to attain the stoichiometry of $Mg_{11}Cu_6Al_{12}$, and $Mg_{17}Al_{12}$ were carried out in the high precision mode with energy cut-offs of 341.6, 341.6, and 300.5 eV, respectively. Optimizations of the unit cell volume, cell shape, and ion positions were performed in sequence using first a 5×5×5 k-point mesh and then with a 9×9×9 mesh. All degrees of freedom were then optimized simultaneously using the same series of k-point meshes. DOS curves were generated for the optimized structures using a 11×11×11 k-point mesh for $Mg_{11}Cu_6Al_{12}$ in the $K_{17}In_{41}$-type and a 13×13×13 k-point mesh for both α-Mn-type structures.

All Mulliken populations were extracted from extended Hückel (eH) tightbinding calculations performed with the program YAeHMOP.[54] Mulliken populations were calculated for elemental models of both $Mg_{17}Al_{12}$ and $Mg_{11}Cu_6Al_{12}$ in which Al is placed on all sites. The Al atoms were modeled with an *sp* single zeta basis set of Slater Type Orbitals, and used parameters developed previously in the study of $Mg_{17}Al_{12}$: $H_{ii}(3s)$ = -12.5 eV, $H_{ii}(3p)$ = -6.5 eV, $\zeta(3s)$ = 1.267 and $\zeta(3p)$ = 1.267. These parameters were shown to reproduce the qualitative features of the LDA-DFT band structure of $Mg_{17}Al_{12}$.[23]

2.13. References

(1) Pauling, L. *J. Am. Chem. Soc.* 1923, *45*, 2777–2780.

(2) Samson, S. *Nature* 1962, *195*, 259–263.

(3) Samson, S. *Acta Cryst.* 1964, *17*, 491–495.

(4) Samson, S. *Acta Cryst.* 1965, *19*, 401–413.

(5) Samson, S. *Acta Cryst.* 1967, *23*, 586–600.

(6) Weber, T.; Dshemuchadse, J.; Kobas, M.; Conrad, M.; Harbrecht, B.; Steurer, W. *Acta Cryst. B* 2009, *65*, 308–317.

(7) Conrad, M.; Harbrecht, B.; Weber, T.; Jung, D. Y.; Steurer, W. *Acta Cryst. B* 2009, *65*, 308–317.

(8) Schobinger-Papamantellos, P.; Fischer, P. *Naturwissenschaften* 1970, *57*, 128–129.

(9) Crivello, J.-C.; Nobuki, T.; Kuji, T. *Intermet.* 2007, *15*, 1432–1437.

(10. Samson, S.; Gordon, E. K. *Acta Cryst. B* 1968, *24*, 1004–1013.

(11) Feuerbacher, M. et al. *Z. Kristallogr.* 2007, *222*, 259–288.

(12) Prince, A.; Effenberg, G. *Ternary Alloys*; VCH, 1991; Vol. 4.

(13) Buhler, T.; Fries, S. G.; Spencer, P. J.; Lukas, H. L. *J. Phase Equilib.* 1998, *19*, 317–333.

(14) Raghavan, V. *J. Phase Equilib.* 2007, *28*, 174–179.

(15) Cordier, G.; Müller, V. *Z. Kristallogr.* 1993, *205*, 353–354.

(16) Cordier, G.; Müller, V. *Z. Naturforsch., B: Chem. Sci.* 1994, *49*, 721–728.

(17) B. Li and J. D. Corbett, *Inorg. Chem.* 2003, *42*, 8768–8772.

(18) Mirgalovskaya, M. S. *Doklady Akademii Nauk SSSR* 1951, *77*, 289–292.

(19) Li, Z.-Q.; Zhang, S.-Y.; Wu, B.-Y. *Mater. Sci. Tech. Ser.* 2001, *17*, 465–471.

(20) Liu, X.-Z.; Yang, M.; Xing, Z.-H.; Ren, X.-F. *Trans. Nonferrous Met. Soc. China* 2003, *13*, 153–157.

(21) Tillard-Charbonnel, M.; Belin, C. *Mater. Res. Bull.* 1992, *27*, 1277–1286.

(22) Lin, Q.; Corbett, J. D. *Inorg. Chem.* 2005, *44*, 512–518.

(23) Fredrickson, D. C.; Lee, S.; Hoffmann, R. *Angew. Chem. Int. Ed.* 2007, *46*, 1958–1976.

(24) Li, B.; Corbett, J. D. *Inorg. Chem.* 2003, *42*, 8768–8772.

(25) Gimarc, B. M. *J. Am. Chem. Soc.* 1983, *105*, 1979–1984.

(26) Longuet-Higgins, H. C.; Rector, C. W.; Platt, J. R. *J. Chem. Phys.* 1950, *18*, 1174–1181.

(27) Miller, G. J. *Eur. J. Inorg. Chem.* 1998, 523–536.

(28) Lee, C. S.; Miller, G. J. *Inorg. Chem.* 2001, *40*, 338–345.

(29) Schmidt, J. T.; Lee, S.; Fredrickson, D. C.; Conrad, M.; Sun, J.; Harbrecht, B. *Chem. Eur. J.* 2007, *13*, 1394–1410.

(30) Berger, R. F.; Lee, S.; Hoffmann, R. *Chem. Eur. J.* 2007, *13*, 7852–7863.

(31) Fredrickson, D. C.; Lidin, S.; Venturini, G.; Malaman, B.; Christensen, J. *J. Am. Chem. Soc.* 2008, *130*, 8195–8214.

(32) Coelho, A. A.; Cheary, R. W. *X-ray Line Profile Fitting Program, XFIT*; University of Technology, Sydney, Australia (2007).

(33) Holland, T. J. B.; Redfern, S. A. T. *Mineral. Mag.* 1997, *61*, 65–77.

(34) Oxford Diffraction. Oxford Diffraction Ltd., Xcalibur CCD system, CrysAlisPro Software system, 2007; Version 1.171.32.

(35) Oszlanyi, G.; Suto, A. *Acta Cryst.* 2004, *A60*, 134–141.

(36) Oszlanyi, G.; Suto, A. *Acta Cryst.* 2005, *A61*, 147–152.

(37) Palatinus, L.; Chapuis, G. *J. Appl. Cryst.* 2007, *40*, 786–790.

(38) Petříček, V.; Dušek, M.; Palatinus, L. *Jana2006. The crystallographic computing system*; Institute of Physics, Praha, Czech Republic.

(39) A crystallographic information file containing further details of the crystal structure investigation of $Mg_{11}Cu_6Al_{12}$ may be obtained from the Fachinformationszentrum Karlsruhe, 76344 Eggenstein-Leopoldshafen, Germany (fax: +49-7247-808-666; e-mail: crysdata@fiz-karlsruhe.de) on quoting the depository number CSD-422849.

(40) Clark, R. C.; Reid, J. S. *Acta Cryst.* 1995, *A51*, 997–897.

(41) Bergerhoff, G.; Brown, I. D. in "Crystallographic Databases," F. H. Allen et al. (Hrsg.) Chester,

International Union of Crystallography, 1987.

(42) Belsky, A.; Hellenbrandt, M.; Karen, V. L.; Luksch, P. *Acta Cryst. B* 2002, *B58*, 364–369.

(43) Kaduk, J. A. *Phys. Rev. B* 2002, *B58*, 370–379.

(44) Ferro, R.; Rambaldi, G. *J Less-Common Met.* 1960, *2*, 383–391.

(45) Ferro, R.; Rambaldi, G.; Capellt, R. *J Less-Common Met.* 1962, *4*, 16–23.

(46) Černý, R.; Renaudin, G.; Favre-Nicolin, V.; Hlukhyy, V.; Pöttgen, R. *Acta Cryst. B* 2004, *B60*, 272–281.

(47) Braga, M. H.; Ferreira, J. J. J.; Siewenie, J.; Proffen, T.; Vogel, S. C.; Daemen, L. L. *J. Solid State Chem.* 2010, *183*, 10–19.

(48) Kresse, G.; Hafner, J. *Phys. Rev. B* 1993, *47*, 558–561.

(49) Kresse, G.; Hafner, J. *Phys. Rev. B* 1994, *49*, 14251–14269.

(50) Kresse, G.; Furthmüller, J. *Comput. Mater. Sci.* 1995, *6*, 15–50.

(51) Kresse, G.; Furthmüller, J. *Phys. Rev. B* 1996, *54*, 11169–11186.

(52) Blöchl, P. E. *Phys. Rev. B* 1994, *50*, 17953–17952.

(53) Kresse, G.; Joubert, D. *Phys. Rev. B* 1999, *59*, 1758–1775.

(54) Landrum, G. A. *YAeHMOP: Yet Another extended Hückel Molecular Orbital Package, Version 3.0.*; YAeHMOP is freely available on the internet at URL: http://sourceforge.net/projects/yaehmop/.

Chapter 3.

Unpublished crystal structures exhibiting structural plasticity

3.1. Generalized targeted synthetic method for phases related to dodecagonal quasicrystals

Synthetic methods targeting quasicrystalline phases often attempt to trap metastable compounds via melt-spinning or vapor deposition techniques.[1] As our work focuses on stability and thermodynamic favorability, the aim was to develop a synthetic program for synthesizing quasicrystals in traditional high-temperature synthetic methods. The family of dodecagonal quasicrystalline compounds and their approximants became an appealing starting point once we found connections to the σ-phase, CrFe, and provided motivation for understanding the structural plasticity of the σ-phase in relation to dodecagonal quasicrystallinity.

The σ-phase can be described as an arrangement of square Cr_3Si-type tiles and triangle tiles, each a half unit cell of the Al_3Zr_4 type.[2,3] This compound represents a simple 3^2434 tiling, as pictured in Figure 3.1. More complex tilings can be found in dodecagonal approximants Mn_7Si_2V and $Mn_{81.5}Si_{18.5}$ (Figure 3.1b-c),[4,5] and dodecagonal patterns based on the same squares and triangles can be envisioned as forming true quasicrystals which cannot be described by the periodic boundaries of a unit cell. Further related phases are also found in TM-Si binary and ternary systems.[2,6–12] Since simpler tilings are observed elsewhere in nature, it is curious that anything more complex than the σ-phase—or even more simply, a

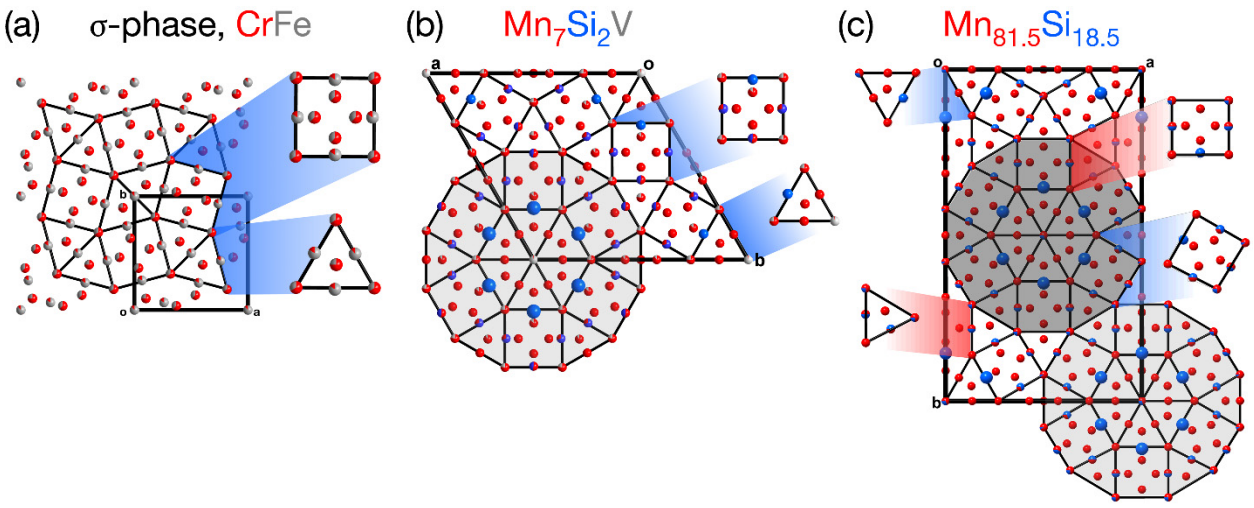

Figure 3.1. Tilings of the (a) σ-phase, (b) Mn_7Si_2V type, and (c) ν-phase, $Mn_{81.5}Si_{18.5}$. Each structure is an arrangement of square tiles (one unit cell of the Cr_3Si type) and triangle tiles (half a unit cell of the Al_3Zr_4 type). (a) The σ-phase represents a simple pattern of the square and triangle tiles, each highlighted in blue. (b) Mn_7Si_2V represents the simplest unit cell containing a pseudo-dodecagonal cluster (shaded in grey). (c) The ν-phase is essentially a body-centered arrangement of these pseudo-dodecagonal clusters; the light and dark grey shaded regions are offset by half a unit cell along c. The ν-phase also contains defect triangle and square tiles, highlighted in red. Throughout the figure, partial occupancies are represented in a pie-chart style coloring of each atomic site.

simple all-square or all-triangle tile arrangement as in Cr_3Si and Al_3Zr_4—should exist as the most stable state of a chemical system.

Many of the phases with complex tilings form in ternary systems between silicon and two transition metal atoms that form a binary σ-phase compound (such as $V_{0.2}Mn_{0.8}$). Based on preliminary chemical pressure calculations, we hypothesized that the addition of main group silicon disrupts the packing of the similarly-sized transition metals, inspiring the 12-fold pseudosymmetries of the quasicrystalline approximants. This hypothesis generated a rich synthetic program based on the addition of silicon to

binary TM systems containing a σ- or σ-related phase. This chapter contains several unpublished crystal structures that emerged from these investigations. While the structural chemistry that has emerged fgom these endeavors supports the fruitfulness of this apprioach, connecting these structures back to the theme of structural plasticity led to a new research direction itself, as will be described in the remaining chapters of this thesis.

3.2. $Mn_{24}Co_{14}Si_{14}$: A new σ-phase variant

This ternary system contains no σ-phase type compounds, but several variants of the σ-phase: $Mn_{81.5}Si_{18.5}$ (ν-phase)[5], $Mn_{16.5}Co_{14.8}Si_{5.7}$ (X-phase),[6] and $Mn_{0.53}Co_{0.20}Si_{0.27}$ (R-phase).[13] Synthesis of the new ternary compound began with finding in the literature a composition for which a phase had been observed, though not fully characterized.[13] Resynthesis of this compound involved arc melting a near-stoichiometric (14:29:14) compressed pellet of the three elemental starting materials. The arc-melted pellet was wrapped in Mo foil and sealed into an evacuated fused silica tube. The sample was annealed at 850 °C for 350 hours, then quenched in ice water to rapidly stop the annealing process. The composition of the new compound is similar to a phase reported in Reference [13] (there referred to as "S-phase"), whose structure was then unreported. The crystallographic tables are available in Appendix A.

Upon initial inspection of this compound depicted in Figure 3.2, $Mn_{24}Co_{14}Si_{14}$ has a strong resemblance to the tetragonal σ-phase, but a comparison of their unit cells reveals the orthorhombic nature of $Mn_{24}Co_{14}Si_{14}$, as well as a rough doubling of the *c*-axis. The tile decoration of this new structure type is less similar to those of the σ-phase than it is to the defect tiles of the ν-phase (Figure 3.2b-c vs.

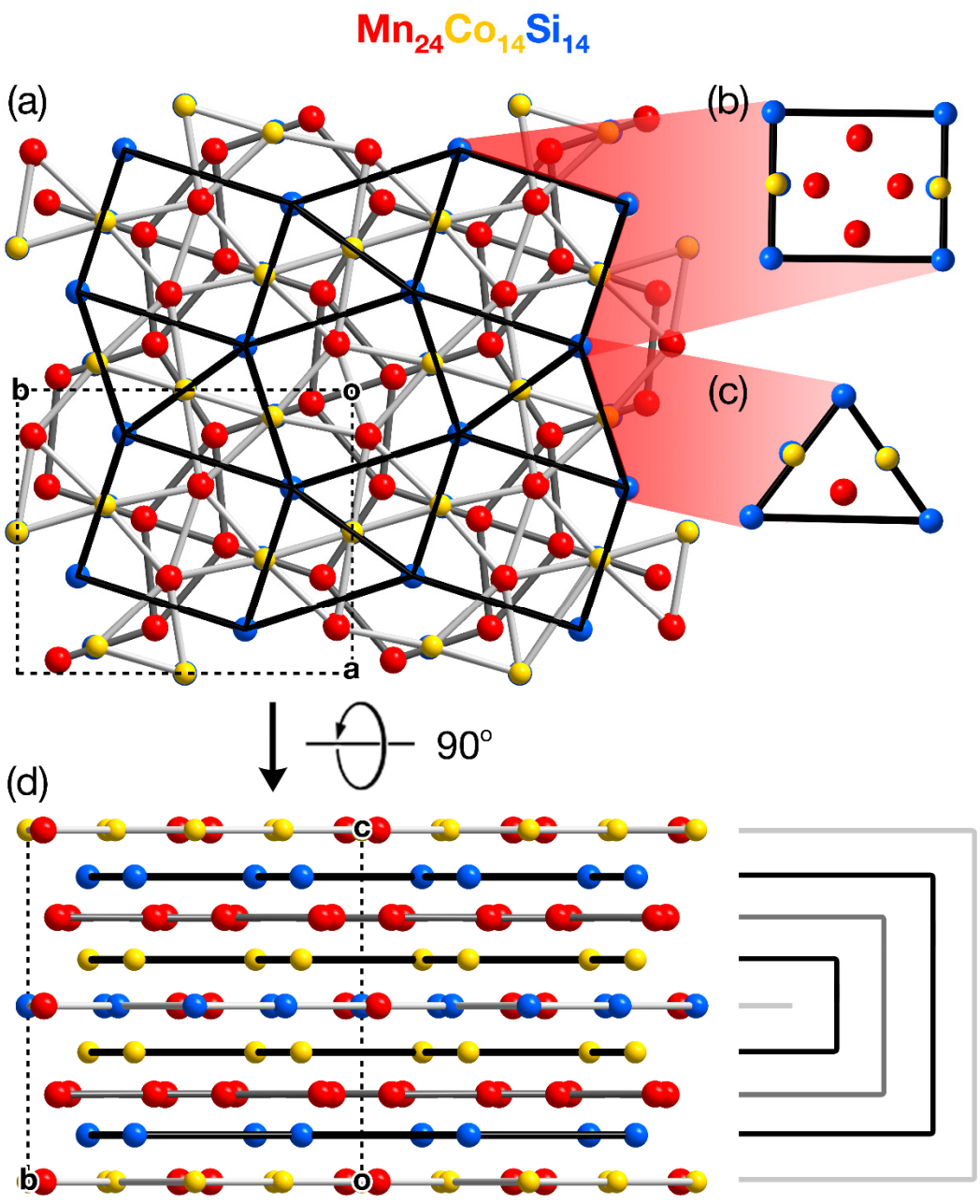

Figure 3.2. The structure of $Mn_{24}Co_{14}Si_{14}$. (a) This phase represents a similar tiling of squares and triangles to that of the σ-phase, but all of the (b) square and (c) triangle tiles are defect tiles, not idealized portions of the Cr_3Si and Al_3Zr_4 types. (d) A view of the compound down the *a*-axis reveals the source of the near-doubling of the unit cell along *c*: coloration of alternating layers adds a mirror plane at $c = ½$. Layers with the same atomic positions are shown as the same shade of grey (light grey at z = 0, ½ , 1; black at z = ⅛, ⅜, ⅝, ⅞ ; medium grey at z = ¼, ¾), but site coloration may vary between layers.

Table 3.1. Unit cell comparison for the σ-phase and $Mn_{24}Co_{14}Si_{14}$

	Space Group	*a*	*b*	*c*
CrFe (σ-phase)[3]	$P4_2/mnm$	8.7996	8.7996	4.5582
$Mn_{24}Co_{14}Si_{14}$	*Pbam*	7.5464	8.9168	9.3703

Figure 3.1c). This asymmetry in the tiles elongates the unit cell, reducing the tetragonal setting to orthorhombic.

Specific features of the tile decoration are emphasized in Figure 3.2a, with a view along the c-axis. Atoms are connected to neighboring atoms with the same z-coordinate, creating three types of nets indicated in light grey, black, and medium grey. The z-coordinates can be referenced in Figure 3.2d.

As seen in Figure 3.2a, the z = 1 light grey net consists of two types of verticies: 3^2535 for every manganese-occupied vertex, and 3535 for every cobalt-occupied vertex. The light grey layer appears at z = 0, ½, and 1, although the site coloring differs between the nets at z = 1 and z = ½. At z = ½, every cobalt atom is replaced by silicon.

The black net happens to outline our square-and-triangle net. At z = ⅛ and ⅞, this net is fully occupied by silicon, while at z = ⅜ and ⅝, this net consists of only cobalt atoms. The medium grey layer is another net of pentagons and triangles, distinct from that seen in light grey. The Mn atoms of the medium grey layer are found at z = ¼ and ¾, and are positioned at the centers of the triangles seen in the light grey layer.

Further work is needed to verify the atomic assignments of the reported compound. EDS or WDS would confirm the reported stoichiometry, and neutron diffraction might prove useful in providing a spatially resolved picture of the distribution of Mn and Co.

3.3. $Fe_7Mo_4Si_8$: A patchwork of Fe_5Si_3 and Mo_5Si_3

Though this system was begun with the intent of finding a phase related to MoFe (σ-phase type), this new compound is more closely related to two silicide binary compounds: Fe_5Si_3 (Mn_5Si_3-type) and Mo_5Si_3 (W_5Si_3-type).[14,15] The new ternary compound takes on a ternary variant of the $Cr_{11}Ge_8$ structure type.[16] It was synthesized from a compressed pellet of its elemental constituents, stoichiometrically. The pellet was arc melted and sealed directly into an evacuated fused silica tube. Annealing at either 850 or 1000 °C for 350 hours yielded the desired compound. EDS data taken on this compound confirms the crystallographic stoichiometry, though the sample was found to contain iron silicide contaminants. A phase pure synthesis and magnetic property data should be obtained for this compound prior to its publication. Crystallographic data is available in Appendix A.

Such strong resemblance between the ternary phase and the two related binaries raises the question of the alteration in stoichiometry, and why, for instance, the iron atoms are not confined to the Fe_5Si_3-type tiles. The increase in silicon in the ternary phase is noted at the vertices where tiles meet, but the latter question is best left to a chemical pressure analysis. The atomic sizes of iron (1.26 Å) and molybdenum (1.39 Å) are expected to play a role in their distinction in this phase. Chemical pressure results will indicate the location of stress in the binary lattices, which can then be compared to the atomic assignments in the ternary compound. It will also be useful to examine the chemical pressures at the interfaces of the two structures to understand the advantages of forming this complex ternary over phase segregating into two compounds of the Mn_5Si_3- and W_5Si_3-types.

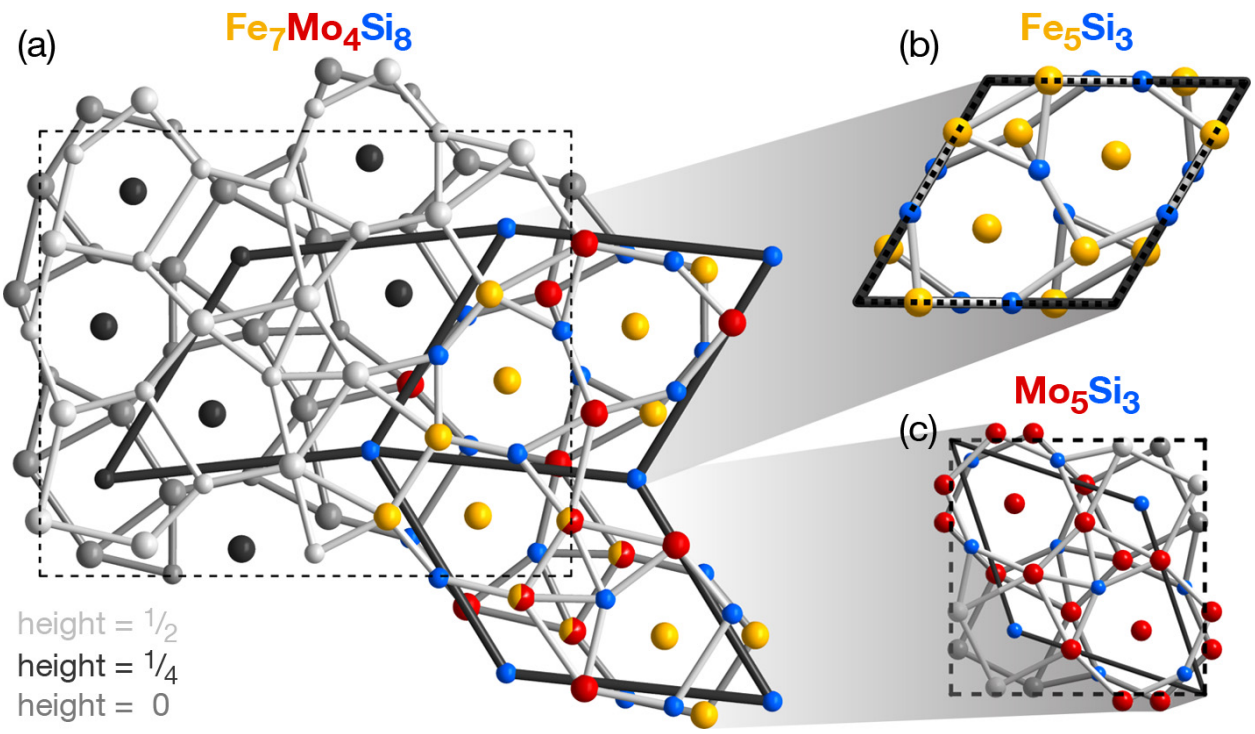

Figure 3.3. Structural picture of (a) $Fe_7Mo_4Si_8$, as a checkerboard pattern of alternating of the binary compounds (b) Fe_5Si_3 and (c) Mo_5Si_3. With respect to atomic coloration, the assignment of metal or silicon atom on the body of each tile corresponds nicely to the two binaries, though Fe and Mo substitute for one another in several locations. The change in TM : Si ratio originates at the interfaces of the tiles, which incorporates more silicon into the structure. The different layers are indicated in shades of grey, while the colored atoms reflect atomic assignment.

3.4. Additional synthetic leads

Several other compounds have been synthesized as a result of pursuing the structural plasticity of the σ-phase. While their crystal structures have been solved, various factors have prevented the development of reliable synthetic procedures for the creations of these compounds.

These include a nickel silicide compound, $Ni_{31-x}Si_{12}$ (for $x \approx 13/3$), originally synthesized by undergraduate student Mariana Gama. This compound represents a three-fold superstructure of the previously reported hexagonal unit cell of $Ni_{31}Si_{12}$.[17] The new compound exhibits systematic ordering to a site that is disordered in the literature compound. We expect that these are indeed separate phases, as we have seen both compounds in the process of collecting crystallographic data. Synthetic efforts to remake this compound have yielded mixed results that suggest a possible contamination as the source of the ordering of the supercell. Because the stoichiometry is similar to the supercell, we have also considered a very subtle temperature dependence. A scanning calorimetry experiment would elucidate any temperature dependent phase transitions that might occur.

Another new phase emerged from attempted synthetic manipulation of the *ν*-phase, $Mn_{81.5}Si_{18.5}$.[5] The crystallographic solution suggests the composition is $Mn_{80}Si_{19}O$, but the assignment of oxygen (as opposed to nitrogen or carbon) has yet to be verified. Only one sample has contained crystals of this phase, and it was synthesized from a pressed pellet on Mn and Si in an alumina crucible with an alumina fiber plug. The sample was shown by EDS to have incorporated small fibers of alumina, which may have been the source of the oxygen found in the compound. Considering this, there may also be aluminum substitution on sites reported as silicon. Subsequent attempts to resynthesize this compound explored the use of SiO_2, MnO, and Al_2O_3 as reagents, but have thus far been unsuccessful.

One other synthetic lead proved to be not only a difficult compound to make, but also a difficult crystal structure to solve; in pursuit of the structural plasticity of the $CaCu_5$-type, we found a reported composition with no crystal structure in the Ca-Ag binary phase diargram, Ca_2Ag_9.[18] Undergraduate Alexandra Mehan attempted to synthesize this compound by directly arc melting a stoichiometric mixture

of the elemental reagents. Crystals were obtained and appeared to be very complexly modulated, but a better data set will be necessary before any attempts at a solution. Further synthetic work on this compound should consider the benefits of flux-growth. This is the most silver-rich phase reported in the available phase diagrams, and a synthesis in silver flux could be successful in obtaining large, high quality crystals of this compound. There is also an 86:14 silver-calcium eutectic ($T_{eutectic}$ = 655 °C) to consider exploiting.[18]

3.5. Continued pursuit of the themes of Structural Plasticity with theoretical development

As suggested in section 3.3, a story for these compounds will only be complete with the addition of chemical pressure calculations. It is readily apparent that these compounds represent new instances of structural plasticity, and comparing them to their simpler alternatives should be the next step in the research on these specific compounds. This contribution to the examples of structural plasticity will also help to solidify the relationship between application of chemical pressure and the structural responses to stress.

3.6. References

(1) Ishimasa, T. *Isr. J. Chem.* **2011**, *51*, 1216–1225.

(2) Shoemaker, D.; Shoemaker, C. *Acta Crystallogr. Sect. B* **1986**.

(3) Yakel, H. L. *Acta Crystallogr. Sect. B Struct. Sci.* **1983**, *39*, 20–28.

(4) Iga, H.; Mihalkovič, M.; Ishimasa, T. *Philos. Mag.* **2011**, *91*, 2624–2633.

(5) Shoemaker, C. B.; Shoemaker, D. P. *Acta Crystallogr. Sect. B Struct. Crystallogr. Cryst. Chem.* **1971**, *27*, 227–235.

(6) Manor, P. C.; Shoemaker, C. B.; Shoemaker, D. P. *Acta Crystallogr. Sect. B.* **1972**, *28*, 1211–1218.

(7) Shoemaker, C.B.; Shoemaker, D. P. *Acta Crystallogr. Sect. B.* **1976**, *5*, 2306–2313.

(8) Shoemaker, C.B.; Shoemaker, D. P. *Acta Crystallogr. Sect. B.* **1978**, *180*, 701–705.

(9) Shoemaker, C.B.; Shoemaker, D. P. *Acta Crystallogr. Sect. B.* **1977,** *33*, 743-754.

(10) Kashimoto, S.; Kocjan, a.; Jagličić, Z.; Jazbec, S.; Iga, H.; Ishimasa, T.; Dolinšek, J. *Phys. Rev. B* **2011**, *84*, 224201.

(11) Shoemaker, C.B.; Shoemaker, D. P.; Hopkins, T. E.; Yindepit, S. *Acta Crystallogr. Sect. B.* **1978**, *34*, 3573–3576.

(12) Shoemaker, C. B.; Shoemaker, D. P. *Metall. Mater. Trans. B* **1971**, *2*, 2296–2299.

(13) Kuz'ma, Y. B.; Gladyshevskii, E. I. *Russ. J. Inorg. Chem.* **1964**, *9*, 373–377.

(14) Weill, A. R. *Nature.* **1943**, *152*, 413–413.

(15) Schachner, H.; Cerwenka, E.; Nowotny, H. *Monatshefte für Chem.* **1954**, *85*, 245–254.

(16) Israiloff, P.; Voellenkle, H.; Wittmann, A. *Monatshefte für Chem.* **1974**, *105*, 1387–1404.

(17) Frank, K.; Schubert, K. *Acta Crystallogr. Sect. B Struct. Crystallogr. Cryst. Chem.* **1971**, *27*, 916–920.

(18) Baren, M. R. Ca-Ag Phase Diagram. In *Binary Alloy Phase Diagrams*. Massalski, T. B., Ed.; ASM International. **1990**; 20–21.

Chapter 4.

First-principles elucidation of atomic size effects using DFT-chemical pressure analysis: Origins of $Ca_{36}Sn_{23}$'s long-period superstructure

This chapter has been published: Engelkemier, J.; Berns, V.M.; Fredrickson, D.C. *J. Chem. Theory Comput.* **2013**, *9*(7), 3170-3180.

4.1. Abstract

The space requirements of atoms are empirically known to play key roles in determining structure and reactivity across compounds ranging from simple molecules to extended solid state phases. Despite the importance of this concept, the effects of atomic size on stability remain difficult to extract from quantum mechanical calculations. Recently, we outlined a quantitative yet visual and intuitive approach to the theoretical analysis of atomic size in periodic structures: the DFT-Chemical Pressure (DFT-CP) analysis. In this Article, we describe the methodological details of this DFT-CP procedure, with a particular emphasis on refinements of the method to make it useful for a wider variety of systems. A central improvement is a new integration scheme with broader applicability than our earlier Voronoi cell method: contact volume space-partitioning. In this approach, we make explicit our assumption that the pressure at each voxel is most strongly influenced by its two closest atoms. The unit cell is divided into regions corresponding to

individual interatomic contacts, with each region containing all points that share the same two closest atoms. The voxel pressures within each contact region are then averaged, resulting in effective interatomic pressures. The method is illustrated through the verification of the role of Ca-Ca repulsion (deduced earlier from empirical considerations by Corbett and coworkers) in the long-period superstructure of the W_5Si_3-type exhibited by $Ca_{36}Sn_{23}$.

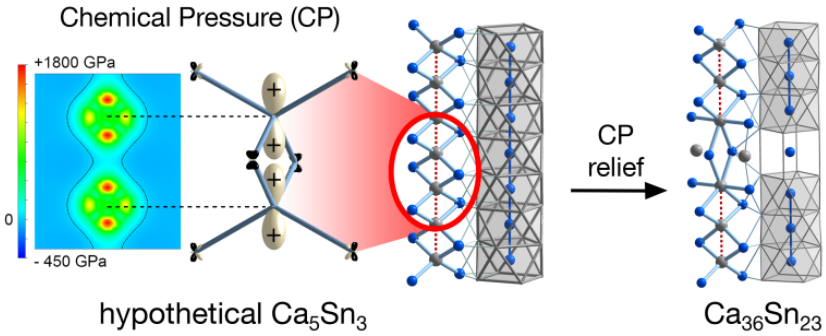

Figure 4.0. Intense chemical pressure between the calcium atoms in Ca_5Sn_3 can be identified in 2-D maps (left) and projections onto spherical harmonics. This pressure is relieved on altering the structure to increase the distance between calcium atoms, forming $Ca_{36}Sn_{23}$.

4.2. Introduction

The concept of atomic size is frequently evoked in the rationalization of experimentally observed chemical phenomena. Examples across the broad spectrum of chemistry include the non-ideality of gases,[1] steric repulsion between alkyl groups influencing the outcomes of organic reactions,[2] the radius ratio rules for rationalizing the crystal structures of ionic salts,[3,4] and the vibrational freedom of rattling atoms in clathrate- or skutterudite-based thermoelectric materials.[5,6] Despite its rich history, the space re-

quirement of atoms remains essentially an empirical notion, largely based on observed interatomic distances and the compilation of these observations in tables of atomic radii. While methods exist for partitioning space between atoms, as offered by Bader's Quantum Theory of Atoms in Molecules,[7,8] theoretical approaches are needed for determining how a structure's stability is affected by the encroachment of one atom upon another atom's domain. Such methods would be valuable for verifying the role of atomic sizes indicated by empirical observations, and elucidating the specific ways in which these sizes wield their influence.

For solid state inorganic compounds this need is pressing, particularly for intermetallic phases. Since the pioneering work of Hume-Rothery, atomic size has been recognized as a key factor in the structural preferences of intermetallics.[9-12] More recently, there has been an emerging theme of size effects interacting with electronic factors to determine the observed structural chemistry.[13-17] Investigating such interactions is quite challenging, however, as the absence of bonding schemes tying composition to geometry makes it difficult to distinguish close contacts supported by substantial bonding from those that are in fact repulsive but forced together by the constraints of atomic packing.

We recently outlined an approach for revealing local interatomic pressures that arise in such circumstances: the DFT-Chemical Pressure (CP) analysis,[18] which offers theoretical insights into size effects and how they emerge from an electronic context. The DFT-CP analysis can be viewed as a chemical application of the concept of stress density,[19-24] in which the total pressure of a system is spatially resolved into a pressure map. Our approach differs from previous work in this area in two respects. First, rather than deriving analytical relationships between the ground state wavefunctions and the stress density, we focus on developing a practical interface with electronic structure programs, particularly the freely-available,

open source ABINIT package.[25,26] This is achieved by taking the simpler method of numerically differentiating energy density grids obtained from a calculation's output. The second difference is in our emphasis on the interpretation of the pressure maps. In moving away from considerations of the formalism of stress densities toward visualization of the conflicts underlying them, vivid schemes for the stability of intermetallic structures arise that are capable of inspiring new experimental endeavors.

In this Article, we build on our earlier outline of the DFT-CP analysis. In the process of describing the methodological details of this approach, we will present improvements that develop the DFT-CP analysis into a generally usable tool for the analysis of bonding optimization in solid state materials. These improvements include a more meaningful treatment of the pressures observed in the regions of the ion cores, and a more reliable method for dividing space between the atoms during the integration of the pressure maps. In addition, we will demonstrate the application of this improved analysis to an intermetallic system with interesting structural chemistry: that of the superstructure variants of the W_5Si_3 structure type in the Ca-Sn system.

4.3. Our model system

As we develop the DFT-CP method in this Article, we will use the complex crystal structure of $Ca_{36}Sn_{23}$ (Figure 4.1) as a model system.[27,28] This compound belongs to a family of intermetallics adopting long-period superstructures of the common W_5Si_3 structure type (Figure 4.1a).[27-34] The W_5Si_3 parent structure is easily visualized as a checkerboard arrangement of columns of Si-centered W square antiprisms and columns of W-centered Si tetrahedra. These two column types extend along the *c*-axis, with the square antiprisms and tetrahedra of each column linked through shared faces and edges, respectively.

In $Ca_{36}Sn_{23}$ and a number of other phases, defect variants of the W_5Si_3 type are adopted in which planar interfaces are inserted perpendicular to *c* (as shown on the right side of Figure 4.1b). At each of these interfaces, the progression along the columns of square antiprisms is interrupted by the incorporation of a cube. The columns of tetrahedra are similarly interrupted, with coordination of the interfacial Ca atoms changing from tetrahedral to octahedral. In $Ca_{36}Sn_{23}$, these interfaces occur at regular intervals of six square-antiprisms along *c*, corresponding to three unit cells of the W_5Si_3 basic structure. For other members of this family, other interface distributions are observed (Figure 4.2). In the structures of $Ca_{31}Sn_{20}$ and $Pu_{31}Pt_{20}$, the interface layers are separated from each other by slabs of the W_5Si_3 type five square antiprisms thick. For Y_3Rh_2 and $Ca_{16}Sb_{11}$, the slab thickness decreases to respectively three and two square antiprisms.

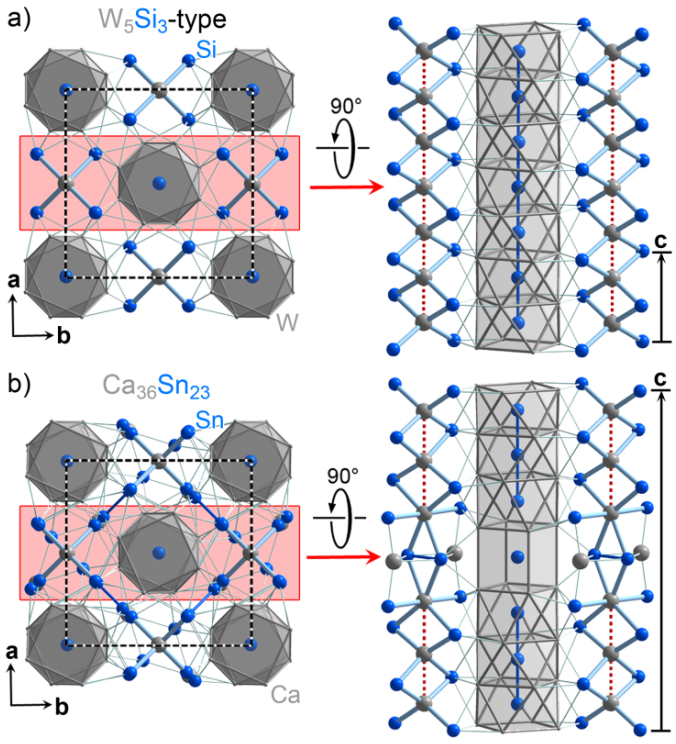

Figure 4.1. The crystal structure of $Ca_{36}Sn_{23}$, whose stability has been attributed to the Ca-Ca repulsion that would occur in its W_5Si_3-type parent structure. (a) The structure of W_5Si_3. (b) The $Ca_{36}Sn_{23}$ structure, which is generated through the introduction of planar defects into the W_5Si_3-type at regular intervals perpendicular to *c*.

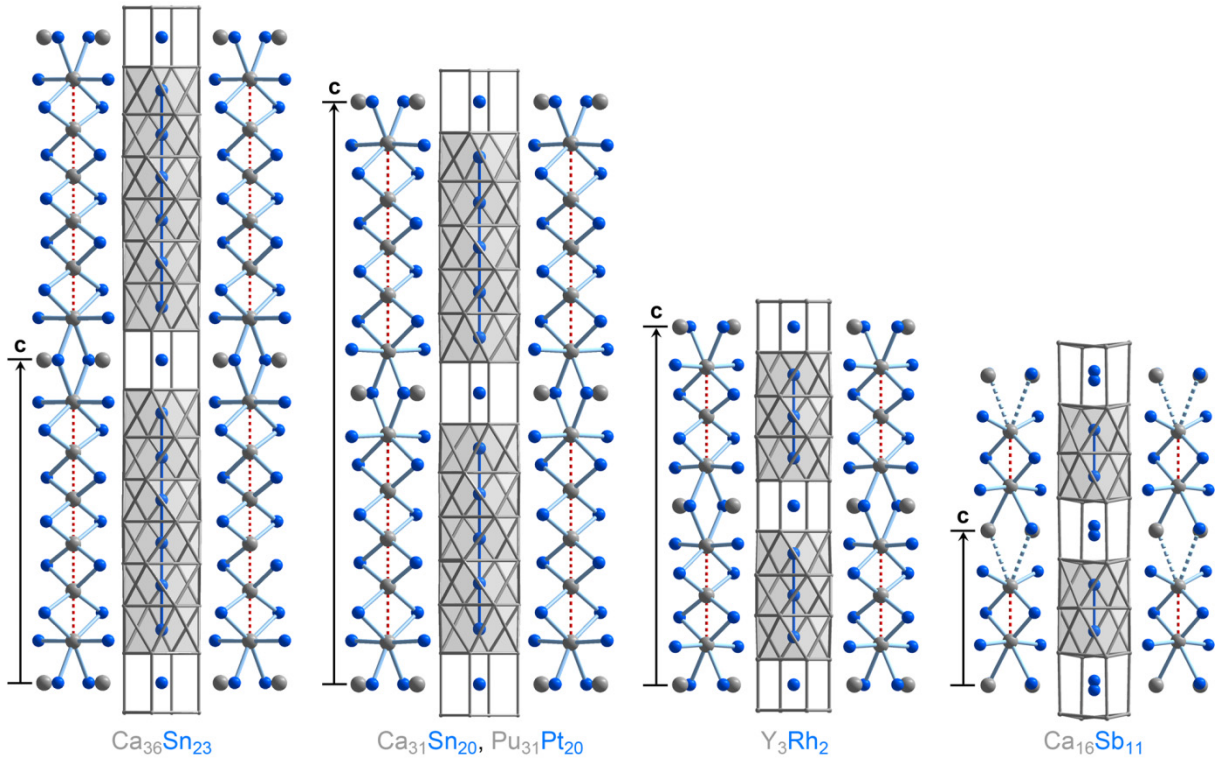

Figure 4.2. A family of long-period superstructures of the W_5Si_3 type with regularly spaced planar interfaces perpendicular to *c*.

The gradual shrinking of the W_5Si_3-type domains across this series is an impressive illustration of the structural flexibility obtained in intermetallic phases, and raises the question of what driving forces motivate such progressions. For this particular series, Corbett and coworkers have provided a plausible explanation for the instability of the simple W_5Si_3 type in, for instance, the Ca-Sn system: in a hypothetical Ca_5Sn_3 phase, the neighboring Ca atoms in the tetrahedral chains would be expected to have unusually short distances to each other (3.3 Å, by our estimation; see Figure 4.3), suggesting that the Ca atoms may be too large for their coordination environment.[34] The interfaces in the observed superstructures in this series could serve to alleviate interatomic repulsion at such contacts.

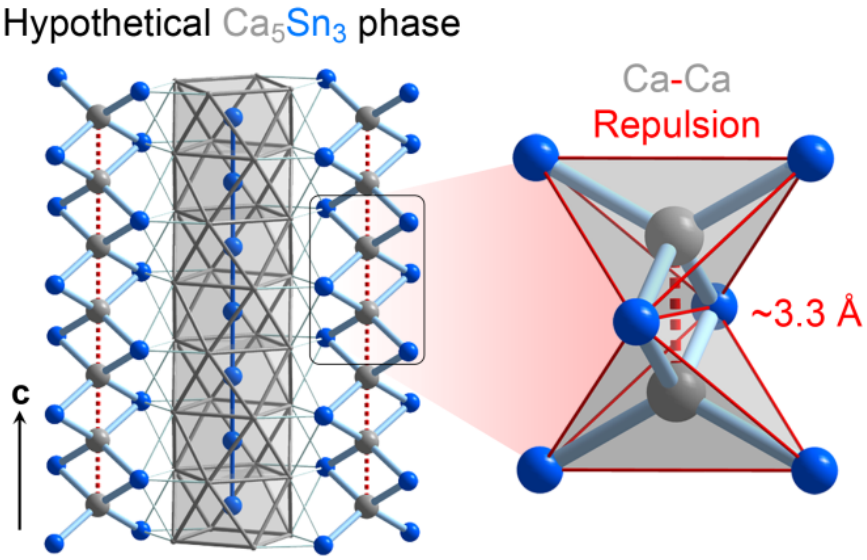

Figure 4.3. The model of Corbett et al. for the instability of the W_5Si_3-type structures in phases with large electropositive atoms at the W-type positions, illustrated with Ca_5Sn_3. The placement of Ca in the edge-sharing tetrahedral chains running along *c* leads to uncomfortably close Ca-Ca contacts. The superstructures of the W_5Si_3 type observed in these systems are hypothesized to relieve interatomic repulsion at these contacts.

Atomic size thus appears to be playing a part in the structural series of Figure 4.2. How might electronic structure calculations be used to support and inform this view? Over the course of this paper, we will see that the DFT-Chemical Pressure analysis provides a first-principles approach to this problem, which reveals in graphical and intuitive terms not only the Ca-Ca repulsion in a hypothetical W_5Si_3-type basic structure, but also its release upon moving to the observed $Ca_{36}Sn_{23}$ structure. A first step will be introducing some improvements to the original DFT-CP scheme described earlier, which makes the method more amenable to systems with atoms of very different sizes and valence electron counts.

4.4. Computational procedures

For all calculations on $Ca_{36}Sn_{23}$ and a hypothetical W_5Si_3-type Ca_5Sn_3 phase, two planewave-based DFT codes were used because of their complementary strengths. The Vienna Ab initio Simulation Package (VASP)[35,36] was used for the geometrical optimization of the two structures due to the highly efficient potentials provided with the package, requiring relatively low energy cut-offs. The geometrical optimizations were performed in two steps: first the ion positions were optimized within a unit cell of fixed dimensions, then all structural parameters were optimized simultaneously. All calculations used the local-density approximation (LDA), and were carried out in the high precision mode, corresponding to an energy cutoff of 106.4 eV. The calculations employed 4×4×8 and 4×4×2 Monkhorst-Pack k-point meshes[37] for Ca_5Sn_3 and $Ca_{36}Sn_{23}$, respectively, and the ultrasoft pseudopotentials provided with the package.[38]

The ABINIT package[25,26] was used for generating the necessary data for the DFT-CP analysis of the VASP-optimized structures, because of the exquisite degree of detail and transparency in its output. For each structure, the raw data for the CP analysis was obtained through three single-point calculations spanning a volume range of 0.6%. The calculations employed the LDA exchange-correlation functional of Goedecker, Teter, and Hutter,[39] and the Hartswigen-Goedecker-Hutter (HGH) pseudopotentials provided with the package.[40] The energy cutoff was set to 816 eV for the calculations on $Ca_{36}Sn_{23}$ and Ca_5Sn_3 when the valence-only Ca HGH potential was used. For Ca_5Sn_3, calculations were also carried out using the semicore Ca HGH potential; here the energy cutoff was set to 1088 eV. These values were found to converge the energy of formation of the hypothetical Ca_5Sn_3 phase to less than 0.5 meV/atom. Monkhorst-Pack k-point meshes[37] distributing 4×4×2 and 4×4×8 points through the Brillouin zone were used for the $Ca_{36}Sn_{23}$-type and W_5Si_3-type phases, respectively. The spacing of the voxels (determined by the

fast Fourier transform grids) was set to 108×108×192 and 108×108×72 grids for $Ca_{36}Sn_{23}$ and Ca_5Sn_3, respectively.

4.5. Creating chemical pressure maps

To set-up the discussion of our improvements to the DFT-Chemical Pressure (CP) scheme and its application to $Ca_{36}Sn_{23}$, let's briefly review the method. The basis of the DFT-CP analysis is the electronic-packing frustration model (Figure 4.4) for the interaction of electronic interactions and atomic size in condensed matter systems.[41,42] Dense atomic packing constraints can lead to correlations between interatomic distances within a structure. Such correlations make it difficult to independently optimize the interactions between different pairs of atoms. The size of atoms becomes manifest when the formation of a chemical bond at one contact requires shortening at other contacts for which there is not sufficient electronic support. Such tension would be expected to result in non-optimal interatomic distances (Figure 4.4b) and local pressures acting between the affected atoms, which might be referred to with the term *chemical pressure* (CP) to distinguish them from physical pressures exerted on the system externally.

The formalism of the quantum mechanical stress density[19-23] offers one approach for determining how such pressures are distributed in a crystal structure. In the DFT-CP analysis, a simpler avenue is taken, in which the structure is divided into a grid of voxels (small finite volume elements) and the pressure experienced by each voxel is calculated as follows.

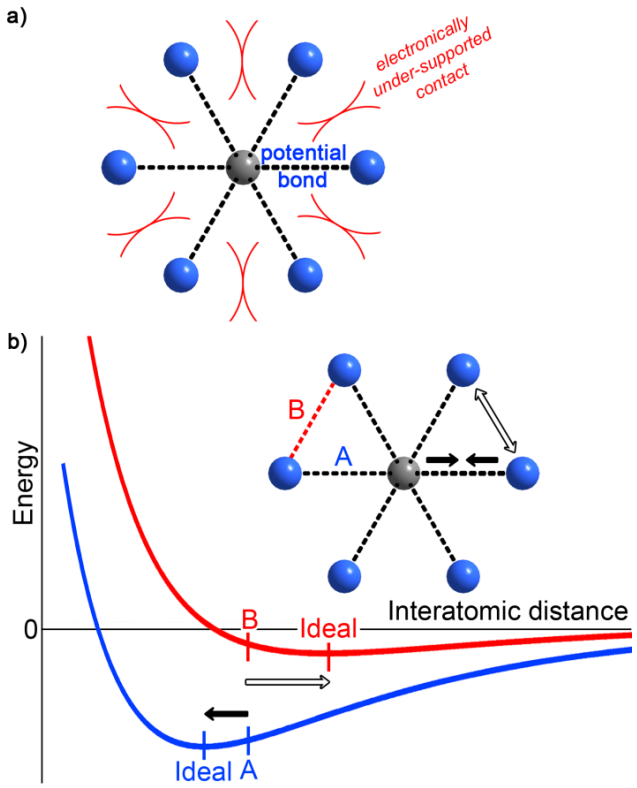

Figure 4.4. Non-ideal interatomic distances and local chemical pressures resulting from electronic packing frustration (EPF). (a) A schematic illustration of the electronic packing frustration model. Reproduced from Ref. 39 with the kind permission of the American Chemical Society. (b) The compromise between the need for contraction along some contacts (A) and expansion along others (B) leads to non-optimal distances. The slope of the energy vs. distance curves at the observed distance is related to a local pressure acting at that contact.

We begin with the expression for the total energy for a system calculated with Kohn-Sham DFT:[43]

$$E_{total} = \iiint_{\substack{unit \\ cell}} \left(\sum_n o_n \psi_n^* \nabla^2 \psi_n + \left(V_{local} + \frac{1}{2} V_{Hartree} + \varepsilon_{XC}(\rho) \right) \rho(\vec{r}) \right) dV + E_{Ewald} + E_{nonlocal} + E_{\alpha} \qquad (4.1)$$

In this expression, the terms under the integral represent the kinetic energy of the system and the local contributions to the potential energy, measured relative to the reference state of an exchange-correlation-free homogeneous electron gas interacting with the ion cores. Outside the integral, the E_{Ewald}+E_a terms together give the energy of that reference state, and $E_{nonlocal}$ provides the potential energy resulting from any nonlocal components of the atomic pseudopotentials (an additional term $E_{-kT\cdot Entropy}$ can be added to correct the total energy from any smearing of the band occupancies about the Fermi energy).

The next step in the determination of the DFT-CP distribution is to recognize that the E_{total} expression has the form of the integral over an energy density plus a remainder:

$$E_{total} = \iiint_{\substack{unit \\ cell}} \rho_{energy}(\vec{r})dV + E_{remainder} \tag{4.2}$$

which can be represented more conveniently for numerical work as a sum over an grid of voxel energies plus a remainder:

$$E_{total} \approx \sum_{n}^{N_{voxels}} \rho_{energy}(\vec{r})V_{voxel} + E_{remainder}$$

$$\approx \sum_{n}^{N_{voxels}} E_{voxel,n} + E_{remainder} \tag{4.3}$$

where N_{voxels} is the number of voxels into which the unit cell volume (V_{cell}) is divided, and V_{voxel} is the volume of each voxel, i.e. $V_{\text{voxel}} = V_{cell}/N_{voxels}$.

Once the total energy is mapped spatially in this way, a similar spatial distribution of the pressure is obtained by taking the negative derivative of E_{total} with respect to V_{cell}:

$$P = -\frac{\partial E_{total}}{\partial V_{cell}} = -\frac{\partial}{\partial V_{cell}}\left(\sum_{n}^{N_{voxels}} E_{voxel,n} + E_{remainder} \right)$$

$$= -\frac{\partial}{\partial V_{cell}}\left(\sum_{n}^{N_{voxels}} E_{voxel,n} \right) + P_{remainder}$$

$$= -\frac{1}{N_{voxels}}\left(\sum_{n}^{N_{voxels}} \frac{\partial E_{voxel,n}}{\partial V_{voxel}} \right) + P_{remainder}$$

$$= \frac{1}{N_{voxels}} \sum_{n}^{N_{voxels}} P_{voxel,n} + P_{remainder} \qquad (4.4)$$

so that the total pressure experienced by the structure, P, becomes resolved into an average over the voxel pressures ($P_{voxel,n}$) plus a remainder pressure arising from the components of the total energy.[44] In practice, this differentiation is performed numerically by constructing energy grids from the output of ABINIT calculations[25,26] on a structure at two slightly different volumes, taking the difference, and dividing by the difference in voxel volumes.

What then is the $P_{remainder}$ term? In Section B.1 of the Supporting Information, we describe how in principle the pressure contributions from E_{Ewald}, E_a, and $E_{nonlocal}$ can be apportioned among the atoms or interatomic regions of the structure. However, in each case, one encounters an unacceptable degree of ambiguity in applying the procedure which leads to unreliable results. Through work with several intermetallic systems, we have concluded that the best treatment of $P_{remainder}$ is also the simplest: we consider it as corresponding to a homogeneous background pressure, which can then be added to each of the voxel pressures.

For metallic phases lacking localized bonds, the pressure grids resulting from this procedure tend to have high-magnitude features near the nuclear positions, occuring in the midst of relatively flat negative

background pressure. This is illustrated for a hypothetical W_5Si_3-type phase Ca_5Sn_3 (the parent structure of the more complex $Ca_{36}Sn_{23}$ structure we discussed above) in Figure 4.5a. Here, cross-sections of the CP map are taken perpendicular to the *a*-axis and centered on the unusually close Ca-Ca contacts. The pressures in the map are indicated using colors ranging from dark blue (-900 GPa) to red (+2100 GPa). The most vivid variations in color occur near the nuclear positions, where negative pressures at the atom centers give way to intense positive pressures slightly further out, arranged in a ring for the Sn and in a cross for the Ca. As the distance from the nuclei increases, the voxel pressures gradually converge on a relatively flat background pressure.

4.6. Isotropic core component averaging

The presence of strong CP oscillations emanating from the ion cores poses a number of problems for the interpretation of the CP maps. First, the magnitudes of the pressures encountered during these undulations dwarf those appearing in the interatomic regions of the map. This makes more subtle features of the map difficult to detect. A second undesirable aspect of these oscillations is that they tend to mask any directional dependence of the pressures in the core region, as might emerge from an interatomic interaction. Finally, as the core region contains both large positive and negative pressures, it is difficult to gauge the net pressure near the nucleus. As we are using pseudopotentials, the question of how seriously to take these oscillations is important. They occur largely in the pseudopotential core regions, where the correspondence is weakest between the true wavefunctions of the system and the pseudo-wavefunctions of the calculation. In other words, their specific forms are artificial products of the atomic pseudopotentials.

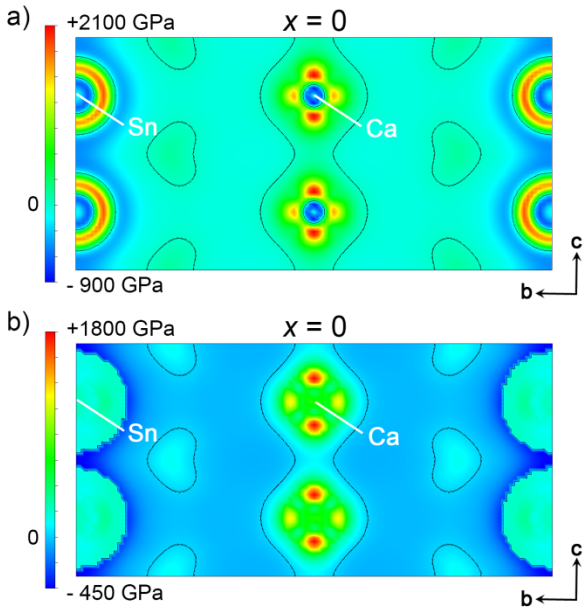

Figure 4.5. Cross-sections of the chemical pressure (CP) map of a hypothetical W_5Si_3-type Ca_5Sn_3, taken through the x=0 plane. The cross-sections are shown (a) before and (b) after flattening of the spherically symmetric oscillations emanating from the ion cores. Black contours corresponding to CP=0 are overlaid on the map. See text for details.

The form of the pseudopotential near the core is typically chosen to be mathematically convenient while still reproducing key atomic properties. Likewise, we can substitute the oscillatory CP features with a simpler CP distribution that captures the same net pressure and directional dependence upon integration over the core region. In order to accomplish this, we have developed an *isotropic core component averaging* procedure for use in the generation of DFT-CP maps.

We begin by choosing a radius for the core region of an atom, typically about 1.0 Å. The voxels within this distance of the nuclear position will be subject to this procedure while all others will be left unchanged. Next, the pressure for any voxel in the core region, say the nth voxel in the grid, is written in terms of its deviation from the average P for that voxel's distance from the nucleus, $r_{n\text{-}ion} = \left| \vec{r}_{voxel,n} - \vec{R}_{ion} \right|$:

$$P_{voxel,n} = \left[P_{voxel,n} - \overline{P_{voxel}(r_{n-ion})}\right] + \overline{P_{voxel}(r_{n-ion})}$$

$$= \Delta P_{voxel,n} + \overline{P_{voxel}(r_{n-ion})} \tag{4.5}$$

In other words, the core voxel pressures are written as the sum of an anisotropic function, representing the directional dependence of the core pressures, and a spherically symmetric function.

The oscillations around the core occur predominantly in the latter function, the isotropic core component. These can be removed by simply replacing the values of this function with its average within the core region:

$$P_{\substack{isotropic \\ core}} = \frac{\int_0^{r_{core}} \overline{P_{voxel}(r_{n-ion})} \cdot 4\pi(\vec{r}_{n\text{-}ion})^2 \, dr_{n-ion}}{\frac{4}{3}\pi {r_{core}}^3} \tag{4.6}$$

In this way, the modified voxel pressures are calculated as

$$P_{voxel,n} = \Delta P_{voxel,n} + P_{\substack{isotropic \\ core}} \tag{4.7}$$

Under this transformation, both the anisotropic component and the average of the isotropic function are left unchanged. As such, the net pressure within the core region and the directional dependence are preserved.

In Figure 4.5b, we replot the DFT-CP cross-section of the hypothetical Ca_5Sn_3 structure through the x=0 layer, this time with the isotropic core component averaging applied with core radii of 0.8 Å for Ca and 1.3 Å for Sn. For both atom types, there is significant reduction in the variation of pressures in the core region. In the case of Sn, the ripples of color are now replaced with a virtually uniform cyan, corresponding to a slightly positive pressure, distributed over large circles with pixilated edges. This pixilation

marks the discontinuous change in the CP distribution upon leaving the averaged core region. This offers a much more straightforward view of the Sn's core pressures than the untreated CP map of Figure 5a: the Sn cores have net positive pressures which are essentially isotropic.

The Ca cores in this plot become similarly smoother. Upon averaging over the spherically symmetric components, the blue cores at the atom centers disappear, yielding a distribution that is uniformly positive. A highly anisotropic character to the Ca core also becomes more apparent. Red spots appear just above and below the Ca nuclear pressures, indicating colossal positive pressures of 1800 GPa. These positive CP features lie along the unusually short Ca-Ca contacts of the structure (2.96 Å in our LDA-DFT optimized geometry), to which Corbett and coworkers attributed the nonexistence of this compound. This is the first of several indications we will see in the DFT-CP analysis of this system of the truly repulsive nature of the interactions at these contacts.

Another difference between the CP maps of Figures 4.5a and 4.5b is notable. Upon removing the oscillatory character of the core pressures, the pressure range seen in the structure shrinks from 3000 GPa down to 2250 GPa. This 750 GPa reduction in the pressure range captured by the color map allows for a greater contrast between features in the space outside of the cores, although in this case the repulsive character of the Ca-Ca contacts remains the most striking aspect of the map.

4.7. Integration and projections of the CP distribution around atoms

The results of the isotropic core component averaging described in the last section reinforce the view of the CP distribution as consisting of core regions with net positive pressure immersed in a background

of negative pressure. Interpreting the overall pressure exerted by the interatomic contacts on each atom then requires an integration of the pressure map and its directionality around the atom's position.

The angular dependence of the pressure distribution surrounding an atom plays a central role here. Because of this, we will now describe in detail our procedure for determining the pressures experienced by the atoms along different directions. This process begins with a projection of the CP distribution onto spherical harmonics as follows:

$$a_{lm} = \frac{1}{N_{voxels,atom}} \sum_{n} w_{n,atom} P_{voxel,n} Y_{l.m}(\theta_n, \varphi_n) \tag{4.7}$$

where $w_{n,atom}$ is the fraction of voxel n's pressure that is attributed to the atom in question, $N_{voxels,atom} = \Sigma_n w_{n,atom}$ is the number of voxels belonging to the atom, and (θ_n, ϕ_n) are the angular components of the spherical polar coordinates of voxel n with the origin being the atom's nucleus. The projections a_{lm} can be used to reconstruct this angular distribution—or the chemical pressure anisotropy, $CP_{aniso}(\theta, \phi)$, of the atom—where all pressure contributions are now mapped onto the unit sphere:

$$CP_{aniso}(\theta,\phi) = \sum_{l \le l_{max}} \left(\sum_{-l \le m \le l} a_{lm} Y_{l.m}(\theta,\phi) \right) \tag{4.8}$$

with l_{max} being the l index of the highest order spherical harmonics to be included in the projection.

The interpretation of this function is made clear by taking a closer look at the a_{00} coefficient. As $Y_{0,0} = 1/(4\pi)^{½}$, a_{00} is simply calculated as

$$a_{00} = \frac{1}{N_{voxels,atom}} \sum_{n} w_{n,atom} P_{voxel,n} \sqrt{\frac{1}{4\pi}} = P_{atom} \sqrt{\frac{1}{4\pi}} \tag{4.9}$$

where P_{atom} is the nominal average pressure experienced by the atom. The summation of terms giving rise to the $CP_{aniso}(\theta, \phi)$ function then begins as

$$CP_{aniso}(\theta,\phi) = P_{atom}\sqrt{\frac{1}{4\pi}}\cdot\sqrt{\frac{1}{4\pi}}+\ldots=\frac{P_{atom}}{4\pi}+\ldots \tag{4.10}$$

In this way, the higher order terms describe how the CP anisotropy function differs from a sphere whose radius is proportional to the average pressure of the atom.

The role of the $1/4\pi$ factor in Equation 4.10 can be understood by taking the integral of the function over the unit sphere. In this case all of the higher-order terms integrate to zero, and we are left with

$$\int_{\phi=0}^{\phi=2\pi}\int_{\theta=0}^{\theta=2\pi}\sin(\theta)CP_{aniso}(\theta,\phi)d\theta d\phi=\int_{\phi=0}^{\phi=2\pi}\int_{\theta=0}^{\theta=2\pi}\sin(\theta)\frac{P_{atom}}{4\pi}d\theta d\phi$$

$$=\frac{P_{atom}}{4\pi}\int_{\phi=0}^{\phi=2\pi}\int_{\theta=0}^{\theta=2\pi}sin(\theta)d\theta d\phi=P_{atom} \tag{4.11}$$

The integral thus recovers the average pressure for the atom. The factor $sin(\theta)d\theta d\phi/4\pi$ can then be thought of as a weight in averaging over the sphere.

We now arrive at a straightforward means of interpreting the numerical values of the $CP_{aniso}(\theta, \phi)$ function: Multiplying the function by 4π yields the net pressure experienced along each direction, $P_{atom}(\theta, \phi)$, i.e.

$$P_{atom}(\theta,\phi)=4\pi\cdot CP_{aniso}(\theta,\phi) \tag{4.12}$$

$$P_{atom}=\overline{P_{atom}(\theta,\phi)}=\int_{\phi=0}^{\phi=2\pi}\int_{\theta=0}^{\theta=2\pi}P_{atom}(\theta,\phi)\frac{sin(\theta)d\theta d\phi}{4\pi} \tag{4.13}$$

Once the $P_{atom}(\theta, \phi)$ function is calculated, it can be easily represented graphically using radial plots, as in Figure 4.6. In these images, a CP surface is plotted on each atom, with the distance of the atom to a point on the surface with coordinates (θ, ϕ) being proportional to the magnitude of the CP experienced along that direction. The signs of the pressures are given by the color of the surface. Black features in the plots correspond to directions along which contraction is favorable (evoking the image of a black hole pulling inwards on its surroundings). Lobes in white indicate directions for which expansion is desired (by analogy with the bright radiance of white hot stars).

There are two parameters involved in the creation of such plots: the l_{max} value and the form of the weighting scheme leading to the $w_{n,atom}$ values. l_{max} simply determines to what detail the angular distributions of the CP map is captured. From our experience, setting l_{max} beyond 4 or 5 substantially increases the processing time without leading to any significant changes in the qualitative pressure schemes. For this reason, we use 4 here for the upper limit. The selection of the scheme for distributing the voxel pressures among the atoms is a more involved issue, and is the focus of the next section.

4.8. The contact volume integration scheme

In the projections of the CP map described above, a key parameter is the way in which the structure is divided among the atoms. For the Sr-Ag and Ca-Ag structures we examined earlier,[18] we tested several schemes for this, including the use of fixed spheres around the atomic positions, the division of space into Voronoi cells[45] ($w_{n,atom}$=1 if voxel n is within the Voronoi cell of the atom), and the atomic domains revealed through the use of Bader's Quantum Theory of Atoms in Molecules.[7,8] For these cases, the Voronoi cell approach provided results that were easiest to interpret, in that the CP surfaces on pairs of atoms agreed

most closely in their signs and magnitudes along the vector separating them. Unresolved is whether the Voronoi scheme works in all cases, and if not, what would provide a more robust partitioning of space.

In Figure 4.6a, we explore this question by showing CP anisotropy surfaces calculated for a W_5Si_3-type Ca_5Sn_3 phase, the hypothetical parent to the complex $Ca_{36}Sn_{23}$ structure, integrated with the Voronoi scheme. The results are shown using two Hartswigen-Goedecker-Hutter pseudopotentials for Ca available with the ABINIT package, to explore how stable the CP picture is to changes in the modeling of the core regions of the atom. The calculation leading to the image in the left panel employed the semicore Ca potential, in which the usual Ca $4s^2$ set of valence electrons is expanded to include lower energy $3p^6$ and $3s^2$ electrons, for a total of 10 valence electrons/Ca atom. The right panel shows the result using the valence-only potential, in which just the Ca $4s^2$ electrons are considered explicitly.

Similarities and differences between the two plots occur. In both cases, the surfaces on the tetrahedrally-coordinated Ca atoms exhibit white lobes pointing across the shared tetrahedral atoms toward their Ca neighbors. This indicates that positive, repulsive pressures occur at these contacts, as is consistent with the unusually short Ca-Ca distances here (2.94 Å in our LDA-DFT optimized structures). However, the shapes of these calcium CP surfaces differ dramatically. For the Ca semicore calculation, triangular positive pressure lobes, resembling the bodies of squid, point toward the neighboring Ca atoms. In the valence-only Ca result, long, nearly cylindrically symmetric lobes appear in these places instead. Additional positive pressure features occur around the equator of the CP anisotropy surfaces.

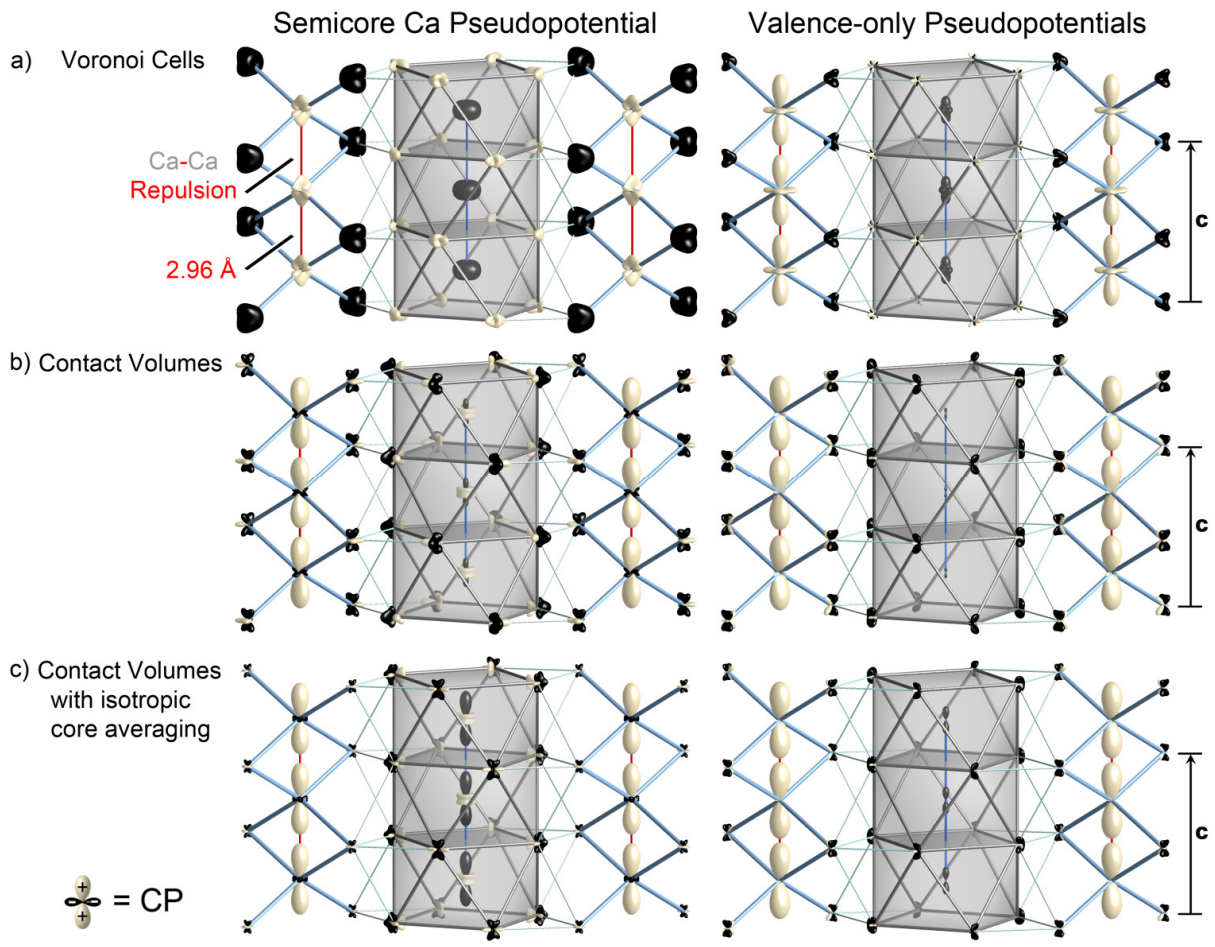

Figure 4.6. The dependence of the chemical pressure (CP) anisotropies of atoms in the hypothetical Ca_5Sn_3 structure on the method of dividing voxels among the atoms, employing Ca pseudopotentials treating semicore electrons explicitly (left column) and as part of the pseudopotential core (right column). The CP distribution around each atom is shown as a radial plot, with the distance between the atom's nucleus and a point on the surface being proportional to the pressure magnitude along that direction. The color of the surface indicates the sign of the pressure: black for negative, white for positive. The plots are shown for results obtained when (a) dividing space into the Voronoi cells of the atoms, (b) dividing space into contact volumes, within which the distributions are averaged before carrying out the projections, and (c) applying the contact volume scheme to a CP map that has undergone isotropic core component averaging. The final method yields the greatest agreement between the two calculations using different models for the Ca core. The scales of the CP surfaces in the various panels are chosen for maximum clarity rather than consistency.

The remaining features in the plot are more difficult to interpret. The Sn atoms appear with black bulbous surfaces, but whose relative sizes and shapes vary between the two plots. For the two results a similar story emerges of Ca-Ca repulsion against a backdrop of the other interactions, but the inconsistencies indicate that the Voronoi approach is rather sensitive to the details of the treatment of the core region.

A more basic drawback of using the Voronoi approach in this system can be seen by beginning with points on the black Sn surfaces in either image and following some of these directions toward the neighboring Ca atoms. In many cases the black Sn surfaces point to white features on Ca surfaces. Along the Ca-Sn contacts, then, we see desires for contraction on the Sn and for expansion on the Ca. Missing here is an immediate answer to the issue of whether these Ca-Sn contact distances are too long or too short.

Unlike the Ca-Ag and Sr-Ag structures we examined earlier, it appears that drawing boundaries between atomic cells at the mid-points between contacts is too crude of an assumption for this system. One could imagine moving the boundaries back and forth to make the atomic cells better reflect the relative sizes of the atoms. Such a procedure is included in our latest version of the *CPintegrate* program, using the additively-weighted Voronoi method.[45] We have found, however, that this approach is of limited use, particularly when examining combinations of atoms with very different numbers of core-like electrons in their valence sets.

A first step toward a more generally useful integration scheme is to clearly express our assumptions about how the CP map should be interpreted. While the pressure calculated for each voxel in the unit cell is a function of the full electronic structure of the compound, we expect that the atoms closer to a voxel will play larger roles in determining its pressure. For the purposes of interpreting the CP map in terms of

pair-wise interatomic interactions, *we will assume that a voxel's pressure is an expression of the interaction between its two closest atoms.* The involvement of other atoms in that voxel's pressure will appear as modulations to the degree of optimization of that specific interatomic interaction.

Once this assumption is articulated, a straightforward approach emerges to obtaining CP anisotropy surfaces that are reflective of the net interactions between an atom and its neighbors. We begin by dividing the unit cell into regions of space whose voxels are associated with the same interatomic contact, regions which we will refer to as *contact volumes*. We then average the pressures of the voxels within each contact volume to obtain average interatomic pressures.[46] Next, in order to evenly distribute the pressures between the atoms at each contact, the individual voxel pressures are replaced with the average pressures for their contact volumes. Finally, the voxels are assigned with a weight of one half to both atoms of their contacts, and the projections described in the last section are carried out.

The CP anisotropy surfaces resulting from the application of this contact volume integration scheme are presented in Figure 6b, where the agreement between the semicore Ca and valence-only Ca results is substantially improved. In particular, the shapes of the positive pressure lobes along the short Ca-Ca contacts are now quite similar. Also, the placement of these black and white lobes now appears to be coordinated between the atoms. In going through the structure contact by contact, one finds that in each case the CP anisotropy surfaces on both sides of interatomic vectors are the same color. In particular, the majority of the contacts between atoms of different layers along the *c*-direction appear with black CP lobes. These contacts are overly long and call for the contraction of the structure's *c*-axis. Such contraction is prevented, of course, by the strained Ca-Ca contacts within the tetrahedral chains.

The largest difference between the semicore and valence-only results is perhaps in the CP surfaces on the Sn atoms with square-antiprismatic coordination. For the semicore calculation, functions resembling d_{z2} orbitals appear on these Sn atoms, with black lobes pointing up and down toward the Sn atoms in neighboring antiprisms, and a white torus of positive pressure directed at the surrounding Ca atoms. On moving to the valence-only result, these Sn CP anisotropy surfaces virtually vanish. In looking closely at the image, a tiny black dumbbell is barely visible at each of these sites.

This difference can be partially bridged with the application of the isotropic core component averaging procedure discussed earlier. This is shown in Figure 6c using the core radii of 0.8 and 1.3 Å for Ca and Sn, respectively. The vertical lobes of d_{z2}-like surfaces for the Sn atoms in the semicore calculation have grown at the expense of the torus, leading to a surface more closely approximating a black dumbbell. Meanwhile, the black dumbbell of the valence-only calculation has grown closer to the sizes of the black lobes on the semicore result.

At this point, one could imagine making refinements on the contact volume scheme to further improve the agreement between the two choices of pseudopotentials. Indeed, the assumption that each voxel is influenced by its two closest atoms is crude in several ways. It neglects the differing sizes of atoms of different elements, and has the potential to coarsely cut off the influence of other neighboring atoms that might be only slightly further out. In the newest version of our *CPintegrate* program, we have included preliminary code for a scheme in which Hirshfeld weights[47] are used in determining the relative importance of the contacts that a voxel could participate in. For Ca_5Sn_3, this yields pictures similar to those of Figure 4.6c, but the option is still under development.

Even with its simplistic assumptions, the contact volume scheme offers a much clearer picture of the competing interactions within Ca_5Sn_3 than the Voronoi scheme. In the application of the DFT-CP method to a number of intermetallic phases, we have seen that these results are representative: in each case the contact volume integration scheme provides a chemically-meaningful interpretation of the CP map.

4.9. Chemical pressure analysis of $Ca_{36}Sn_{23}$

In the above sections, we worked through the technical details of the DFT-CP analysis and refinements to the method to improve its generality. Having built this foundation, we will now demonstrate the use of this approach in the theoretical investigation of the experimentally-deduced role of size-effects in solid state structures. As a model system we will use the superstructure series based on the insertion of planar interfaces into the W_5Si_3 type (Figures 4.1 and 4.2). The driving force for such superstructure ordering was hypothesized by Corbett et al. to be the presence of overly short contacts between the larger, more electropositive atoms in the centers of the edge-sharing tetrahedra in the basic structure (Figure 4.3).

As a first step in exploring this idea, let's look again at the CP distribution in a hypothetical W_5Si_3-type Ca_5Sn_3 phase, as would arise from removing the interfaces from the $Ca_{36}Sn_{23}$ or $Ca_{31}Sn_{20}$ structures. In Figure 4.7a, we show the LDA-DFT optimized structure of this phase (using the valence-only Ca pseudopotential), overlaid with its atomic CP anisotropy surfaces.

For the most part, the features of the plot appear very small. The exception occurs in the chains of edge-sharing tetrahedra: for the Ca atoms at the tetrahedral centers, large white lobes are pointing up and down toward the Ca atoms in the neighboring tetrahedra (right panel). These are the largest lobes in the

structure, corresponding to a positive pressure of 176 GPa. As these lobes occur along the Ca-Ca contacts in the tetrahedron chains, this suggests that the Ca-Ca distances within these chains are overly short.

Expansion of the structure to alleviate these positive pressures would then be desirable. However, such a response is prevented by the remainder of the structure, which appears decorated by small, black negative pressure features. These results confirm the model of Corbett and coworkers of the W_5Si_3 structure type being destabilized by the presence of large electropositive atoms in the tetrahedron centers.

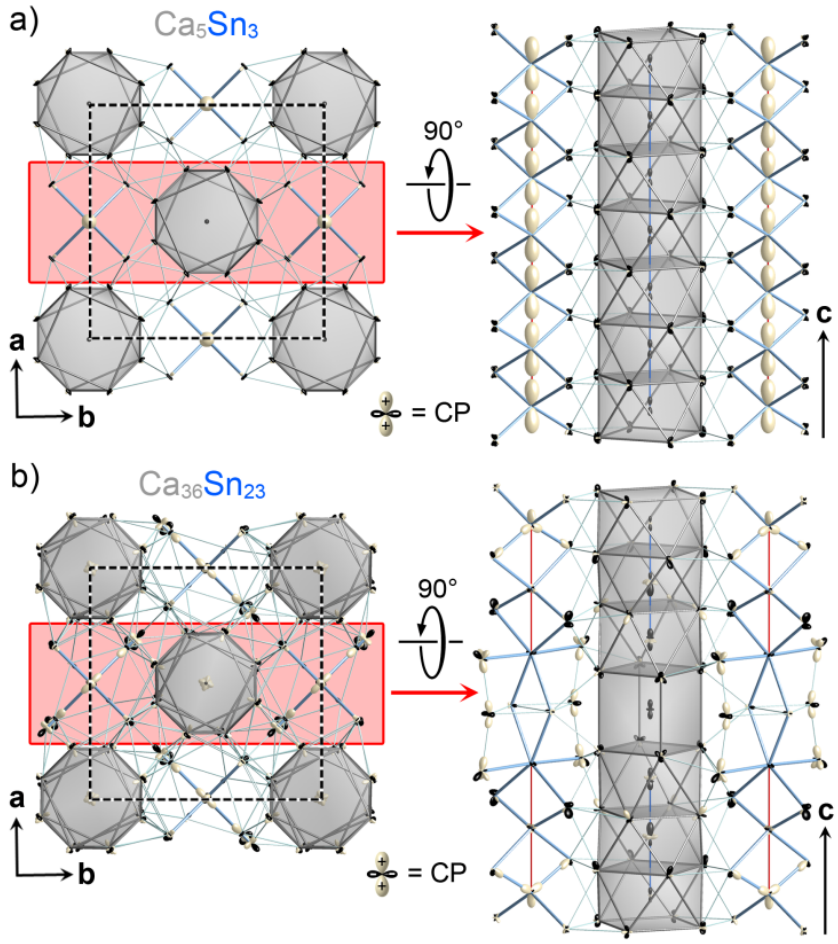

Figure 4.7. Comparison of the DFT-chemical pressure (CP) distributions in (a) a hypothetical W_5Si_3-type Ca_5Sn_3 phase, and (b) the observed superstructure variant $Ca_{36}Sn_{23}$. See the caption of Figure 6 for plotting conventions. The CP surfaces of panels a and b are plotted at the same scale, allowing direct comparison of their features.

How might the insertion of interfaces relieve these positive pressures experienced by the tetrahedrally-coordinated Ca atoms? Symmetry plays a role in the CP situation of these atoms. The contacts above and below each Ca are equivalent by the mirror planes of the W_5Si_3 type's space group, *I*4/*mcm*. Moving upwards away from the Ca atom below would increase the positive pressures along the contact above, and vice versa. The insertion of a defect plane either above or below a Ca atom would break this stalemate by providing open space for the atom to move into.

In Figure 4.7b, we test this expectation by plotting the CP anisotropy surfaces for the $Ca_{36}Sn_{23}$ structure, in which interfaces cut the Ca_5Sn_3 structure into 3-unit-cell-thick slabs. The right panel of Figure 7b focuses on the region near one of the interfaces. Red bars are used to connect the Ca atoms corresponding to tetrahedrally-coordinated Ca atoms in the hypothetical Ca_5Sn_3 phase. Along these red bars, the vertical white lobes corresponding to Ca-Ca repulsion have essentially vanished, with the exception of those furthest from the interface at the top and bottom of the panel.

As is shown in Figure 4.8, a comparison of the Ca coordination environment in the tetrahedral chain in the hypothetical Ca_5Sn_3 phase with those in $Ca_{36}Sn_{23}$ allows for this chemical pressure release to be framed in familiar chemical terms. In Ca_5Sn_3, these atoms lie at the centers of edge-sharing tetrahedra of Sn. As is well-known from Pauling's rules,[48] the shared edges between tetrahedra force the tetrahedral centers into close proximity. The tetrahedral coordination environments of large atoms are thus expected to avoid fusing at edges. It would appear that $Ca@Sn_4$ tetrahedra lie in this category.

In the corresponding regions of $Ca_{36}Sn_{23}$, a simple solution to the issue of Ca-Ca repulsion is found. Each interface bisects a Ca-Ca pair in the tetrahedral chain and places four additional Sn atoms between

them. Through the incorporation of these Sn atoms, the edge-sharing tetrahedral arrangement is converted to a pair of edge-sharing *octahedra*. This configuration is expected to be much less sterically demanding: the ideal Sn-Ca-Sn angles in these polyhedra decrease from 109.5° in the tetrahedra to 90° in the octahedra. As a result, the polyhedral edges occur further out from the centering Ca atoms, and the Ca-Ca distances between neighboring polyhedra are substantially increased. This provides relief to the repulsive CPs between the Ca atoms at the interface (between which no positive CP lobe is apparent in Figure 8b), but also to the Ca atoms deeper in the W_5Si_3-type slabs which are free to relax toward the space provided by the octahedral Ca atoms.

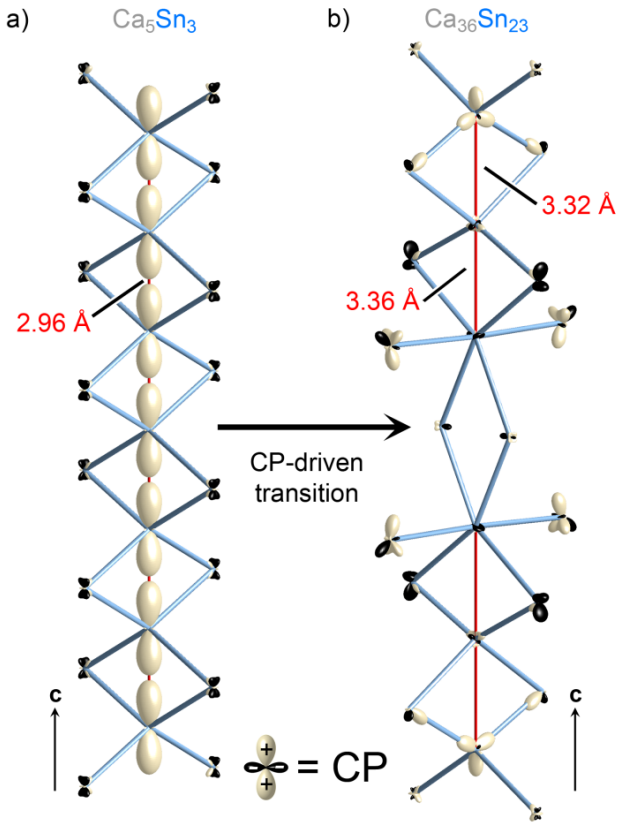

Figure 3.8. Chemical pressure release in the chains of Ca-centered tetrahedra on going from (a) the hypothetical W_5Si_3-type Ca_5Sn_3 to (b) the observed structure of $Ca_{36}Sn_{23}$. Note that on going from (a) to (b) larger Ca-Ca distances are achieved by replacing edge-sharing tetrahedra with edge-sharing octahedra. As in Figure 4.7, the same scale is used for all CP surfaces. For plotting conventions, see the caption to Figure 4.6.

In the Ca-Sn system, the appearance of planar interfaces in the W_5Si_3 type, as in $Ca_{36}Sn_{23}$ and $Ca_{30}Sn_{21}$, can thus be seen as driven by chemical pressure. The picture which emerges from this analysis confirms the insightful model of Corbett et al. for this family of superstructure phases, and illustrates how DFT-CP analysis allows for the theoretical investigation and confirmation of hypotheses based on atomic size effects.

4.10. Conclusions

In this paper, we develop the idea behind DFT-chemical pressure (CP) analysis into a general tool for analyzing the role atomic size has in shaping the structures of solid state materials. We described several improvements over our earlier outline of the method, including (1) the use of isotropic core component averaging to make the essential CP features in the ion core regions more apparent in the CP maps, and (2) the creation of the contact volume integration scheme, in which interatomic interactions appear as mutually attractive or repulsive from the points of view of the participating atoms. The revised DFT-CP approach was then applied toward revealing the origin of the $Ca_{36}Sn_{23}$ structure, a superstructure variant of the W_5Si_3 type.

Our analysis of $Ca_{36}Sn_{23}$ confirmed the empirically-derived model of Corbett et al. for this family of structures: a hypothetical W_5Si_3-type Ca_5Sn_3 phase would have chains of edge-sharing Ca-centered Sn tetrahedra, i.e. $(CaSn_{4/2})_\infty$, which would enforce unreasonably short Ca-Ca distances. Large positive CPs occur along these Ca-Ca contacts, indicating that the distances are indeed overly short. An advantage of the DFT-CP approach is that further details can be seen in how these distances are constrained by the remainder of the structure. For $Ca_{36}Sn_{23}$, the predominant features apart from the short Ca-Ca contacts

are small black lobes pointing along a variety of interactions. Such details provide clarity and precision to the useful concept of "matrix effects."[49-51]

The DFT-CP analysis joins a number of other theoretical tools for extracting chemical insight from electronic structure results on solid state structures. Methods in common use include the crystal orbital overlap and Hamiltonian population analyses (COOP and COHP);[52-54] the electron localization function (ELF) and its successor, the electron localization indicator (ELI);[55-59] and the analysis of electron density features using the quantum theory of atoms and molecules (QTAIM).[7,8] How does the DFT-CP analysis relate to these analytical tools?

A common feature of each of the other tools listed above is that they explore the presence or strength of bonding interactions in a system with a given geometry. For example, the COHP analysis for a contact quantifies the strength of that interatomic interaction, and whether this interaction would be strengthened or weakened by a change in the electron count of the compound. Similarly an ELI analysis reveals at what points in the structure electron pairs tend to be localized, which can then be correlated with the presence of bonds or lone-pairs.

The DFT-CP analysis provides complementary information: by determining the pressures at work at each interatomic contact, it reveals to what extent the bonding strength is optimized with respect to interatomic distances. Examining the geometrical arrangements made by these pressures throughout a structure can point to where frustration arises in the optimization of these interactions, and where structural transformations may be necessary. These insights may contribute to materials design principles, growing out of a tighter integration of the roles of electronics and atomic sizes in our understanding of solid state compounds.

Acknowledgements

We thank Brandon Kilduff for engaging discussions on the application of DFT-CP analysis to intermetallic phases, and Yiming Guo for suggesting improvements to the code of our DFT-CP programs. We also gratefully acknowledge the financial support of the National Science Foundation (NSF) through grant DMR-1207409. This research involved calculations using computer resources supported by NSF grant CHE-0840494.

4.11. References

(1) van der Waals, J. D. *Nobel Lectures, Physics 1901-1921*; Elsevier Publishing Company: New York, 1967, pp 254-265.

(2) Smith, M.; March, J. *March's advanced organic chemistry: reactions, mechanisms, and structure*; 6th ed.; Wiley-Interscience: Hoboken, NJ, 2007, pp 397-401.

(3) Goldschmidt, V. M. *Trans. Faraday Soc.* **1929**, *25*, 253.

(4) Pauling, L. *J. Am. Chem. Soc.* **1927**, *49*, 765.

(5) Nolas, G. S.; Cohn, J. L.; Slack, G. A.; Schujman, S. B. *Appl. Phys. Lett.* **1998**, *73*, 178.

(6) Nolas, G. S.; Cohn, J. L.; Slack, G. A. *Phys. Rev. B* **1998**, *58*, 164.

(7) Bader, R. F. W. *Atoms in molecules: a quantum theory*; Oxford University Press: Oxford, England, 1994, pp 133-137.

(8) Baranov, A.; Kohout, M.; Wagner, F. R.; Grin, Y.; Kniep, R.; Bronger, W. *Z. Anorg. Allg. Chem.* **2008**, *634*, 2747.

(9) Hume-Rothery, W.; Raynor, G. V. *The structure of metals and alloys*; 4th ed.; Institute of Metals: London, 1962, pp 217-245.

(10) Laves, F. in *Theory of alloy phases; a seminar on theory of alloy phases held during the Thirty-seventh National Metal Congress and Exposition, Philadelphia, October 15 to 21, 1955*; American Society of Metals: Cleveland, 1956, pp 124-198.

(11) Pearson, W. B. *The crystal chemistry and physics of metals and alloys*; Wiley-Interscience: New York, 1972, pp 73-79.

(12) Simon, A. *Angew. Chem. Int. Ed. Engl.* **1983**, *22*, 95.

(13) Amerioun, S.; Häussermann, U. *Inorg. Chem.* **2003**, *42*, 7782.

(14) Mozharivskyj, Y.; Tsokol, A. O.; Miller, G. J. *Z. Kristallogr. Cryst. Mater.* **2006**, *221*, 493.

(15) Li, B.; Corbett, J. D. *Inorg. Chem.* **2007**, *46*, 8812.

(16) Xia, S.-q.; Bobev, S. *J. Am. Chem. Soc.* **2007**, *129*, 10011.

(17) Fredrickson, D. C.; Lidin, S.; Venturini, G.; Malaman, B.; Christensen, J. *J. Am. Chem. Soc.* **2008**, *130*, 8195.

(18) Fredrickson, D. C. *J. Am. Chem. Soc.* **2012**, *134*, 5991.

(19) Nielsen, O. H.; Martin, R. M. *Phys. Rev. B* **1985**, *32*, 3780.

(20) Godfrey, M. J. *Phys. Rev. B* **1988**, *37*, 10176.

(21) Ziesche, P.; Gräfenstein, J.; Nielsen, O. H. *Phys. Rev. B* **1988**, *37*, 8167.

(22) Filippetti, A.; Fiorentini, V. *Phys. Rev. B* **2000**, *61*, 8433.

(23) Rogers, C. L.; Rappe, A. M. *Phys. Rev. B* **2002**, *65*, 224117/1.

(24) Treglia, G. In *Stress and strain in epitaxy; theoretical concepts, measurements, and applications*; Elsevier Science B.V.: 2001, pp 119-150.

(25) Gonze, X.; Rignanese, G.-M.; Verstraete, M.; Beuken, J.-M.; Pouillon, Y.; Caracas, R.; Jollet, F.; Torrent, M.; Zerah, G.; Mikami, M.; Ghosez, P.; Veithen, M.; Raty, J.-Y.; Olevano, V.; Bruneval, F.; Reining, L.; Godby, R.; Onida, G.; Hamann, D. R.; Allan, D. C. *Z. Kristallogr.* **2005**, *220*, 558.

(26) Gonze, X.; Amadon, B.; Anglade, P. M.; Beuken, J. M.; Bottin, F.; Boulanger, P.; Bruneval, F.; Caliste, D.; Caracas, R.; Cote, M.; Deutsch, T.; Genovese, L.; Ghosez, P.; Giantomassi, M.; Goedecker, S.; Hamann, D. R.; Hermet, P.; Jollet, F.; Jomard, G.; Leroux, S.; Mancini, M.; Mazevet, S.; Oliveira, M. J. T.; Onida, G.; Pouillon, Y.; Rangel, T.; Rignanese, G. M.; Sangalli, D.; Shaltaf, R.; Torrent, M.; Verstraete, M. J.; Zerah, G.; Zwanziger, J. W. *Comput. Phys. Commun.* **2009**, *180*, 2582.

(27) Leon-Escamilla, E. A.; Corbett, J. D. *Inorg. Chem.* **1999**, *38*, 738.

(28) Palenzona, A.; Manfrinetti, P.; Fornasini, M. L. *J. Alloys Compd.* **2000**, *312*, 165.

(29) Moreau, J. M.; Paccard, D.; Parthé, E. *Acta Crystallogr. B* **1976**, *32*, 1767.

(30) Cromer, D. T.; Larson, A. C. *Acta Crystallogr. B* **1977**, *33*, 2620.

(31) Fornasini, M. L.; Franceschi, E. *Acta Crystallogr. B* **1977**, *33*, 3476.

(32) Ganguli, A. K.; Guloy, A. M.; Leon-Escamilla, E. A.; Corbett, J. D. *Inorg. Chem.* **1993**, *32*, 4349.

(33) Leon-Escamilla, E. A.; Hurng, W.-M.; Peterson, E. S.; Corbett, J. D. *Inorg. Chem.* **1997**, *36*, 703.

(34) Ganguli, A. K.; Gupta, S.; Zhao, J.-T.; Alejandro Leon-Escamilla, E.; Corbett, J. D. *J. Solid State Chem.* **2005**, *178*, 2959.

(35) Kresse, G.; Furthmüller, J. *Phys. Rev. B* **1996**, *54*, 11169.

(36) Kresse, G.; Furthmüller, J. *Comput. Mater. Sci.* **1996**, *6*, 15.

(37) Monkhorst, H. J.; Pack, J. D. *Phys. Rev. B* **1976**, *13*, 5188.

(38) Vanderbilt, D. *Phys. Rev. B* **1990**, *41*, 7892.

(39) Goedecker, S.; Teter, M.; Hutter, J. *Phys. Rev. B* **1996**, *54*, 1703.

(40) Hartwigsen, C.; Goedecker, S.; Hutter, J. *Phys. Rev. B* **1998**, *58*, 3641.

(41) Fredrickson, D. C. *J. Am. Chem. Soc.* **2011**, *133*, 10070.

(42) Harris, N. A.; Hadler, A. B.; Fredrickson, D. C. *Z. Anorg. Allg. Chem.* **2011**, *637*, 1961.

(43) Martin, R. M. *Electronic structure : basic theory and practical methods*; 1st pbk. ed.; Cambridge University Press: Cambridge, UK ; New York, 2008, pp 255-256.

(44) An interesting alternative spatial resolution of the pressure was recently described in Ouahrani, T.; Menendez, J. M.; Marqués, M.; Contreras-García, J.; Baonza, V. G.; Recio, J. M. *Europhys. Lett.* **2012,** *98,* 56002. Here, the focus is on the inverse of the total pressure: $1/P = -\partial V/\partial E$. The $-\partial V/\partial E$ expression is then split into a sum of volume differentials for individual atomic cells (as obtained from a QTAIM analysis) over a common ∂E denominator. Each atomic ∂V is then proportional to an inverse atomic pressure.

(45) Okabe, A.; Boots, B.; Sugihara, K.; Chiu, S. N. *Spatial tessellations: concepts and applications of Voronoi diagrams*; 2nd ed.; Wiley: Chichester ; New York, 2000, pp 123-127.

(46) A relatively small group of voxels in any given structure may lie in the centers of the interstitial spaces that gives them a number of nearest neighbors at the same distance. As the number of first nearest neighbors grows beyond two, the number of contact volumes that a voxel can participate in rapidly grows. For simplicity, we treat such voxels as shared equally between its neighbors, without associating them to particular contact volumes. They are thus not included in the averaging within the contact volumes.

(47) Hirshfeld, F. L. *Theoret. Chim. Acta* **1977**, *44*, 129.

(48) Pauling, L. *J. Am. Chem. Soc.* **1929**, *51*, 1010.

(49) Guloy, A. M.; Corbett, J. D. *Inorg. Chem.* **1996**, *35*, 2616.

(50) Maggard, P. A.; Corbett, J. D. *Inorg. Chem.* **1998**, *37*, 814.

(51) Maggard, P. A.; Corbett, J. D. *Inorg. Chem.* **2001**, *40*, 1352.

(52) Hughbanks, T.; Hoffmann, R. *J. Am. Chem. Soc.* **1983**, *105*, 1150.

(53) Hughbanks, T.; Hoffmann, R. *J. Am. Chem. Soc.* **1983**, *105*, 3528.

(54) Dronskowski, R.; Bloechl, P. E. *J. Phys. Chem.* **1993**, *97*, 8617.

(55) Becke, A. D.; Edgecombe, K. E. *J. Chem. Phys.* **1990**, *92*, 5397.

(56) Savin, A.; Becke, A. D.; Flad, J.; Nesper, R.; Preuss, H.; von Schnering, H. G. *Angew. Chem. Int. Ed. Engl.* **1991**, *30*, 409.

(57) Savin, A.; Nesper, R.; Wengert, S.; Fässler, T. F. *Angew. Chem. Int. Ed. Engl.* **1997**, *36*, 1808.

(58) Kohout, M.; Pernal, K.; Wagner, F. R.; Grin, Y. *Theor. Chem. Acc.* **2004**, *112*, 453.

(59) Wagner, F. R.; Bezugly, V.; Kohout, M.; Grin, Y. *Chem. Eur. J.* **2007**, *13*, 5724.

Chapter 5.

Problem Solving with Pentagons: the Tsai-type Quasicrystal as a Structural Response to Chemical Pressure

This chapter has been published: Berns, V.M.; Fredrickson, D.C. *Inorg. Chem.* **2013**, *52*, 12875-12877.

5.1. Abstract

Even after significant advances in the structural characterization of quasicrystals—phases whose diffraction patterns combine the sharp peaks normally associated with lattice periodicity and rotational symmetries antithetical to such periodicity—this new form of long-range order remains enigmatic. Here, we present DFT-Chemical Pressure calculations on the 1/1 Tsai-type quasicrystal approximant $CaCd_6$, which reveal how its icosahedral clusters can be traced back to simple $CaCu_5$-type intermetallics, with their humble 6 atom unit cells. The results indicate that the Tsai-type clusters emerge from an atomic-size driven transformation from planar arrangements to spherical clusters, recalling the relationship between graphene and the C_{60} fullerene. Even after significant advances in the structural characterization of quasicrystals this new form of long-range order remains enigmatic. Here, we present DFT-Chemical Pressure calculations on the 1/1 Tsai-type quasicrystal approximant $CaCd_6$, which reveal how its icosahedral clusters can be traced back to simple $CaCu_5$-type intermetallics. The results indicate that the Tsai-type clusters

emerge from an atomic-size driven transformation from planar arrangements to spherical clusters, recalling the relationship between graphene and the C_{60} fullerene.

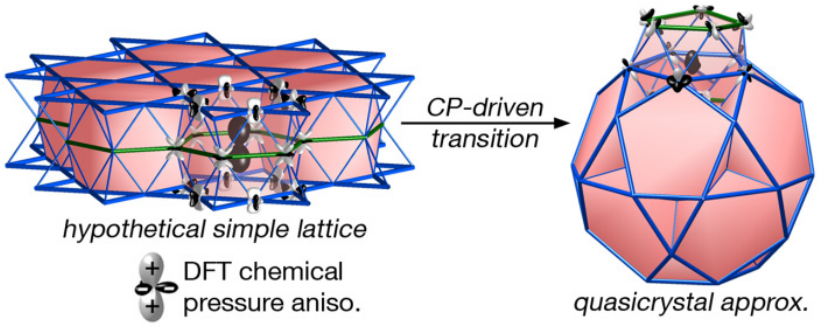

Figure 5.0. A hypothetical simple lattice of the $CaCu_5$-type undergoes a chemical pressure driven transition to yield the quasicrystalline approximant, $CaCd_6$. Chemical pressure analysis clarifies the relationship between the two structure types.

5.2. Introduction

Quasicrystals (QCs) are a new form of condensed matter exhibiting the seemingly contradictory properties of long-range atomic order and rotational symmetries incompatible with the translations of crystalline atomic packing.[1,2] The development of higher-dimensional approaches to quasiperiodic crystals, culminating in the structure determination and refinement of the Tsai-type icosahedral phase $YbCd_{5.7}$,[3] represents a major advance in structural science. As the geometrical details of QCs and their approximants (QCAs) emerge, they inspire still more wonder that such arrangements arise in materials.[4,5] Understanding and ultimately harnessing the driving forces that shape their long- and short-range order could offer avenues to the design of new atomic arrangements and physical properties enhanced by aperiodicity.[4,5]

The formation of icosahedral QCs has been connected to the Hume-Rothery rules for intermetallic compounds, in which valence electron concentration (VEC) and atomic size differences are key factors

influencing the stability of a structure.[6-8] The importance of VEC is supported by theoretical calculations that show the frequent presence of pseudogaps in the electronic DOS at the Fermi energy. This has led to the productive strategy of pseudogap tuning for the discovery of new QCs and QCAs.[9,10] Atomic size requirements, on the other hand, are difficult to elucidate with theoretical calculations, and are mainly inferred from empirical stability ranges.[8,10,11] Further development is needed to determine how electronic and size factors interact to stabilize icosahedral arrangements in QCs.

Herein, we describe how our recently developed DFT-Chemical Pressure (CP) analysis[12,13] reveals a visual, intuitive picture for the formation of icosahedral clusters in the Tsai family over simple periodic structures. As our first step, it is helpful to view metallic QCs and QCAs in their broader context: they are a specific subset of intermetallic phases, a vast family of solid state compounds formed between metallic elements. Intermetallics exhibit a broad structural diversity, with some adopting crystal structures whose unit cells contain thousands of atoms, such as $NaCd_2$ ($cF1157$)[14] and $Al_{55.4}Cu_{5.4}Ta_{39.1}$ ($cF23134$).[15,16] A majority of intermetallics, however, crystallize in simple structures with relatively few atoms per unit cell, such as the CsCl-type phases ($cP2$) and the Laves phases (e.g. $MgZn_2$, $hP12$). In surveying these structures, a striking observation can be made: complex structures often have similar compositions to simple ones in related binary systems. For instance, if we begin with the Tsai-type icosahedral QC $CaCd_{5.7}$ and its 1/1 approximant $CaCd_6$ (Figure 5.1a),[17,18] then look to the corresponding region in the Ca-Zn system, we find the $CaCu_5$-type $CaZn_5$ phase with only 6 atoms per hexagonal unit cell.[19] Comparing the Ca coordination environments in $CaCd_6$ and $CaZn_5$ yields a structural relationship in which pentagonal transition metal (TM) rings are replaced with hexagonal ones (Figures 5.1b,c).[20]

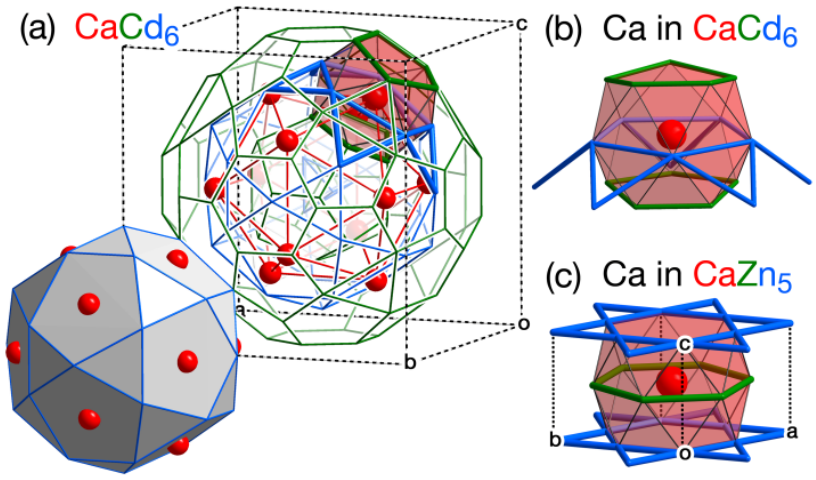

Figure 5.1. Connections between the Tsai-type QC and the $CaCu_5$ type. (a) The QC approximant $CaCd_6$, (b) The Ca coordination environment in $CaCd_6$, and (c) its counterpart in the $CaCu_5$-type $CaZn_5$.

5.3. Chemical pressure of $CaCd_5$ and $CaCd_6$

The driving forces leading to the $CaCd_6$ Tsai-type approximant can be seen in the electronic structure of the simpler alternative offered by the $CaCu_5$ type. To see this, we show in Figure 5.2 the results of DFT-CP calculations[21] on a hypothetical $CaCu_5$-type $CaCd_5$ phase. Large negative CP lobes (black) appear on the central Ca atom, corresponding to a net CP of –559 GPa. The Ca atoms contacts are thus longer than their energetically optimal distances. However, contraction along these contacts is prevented by positive CPs (white) within the Cd sublattice. Optimizing the Ca-Cd and Ca-Ca contacts would mean putting increased strain on already overly-short Cd-Cd distances.

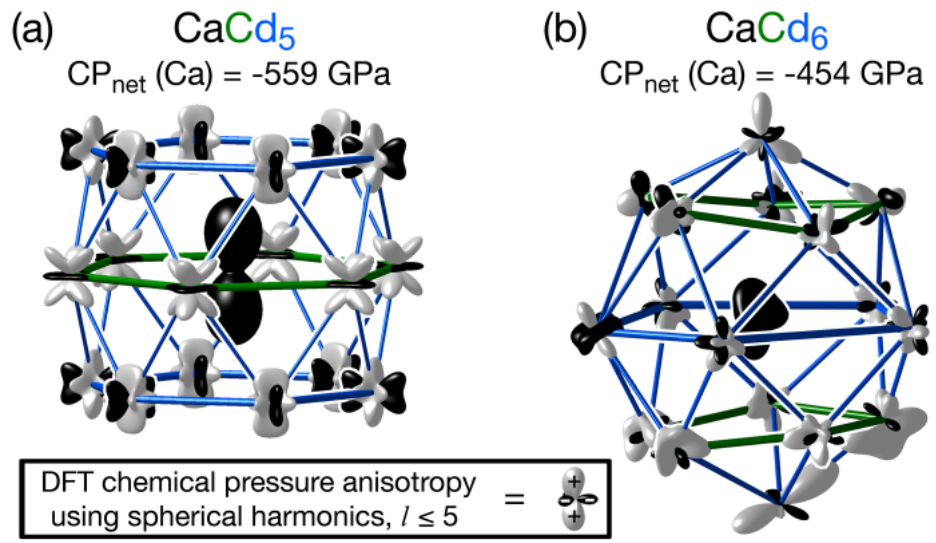

Figure 5.2. Local CP relief in the Tsai-type QCA. Comparison of the CP anisotropies around (a) the Ca atoms in the hypothetical $CaCd_5$ and (b) the most strained Ca atom of $CaCd_6$. The size of each lobe is proportional to the CP magnitude for calculated for that direction, while the color indicates the sign: black for negative, white for positive.

The Pressure-Distance Paradox[22] of pressure-induced phase transitions provides a guide to how the structure might respond to this: phases under high external pressure tend to adopt higher coordination numbers. As a consequence, the individual bond lengths increase despite the high pressure. Similarly, under low pressure atoms in a compound will prefer fewer neighboring atoms but at shorter distances. With the large negative CPs on the Ca atoms, we would expect Ca coordination environments adapted for a smaller atom—fewer neighbors with shorter interatomic distances to the central Ca atom.

Earlier, we showed that similar forces were at work in the Ca-Ag system.[12] There, large negative CPs on the Ca atoms are relieved through interfaces between $CaCu_5$-type slabs to form the Ca_2Ag_7 structure. The Ca-Cd system exhibits more exotic structural solutions to the same issues: instead of the expected $CaCu_5$-type phase, several compounds appear near the 1:5 Ca:Cd ratio, [23] including the $CaCd_6$ QCA.

5.4. Structural analysis of $CaCd_6$

The $CaCd_6$ structure has been described previously as a body-centered cubic packing of Tsai-type clusters, with the clusters themselves built from nested polyhedra (Figure 5.1a). Though the unit cell as a whole initially bears little resemblance to the $CaCu_5$ type, highlighting the local calcium environment (Figure 5.1b) yields a pentagonal analog to its familiar hexagonal counterpart in the $CaCu_5$-type (Figure 5.1c). Like tightening a too-loose belt, pentagons are expected to provide the smaller coordination environment needed by the Ca atoms.

A DFT-CP analysis of the Tsai-type approximant $CaCd_6$ supports its comparison with the $CaCu_5$ type. As in the hypothetical $CaCd_5$ phase (Figure 5.2a), the Ca coordination environments of the $CaCd_6$ (Figures 5.2b and c) exhibit a tension between negative pressures along the Ca-Cd contacts and positive pressures along the Cd-Cd ones. However, the transition from hexagonal to pentagonal polyhedra changes the balance of this tension. While in $CaCd_5$ the Ca CP surfaces are highly anisotropic and large (net CP = –559 GPa), the corresponding surfaces in the Tsai-type approximant are more spherical and smaller (net CPs between –451 and –418 GPa). This is in accord with our earlier predictions based on the Pressure-Distance Paradox; moving to fewer, but closer Cd neighbors alleviates negative pressure on the Ca sites.

$CaCd_6$'s use of pentagons provides a way of locally relieving CP issues, but poses an challenge for the long-range atomic arrangements of the structure. Pentagons are more difficult to tile than the hexagons of the original $CaCu_5$ type. The solution taken by $CaCd_6$ is found in curvature, as is shown in Figure 5.3 where the $CaCu_5$ and $CaCd_6$ structures are dissected layer by layer. The $CaCu_5$ type is presented as a stacking of a Cu honeycomb net (Figure 5.3a), a Ca hexagonal net (Figure 5.3b), then a Cu kagome net

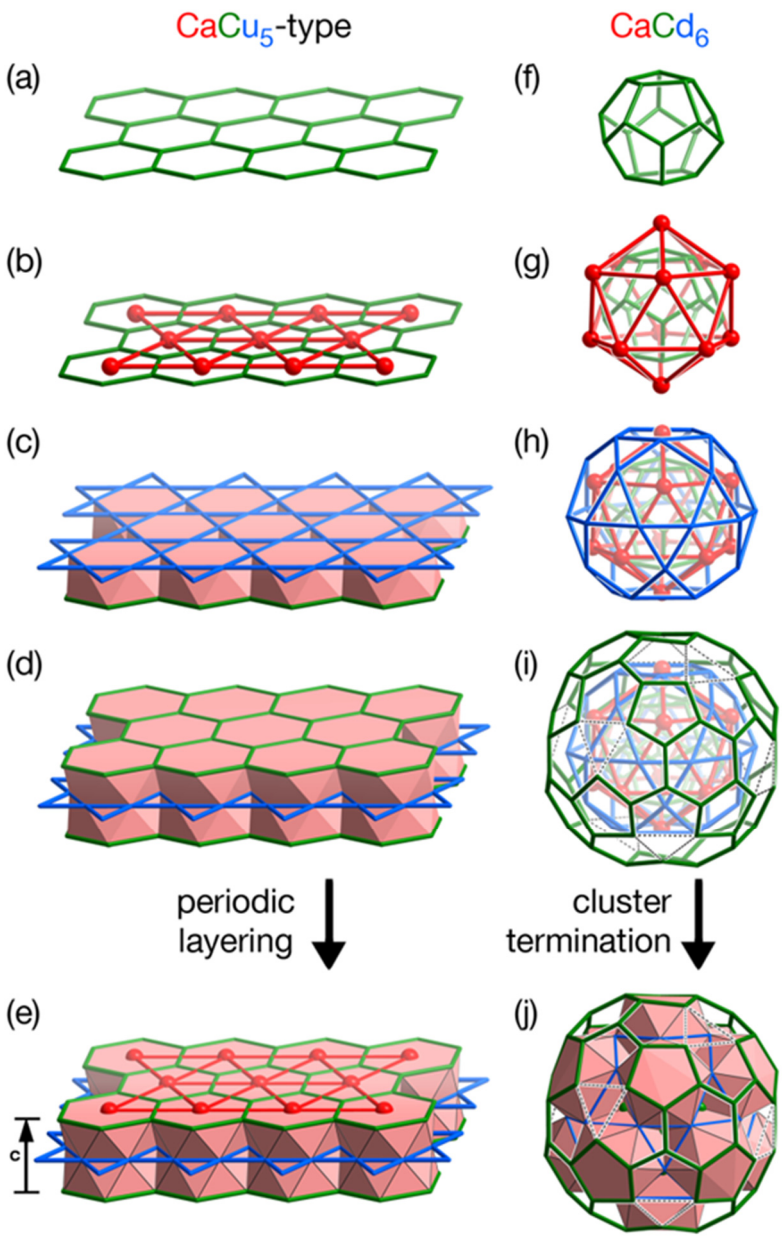

Figure 5.3. Parallels between the atomic nets of the $CaCu_5$ type and the shells of a Tsai-type cluster. The $CaCu_5$-type is built from a stacking of hexagonally-symmetric nets (a)-(d), and then repeating the sequence periodically to give (e) the full crystal structure. The Tsai-type cluster has corresponding shells based on pentagons shown in (f)-(i), but ends with (j) cluster termination as the Ca coordination environments are completed rather than periodicity. For clarity, the disordered tetrahedron at the center Tsai-type cluster is not shown.

(Figure 5.3c). These layers stack neatly along the *c* axis, repeating in a periodic fashion. When each 6-membered ring is reduced to a pentagon in the observed $CaCd_6$, planar packing is no longer the simplest option. Where the $CaCu_5$-type exhibits a honeycomb network of TM atoms, the Tsai-type curls its pentagonal "net" into a nearly regular dodecahedron (Figure 5.3f). Much like a graphene sheet could roll into a C_{60} molecule by reducing some hexagons to pentagons, here a pentagonal dodecahedron forms when every hexagon contracts to a pentagon. Likewise, the hexagonal net of Ca atoms in $CaCu_5$-type becomes an icosahedron in the Tsai cluster (Figure 5.3g). In the $CaCu_5$ type, the stacking of layers continues in the creation of a periodic structure, while in $CaCd_6$ the corresponding polyhedra nest concentrically until the Ca coordination environments are complete.

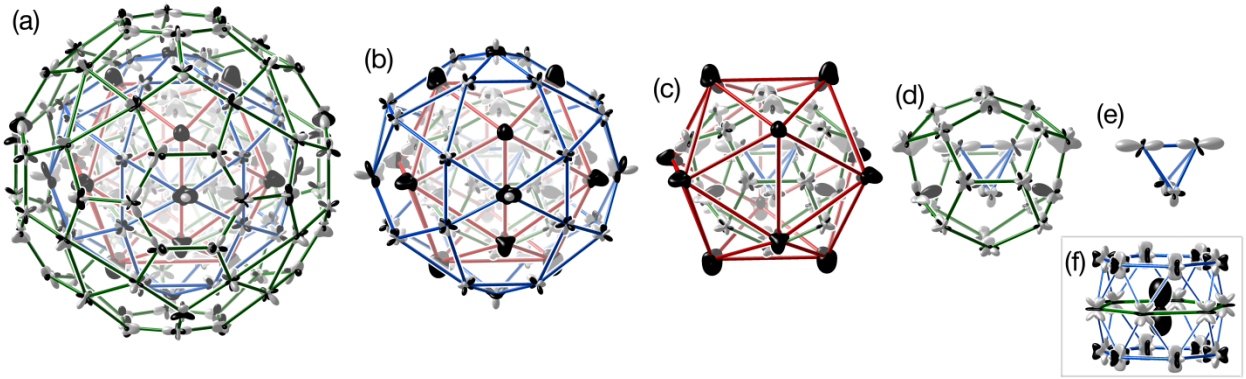

Figure 5.4. CP analysis of the Tsai-type cluster in $CaCd_6$. The entire Tsai-type cluster is shown in (a), then layers are removed to show (b) a Cd icosidodecahedron, (c) a Ca icosahedron, (d) a Cd dodecahedron and (e) the central Cd tetrahedron (disordered in the experimental structure). For reference, the corresponding results for $CaCd_5$ are plotted to scale in (f).

In Figure 5.4, we show the CP anisotropies for the full Tsai-type cluster. Now familiar themes recur: the Ca atoms experience negative pressures which are counteracted by positive pressures between the Cd atoms as in the original $CaCu_5$-type structures. A comparison of the CP anisotropy surfaces throughout

this cluster with those of the hypothetical $CaCu_5$-type $CaCd_5$ phase (Figure 5.4f) shows that the CPs of nearly all of the Ca and Cd atoms have been soothed on moving to their corresponding positions in $CaCd_6$.

The CP scheme of $CaCd_6$ also offers insights into another remarkable feature of the Tsai-type clusters we have set aside until now: the disordered tetrahedra at their cores.[18,24] As in other places in the structure, some of the Cd-Cd contacts between the central tetrahedron and surrounding dodecahedron experience positive pressure. This would be minimized when the Cd atoms of the tetrahedron lie in the pentagonal hollows of the dodecahedron. However, the symmetry incompatibility[25] between the two polyhedra means that when two Cd atoms on the tetrahedron lie in these hollows, the other two directly align with vertices on the dodecahedron (Figure 5.4d). The resulting interactions exhibit the largest positive pressures in the structure. In our DFT-optimization, all tetrahedra were forced to have the same, static orientation, allowing systematic strains to build up over the entire crystal. The experimentally observed disorder in the orientation of these tetrahedra may serve to diffuse this strain.

5.5. Conclusions

Over the course of this Communication, we have traced the formation of quasicrystal approximant $CaCd_6$ to the severity of CPs in the simple $CaCu_5$ type. The Ca atoms in the hypothetical $CaCu_5$-type $CaCd_5$ experience strong negative CPs caused by the size of their hexagonal environments. Replacing these hexagons with pentagons, as in the Tsai-type clusters, provides local relief, but introduces non-crystallographic 5-fold symmetry. An elegant solution is found in curvature: whereas the $CaCu_5$-type is composed of flat sheets of neatly periodic hexagonal rings, the introduction of pentagons leads to curved nets and ultimately the spheroidal Tsai-type cluster. The resulting picture illustrates the ability of the DFT-CP

analysis to integrate the size and electronic components of the Hume-Rothery view of QCs into an intuitive understanding of the origins of icosahedral order. We look forward to exploring the implications of this CP scheme for synthesis: elemental substitutions adjusting atomic sizes should modulate the relative stabilities of simple periodic ($CaCu_5$-type) and icosahedral (Tsai-type) arrangements, allowing us to probe the boundaries between these two forms of long-range atomic order.

Acknowledgements

We thank Joshua Engelkemier, Yiming Guo, and Brandon Kilduff for helpful discussions about the DFT-CP method. We also gratefully acknowledge financial support from the NSF through grant DMR-1207409. Computations contributing to this work were performed on computer resources supported by NSF grant CHE-0840494.

5.6. References

(1) Shechtman, D.; Blech, I.; Gratias, D.; Cahn, J. W. *Phys. Rev. Lett.* **1984**, *53*, 1951-1953.

(2) Steurer, W. *Chem. Soc. Rev.* **2012**, *41*, 6719-6729.

(3) Takakura, H.; Gómez, C. P.; Yamamoto, A.; De Boissieu, M.; Tsai, A. P. *Nature Mater.* **2007**, *6*, 58-63.

(4) Dubois, J.-M. *Useful quasicrystals*; World Scientific: Hackensack, NJ, 2005.

(5) Goldman, A. I.; Kong, T.; Kreyssig, A.; Jesche, A.; Ramazanoglu, M.; Dennis, K. W.; Bud'ko, S. L.; Canfield, P. C. *Nature Mater.* **2013**, *12*, 1-4.

(6) Mizutani, U.; Takeuchi, T.; Sato, H. *J. Non-Cryst. Solids* **2004**, *334-335*, 331-335.

(7) Takeuchi, T.; Mizutani, U. *Phys. Rev. B* **1995**, *52*, 9300-9309.

(8) Tsai, A. P. *J. Non-Cryst. Solids* **2004**, *334-335*, 317-322.

(9) Lin, Q.; Corbett, J. D. *Proc. Natl. Acad. Sci. USA* **2006**, *103*, 13589-13594.

(10) Lin, Q.; Corbett, J. D. *Inorg. Chem.* **2008**, *47*, 7651-7659.

(11) Wu, L.-m.; Seo, D.-k. *J. Am. Chem. Soc.* **2004**, 4398-4403.

(12) Fredrickson, D. C. *J. Am. Chem. Soc.* **2012**, *134*, 5991-5999.

(13) Engelkemier, J.; Berns, V. M.; Fredrickson, D. C. *J. Chem. Theory Comput.* **2013**, *9*, 3170-3180.

(14) Samson, S. *Nature* **1962**, *195*, 259-262.

(15) Conrad, M.; Harbrecht, B.; Weber, T.; Jung, D. Y.; Steurer, W. *Acta Crystallogr. B* **2009**, *65*, 318-325.

(16) Weber, T.; Dshemuchadse, J.; Kobas, M.; Conrad, M.; Harbrecht, B.; Steurer, W. *Acta Crystallogr. B* **2009**, *65*, 308-317.

(17) Bruzzone, G. *Gazz. Chim. Ital.* **1972**, *102*, 234-242.

(18) Gómez, C. P.; Lidin, S. *Phys. Rev. B* **2003**, *68*, 024203.

(19) Haucke, W. *Z. Anorg. Allg. Chem.* **1940**, *244*, 17-22.

(20) A similar pentagonal version of the $CaCu_5$-type Ca polyhedron has been been noted in Ru-Sn-Zn dodecagonal QC approximants. See Ref. 25.

(21) As described in detail in the Supporting Information, the DFT-CP calculations were performed on electronic structure calculations with LDA-DFT using the Vienna Ab initio Similation Package (VASP) and/or ABINIT. VASP references: (a) Kresse, G.; Furthmüller, J. *Phys. Rev. B* **1996,** *54,* 11169-11186; (b) Kresse, G.; Furthmüller, J. *Comput. Mater. Sci.* **1996,** *6,* 15-50; (c) Vanderbilt, D. *Phys. Rev. B* **1990,** *41,* 7892-7895. ABINIT references: (a) Gonze, X.; Rignanese, G.-M.; Verstraete, M.; Beuken, J.-M.; Pouillon, Y.; Caracas, R.; Jollet, F.; Torrent, M.; Zerah, G.; Mikami, M.; Ghosez, P.; Veithen, M.; Raty, J.-Y.; Olevano, V.; Bruneval, F.; Reining, L.; Godby, R.; Onida, G.; Hamann, D. R.; Allan, D. C. *Z. Kristallogr.* **2005,** *220,* 558-562; (b) Hartwigsen, C.; Goedecker, S.; Hutter, J. *Phys. Rev. B* **1998,** *58,* 3641-3662.

(22) Kleber, W. *Kristall und Technik* **1967**, *2*, 13-14.

(23) Subramanian, P. R. In *Binary Alloy Phase Diagrams, 2nd Ed.*; Massalski, T. B., Ed.; ASM International: Materials Park, Ohio, 1990; Vol. 44, p 899-901.

(24) Widom, M.; Mihalkovič, M. *MRS Online Proceedings Library* **2003**, *805*, LL1.10.

(25) Xiong, D.-B.; Okamoto, N. L.; Inui, H. *Inorg. Chem.* **2011**, *50*, 827-835.

Chapter 6.

Progress in Visualizing Atomic Size Effects with DFT-Chemical Pressure Analysis: From Isolated Atoms to Trends in AB_5 Intermetallics

Has been accepted for publication: Berns, V.M.; Engelkemier, J.; Guo, Y.; Kilduff, B.; Fredrickson, D.C. *J. Chem. Theory Comput.* Accepted.

6.1. Abstract

The notion of atomic size poses an important challenge to chemical theory: empirical evidence has long established that atoms have spatial requirements, which are summarized in tables of covalent, ionic, metallic, and van der Waals radii. Considerations based on these radii play a central role in the design and interpretation of experiments, but few methods are available to directly support arguments based on atomic size using electronic structure methods. Recently, we described an approach to elucidating atomic size effects using theoretical calculations: the DFT-Chemical Pressure analysis, which visualizes the local pressures arising in crystal structures from the interactions of atomic size and electronic effects. Using this approach, a variety of structural phenomena in intermetallic phases have already been understood in terms that provide guidance to new synthetic experiments. However, the applicability of the DFT-CP method to the broad range of the structures encountered in the solid state is limited by two issues: (1) the difficulty of interpreting the intense pressure features that appear in atomic core regions, and (2) the need to divide

space among pairs of interacting atoms in a meaningful way. In this Article, we describe general solutions to these issues. In addressing the first issue, we explore the CP analysis of a test case in which no core pressures would be expected to arise: isolated atoms in large boxes. Our calculations reveal that intense core pressures do indeed arise in these virtually pressure-less model systems, and allow us to trace the issue to the shifts in the voxel positions relative to atomic centers upon expanding and contracting the unit cell. A compensatory grid unwarping procedure is introduced to remedy this artifact. The second issue revolves around the difficulty of interpreting the pressure map in terms of interatomic interactions in a way that respects the size differences of the atoms and avoids artificial geometrical constraints. In approaching this challenge, we have developed a scheme for allocating the grid pressures to contacts inspired by the Hirshfeld charge analysis. Here, each voxel is allocated to the contact between the two atoms whose free atom electron densities show the largest values at that position. In this way, the differing sizes of atoms are naturally included in the division of space without resorting to empirical radii. The use of the improved DFT-CP method is illustrated through analyses of the applicability of radius ratio arguments to Laves phase structures and the structural preferences of AB_5 intermetallics between the $CaCu_5$ and $AuBe_5$ structure types.

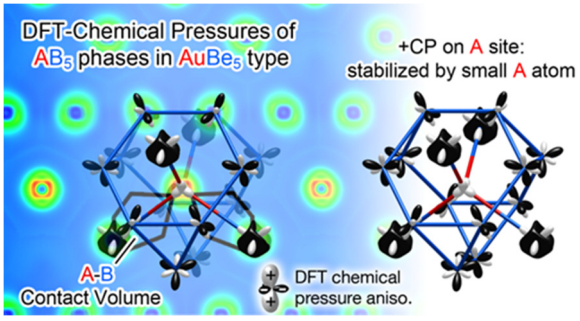

Figure 6.0. Schematic illustration of chemical pressure in an AB_5 compound of the $AuBe_5$ structure type. On the left, we see a 2-dimensional chemical pressure map, overlayed with key contact volumes. This new division of space enables analysis of the $AuBe_5$ structure type, which is shown to be stabilized by a small atom on the A site.

6.2. Introduction

While chemistry has long since stripped itself of the mysticism of the alchemists, its deep roots in experimental observation have led to a number of useful empirical concepts that have their own sort of poetry and allure, such as the chemical bond, electronegativity, and acidity. One goal of modern theoretical chemistry is the mapping of these notions to aspects of a compound's electronic structure, in ways that are both theoretically rigorous yet honor the richness of their historical uses and connotations. Atomic size is perhaps one of the most problematic of these empirical ideas. Experience with molecular and solid state structures suggests that atoms have measurable sizes,[1-3] yet the Schrödinger equation contains no terms involving atomic radii or explicit penalties for atoms encroaching upon each other. Indeed, the gradual and asymptotic decay of wavefunctions away from a system's nuclei is far from conducive to the construction of clear-cut boundaries defining the space occupied by individual atoms.[4] Given the importance of atomic size arguments throughout chemistry, theoretical tools which overcome these challenges could be extremely beneficial to deepening the roles theory can play in the design of experiments.

For inorganic solid state materials, the need for such theoretical methods for analyzing atomic size effects is particularly pressing, as can be seen in a quick survey of the recent literature. Atomic sizes or radius ratios are frequently invoked in discussions of the factors stabilizing particular crystal structures,[5-16] and in the interpretation of physical properties in terms of the presence of rattling atoms or interstitial spaces for guest atoms.[17,18] Furthermore, the empirical concept of chemical pressure, in which elemental substitutions create local stresses in a crystal structure, has been used as a framework for understanding relationships between composition and properties.[19-28]

While energy terms corresponding to atomic size effects are difficult to extract from an electronic structure calculation, we have recently found that their impact on stability can be productively inferred from a quantum mechanical adaptation of the chemical pressure concept just mentioned.[29-32] The basis of this method is the recognition that the size requirements of atoms are most apparent when interatomic repulsion at one contact in a structure impedes bonding at other contacts. As the repulsion and bonding interactions cannot be optimized simultaneously, local stresses are expected to result which, unlike the atomic sizes themselves, can be evaluated naturally using quantum mechanics through such concepts as the stress density.[33-38]

The DFT-CP analysis offers a way to examine these local pressures using the results of standard electronic structure calculations. The method uses the density and potential grids determined in the course of a DFT calculation to create maps of the pressure within crystal structures, which reveal points of frustration within those structures. This approach has been particularly fruitful in the study of the structural chemistry of intermetallic phases, where it has offered explanations for such phenomena as the creation of complex structures through the insertion of planar interfaces into simpler ones,[30,32] the formation of local icosahedral order in quasicrystal approximants,[39,40] and the ability of some $AuCu_3$-type lattices to accommodate guest atoms.[41]

Over the course of these and other applications, we have found that there are still several issues limiting the range of applicability of the DFT-CP analysis: (1) the proper treatment of the intense pressures that are calculated to occur near the core regions of an atom, and (2) the best scheme to interpret the pressure maps in terms of interatomic interactions.

In this Article, we will describe improved solutions to both of these challenges. Beginning with the CP calculations on individual atoms isolated in large unit cells, we will show that the introduction of an unwarping procedure to correct for the drift of the voxel positions relative to the nuclei upon expanding and contracting the unit cell can significantly reduce the severe pressures in the atomic core regions obtained in the original procedure. Including this step in the generation of CP-maps allows for more subtle CP features to come to the foreground, and eliminates the need for our earlier isotropic core averaging technique.

After describing this improved method for the construction of CP maps, we will then move to issues with their interpretation. As the CP distributions generally involve positive pressures near the core regions and negative pressures in the interstitial regions, evaluating the net pressure along a contact involves an averaging process over the voxels associated with that contact. The overall results are strongly tied to the scheme used in assigning these voxels to contacts. In our previous applications, we have found that assuming that a voxel's pressure is determined by the contact between its two closest atoms often provided intuitive results. However, this purely geometrical construction does not always assign differing spheres of influence to atoms of vastly different sizes. In this Article, we present a more sophisticated approach inspired by the Hirshfeld method for calculating atomic charges,[42] in which the electron density distributions of free atoms are used in determining which atoms will have the largest influence on a voxel's pressure.

In introducing these methodological improvements, we will make reference to structural trends in intermetallics that have been attributed to atomic size effects (Figure 6.1): the role of radius ratios in the Laves phases, and the transition from the $CaCu_5$ type to the $AuBe_5$ type for AB_5 intermetallics with increasingly small A atoms.[43] Through the use of the updated DFT-CP method, the latter structural trend

will become simply explained as a CP-driven transition in line with the pressure-distance paradox.[4,44] We anticipate that these results could provide a foundation for analyses of the origins of a series of complex intermetallic phases built from the intergrowth of the $AuBe_5$ and $MgCu_2$ types, at compositions near which a $CaCu_5$-type phase might be expected, such as $YbCu_{4.5}$ with its giant 7,448-atom monoclinic unit cell.[45-48]

6.3. Computational procedures

Electronic structure calculations for the geometrical optimization of crystal structures and the output of electron densities, kinetic energy densities, and components of the Kohn-Sham potentials were carried out with the ABINIT program.[49,50] All calculations employed the density functional theory (DFT) with the local density approximation (LDA) of Goedecker, Teter, and Hutter,[51] and the HGH atomic pseudo-potentials.[52] Further details, including the energy cut-offs, number of k-points used in the calculations, and the optimized atomic coordinates of the intermetallic structures discussed in this Article, are given in the Supporting Information.

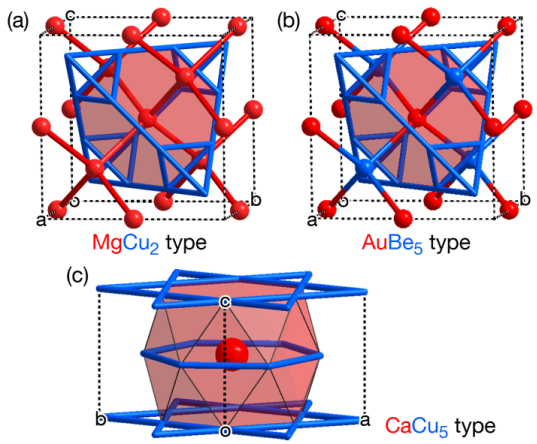

Figure 6.1. Structure types discussed in this Article whose stability ranges are empirically connected to atomic size: (a) The $MgCu_2$ (cubic Laves phase) type. (b) The $AuBe_5$ type. (c) The $CaCu_5$ type.

The output of the ABINIT calculations was used for the generation of CP maps through the scheme described below. The resulting CP maps were visualized with the program VESTA 3.[53] The projections of the CP maps onto spherical harmonics were plotted with Matlab. Software for the calculation and integration of CP maps using the method described in this paper is available at our research group website (http://www.chem.wisc.edu/~danny).

In the determination of Hirshfeld-inspired contact volumes, free atom electron densities were taken either from the ABINIT website, or calculated using the Atomic Pseudopotentials Engine (APE).[54]

6.4. Grid unwarping near atomic centers

The basis of the DFT-CP method lies in the ability of the DFT total energy to be at least partially represented as an integral over a spatially resolved energy density:

$$E_{DFT} = \iiint\limits_{\substack{unit \\ cell}} \rho_{energy}(\vec{r})dV + E_{remainder} \qquad (6.1)$$

where $E_{remainder}$ contains energetic contributions that are not easily traced to specific points in space, such as the Ewald energy and nonlocal components of the potential energy. Using the output of the ABINIT program, such an energy density function can be constructed in the form of discrete points on a grid, i.e.

$$E_{DFT} \approx \sum_{n}^{N_{voxels}} \rho_{energy}(\vec{r}_n)V_{voxel} + E_{remainder} = \sum_{n}^{N_{voxels}} E_n + E_{remainder} \qquad (6.2)$$

where N_{voxels} and V_{voxel} are respectively the number of voxels in the structure's unit cell and the volume of each individual voxel.

When we recall that pressure and total energy are related as $P = -\partial E/\partial V$, a straightforward approach to constructing pressure maps emerges. We can simply generate energy grids for a structure at volumes that are slightly contracted and expanded relative to the geometry of interest, and use the resulting energy difference at each voxel as the basis for the calculation of voxel pressures:

$$P_n = -\partial E_n / \partial V \tag{6.3}$$

The representation of the total energy as a sum over an energy grid then gives way to the net pressure experienced by a phase being expressed as the average over a pressure grid:

$$P = -\frac{\partial E_{DFT}}{\partial V_{cell}} = -\sum_{n}^{N_{voxels}} \frac{\partial E_n}{N_{voxels}\partial V_{voxel}} - \frac{\partial E_{remainder}}{\partial V_{cell}}$$

$$= \frac{1}{N_{voxels}} \sum_{n}^{N_{voxels}} P_n - P_{remainder} \tag{6.4}$$

In our applications of this procedure, we have found that a rather consistent result is obtained over a wide range of solid state compounds: the pressure maps are marked by intense pressures (of several TPa) near the core regions of the atoms, with much shallower features in the interstitial portions of the structure. The extreme magnitudes of these core pressures mean that success in the interpretation of the pressure map is strongly dependent on how the cores are divided among interatomic interactions.

A key question here is whether the strong pressures in the core regions represent the interactions between atoms, or are instead an artifact of the pseudopotential models for the atoms or the procedure for the generation of the pressure maps. A simple way to answer this question is to consider a case in which

interatomic interactions should be absent: isolated atoms. In Figure 6.2a, we show cross-sections of CP maps calculated for individual atoms placed in large unit cells, for which the interatomic distances are sufficiently long (10 Å) that each atom should exhibit virtually no influence on its neighbors. Maps are shown for a variety of elements, but common features are present: the atomic position at the center of the map is clearly decorated with intense oscillating pressure features emanating from the atomic cores. Depending on the diffuseness of the valence electron wavefunctions, the scales of these features vary over a significant range: from 0.07 atomic units for the valence-only Ca pseudopotential, to 120 atomic units for the semi-core Ga pseudopotential. In all but the shallowest pseudopotentials, pressures of more than 1 atomic unit are attained. When we recall that 1 atomic unit of pressure is equal to 96,000 GPa, it is apparent that they represent pressure responses that are incommensurately large relative to the minuteness of the perturbations on these systems induced by a small expansion or contraction of the unit cell.

Why should such strong pressures arise in the absence of interatomic interactions? An assumption of the above formulation of the DFT-CP approach is that upon changing a unit cell's volume, the features of the potentials and electron density expand or contract along with the voxel grid.[30] In this way, the pressure calculated for a specific voxel (P_n) is then related to the difference in energies calculated for that voxel in slightly expanded and contracted structures:

$$P_n^{DFT-CP} \approx -\frac{E_n^+ - E_n^-}{V_{voxel}^+ - V_{voxel}^-} \tag{6.5}$$

This may be expected to apply well to the regions in the interstitial spaces, where atoms are most responsive to changes in their surroundings. Near the atomic cores, however, where electrons cling tightly

to the nuclei, such an assumption is harder to justify. In the cores, the depths of the atomic pseudopotentials are such that variations in the cell volume would represent only minor changes. The electron density would not be expected to migrate along with an expanded or contracted voxel grid.

It would seem that a more careful consideration is needed for the high electron densities of the core regions. The pressure response at these points in space might be better approximated by assuming that a volume element of fixed size and position relative to the associated atomic core should be sampled for the expanded and contracted structure.

This can be accomplished by supplementing the original DFT-CP methodology with an unwarping procedure. Consider energy density distributions calculated for the equilibrium geometry of a crystal structure, a slightly expanded structure, and a contracted structure, which we can represent respectively as $\rho^{o}_{energy}(\vec{r})$, $\rho^{+}_{energy}(\vec{r})$, and $\rho^{-}_{energy}(\vec{r})$. If we then write the pressure of voxel *n* in terms of its relationship to its nearby atom *j* ($\vec{r}_n = \Delta\vec{r}^{\,o}_n + \vec{r}^{\,o}_{atom\ j}$), then the pressure at that point, assuming that the energy density does not dilate with the voxel grid, can be calculated as

$$P_n \approx -\frac{\left\{\rho^{+}_{energy}\left(\Delta\vec{r}^{\,o}_n + \vec{r}^{\,+}_{atom\ j}\right) - \rho^{-}_{energy}\left(\Delta\vec{r}^{\,o}_n + \vec{r}^{\,-}_{atom\ j}\right)\right\}V^{o}_{voxel}}{V^{+}_{voxel} - V^{-}_{voxel}} \tag{6.6}$$

Calculating pressures in this way is complicated by the fact that the energy densities obtained over the course of a CP calculation are expressed in terms of the discrete points of a voxel grid. The vectors $\Delta\vec{r}^{\,o}_n + \vec{r}^{\,+}_{atom\ j}$ and $\Delta\vec{r}^{\,o}_n + \vec{r}^{\,-}_{atom\ j}$ then often will lie in between grid points, and the energy densities at those points cannot be determined exactly. Trilinear interpolation, however, can be used to obtain an estimate based on the values for the surrounding voxels. The magnitude of the errors is then related to the fineness of voxel grid spacing relative to the complexity of the electron density function.

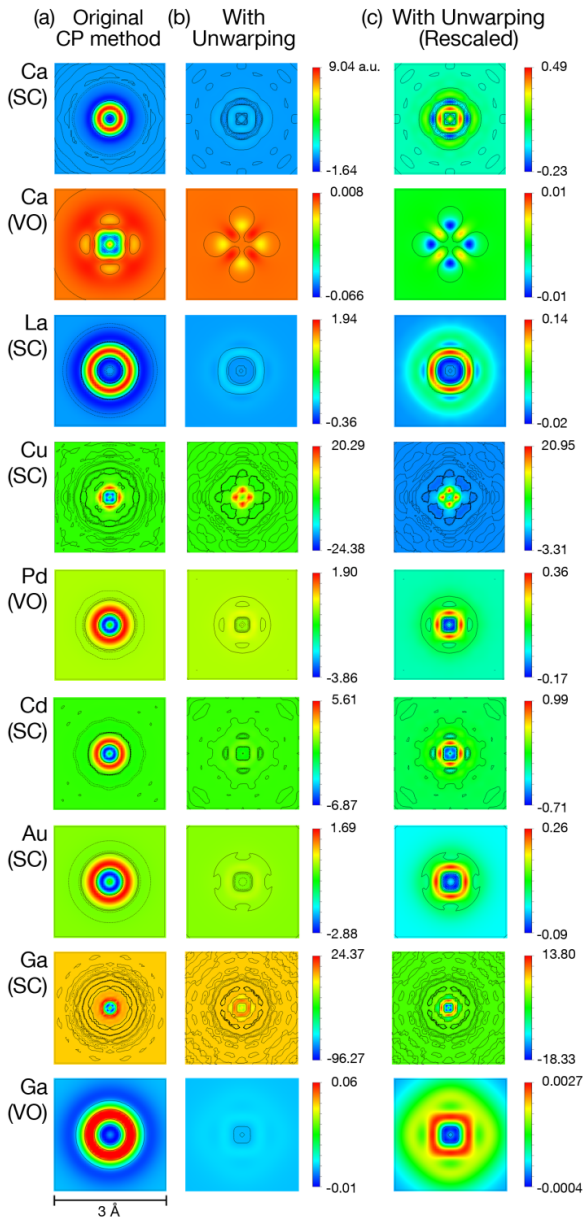

Figure 6.2. DFT-Chemical Pressure (CP) maps for individual atoms isolated in large unit cells (cell edges of 10 Å). (a) Cross sections through the nuclear positions using the original DFT-CP scheme. (b) The corresponding CP maps calculated using the process for unwarping the energy grids near the atomic cores, plotted using the same color map as in (a). (c) The unwarped maps with the color map adjusted to a narrower range. Note that the unwarping procedure significantly reduces the strong core-like features around the atomic position (which should be essentially absent in these calculations on virtually isolated atoms). SC and VO refer to the semicore and valence-only versions of the atomic pseudopotentials, respectively, where applicable. Black contours trace isosurface levels at increments of 0.05 between -0.1 and 0.1 a.u.

This methodology is implemented in our current version of the program *CPmap*. The voxel energies for the expanded and contracted structure are first calculated according to Equation 2. The voxels are then associated with specific atomic cores, which can be done by specifying cutoff radii, using a Voronoi scheme,[55] a more complicated division of space as offered by Bader's QTAIM,[56] or, as we will describe in more detail below, a Hirshfeld-type weighting.[42] The voxel centers in the expanded ($\vec{r}_n^{+}$) and contracted ($\vec{r}_n^{-}$) structures are then shifted to their corresponding positions relative to their atom's nuclear position as in the equilibrium volume structure ($\vec{r}_n = \Delta\vec{r}_n^{o} + \vec{r}_{atom\ j}^{o}$). Finally, the pressures at the voxel positions are calculated according to equation 6.6.

As the shifts in the voxel positions represent a different sampling of the same energy density maps, this interpolation leads to only small changes to the total energy obtained by integrating over the voxel grid (ca. 0.05%). Any small residual pressure resulting from differences in the interpolation error for the expanded and contracted structures is added homogeneously to the pressure map.

In Figures 6.2b-c, we illustrate the effect of applying this fixed core correction procedure to atoms isolated in boxes. Figure 6.2b shows cross-sections of the pressure maps for the atoms drawn with the same color map as in Figure 6.2a. The correction leads to a substantial change in the pressure distribution. The original, strongly oscillating ripples of pressure are now replaced with flatter maps and less isotropic features. Figure 6.2c focuses on narrower pressure ranges to allow the more subtle features of these maps to be visible. Here, it can be seen that the variations are in many cases more associated with the corners and faces of the unit cell than with the distance to the atomic core.

6.5. Grid unwarping between atoms

Atoms in more realistic environments should also benefit from this type of core treatment. Figure 6.3a shows two-dimensional slices of CP maps calculated for a diverse array of intermetallic compounds. For most examples using the original method, the maps show the most intense pressures as nearly perfect circles around the atomic positions. These core regions are set against what appears to be a shallow, nearly homogeneous negative background pressure. As such features are reminiscent of our uncorrected treatment of the atoms-in-boxes of Figure 6.2a, it seems likely that implementing grid interpolations here should lead to more meaningful CP maps.

For voxels near the cores of any given atom, the path to applying the above procedure is clear: the voxels can be assigned to their nearby atom, and then treated according to Equation 6. The situation becomes less clear for voxels deeper in the interstitial spaces between the atomic cores, where the energy density features might be expected to migrate to various degrees with the voxel grid as the structure is expanded and contracted. How should the unwarping process be applied to these regions?

A voxel's position in the equilibrium grid can be represented in terms of its placement relative to any of the atoms in the structure:

$$\vec{r}_n = \Delta\vec{r}^{\,o}_{n,atom\ 1} + \vec{r}^{\,o}_{atom\ 1} = \Delta\vec{r}^{\,o}_{n,atom\ 2} + \vec{r}^{\,o}_{atom\ 2} = \cdots \tag{6.7}$$

As we move to the expanded or contracted volumes, the various atoms will shift to different positions, so that the various equalities of Eq. 6.7 cannot be satisfied simultaneously if we keep the $\Delta\vec{r}^{\,o}_{n,atom\ j}$ vectors constant. Instead, we will need to decide to what degree each of the $\Delta\vec{r}^{\,o}_{n,atom\ j}$ terms will be weighted in the determination of the $\vec{r}_n^{+}$ and $\vec{r}_n^{-}$ vectors.

One approach to determining these weights can be found in the Hirshfeld method for the extraction of atomic charges from electronic structure calculations.[42] In the Hirshfeld approach, one begins with a hypothetical case in which the electron density of a compound is simply a superposition of free atom electron densities centered at the nuclear positions of a structure. The relative contributions from these free atom densities at a given point in space is then translated into relative weights for the apportioning of the true electron density between the atoms in the calculation of charges. The free atom electron densities thus serve as a measure of the distance dependence of each atom's influence.

In a similar way, the Hirshfeld method for the atoms surrounding a voxel can be used in assigning weights to each of the equalities in Equation 6. 7. We first define a Hirshfeld weight for the influence of atom *j* on the position of voxel *n*:

$$w_{j,n} = \frac{\rho^{FA}_{atom\ j}(\vec{r}^{\,o}_n)}{\sum_k^{all\ atoms} \rho^{FA}_{atom\ k}(\vec{r}^{\,o}_n)} \tag{6.8}$$

where $\rho^{FA}_{atom\ k}(\vec{r}^{\,o}_n)$ gives the electron density at the position of voxel *n* calculated for a free atom of the proper element centered at the nuclear coordinates of atom *k*.

Having defined these weightings, we can then use them in determining how much a voxel should maintain its position relative to each of the atomic centers as the cell is expanded and contracted for the calculation of CP maps:

$$\vec{r}^{\,+}_n = \sum_j^{all\ atoms} w_{j,n}(\Delta\vec{r}^{\,o}_{n,j} + \vec{r}^{\,+}_{atom\ j}) \tag{6.9a}$$

$$\vec{r}^{\,-}_n = \sum_j^{all\ atoms} w_{j,n}(\Delta\vec{r}^{\,o}_{n,j} + \vec{r}^{\,-}_{atom\ j}) \tag{6.9b}$$

For voxels near an atomic core, the weight for that atom will dominate these averages, and the original atom-centered interpolation of the previous section is obtained.

In performing this distortion of the voxel grid around the atom centers, the grid points are no longer uniformly distributed, and the voxel volumes become varied throughout the structure. The calculation of the voxel pressures then becomes slightly modified from equation 6.6:

$$P_n \approx -\frac{\rho^+_{energy}(\vec{r}^+_n)V^+_{voxel,n} - \rho^-_{energy}(\vec{r}^-_n)V^-_{voxel,n}}{V^+_{voxel} - V^-_{voxel}} \tag{6.10}$$

where the numerator involves the volumes of the specific voxel *n* in the expanded and contracted structures, and the denominator uses the average voxel volumes for the two structures. A discussion of the determination of the voxel volumes in the distorted grid is provided in the Supporting Information.

Turning on the unwarping procedure (Figures 6.3b and c) significantly reduces the magnitudes of the pressures of the core regions, allowing more subtle features in the interatomic regions to come more to the foreground. Also, in some cases, particularly La_5Sn_3 and $CaAu_5$, the spherical character of the core regions has diminished, making the centers of the atoms appear more responsive to their surroundings. This is more consistent with the philosophy of pseudopotentials which aims to treat explicitly only those electrons that are perceptibly affected by interatomic interactions as part of the valence set.

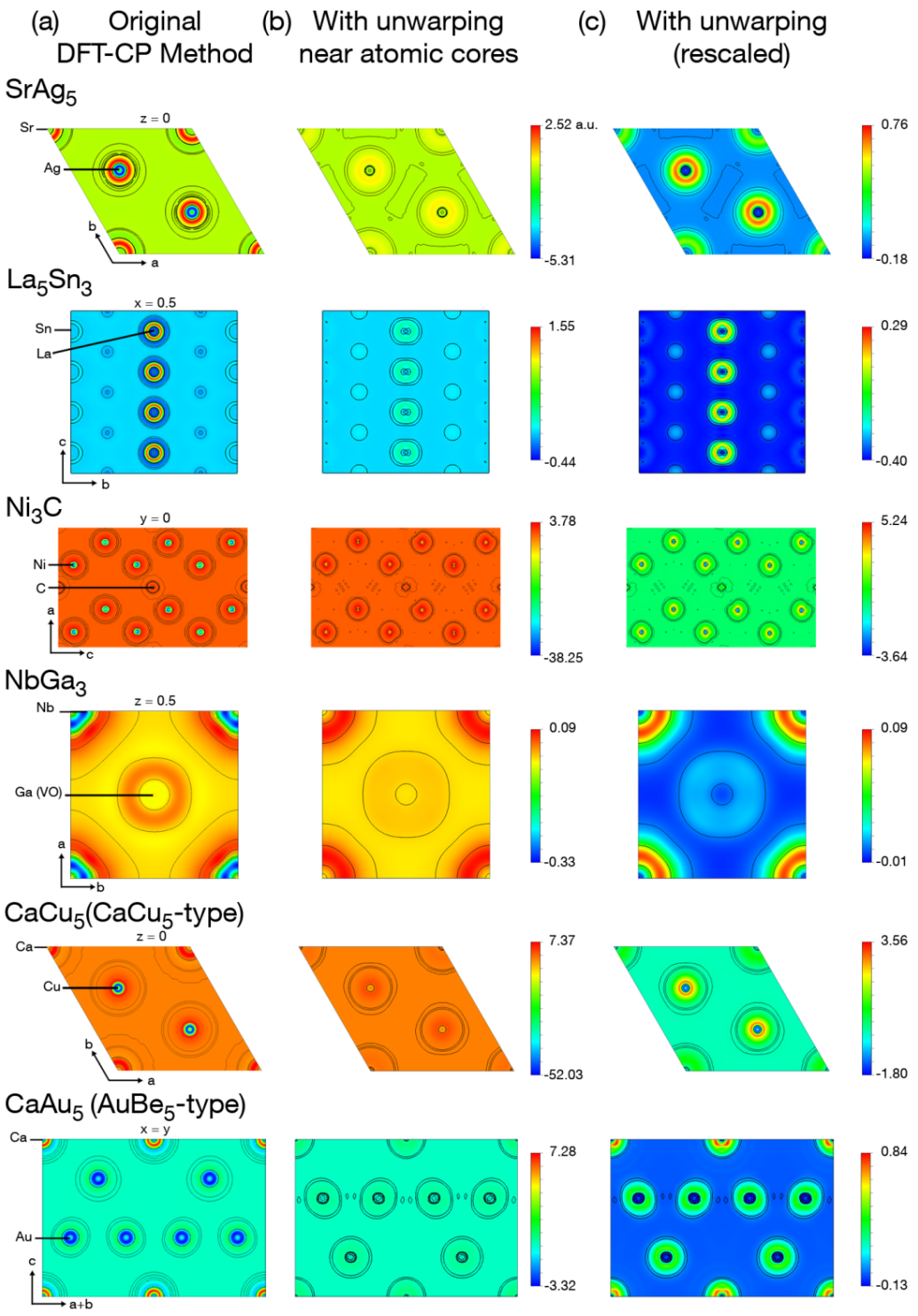

Figure 6.3. Cross sections for the DFT-CP maps of a variety of intermetallic phases calculated (a) before and (b) after the unwarping of the energy grids using the same color map, and (c) the unwarped maps plotted with more appropriately tailored color maps.

6.6. Hirshfeld-inspired contact volumes

In the previous section, we saw how the features of a CP map could be substantially clarified by introducing a step in which corresponding grid points of the expanded and contracted unit cells are shifted to the same position in space relative to an atom assigned to it. By implementing this procedure, the severe isotropic pressures appearing around the atomic cores are reduced, allowing more subtle features to come to the foreground. Even with this improvement, however, the CP distributions still largely consist of positive regions around the atomic centers that are immersed in a shallower negative background pressure. In examining the overall pressures at particular interatomic contacts, we will then need to examine the net effect of these core-like and interstitial pressures through the integration of the pressure map within domains assigned to individual contacts.

In performing such an integration, the pressure between a pair of atoms will be given by

$$P_{jk}^{contact} = \sum_{n}^{N_{voxels}} w_{jk,n} P_n \tag{6.11}$$

where $w_{jk,n}$ is the fraction of the pressure at voxel n that is attributed to the interaction between atom j and atom k. The central challenge in carrying out the integrations in a meaningful way is then the determination of the proper weighting scheme, the set of $w_{jk,n}$'s. In our recent applications of the DFT-CP method, we derived our choice of weights from an assumption that a voxel's pressure is determined by the interaction of its two nearest atoms, i.e.

$$w_{jk,n} = \begin{Bmatrix} 1, if\ atoms\ j\ and\ k\ are\ two\ closest\ to\ voxel\ n \\ \frac{1}{m}, if\ m\ contacts\ are\ tied\ in\ above\ criterion \\ 0, if\ j\ or\ k\ are\ not\ two\ atoms\ closest\ to\ voxel\ n \end{Bmatrix} \tag{6.12}$$

This scheme is advantageous in its simplicity. However, as it is entirely based on geometrical constructions, it neglects the differing ranges of influence of different atom types, and should be considered as only a first step toward a more realistic division of space between contacts.

Over the course of our ongoing exploration of intermetallic phases using the DFT-CP method, we have found that for one large and important class of compounds, the Laves phases and their variants, refinements to the weighting scheme are particularly vital. In these AB_2 compounds (see Figure 6.1a for one example), the A positions (usually occupied by a relatively electropositive element) form a diamond network, a hexagonal diamond network, or an intergrowth of the two. The B atoms occupy the interstitial spaces of the A diamondoid framework, and form truncated tetrahedra (TT) around the A atoms. The resulting coordination environment around the A sites is known as a Friauf polyhedron, consisting of a TT of B atoms with A atoms sitting above the hexagonal faces of the TT.

The geometrical features of the Friauf polyhedron make it a challenging test case for the division of space among interatomic contacts. The A-A and A-B distances exhibit a ratio of 1.0445 (for the high symmetry $MgCu_2$-type case), with the longer A-A lengths being consistent with the trend that the A sites are generally occupied by the larger atom type. However, using the distance-based criterion described above, the voxels inside the Friauf polyhedron will be assigned to the pairs of atoms to which they are closest. As the A-B interatomic distances are shorter than the A-A ones, these will tend to absorb more voxels, despite the A atoms being larger.

This dominance of the A-B contacts in the voxel assignments has interesting consequences for the integrated CP schemes. In Figure 4a, we show the results for the $MgCu_2$-type phase $CaPd_2$,[57,58] using the projection scheme described previously. Here, the distribution of voxel pressures around each atom is

represented by radial surfaces around its nuclear position. The distance of a point on the surface from the nucleus is proportional to the sums of the voxel pressures along that direction, while the color of the surface gives the sign of the pressure. Lobes in black point along directions where the pressure is negative, i.e. contraction would be favorable, while portions of the surfaces in white correspond to positive pressures, where the structure would prefer to expand.

For the Friauf polyhedron of $CaPd_2$ using the original geometrical construction of contact volumes, the white and black features are divided largely by element type. The Ca atoms appear as black tetrapods, with large negative pressure lobes pointing along the Ca-Ca contacts (red). These forces calling for the contraction of the lattice are counteracted by white, positive pressure lobes along the Pd-Pd contacts (blue), with the Ca-Pd contacts appearing to be relatively satisfied. This result is encouraging in the sense that the heteroatomic interactions, the usual driving force for the formation of a binary phase from its elements, are well-optimized.

However, inspection of the contact distances uncovers some counterintuitive aspects of this picture. Note that in the Ca-Ca/Pd-Ca distance ratio of 1.0445, the Ca-Ca contacts are only slightly longer than the Ca-Pd ones, despite the metallic radius of Ca being significantly larger than that of Pd (1.97 vs. 1.37 Å[59]). As a consequence, the Ca-Ca distance is much shorter than the sum of the metallic radii (3.32[57] vs. 3.94 Å[59]). This distance is still within the ranges observed for Ca-Ca interactions in the Inorganic Crystal Structure Database,[60,61] but would hardly be the occasion for large negative pressures demanding even closer Ca-Ca contacts. If anything, a positive pressure pushing toward distances more in-line with twice the metallic radius would be expected.

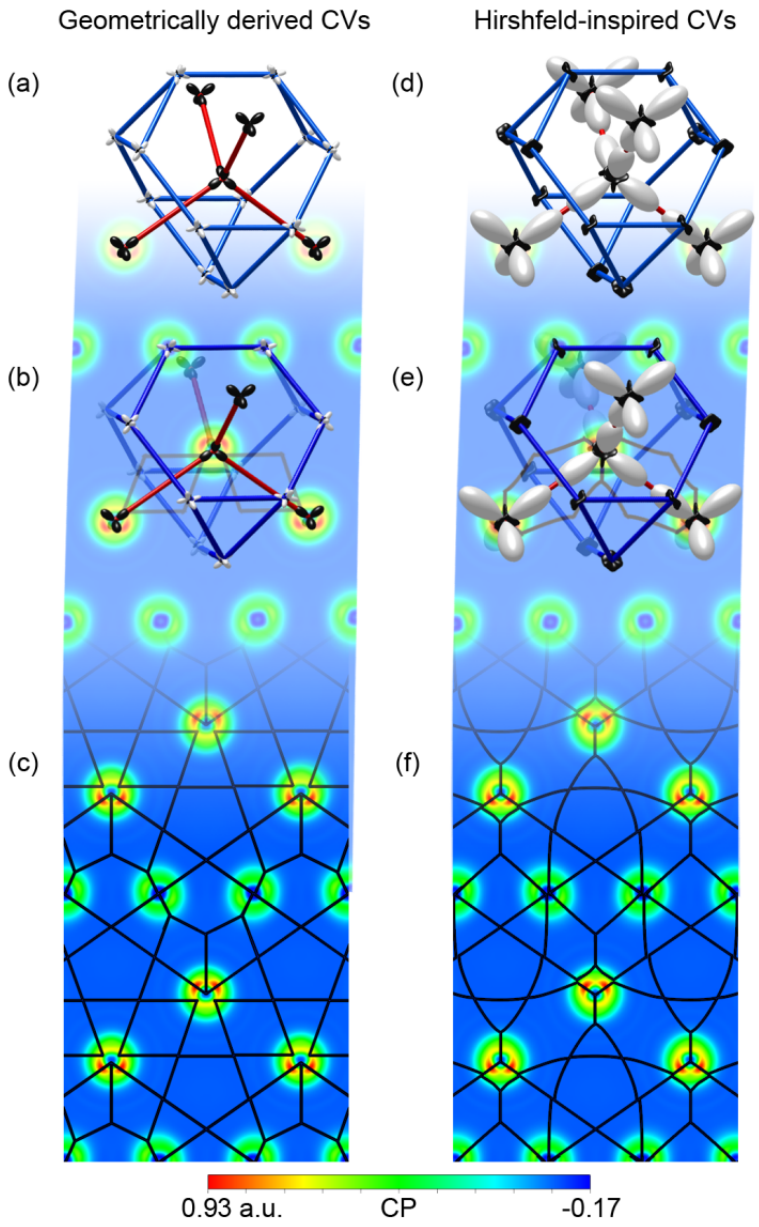

Figure 6.4. Comparison of integrated DFT-CP anisotropies and contact volumes for $CaPd_2$. (a) The DFT-CP distribution calculated for $CaPd_2$ using the original contact volume (CV) scheme. (b) The DFT-CP distribution plotted together with a cross section of the original DFT-CP map. (c) The DFT-CP cross-section shown separately with the contact volume borders indicated. (d)-(e) The corresponding images generated using the Hirshfeld-inspired contact volume scheme (see text). In (a) and (d), the pressure distribution around each atom is represented by a radial plot, with the radial distance indicating the magnitude of the sum of voxel pressures along that direction. The sign of the pressure is indicated with color: black for negative (evoking the image of a black hole acting on the structure), white for positive.

A look at the volumes assigned to each contact in our integration provides an explanation for the appearance of these negative Ca-Ca pressures. In Figures 6.4b,c, we present a cross section of the DFT-CP map for $CaPd_2$ taken through one of the Ca-Ca contacts, with the boundaries between contact volumes drawn in black. The contact volume of the Ca-Ca interaction appears here as a diamond between the two atoms. A brief glance reveals why negative pressures are assigned to this contact: whereas positive pressure features occur around both the Ca atoms of the contact, only the tips of the narrow corners of the contact volume reach into these regions. Instead, the contact volume contains mainly the negative pressure interstitial space between the Ca atoms. The core regions themselves are dominated by Ca-Pd contact volumes.

In other words, the Ca-Pd distances are short enough relative to the Ca-Ca ones that the distance criterion grants them most of the Ca core voxels. As a result, only small positive pressure components are allocated to the Ca-Ca contacts, and negative pressures thus dominate despite the short Ca-Ca distances.

Now that we see the origin of the Ca-Ca negative pressures, a way to correct the CP picture becomes apparent: the Ca-Ca contact volumes should be expanded into the Ca core regions to better reflect the larger size of the Ca atoms relative to Pd atoms. To do this, a change in the weighting scheme of equation 6.12 is needed that takes into account the differing electronic structures of Ca and Pd atoms.

As for our grid-interpolation scheme above, the Hirshfeld approach can be adapted to this task, the essential change being that we are now assigning points in space to pairs of atoms rather than individual atoms. The influence of a contact on a point in space will depend on the sizes of the free atom electron densities for the two atoms at that point. A way of quantifying this is to consider the weights in equation 6.11 as being proportional to the products of the free atom (FA) electron densities for the atoms of the contact:

$$w_{jk,n} \propto \rho^{FA}_{atom\ j}(\vec{r}_n) \cdot \rho^{FA}_{atom\ k}(\vec{r}_n) \tag{6.13}$$

In this way, every voxel would be shared among multiple contacts, with weights that are proportional to the overlaps between the FA electron densities for each contact.

In experimenting with such integration schemes, we have found that following through with this Hirshfeld-based approach in its entirety leads to some issues with interpretation: it is difficult to see which points in space are influencing which contacts. Instead, it is more practical to keep the division of space into discrete contact volumes as in equation 12, but using the products of FA electron densities as a guide to their construction. The corresponding weighting is then:

$$w_{jk,n} = \begin{cases} 1, if\ \rho^{FA}_{atom\ 1}(\vec{r}_n)\rho^{FA}_{atom\ 2}(\vec{r}_n)\ is\ largest\ for\ j,k\ pair \\ \dfrac{1}{m}, if\ m\ contacts\ are\ tied\ in\ above\ criterion \\ 0, if\ \rho^{FA}_{atom\ 1}(\vec{r}_n)\rho^{FA}_{atom\ 2}(\vec{r}_n)\ \ not\ largest\ for\ j,k\ pair \end{cases} \tag{6.14}$$

The result of using this Hirshfeld-inspired scheme is shown in Figures 4d-e. The Ca-Ca contact volume (Figure 6.4e) now reaches much deeper into the Ca cores so that a corner lies on each Ca nuclear position. The angle at each of these corners has also expanded to encompass more of the core's volume. In fact, the core is now entirely divided between the four Ca-Ca contacts arranged in a tetrahedron around the central Ca atom.

At first glance, the new contact volume boundaries do not appear to align with the prominent features of the Ca core regions. In the cross-section of Figure 6.4f, each Ca atom exhibits a pair of red bulges corresponding to high positive pressures. Their directional character would lead us to think that they are associated with particular interatomic interactions. However they are almost perfectly bisected by the borders of the CVs, rather than being centered within a specific CV. A deeper investigation of these features resolves this apparent discrepancy. As is illustrated in the Supporting Information, we have found that the

highest pressures within the core regions tend to accumulate in the spaces lying between important interatomic interactions, rather than along them. The source of this is a negative pressure contribution arising from the overlap of the local pseudopotentials along the interatomic vector. The core regions not aligned with these vectors then tend to be the spaces where the positive core pressures are most prominent.

The increased contribution from the Ca cores to the Ca-Ca contact volumes has a profound effect on the integrated CP distributions (Figure 6.4d). The Ca-Ca contacts now exhibit intense positive pressures that seem appropriate to the relatively short Ca-Ca distances. These positive pressures are balanced by the negative pressure lobes oriented along the Ca-Pd interactions. The Pd-Pd contacts, meanwhile, are largely devoid of CP features, indicating that the distances here are nearly optimal.

In comparing Figures 6.4a and 6.4d, it is somewhat surprising that they represent the same original CP map, and differ only in the integration scheme used. In what ways are they connected? To see their relationship to each other, it is helpful to note that the Ca-Ca contacts pass through hexagons of Pd atoms. The integrated pressures in this region of the structure will depend on the relative sizes and shapes of Ca-Ca, Ca-Pd, and Pd-Pd contact volumes. In the original scheme, the size of the Pd atoms is overestimated relative to the Ca ones, which leads to the Ca-Pd and Pd-Pd volumes dominating the positive cores of the Ca and Pd atoms. The result is positive pressures along the Pd-Pd interactions and only small negative pressures along the Ca-Pd ones.

In moving to the Hirshfeld-inspired scheme, the Ca-Ca volumes are increased at the expense of the Ca-Pd and Pd-Pd volumes. The contact volumes involving Ca then pick up more of the positive core pressures, leading to large positive pressures between the Ca atoms, the removal of positive pressures from the

Pd-Pd interactions, and only smaller changes to the Ca-Pd interactions (which lose core contributions from the Ca but gain them from the Pd).

The better treatment of atomic sizes is not the only reason for which the revised CP scheme is attractive: it also corresponds closely with expectations based on the sphere-packing view of the Laves phases. Consider a $MgCu_2$-type AB_2 structure constructed from hard spheres with radius r_A for the A atoms and r_B for the B atoms. The high symmetry of the structure means that the distances are entirely determined by the length of the cubic unit cell edge, and no other degrees of freedom exist for adjusting the structure to accommodate the values of r_A and r_B. If the B atoms are in contact with each other at an interatomic distance of 2 r_B, then the surfaces of the A atoms touch each other when the r_A/r_B radius ratio is $(3/2)^{1/2}$ = 1.225. However, the surfaces of the A atoms would not touch those of the B atoms until $r_A/r_B = (11/2)^{1/2}$-1 = 1.345. As such, bringing the A and B spheres in contact would require allowing the A atoms to slightly interpenetrate each other.

We can now compare these radius ratios for that of the metallic radii for $CaPd_2$, r_{Ca}/r_{Pd} = 1.97 Å/1.37 Å = 1.44. For this ratio, having sphere surfaces touch at the Pd-Pd or Ca-Pd contacts would require the Ca spheres to overlap. In this situation, positive pressures could be expected to arise between the Ca atoms as the structure strives to achieve closer contacts along the Pd-Pd and Ca-Pd interactions. This picture agrees well with the CP scheme of Figures 4d-f. We anticipate that the revised CP scheme obtainable for Laves phases will offer opportunities to examine the driving forces for the creation of complex structures through the fragmentation of these simpler structures,[62-70] and will improve our ability to discern the reasons for the intergrowth of Ca-Cd and Cd-Cu interactions in the Bergman-type quasicrystal approximant $Ca_{10}Cu_2Cd_{27}$.

It is important to mention, however, that this result is dependent on the use of a semicore Ca pseudopotential in which not only the Ca 4s but also 3p and 3s electrons are considered as part of the valence set. Using a "valence-only" Ca pseudopotential with just the 4s electrons treated explicitly leads to a CP scheme similar to Figure 4a regardless of what map generation and integration procedures are applied. We believe that this can be attributed to the relatively high ionicity expected for the $CaPd_2$ phase. Indeed a Bader charge analysis using the *BADER* program[71-73] of our valence-only electron density for this phase gives a charge on the Ca atoms of +1.7, indicating that only 0.3 electrons lie near the Ca cores. With so few valence electrons present on Ca atoms, it is understandable that the explicit inclusion of semicore electrons would be necessary to model the atom's responses to its surroundings. From this, we arrive at a recommendation that semicore potentials be used in cases where atoms are expected to be highly cationic.

Using the improved method including Hirshfeld-inspired contact volumes and interpolation within atomic cells, we have also been able to reproduce the conclusions of our earlier studies examining the stability of the complex Ca_2Ag_7 and $Ca_{36}Sn_{23}$ structures relative to simpler structural alternatives. In the remainder of this Article, we will describe a different application of the DFT-CP method: determining the role of atomic size in the relative stabilities of competing structure types. Our focus will be on the structural preferences of AB_5 structures for $CaCu_5$- or $AuBe_5$-type structures, for which atomic size has been considered a key factor.

6.7. Stability trends in AB_5 intermetallics

In the previous sections of this paper, we described improvements to the DFT-CP method, and showed how they offer a CP scheme for the Laves phase $CaPd_2$ that is in close accord with radius ratio

considerations. Using the same implementation of the CP concept, it is also possible to explain the stability trends for another intermetallic structure type that is closely related to the Laves phases: the $AuBe_5$ type. This AB_5 structure type can be derived from the AB_2 $MgCu_2$-type by replacing every other A atom in the structure with a B atom, i.e. $A_2B_4 \rightarrow ABB_4 = AB_5$ (Figure 6.1b). For AB_5 intermetallics with A being an alkaline earth or lanthanide and B being a late transition metal, the $AuBe_5$ type appears to be in competition with the more common $CaCu_5$ type. The factor determining the relative stabilities of these two structure types appears to be the relative sizes of A and B atoms,[43] an effect that should be amenable to CP analysis.

Let's begin by examining the DFT-CP distribution for a representative of the $AuBe_5$ type: $CaAu_5$.[74] In Figure 6.5, we present CP anisotropy surfaces for this structure calculated with the range of procedures discussed in the previous section. First, in Figure 5a, we show the result using the original methodology without interpolation within atomic cells and using a geometrical construction for the contact volumes. In Figures 6.5b-c, we turn on either the interpolation procedure or the Hirshfeld-inspired determination of contact volumes (CVs). Finally, in Figure 6.5d, we use the fully improved method, with both the interpolation and new contact volumes.

Using the original DFT-CP scheme, the integrated CP distribution closely resembles that obtained in this way for the Laves phase $CaPd_2$ (Figure 6.4a), despite having replaced four Ca-Ca contacts with Ca-transition metal ones. Negative pressure lobes (black) point through the faces of the truncated tetrahedron just as in $CaPd_2$, while the edges of the truncated tetrahedron itself are decorated with positive pressure lobes. The Ca atom, overall, has large negative pressure indicating that it would benefit from contraction of the lattice, which is prevented by positive pressures within the Au truncated tetrahedra. As such,

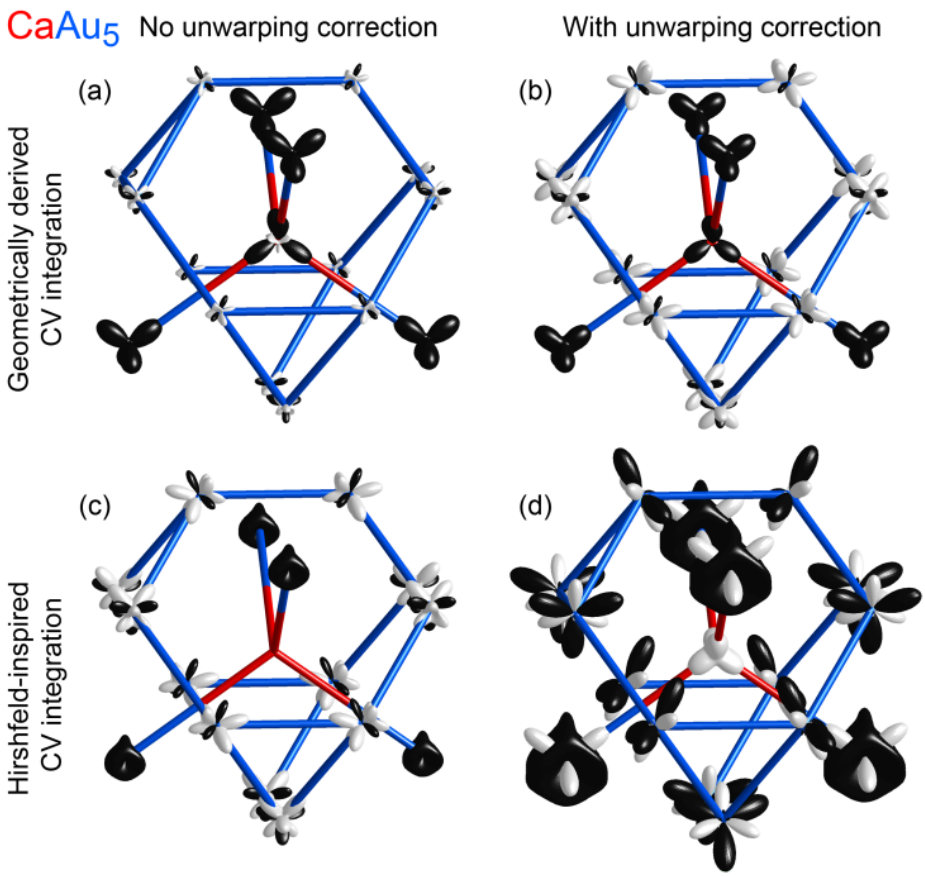

Figure 6.5. Comparison of DFT-CP anisotropy schemes calculated for $CaAu_5$ using (a) the original methodology, (b) the improved map generation (with the unwarping procedure applied) but original geometrically constructed contact volumes, (c) the original map generation but the Hirshfeld-inspired contact volume determination, and (d) the improved methods for the both the creation of maps and contact volumes. See the caption to Figure 6.4 for plotting contentions.

this scheme predicts that the structure would be stabilized by replacing the Ca with a larger atom—which of course runs counter to the empirical trend of the $AuBe_5$ type being observed for small A atoms.

Turning on either the interpolation near atomic cores (Figure 5b) or the Hirshfeld-inspired CVs (Figure 6.5c), introduces qualitative changes to the CP distributions on the $Ca@Au_4$ tetrahedron, but leaves

the positive pressures between the Au atoms of the truncated tetrahedron largely intact. The most dramatic change occurs upon turning on both features of the improved DFT-CP method simultaneously (Figure 6.5d). Here, positive CP lobes point along all of the Ca-Au contacts, while negative CP is reserved for the Au-Au interactions with the longest interatomic distances. Unlike that of the original DFT-CP scheme, the final integrated result is in close agreement with experimental trends: the positive pressures surrounding the Ca atoms indicate that the stability of this structure will be largely dependent on having a relatively small atom at this position.

In comparing Figures 5b and 5d, it is evident that the use of Hirshfeld-inspired CVs plays a significant role in obtaining positive pressures on the Ca sites. As for $CaPd_2$, a comparison of the CVs generated with the original and Hirshfeld-inspired schemes is helpful in seeing how these differences arise (Figure 6.6). On moving from the $MgCu_2$ type to the $AuBe_5$ type, the relative interatomic distances are left unchanged. Because of this, the Ca-Ca geometrically derived CV in $CaPd_2$ (Figure 6.4b) is identical to the corresponding one in $CaAu_5$ (Figure 6b), although now it corresponds to a Ca-Au CV. In the slice through the structure of Figure 6.6, this CV appears as a diamond-shaped polygon. Only the narrow corners of this polygon cross into the positive core regions of the Ca and Au atoms, leading to a net negative pressure for the contact.

As we switch to the Hirshfeld-inspired scheme, the larger size of the Ca atoms relative to Au will lead to the growth of the Ca-Au CVs at the expense of the Au-Au ones. Because the Ca is surrounded by Au atoms, in the shapes of the CVs near the Ca center are essentially unchanged. However, on the Au atoms, there is a marked expansion of the Ca-Au CVs into regions previously occupied by Au-Au ones (Figures 6.6c,f). The Au-Ca CVs then acquire more of the positive core pressures on the Au atoms, leading to the

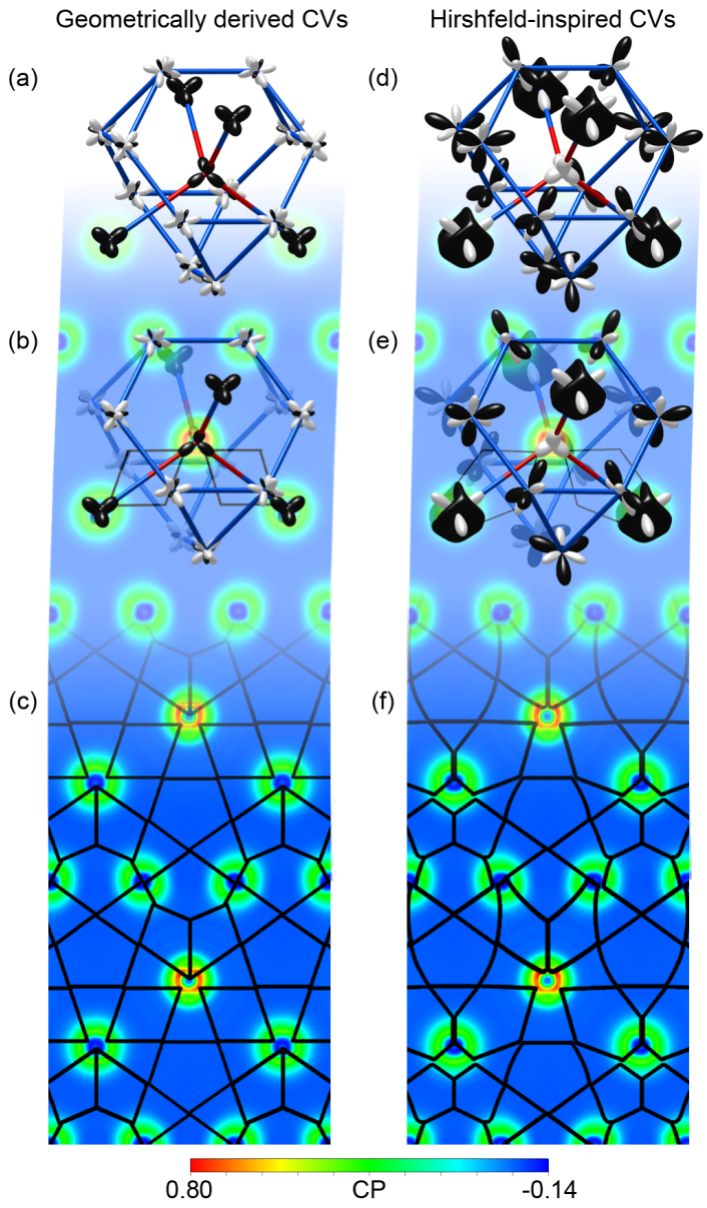

Figure 6.6. Effect of the use of Hirshfeld-inspired contact volumes (CVs) on the integrated DFT-CP results for $CaAu_5$ ($AuBe_5$ type). (a) Atomic DFT-CP anisotropy surfaces calculated for $CaAu_5$ using the original geometrical definition of CVs. (b) The DFT-CP anisotropy surfaces drawn in the context of a cross section of the DFT-CP map with two Ca-Au CVs in the original scheme indicated. (c) The same cross section of the CP map as in (b) with additional CV borders drawn. (d)-(f) The corresponding plots obtained using the Hirshfeld-inspired CV scheme. Note that the CV borders are determined only to the resolution of voxel grid used in the CP calculation. The smooth curves drawn should thus be considered as approximate. See the caption to Figure 4 for an explanation of plotting conventions for the DFT-CP anisotropies.

overall positive CPs between the Ca atom and its neighbors.

As we mentioned earlier, the positive pressures calculated for the Ca atom with the revised CP scheme (Figure 6.5d) suggest that the $AuBe_5$ type would be stabilized by the replacement of relatively small atoms on this site. Whether a $AuBe_5$ phase forms, however, is not just a factor of the favorability of that single phase, but will depend also on the free energy of the $AuBe_5$-type compound relative to those with alternative structures (or multi-phase mixtures of compounds with an average A:B ratio of 1:5). For AB_5 intermetallics formed between an electropositive metal such as an alkaline earth or lanthanide (for the A sites) and a late transition metal (for the B sites), the $AuBe_5$ type has a fierce competitor: the $CaCu_5$ type (Figure 6.1c). What does the improved DFT-CP approach predict about the relative virtues of these two structure types?

In Figure 6.7, we present a comparison of the CP schemes calculated for the $CaCu_5$- and $AuBe_5$-type structures for two different compounds: $CaCu_5$ and $CaAu_5$, which are experimentally known to prefer the former and latter structure type, respectively (green boxes).[74,75] The plots shown focus on the coordination environment of the Ca atoms (A site) as the relative size of the atom here has been perceived as a key factor in determining which structure type is adopted. In the $CaCu_5$-type structures, this Ca environment consists of an 18-coordinate hexagonal polyhedron built from the layering of honeycomb and kagome sheets of Cu/Au atoms. For the $AuBe_5$-type structures, the Ca coordination environment is the same Friauf polyhedron of Cu/Au atoms that we saw earlier in Figures 6.5 and 6.6.

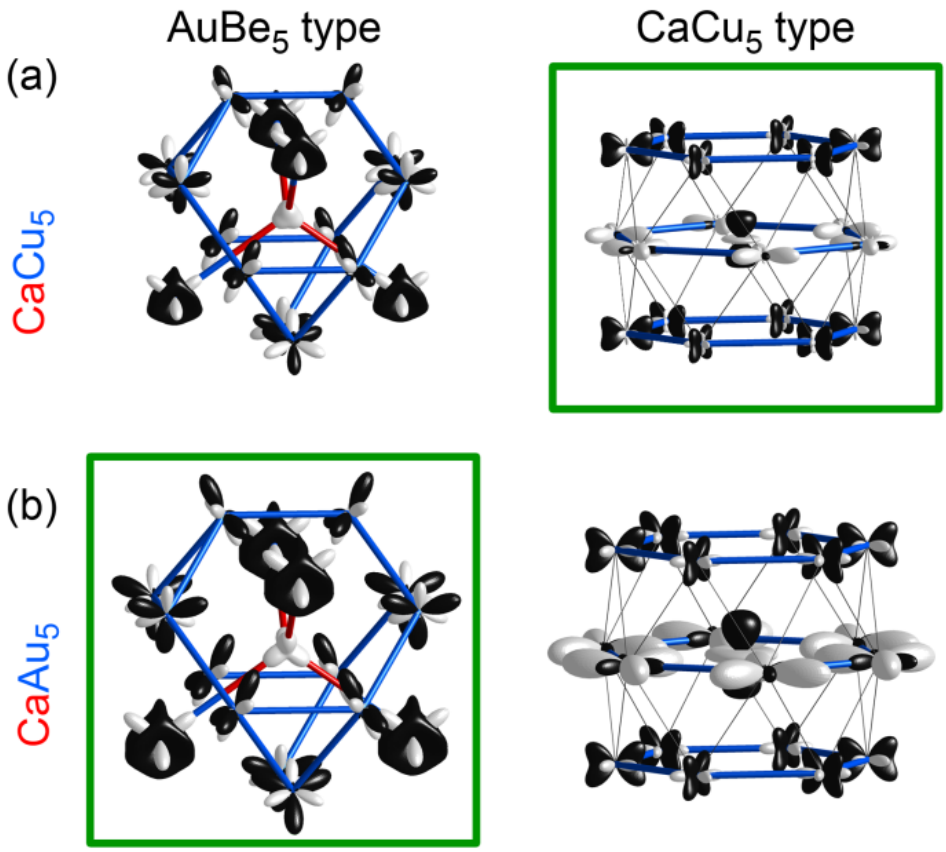

Figure 6.7. DFT-CP analysis of the AB_5 structure types $CaCu_5$ and $AuBe_5$. (a) $CaCu_5$ in the $AuBe_5$ and $CaCu_5$ types. (b) $CaAu_5$ in the same two structure types. Plotting conventions are given in the caption to Figure 4.

A comparison of the results for $CaCu_5$ and $CaAu_5$ reveals that, while differences occur in the sizes of the various lobes, the qualitative features of the CP plots are very similar between the phases of the same structure types. For both $CaCu_5$-type compounds, the Ca atom's CP surface has the shape of a d_{z2} orbital, with negative lobes pointing up and down, and a torus of positive pressure running around the middle. This shape can be interpreted as the Ca atom desiring shorter contacts to the Cu/Au atoms in the layers above and below it, but longer contacts to those in the same plane. Overall, the pressures on the Ca sites are negative (–389 GPa on $CaCu_5$ and –21 in $CaAu_5$), indicating that the combined effect of the 12 overly

long contacts to the Cu/Au atoms above and below, outweighs the 6 overly short contacts in the plane. The net negative CP for the Ca could be relieved by the placement of a larger atom on this site, leading to the prediction that the stability of the phase is enhanced for larger A atoms.

In both of the $AuBe_5$-type phases, on the other hand, the Ca sites are subject to positive pressures, indicative of a desire for the expansion of the lattice. This driving force of enlarging the unit cell is resisted largely by the presence of negative pressure lobes between the Cu/Au atoms of the truncated tetrahedron and the Cu/Au atoms on the diamondoid network, which like the Ca atoms lie in Friauf polyhedra. Due to the symmetry of the structure, the interatomic distances between the atoms in the Friauf polyhedra and their surroundings are the same, regardless of whether the position is occupied by a Ca atom or a Cu/Au one. As such, the structure would be best served by placing an atom on the Ca site with a size more similar to a Cu/Au atom, i.e. a smaller atom.

From these considerations, we can conclude that the $CaCu_5$ and $AuBe_5$ structure types are indeed tailored for a larger and smaller atom on the A atom positions, respectively. Let's now examine how the CP results for the experimentally observed phases compare with the hypothetical ones. As a first step, we need to calibrate ourselves in terms of the significance of the sizes of the CP features in Figure 6.7a. The CP lobes for the two $CaCu_5$ phases in panel a are drawn to scale, as are the two $CaAu_5$ phases in panel b. Between the panels a and b, it is not practical to show the plots at the same scale: Cu with its highly localized 3d electrons generally shows inherently larger pressures numerically than Au, regardless of the structure. Instead panels a and b are scaled so that the relative features of the $CaCu_5$- and $AuBe_5$-type structures are maximally comparable.

A good place to begin is a comparison of the two $AuBe_5$-type phases. As we noted earlier, the CP features are very similar between $CaCu_5$ and $CaAu_5$ in this structure type. However, a close examination of the Ca CP anisotropy surfaces for the two compounds reveals an important difference: in $CaAu_5$ the positive pressures around the Ca are largely focused along the diamondoid network. The contacts between the Ca and the truncated tetrahedron are more satisfied, and in fact represent the interactions in the structure that are most optimized. Upon replacing the Au atoms with smaller Cu ones to create a $AuBe_5$-type $CaCu_5$ phase, we obtain a different situation. The smaller size of Cu translates into a larger relative size for the Ca, and now the positive pressures around the Ca are more uniformly distributed.

By contrast, the replacement for Au with the smaller Cu atoms to make the $CaCu_5$-type $CaCu_5$ phase leads to a tighter coordination environment around the Ca. As a result, the size of the Ca CP features decreases in the $CaCu_5$ type during this substitution, relative to those of the $AuBe_5$-type phase of the same composition.

These observations are in-line with the trend that moving from $CaAu_5$ to $CaCu_5$ increases the favorability of the $CaCu_5$ type relative to the $AuBe_5$ type. What is more difficult to determine is where the crossing point between the two structure types should occur. This difficulty, in fact, reflects one of the limitations of the use of the DFT-CP method in comparing very different crystal structures. Chemical pressures represent derivatives of the total energy with respect to structural perturbations, and not the magnitudes of the total energy itself. For structures that are closely related, such as a superstructure and the basic structure that it is derived from, the CPs are charting similar energy vs. distance curves for interatomic interactions. As such, minimizing the CPs can be seen as a qualitative surrogate for the minimization of the total energy. For more distantly related structures, such as the $CaCu_5$ and $AuBe_5$ types, the energy vs.

distance relationships may be expected to be quite different. We should then seek complementary methods, such as the crystal orbital Hamilton population,[76] to measure the magnitudes of the bond strengths to go along with the derivatives provided by the DFT-CP analysis.

6.8. Conclusions

The concept of chemical pressure offers a means to track the effects of atomic size on the electronic structure. In this Article, we have described advances in the generation of chemical pressure maps for solid state structures using the output of DFT calculations and the interpretation of these maps in terms of interatomic interactions. For the calculation of CP maps, we introduced a correction for the incompressibility of atomic cores in which voxel positions between structures of different sizes are interpolated to the same position relative to the atom with which they are associated. The result is the large reduction of the isotropic core pressures (by factors of up to 15) that have proven so challenging to analyze in previous applications of the DFT-CP approach.

We also introduced an improved scheme for assigning voxels to interatomic contacts for the integration of interatomic pressures: the use of Hirshfeld-inspired contact volumes. In this approach, the relative sizes of the free atom electron densities centered at the atomic positions within a crystal structure are used to evaluate their relative degrees of influence on the pressure at a given voxel. The voxel is then assigned to the interaction between the pair of atoms whose influence is greatest on it. Through the use of the free atom electron density profiles, the differing size of the atoms becomes naturally incorporated into the construction of contact volumes, unlike our earlier geometrical procedure. This formalism is also easily gen-

eralized: the radial electron density of the free atom could easily be replaced in the input to the CP programs with other relevant profile functions, such as the local energy component of the atomic pseudopotentials.

The utility of the improved DFT-CP approach was illustrated using several structures whose stability ranges have been associated with atomic size effects: the $MgCu_2$ (cubic Laves phase), $AuBe_5$, and $CaCu_5$ structure types. For the $MgCu_2$-type $CaPd_2$, the CP scheme obtained exhibited parallel features with the sphere-packing view of the Laves phases, and thus affirms the efforts of several researchers to apply and adapt radius ratio type analyses to this large family of compounds.[2,77-79] In the case of competition between the $AuBe_5$ and $CaCu_5$ types for AB_5 structures, our analyses confirmed the role of atomic size in stabilizing one phase over the other. A moderately sized A atom is predicted to experience positive pressures in the $AuBe_5$ type, and negative pressures in the $CaCu_5$ type. Relatively large A atoms are then expected to prefer the $CaCu_5$-type, while smaller A atoms would prefer the $AuBe_5$ type.

We have already found that these advances in the DFT-CP method have made its use much more straightforward for a wide variety of intermetallic systems, and are looking forward to exploring its capabilities through further applications. Motivated by the insights the method has provided regarding the factors influencing the stabilities of the Laves phases and the AB_5 structure types, we are particularly excited to see what it might reveal concerning the complex intergrowth structures of the $AuBe_5$ and $MgCu_2$ structure types in lanthanide-copper systems, some with thousands of atoms per unit cell.[45-48]

Acknowledgement

We gratefully acknowledge the financial support of the National Science Foundation through grant DMR-1207409. This research involved calculations using computer resources supported by National Science Foundation Grant CHE-0840494.

6.9. References

(1) Bondi, A. *J. Phys. Chem.* **1964**, *68*, 441-451.

(2) Simon, A. *Angew. Chem. Int. Ed.* **1983**, *22*, 95-113.

(3) van der Waals, J. D. *Nobel Lectures, Physics 1901-1921*; Elsevier Publishing Company: New York, 1967.

(4) Müller, U. *Inorganic structural chemistry*; 2nd ed.; Wiley: Chichester, England ; Hoboken, NJ, 2007.

(5) Levy, O.; Jahnátek, M.; Chepulskii, R. V.; Hart, G. L. W.; Curtarolo, S. *J. Am. Chem. Soc.* **2010**, *133*, 158-163.

(6) Wang, H.; Wang, F.; Jones, K.; Miller, G. J. *Inorg. Chem.* **2011**, *50*, 12714-12723.

(7) Wendorff, M.; Röhr, C. *Z. Anorg. Allg. Chem.* **2011**, *637*, 1013-1023.

(8) Deringer, V. L.; Goerens, C.; Esters, M.; Dronskowski, R.; Fokwa, B. P. T. *Inorg. Chem.* **2012**, *51*, 5677-5685.

(9) Lin, Q.; Smetana, V.; Miller, G. J.; Corbett, J. D. *Inorg. Chem.* **2012**, *51*, 8882-8889.

(10) Osters, O.; Nilges, T.; Schöneich, M.; Schmidt, P.; Rothballer, J.; Pielnhofer, F.; Weihrich, R. *Inorg. Chem.* **2012**, *51*, 8119-8127.

(11) Samal, S. L.; Lin, Q.; Corbett, J. D. *Inorg. Chem.* **2012**, *51*, 9395-9402.

(12) Smetana, V.; Miller, G. J.; Corbett, J. D. *Inorg. Chem.* **2012**, *51*, 7711-7721.

(13) Crivello, J.-C.; Breidi, A.; Joubert, J.-M. *Inorg. Chem.* **2013**, *52*, 3674-3686.

(14) Khatun, M.; Stoyko, S. S.; Mar, A. *Inorg. Chem.* **2013**, *52*, 3148-3158.

(15) Samal, S. L.; Gulo, F.; Corbett, J. D. *Inorg. Chem.* **2013**, *52*, 2697-2704.

(16) Pöttgen, R. *Z. Anorg. Allg. Chem.* **2014**.

(17) Emami, H.; Souques, R.; Crivello, J.-C.; Cuevas, F. *J. Solid State Chem.* **2013**, *198*, 475-484.

(18) Shoko, E.; Kearley, G. J.; Peterson, V. K.; Mutka, H.; Koza, M. M.; Yamaura, J.-i.; Hiroi, Z.; Thorogood, G. J. *arXiv ePrints* **2013**.

(19) Yzambart, G.; Bellec, N.; Nasser, G.; Jeannin, O.; Roisnel, T.; Fourmigué, M.; Auban-Senzier, P.; Íñiguez, J.; Canadell, E.; Lorcy, D. *J. Am. Chem. Soc.* **2012**, *134*, 17138-17148.

(20) Sung, N. H.; Roh, C. J.; Kang, B. Y.; Cho, B. K. *J. Appl. Phys.* **2012**, *111*, 07-117.

(21) Huang, W.-Y.; Yoshimura, F.; Ueda, K.; Shimomura, Y.; Sheu, H.-S.; Chan, T.-S.; Chiang, C.-Y.; Zhou, W.; Liu, R.-S. *Chem. Mater.* **2014**, Article ASAP.

(22) Lue, C. S.; Wong, S. F.; Huang, J. Y.; Hsieh, H. L.; Liao, H. Y.; Ramachandran, B.; Kuo, Y. K. *J. Appl. Phys.* **2013**, *113*, 013710.

(23) Nam, G.; Jeon, J.; Kim, Y.; Kang, S. K.; Ahn, K.; You, T.-S. *J. Solid State Chem.* **2013**, *205*, 10-20.

(24) Wang, P. L.; Kolodiazhnyi, T.; Yao, J.; Mozharivskyj, Y. *J. Am. Chem. Soc.* **2012**, *134*, 1426-1429.

(25) Zhao, H. J.; Ren, W.; Chen, X. M.; Bellaiche, L. *J. Phys.: Condens. Matter* **2013**, *25*, 385604.

(26) Ishida, S.; Nakajima, M.; Liang, T.; Kihou, K.; Lee, C.-H.; Iyo, A.; Eisaki, H.; Kakeshita, T.; Tomioka, Y.; Ito, T.; Uchida, S.-i. *J. Am. Chem. Soc.* **2013**, *135*, 3158-3163.

(27) Lehr, G. J.; Morelli, D. T.; Jin, H.; Heremans, J. P. *J. Appl. Phys.* **2013**, *114*, 223712.

(28) Demirel, S.; Avci, S.; Altin, E.; Altin, S.; Yakinci, M. E. *Ceram. Int.* **2014**, *40*, 5217-5222.

(29) Fredrickson, D. C. *J. Am. Chem. Soc.* **2011**, *133*, 10070-10073.

(30) Fredrickson, D. C. *J. Am. Chem. Soc.* **2012**, *134*, 5991-5999.

(31) Stacey, T. E.; Fredrickson, D. C. *Dalton Trans.* **2012**, *41*, 7801-7813.

(32) Engelkemier, J.; Berns, V. M.; Fredrickson, D. C. *J. Chem. Theory Comput.* **2013**, *9*, 3170-3180.

(33) Nielsen, O. H.; Martin, R. M. *Phys. Rev. B* **1985**, *32*, 3780-3791.

(34) Godfrey, M. J. *Phys. Rev. B* **1988**, *37*, 10176-10183.

(35) Ziesche, P.; Gräfenstein, J.; Nielsen, O. H. *Phys. Rev. B* **1988**, *37*, 8167-8178.

(36) Filippetti, A.; Fiorentini, V. *Phys. Rev. B* **2000**, *61*, 8433-8442.

(37) Treglia, G. In *Stress and strain in epitaxy; theoretical concepts, measurements, and applications*; Elsevier Science B.V.: 2001, p 119-150.

(38) Rogers, C. L.; Rappe, A. M. *Phys. Rev. B* **2002**, *65*, 224117/224111-224117/224118.

(39) Hadler, A. B.; Harris, N. A.; Fredrickson, D. C. *J. Am. Chem. Soc.* **2013**, *135*, 17369-17378.

(40) Berns, V. M.; Fredrickson, D. C. *Inorg. Chem.* **2013**.

(41) Fulfer, B. W.; McAlpin, J. D.; Engelkemier, J.; McCandless, G. T.; Prestigiacomo, J.; Stadler, S.; Fredrickson, D. C.; Chan, J. Y. *Chem. Mater.* **2014**, *26*, 1170-1179.

(42) Hirshfeld, F. L. *Theoret. Chim. Acta* **1977**, *44*, 129-138.

(43) Buschow, K. H. J.; Van Der Goot, A. S.; Birkhan, J. *J. Less Common Met.* **1969**, *19*, 433-436.

(44) Kleber, W. *Krist. Technik* **1967**, *2*, 13-14.

(45) Cerný, R.; François, M.; Yvon, K.; Jaccard, D.; Walker, E.; Petrícek, V.; Císarová, I.; Nissen, H. U.; Wessicken, R. *J. Phys.: Condens. Matter* **1996**, *8*, 4485.

(46) Černý, R.; Guénée, L.; Wessicken, R. *J. Solid State Chem.* **2003**, *174*, 125-131.

(47) Giovannini, M.; Pasero, R.; De Negri, S.; Saccone, A. *Intermetallics* **2008**, *16*, 399-405.

(48) Gottlieb-Schönmeyer, S.; Brühne, S.; Ritter, F.; Assmus, W.; Balanetskyy, S.; Feuerbacher, M.; Weber, T.; Steurer, W. *Intermetallics* **2009**, *17*, 6-10.

(49) Gonze, X.; Rignanese, G.-m.; Verstraete, M.; Beuken, J.-m.; Pouillon, Y.; Caracas, R.; Raty, J.-y.; Olevano, V.; Bruneval, F.; Reining, L.; Godby, R.; Onida, G.; Hamann, D. R.; Allan, D. C. *Z. Kristallogr.* **2005**, *220*, 558-562.

(50) Gonze, X.; Amadon, B.; Anglade, P.-M.; Beuken, J.-M.; Bottin, F.; Boulanger, P.; Bruneval, F.; Caliste, D.; Caracas, R.; Côté, M.; Deutsch, T.; Genovese, L.; Ghosez, P.; Giantomassi, M.; Goedecker, S.; Hamann, D. R.; Hermet, P.; Jollet, F.; Jomard, G.; Leroux, S.; Mancini, M.; Mazevet, S.; Oliveira, M. J. T.; Onida, G.; Pouillon, Y.; Rangel, T.; Rignanese, G.-M.; Sangalli, D.; Shaltaf, R.; Torrent, M.; Verstraete, M. J.; Zerah, G.; Zwanziger, J. W. *Comput. Phys. Commun.* **2009**, *180*, 2582-2615.

(51) Goedecker, S.; Teter, M.; Hutter, J. *Phys. Rev. B* **1996**, *54*, 1703-1710.

(52) Hartwigsen, C.; Goedecker, S.; Hutter, J. *Phys. Rev. B* **1998**, *58*, 3641-3662.

(53) Momma, K.; Izumi, F. *J. Appl. Crystallogr.* **2011**, *44*, 1272-1276.

(54) Oliveira, M. J. T.; Nogueira, F. *Comput. Phys. Commun.* **2008**, *178*, 524-534.

(55) Okabe, A.; Sugihara, K.; Chiu, S. N. *Spatial tessellations : concepts and applications of Voronoi diagrams*; 2nd ed.; Wiley: Chichester; New York, 2000.

(56) Bader, R. F. W. *Atoms in molecules: a quantum theory*; Oxford University Press: Oxford, England, 1994.

(57) Wood, E. A.; Compton, V. B. *Acta Crystallogr.* **1958**, *11*, 429-433.

(58) Palenzona, A.; Manfrinetti, P. *J. Less Common Met.* **1982**, *85*, 307-312.

(59) Greenwood, N.; Earnshaw, A. In *Chemistry of the Elements*; 2 ed.; Butterworth-Heinemann: Oxford, UK, 1997.

(60) Bergerhoff, G.; Brown, I. D. In *Crystallographic Databases*; Allen, F. H., Bergerhoff, Sievers, R., Eds.; International Union of Crystallography: Chester, 1987.

(61) Belsky, A.; Hellenbrandt, M.; Karen, V. L.; Luksch, P. *Acta Crystallogr. B* **2002**, *58*, 364-369.

(62) Samson, S. *Nature* **1962**, *195*, 259-262.

(63) Samson, S. *Acta Crystallogr.* **1965**, *220*, 401-413.

(64) Samson, S. *Acta Crystallogr.* **1967**, *23*, 586-600.

(65) Andersson, S. *Acta Crystallogr. B* **1980**, *36*, 2513-2516.

(66) Cenzual, K.; Parthé, E.; Waterstrat, R. M. *Acta Crystallogr. C* **1986**, *42*, 261-266.

(67) Yang, Q.-B.; Andersson, S.; Stenberg, L. *Acta Crystallogr. B* **1987**, *43*, 14-16.

(68) Fredrickson, D. C.; Lee, S.; Hoffmann, R. *Angew. Chem., Int. Ed.* **2007**, *46*, 1958-1976.

(69) Berns, V. M.; Stacey, T. E.; Sapiro, M.; Fredrickson, D. C. *Eur. J. Inorg. Chem.* **2011**, *2011*, 3936-3949.

(70) Stacey, T. E.; Fredrickson, D. C. *Inorg. Chem.* **2013**.

(71) Henkelman, G. A., A.; Jónsson, H. *Comput. Mater. Sci.* **2006**, *36*, 254-360.

(72) Sanville, E.; Kenny, S. D.; Smith, R.; Henkelman, G. *J. Comput. Chem.* **2007**, *28*, 899-908.

(73) Tang, W.; Sanville, E.; Henkelman, G. *J. Phys. Condens. Matter* **2009**, *21*, 084204/084201-084204/084207.

(74) Raub, C. J.; Hamilton, D. C. *J. Less-Common Metals* **1964**, *6*, 486-488.

(75) Haucke, W. *Z. Anorg. Allg. Chem.* **1940**, *244*, 17-22.

(76) Dronskowski, R.; Bloechl, P. E. *J. Phys. Chem.* **1993**, *97*, 8617-8624.

(77) Dwight, A. E. *Trans. Am. Soc. Met.* **1961**, *53*, 479-500.

(78) Joseph, R. R.; Gschneidner, K. A., Jr. *Scr. Met.* **1968**, *2*, 631-634.

(79) Pearson, W. B. *Acta Crystallogr., Sect. B* **1968**, *24*, 7-9.

Chapter 7.

Structural plasticity of the $CaCu_5$-type in Ca-TM systems: Paths for dimensionality reduction under chemical pressure

7.1. Abstract

Unlike other areas of chemistry, the field of intermetallics is still in need of organized principles for making sense of its vast structural diversity, and guiding the search for new materials. Hints of such a principle can be found in the observation that the crystal structures of many of the most complex intermetallics, such as $NaCd_2$ and β-Mg_2Al_3 (whose giant cubic unit cells contain more than 1000 atoms), can be viewed as the result of the insertion of defect planes into much simpler crystal structures. These interfaces between periodic domains bear a certain structural resemblance to the dislocations encountered in malleable metals, whose formation and migration serves as the mechanism allowing for the deformation of the material in response to external stresses.

In this Chapter, we pursue this analogy by exploring the concept of *structural plasticity*, the hypothesis that the interfaces in complex intermetallics share a common origin with the dislocations encountered in malleable metals—they also appear as a result of stresses, but rather than ones applied externally, these are inherent in the defect-free parent structure. Using our recently developed DFT-chemical pressure analysis, we show that one such simple intermetallic structure, the $CaCu_5$ type (as adopted by AT_5 phases; A = alkaline earth metal, T = late transition metal), suffers from local internal stresses whose

relative severity is affected by the ratios of the atomic sizes on the A and T positions. Most prominent here is the presence of large negative chemical pressures on the A positions, which call for a tighter A coordination environment. We then demonstrate that three complex structures appearing in the Ca-Ag and Ca-Cd systems trace out paths for release of the calcium's negative pressures. The structures of Ca_2Ag_7 (Yb_2Ag_7 type) and $Ca_{14}Cd_{51}$ ($Gd_{14}Ag_{51}$ type) represent a T atom-poor pathway, in which lower coordination numbers are achieved through defects which eliminate T atoms from the structure, with domains of the $CaCu_5$-type being reduced to slabs, and undulating columns, respectively. The 1/1 Tsai-type quasicrystal approximant $CaCd_6$, on the other hand, follows a T atom-rich path, in which the addition of spacer Cd atoms allows for a contraction of the coordination environment of one Ca atom, without necessitating expansion of those of other Ca atoms. Our ability to connect each of these structures to the presence of tension in a common progenitor structure highlights the diverse paths by which intermetallic chemistry can cope with competing interactions, and the role that the concept of structural plasticity may play in navigating this diversity.

7.2. Introduction

Intermetallic phases represent perhaps one of the few remaining untamed wildernesses for chemical bonding theory and structural chemistry. The diversity of their crystal structures spans not only simple close-packings of spheres, but also complex structures whose unit cells contain tens, hundreds or thousands of atoms[1,2]—all the way to quasicrystals, whose rotational symmetries are incompatible with the notion of a 3-D unit cell.[3] Numerous schemes have been derived for systemizing this range of structures, such as descriptions in terms of layered nets,[1] concentric polyhedra,[4] projections from higher dimensional spaces,[5] and the identification of recurring cluster units.[6-9] As these approaches reveal ever deeper

geometrical connections between intermetallic structures, the need becomes more apparent for a conceptual framework for understanding the driving forces shaping these structural features.

One approach to interpreting crystal structures with the potential to grow into such a theoretical framework is the identification of fragments of simpler structures within the unit cells of much more complex ones. For instance, domains of the simple Laves phase crystal structures (i.e. $MgZn_2$, *hP*12) can be perceived in the structures of Fe_7W_6 (the μ-phase, *hR*13),[1] α-Mn (*cI*58),[10] γ-brass (*cI*52), [11] $Zr_{21}Re_{25}$ (*hR*92),[12] and $NaCd_2$ (*cF*1176).[10,13] This description immediately reduces the mysterious complexity and diversity of these compounds to a simple question: how is the stability of the Laves phase structural features enhanced in these systems by the insertion of interfaces, such that a simple structure is fragmented to make a much more complex one?

In this Chapter, we will offer one answer to this question, which draws on an analogy between the interfaces observed in complex intermetallics and the dislocations that are observed in malleable metals. It is well known that the ductility of metals such as Cu is due to the ability of dislocations to form and migrate in response to physical stresses. This mechanism for malleability led us to wonder whether the similar interruptions of a simple periodic structure in complex intermetallics could also result from stresses, but here we are concerned with stresses arising from internally in a structure, rather than exerted physically on it. Interfaces originating in this manner would then represent the ability of a crystal structure to deform itself in response to internal structures, an effect we will call *structural plasticity*.

With the advent of our recently developed DFT-chemical pressure analysis,[14,15] we have begun to see that the requisite internal stresses necessary for structural plasticity are a frequent occurrence in simple intermetallic structures.[14-19] For example, $CaCu_5$-type phases often exhibit negative pressures along key heteroatomic contacts, which are prevented from being resolved by the presence of competing positive

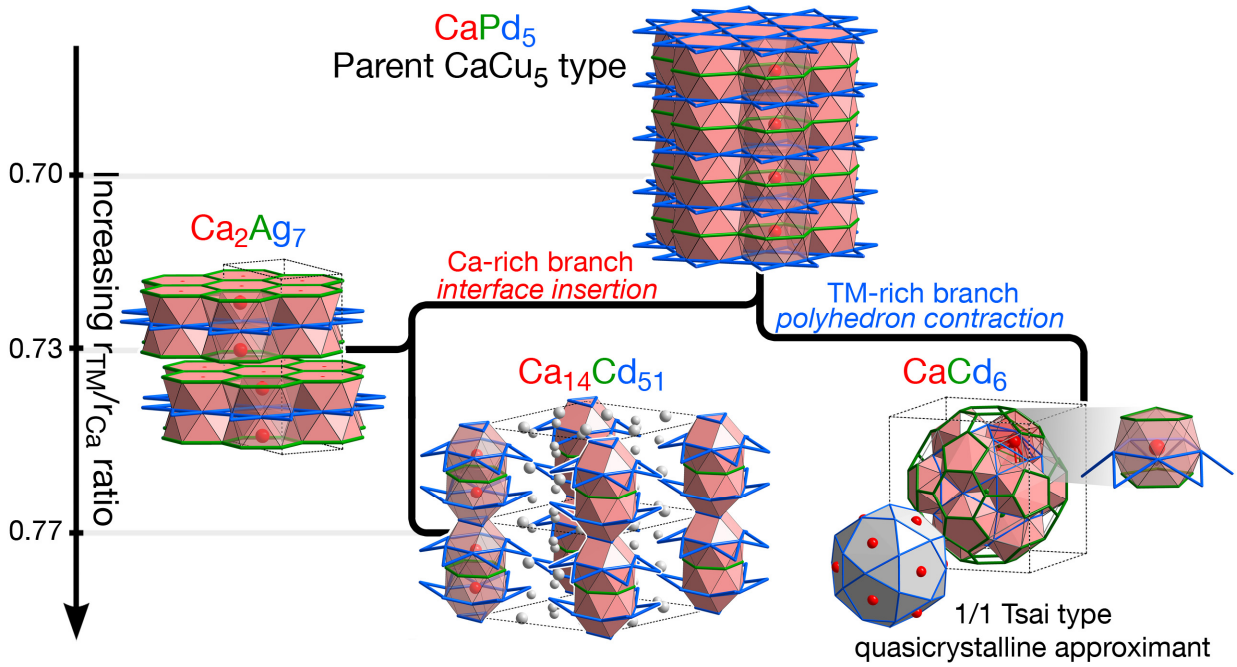

Figure 7.1. Structural relationships in Ca-TM systems near a stoichiometry of 1:5. As the radius ratio (TM:Ca) increases, the simple $CaCu_5$-type fragments into more complex compounds. A slightly more calcium-rich stoichiometry leads to Ca_2Ag_7 or $Ca_{14}Cd_{51}$, while TM-rich options lead to the Tsai-family of quasicrystals.

pressures elsewhere. In severe cases, these local pressures can drive structural transformations, as expected by the analogy with dislocations, leading to new crystal structures.

Over the course of this Chapter, we will explore how far this concept can be taken in explaining the range of crystal structures encountered in intermetallic systems. Focusing on one simple structure type as a model system, the $CaCu_5$ type, we will show how the various degrees of chemical pressure can give rise to a progression of crystal structures (Figure 7.1). The $CaCu_5$ type will emerge here as the progenitor to three more complex structures: the Yb_2Ag_7-type Ca_2Ag_7, the $Gd_{14}Ag_{51}$-type $Ca_{14}Cd_{51}$, and the 1/1 Tsai-type quasicrystal approximant $CaCd_6$.

Two distinct structural paths will become apparent for the release of negative pressures on the Ca atoms: One may be called the Ca-rich branch and is characterized by the deletion of transition metal layers lowers the dimensionality of the $CaCu_5$-type features to slabs (Ca_2Ag_7) and columns ($Ca_{14}Cd_{51}$). The second path, the transition metal (T)-rich branch, involves the insertion rather than deletion of T atoms, and ultimately supports the creation of curvature underlies the icosahedral clusters of the Tsai-type approximant. The resulting "family tree" of structures illustrates the potential of the structural plasticity concept to describe and relate intermetallic crystal structures in terms that reflect the driving forces shaping them, and offer suggestions for synthetic experiments aimed at modulating these driving forces.

7.3. Technical procedures

The DFT-chemical pressure (CP) analysis was applied to the results of LDA-DFT calculations on a variety of $CaCu_5$-type phases, Ca_2Ag_7 and Ca_2Cd_7 in the Yb_2Ag_7 type, and ordered models of $Ca_{14}Cd_{51}$ and $CaCd_6$. The LDA-DFT calculations were performed with the open-source program ABINIT,[20,21] using plane-wave basis sets. All calculations in ABINIT utilized the LDA exchange-correlation functional of Goedecker, Teter, and Hutter[22] and the Hartswigen-Goedecker-Hutter (HGH) norm-conserving pseudopotentials[23] provided with the package. Details of these technical procedures, such as k-point grids and energy cutoffs for each calculation, can be found tabled in the Supporting Information.

All crystal structures were first geometrically optimized with ABINIT using a two step procedure: first, the cell dimensions were fixed while the ion positions were optimized, then all parameters were simultaneously optimized. Three single-point calculations were then performed, one at the geometrically optimized volume, one at a slightly reduced volume, and one at an increased volume. From these cal-

culations, the grid data for the kinetic energy densities, electronic densities, and local components of the potential energy were extracted as input for the DFT-CP analysis.

The DFT-CP analysis itself is carried out in two programs: *CPmap* and *CPintegrate*. *CPmap* utilizes the spatially resolved energy outputs from the single-point calculations to create a pressure map of the entire unit cell. *CPintegrate* interprets this map through integrating the pressures with the region assigned to each interatomic contact and projecting the results onto spherical harmonics. Calculations presented herein utilized the most recently published versions of these programs, employing the grid unwarping procedure.

The integration and projection scheme used for the maps used Hirshfeld-inspired contact volumes, in which radial electron density profiles placed on the atomic centers are used to determine which pair of atoms contributes most to the pressure calculated for each voxel. However, rather than using electron density profiles from the free atoms as original proposed, more context-specific radial functions were created by using the Nelder-Mead Simplex algorithm[24] to fit modified pseudo-Voigt functions at the atomic centers to the electron densities maps calculated for the $CaCu_5$-type $CaPd_5$, $CaAg_5$, $CaCd_5$ phases at their equilibrium volume. The profiles used in the work presented in this Chapter should be considered preliminary. However, the systems presented here have proven rather robust to the use of various profiles, and we expect any improvement in profile fitting from this point to lead to only minor changes in the results.

7.4. Chemical pressure in $CaCu_5$-type compounds

As we will see herein, the potential great deal of structural chemistry lies in the distribution of local pressures of the simple $CaCu_5$ structure type. In this section, we describe the chemical pressure (CP)

schemes calculated for a series of $CaCu_5$-type phases, which will serve as our reference point as we move to more complex phases. In the process, we will also show how the latest improvements to the DFT-chemical pressure methodology modify the CP results for these phases that we described earlier.

The $CaCu_5$ type can be viewed in terms of a simple stacking of hexagonal layers (Figure 7.2a), which kagome (blue) and honeycomb (green) nets of transition metal atoms alternate. Atoms of the second, relatively electropositive element (red), such as an alkaline earth or lanthanide, lie in the hexagonal void spaces that arise from this stacking of layers. This arrangement is results in a simple hexagonal unit cell containing only six atoms.

The very simplicity of this structure, however, leads to the possibility of internal strain: all of the atoms lie on high-symmetry positions, and the only parameters that can be adjusted to optimize the various Ca-Ag, Ca-Ca, and Ag-Ag interatomic distances are the unit cell volume and the c/a ratio. Clearly the structure type is not sufficiently flexible enough to simultaneously achieve ideal distances for all interaction types. The experimentally observed distances will then reflect some sort of compromise.

An inspection of the CP distributions for a series of $CaCu_5$-type phases shows how the resulting compromises made can be very uneasy, depending on the specific combination of elements involved. In Figures 7.2b-d, we illustrate this by plotting CP anisotropies for three $CaCu_5$-type phases, one experimentally observed ($CaPd_5$) and two that are hypothetical ($CaAg_5$ and $CaCd_5$). Here, the distributions of pressures around the atoms are represented with surfaces centered on the nuclear positions. The distance from an atomic center to a point on its CP surface represents the magnitude of the pressures experienced along that direction, while the color of the surface represents the sign of the pressure. Black indicates negative pressures calling for the contraction of the structure, while white is used to label positive pressures which push for the expansion of the structure (this color scheme can be made intuitive by ref-

erence to astronomy: black holes pull their surroundings toward them, while stars appear white due to the light that they radiate).

Let's begin with the CP scheme for $CaPd_5$, where several features common to all three can be seen. The Ca atom at the center of the plot appears with a large CP surface resembling a d_{z2} orbital: large black lobes dominate along the vertical direction, while a small donut of white runs along the equation. The negative pressure lobes correspond to Ca-Pd distances that are longer than ideal for the palladium on the kagome nets above and below (blue), while the positive pressures of the ring indicate that the Ca-Pd contacts in the plane are already too short. Between the Pd atoms, the pressure magnitudes appear smaller, with the contacts within the kagome and honeycomb layers exhibiting small positive and nega-

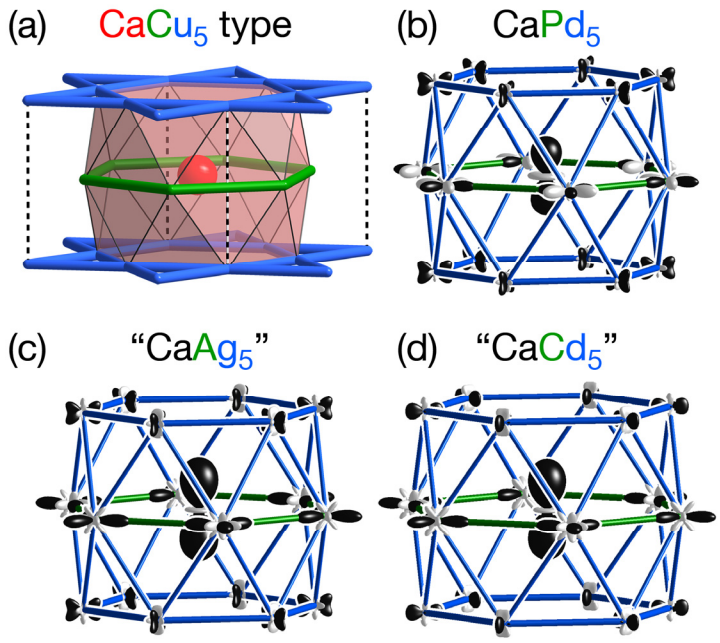

Figure 7.2. The $CaCu_5$ type structure is comprised of alternating layers of copper Kagome (blue) and honeycomb (green) nets. The honeycomb nets contain a calcium stuffing atom in each hexagonal ring. Chemical pressure in $CaCu_5$-type compounds, (b) $CaPd_5$, (c) $CaAg_5$, and (d) $CaCd_5$. Of these, $CaPd_5$ is the only observed compound, the other two are hypothetical. CP lobes are scaled to normalize the size of the negative pressure lobes on calcium atoms. See text for further information on plotting conventions.

tive pressures, respectively, and positive pressures between the layers. Overall, the major competition here is between the in-plane and out-of-plane Ca-Pd contacts, which are overly short and long, respectively, for their specific electron context.

This balance changes substantially when we replace Pd with Ag or Cd. Replacing Pd with larger atoms leads to an expansion of the transition metal sublattice, including the hexagonal voids in which the Ca atoms lie. The chemical pressure scheme of $CaAg_5$ reflects this, with the donuts of positive pressure around the Ca atom beginning to vanish, as the in-plane Ca-Ag contacts become relatively less short. In its place grow increasing positive pressure features between the Ag atoms. By the time we reach $CaCd_5$, the competition between in-plane and out-of-plane Ca-Cd contacts has given way to a tension between the out-of-plane Ca-Cd distances being too long, and the contacts within the Cd sublattice being too short.

From this perspective, we can rationalize why $CaPd_5$ is an experimentally observed compound, while for $CaAg_5$ and $CaCd_5$ no such $CaCu_5$-type phase exists. In $CaPd_5$, the Ca experiences an awkward fit in its coordination environment, with some neighbors being too close and some too distant. However, this compromise chiefly involves optimizing the heteroatomic interactions which drive the formation of the intermetallic phase. As we move to $CaAg_5$ and $CaCd_5$, the situation shifts more and more toward the formation of optimal heteroatomic Ca-TM contacts being impeded by repulsion between the TM atoms. By $CaCd_5$, the Ca atom is becoming simply too small for its coordination environment. As we will see in the next sections of this paper, the presence of such internal stresses in the hypothetical $CaAg_5$ and $CaCd_5$ phases sets the stage for structural plasticity, which becomes expressed in a variety of structural transformations.

7.5. Structural plasticity in the Ca-Ag system

In the previous section, we saw that the Ca-Ag system does not contain the $CaCu_5$-type phase that is often observed in the alkaline earth-late transition metal binary phase diagrams. Our DFT-CP analysis pointed toward a reason for this: the coordination environments that such a phase has to offer the Ca atoms would be too constrained by Ag-Ag repulsion to provide suitably short contacts between the Ca and the Ag atoms in the kagome nets above and below. Here, we will see how a CP scheme can be used to explain the formation of the closest experimentally observed analog to a $CaCu_5$-type phase in the Ca-Ag system: Ca_2Ag_7.

As is shown in Figure 7.3, the Ca_2Ag_7 structure (Yb_2Ag_7 type) is indeed closely related to the $CaCu_5$-type phase. Just as in the CaCu5 type, the structure is built up from a layering of TM honeycomb and kagome nets, with the Ca atoms placed in the hexagons of the honeycomb nets. However, the overall architecture is different: whereas the $CaCu_5$ type exhibits a simple alteration between honeycomb and kagome nets, in Ca_2Ag_7, every other kagome net is missing. These deletions divide the structure into $CaCu_5$-type slabs, which are shifted relative to each other at interfaces.

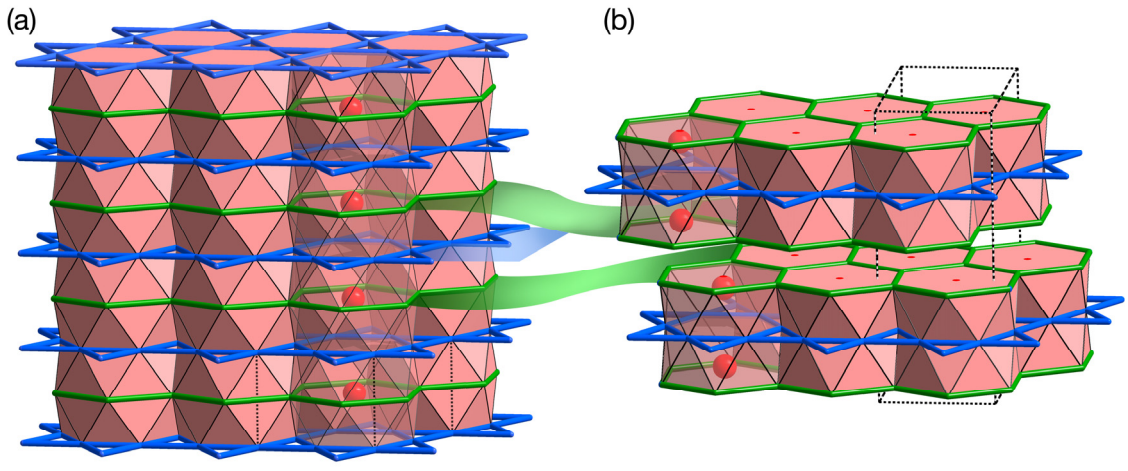

Figure 7.3. The structural relationship between the (a) $CaCu_5$ type and (b) the crystal structure of Ca_2Ag_7.

Some of the features of the Ca_2Ag_7 structure are anticipated by the DFT-CP scheme that we saw earlier for the hypothetical $CaAg_5$ (Figure 7.2c). The dominant features in the CP plot here is the presence of large negative pressure lobes pointing up and down from the Ca atom, which express a strong desire for shorter contacts to the Ag atoms in the layers above and below. The desire of either one of these lobes could be satisfied by the vertical motion of the Ca atom toward either of these layers, but this would solve only half of the issue. Moving the Ca atom up would create shorter Ca-Ag contacts to the layer above, but at the expense of stretching the already too long contacts to the layer below, while the reverse situation would occur for moving the Ca atom down. In other words, the symmetry-equivalence of the negative pressure lobes leads to a stale-mate.

The stale-mate ends, however, if a superstructure is created that breaks the symmetry relating the upper and lower Ag layers. This is what is accomplished by the layer-deletions that lead to the Ca_2Ag_7 structure (Figure 7.4, right). The removal of one kagome layer, allows for the Ca atom to move toward the remaining layer and achieve closer Ca-Ag contacts (as well as relieve some of the positive pressures along the in-plane Ca-Ag interactions). The motion is further supported by the horizontal shift that occurs occurs between the two sides of the deletion as the structure heals. The shift between the $CaCu_5$-type slabs places two Ag atoms from the neighboring layer almost directly above each Ca atom at a distance of 3.14 Å (in our geometrically optimized structure) vs. 3.56 Å for the interlayer Ca-Ag contact in $CaAg_5$.

These trends in the coordination number and distances can be connected to a classic guideline for pressure-induced phase transitions: the Pressure-Distance Paradox. Structural transformations induced by the application of physical pressure generally involve an increase in the average coordination numbers

of the atoms in the phase. This increase in neighbors means that the strength of each individual interaction is weaker, and the near-neighbor distances increase. We observe then a counter-intuitive lengthening of bond distances under pressure. The opposite trend is seen on going from a high pressure phase to a low pressure one: atoms will then take on fewer neighbors at shorter distances. Such a situation occurs

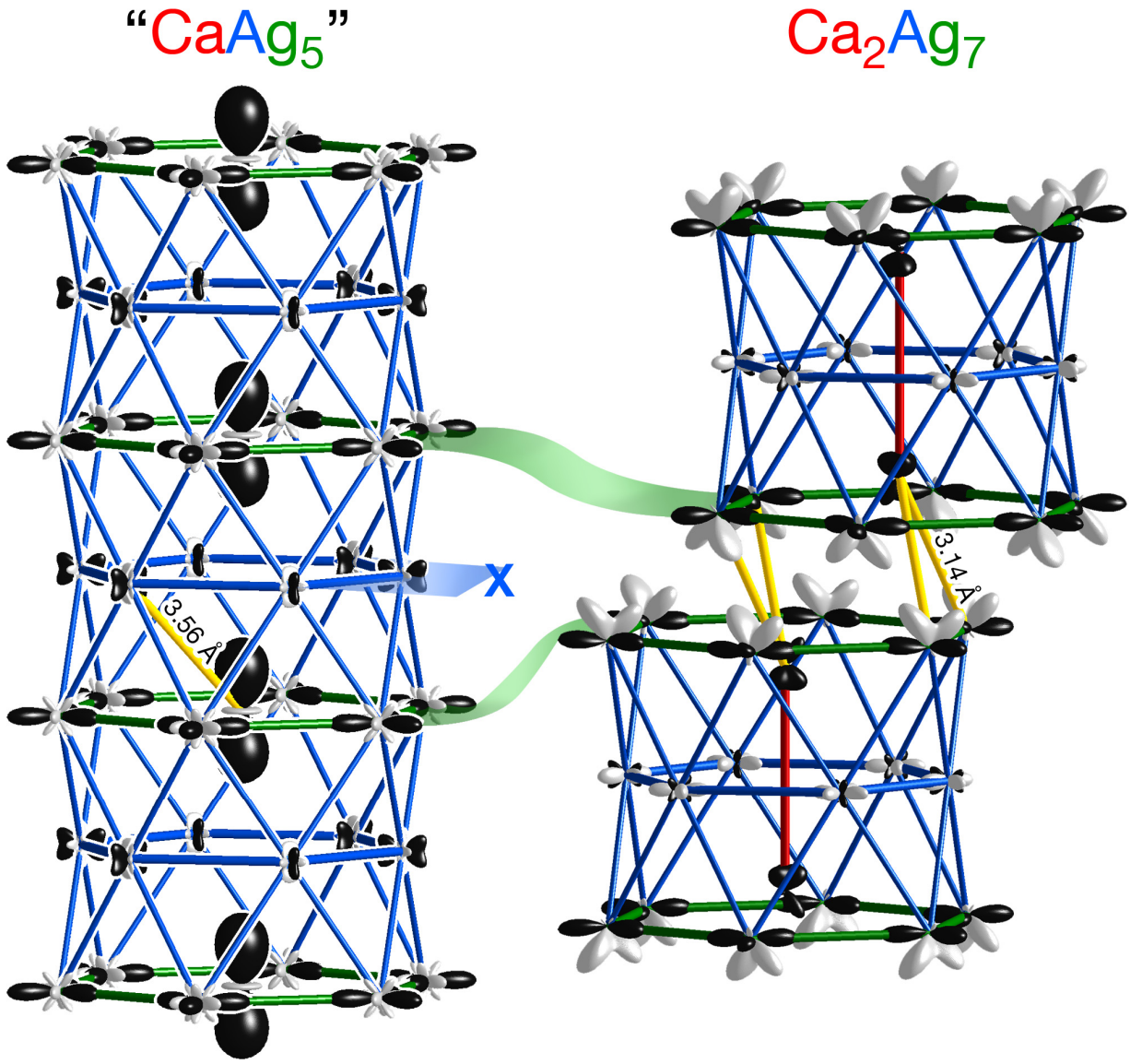

Figure 7.4. Chemical pressure in the hypothetical $CaCu_5$-type structure $CaAg_5$ and the observed Ca_2Ag_7. Pressures are plotted to scale across the figure. See text for other plotting conventions.

as the Ca_2Ag_7 structure forms in response to negative pressures in the Ca environment of the $CaCu_5$ type: the calcium atoms decrease their Ag neighbor count from 18 at an average distance of 3.42 Å to 14 with an average distance of 3.20 Å.

The favorability of this new arrangement is evident in the CP features calculated for Ca_2Ag_7. On the Ca atoms, the large negative pressure lobes have become substantially reduced, so much so that they are no longer the most prominent features in the CP scheme. The locus of the stresses is now at the interfaces between $CaCu_5$-type slabs, where white positive CP lobes point along interlayer Ag-Ag contacts. The presence of such positive pressures between the layers may help explain why this structure type is not adopted in the Ca-Cd system, despite the similar CP issues encountered in the $CaCu_5$ type. Instead, as we will see below, more substantial structural changes emerge here, which branch into two paths for CP release.

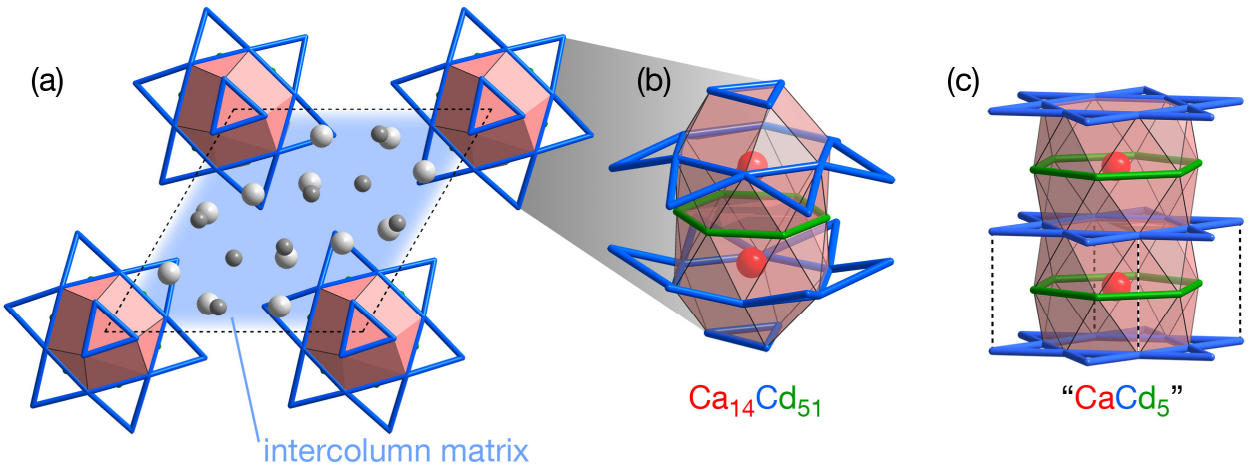

Figure 7.5. Columns of the $CaCu_5$-type features in the crystal structure of $Ca_{14}Cd_{51}$. (a) The distribution of columns within the unit cell of $Ca_{14}Cd_{51}$. (b) One repeat length of the column, shown alongside (c) the $CaCu_5$ structure type.

7.6. Manifestations of structural plasticity in the Ca-Cd system

From the similarities encountered in the CP schemes calculated for the $CaAg_5$ and $CaCd_5$ in the $CaCu_5$ type, it is not surprising the Ca-Cd system would also seek structure alternatives to this simple structure. What is striking, however, is the number of solutions that the Ca-Cd system finds. At least four phases exist near the 1:5 composition in this system: $Ca_{14}Cd_{51}$,[25,26] $CaCd_{5.7}$, $Ca_{13}Cd_{76}$,[27] and $CaCd_6$.[28] The first of these represents a continuation of the fragmentation of the $CaCu_5$ type seen in the Ca_2Ag_7 structure, while the latter three correspond to a Tsai-type icosahedral quasicrystal and two periodic approximants to it. Through CP analysis of $Ca_{14}Cd_{51}$ and the simplest Tsai-type approximant, $CaCd_6$, we will be able to frame this structural diversity in terms of structural plasticity.

7.6.1 Structural plasticity-inspired view of $Ca_{14}Cd_{51}$'s structure

Let's begin with $Ca_{14}Cd_{51}$, as it shares common themes with the Ca_2Ag_7 structure we examined in the last section. One simple yet crucial contribution that the theme of structural plasticity can make to our understanding of this compound is to provide a framework for describing its crystal structure. $Ca_{14}Cd_{51}$ crystallizes in the $Gd_{14}Ag_{51}$ structure type, whose moderately large hexagonal unit cell of 65 atoms is difficult to reduce to a handful of intuitive structural motifs. However, its proximity in composition to a hypothetical $CaCu_5$-type phase encourages us to seek connections to this simpler structure type.

Such a connection becomes immediately apparent upon looking at the coordination environments of the Ca1 sites, which lie along high-symmetry hexagonal axes of the structure. The Ca1 atoms occur in pairs that lie in spaces created by the stacking of three Cd hexagons, the top and bottom of which can be extended through inclusion of neighboring Cd atoms to make larger fragments of kagome nets (blue). These hexagonal features bear some resemblance to the hexagonal channels hosting the Ca atoms in the

$CaCu_5$-type. Here, though, the stack is only three hexagons tall, and is terminated on the top and bottom by Cd triangles (which are disordered over two orientations in the refined crystal structure, due to their lying on a 6-fold rotational axis). These $CaCu_5$-type units occur periodically along *c*, separated by shared triangles; were these triangles to be replaced with hexagons, a continuous column of the $CaCu_5$-type would be obtained.

At first glance, the remainder of the structure seems little more than a matrix of atoms separating these $CaCu_5$-derived columns from each other (Figure 7.5a). However, when we recall that the $CaCd_5$ is predicted to exhibit more internal strain than $CaAg_5$, it becomes clear that any $CaCu_5$-type features remaining in this phase made be even more degraded than in Ca_2Ag_7. In fact, somewhat tenuous connections to Ca_2Ag_7 can be found in this matrix region, as is seen by looking the coordination environments of the remaining symmetry-distinct Ca atoms in the structure Ca1 and Ca2.

The environments of these sites are shown in Figure 7.6. As with the Ca1 sites, the Ca2 and Ca3 atoms appear in pairs. In both cases, their nearest neighbors can be sorted into three, nearly-planar, distorted rings, which can be viewed as analogous to the three hexagons of the Ca coordination polyhedra in the $CaCu_5$ type. While the sizes of these rings exhibit severe distortions relative the $CaCu_5$ type, certain aspects can be understood from the CP-scheme calculated for $CaCd_5$. For example, at the Ca2 site, the middle ring has expanded to include 7 members rather than six, and the upper and lower faces have contracted to three or four atoms. This appears to be excellent tailoring for a Ca coordination environment which exhibited negative pressure lobes pointing up and down, and a positive pressure ring in the horizontal plane. Similar expectations are seen for the Ca3 site: the replacement of the upper and lower hexagons with a triangle and pentagon (or square, depending on the orientation of the disordered triangle) should certainly bring CP relief to the large negative CP lobes.

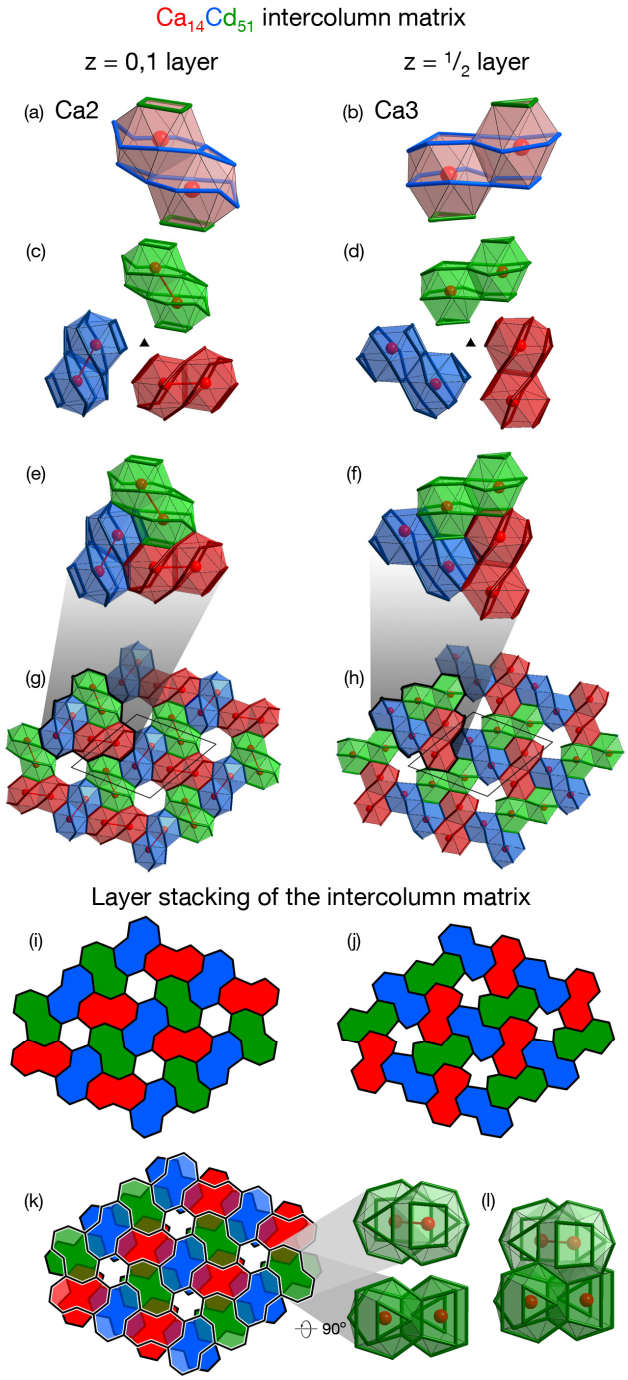

Figure 7.6. Structure of the intercolumnar matrix in $Ca_{14}Cd_{51}$. (a,b) The coordination environments of the Ca2 and Ca3 sites occur as dumbbell-shaped homodimers. (c,d) The dumbbells pack neatly into triangular units in a head-to-neck fashion, which is supported by (e,f) the sharing of complementary phases. (g,h) The triangular units in turn fuse with each other into sheets, which are represented schematically in (i,j). (k) The Ca2 and Ca3 layers stack in an alternating fashion along *c* with neighboring dumbbells staggered to allow the sharing of atoms at neck-to-neck contacts.

Now that we have rationalized the shapes of these irregular coordination polyhedra, we are now faced with seeing how they are arranged in the matrix space between Ca1columns. The polyhedra surrounding the Ca2 and Ca3 dimers have a dumbbell-like shape (Figures 7.6a,b), which allow them to pack efficiently in a triangular fashion such that the head of each dimer lies in the hollow of another (Figures 7.6c,d). This packing is supported by an arrangement of square and triangular faces around the perimeters of the dumbbells that is complementary between head and hollow. The compatibility is such that the triangular units seamlessly fuse through the sharing of these faces (Figures 7.6e,f). Through similar face-sharing the Ca2 and Ca3 triangular units join into sheets with openings for the Ca1 columns to pass through (Figures 7.6g-j).

The Ca2 and Ca3 sheets stack in an alternating fashion along the *c*-axis, with the dimer orientations shifting by almost 90 degrees between neighboring sheets (Figure 7.6k). The staggering of the dimer orientations allows the neighboring dimers to nestle closely neck-to-neck (Figure 7.6l), and share faces. Further details concerning the inter-layer contacts can be found in the Supporting Information.

In this discussion of the Ca coordination environments of $Ca_{14}Cd_{51}$, we have accounted for all of the symmetry-distinct sites of the crystal structure. All atoms in the crystal structure participate in the Ca-Cu_5-derived columns surrounding the Ca1 sites, and/or the irregular polyhedra of the Ca2 and Ca3 sites, whose shapes seem adapted to respond to the chemical pressures experienced by the Ca atoms in the $CaCu_5$ type. In this way, the full structure can be expressed as providing a favorable alternative to the constrained geometry of the $CaCu_5$-type.

7.6.2 Chemical Pressure Release in $Ca_{14}Cd_{51}$

How well do these structural features we just described for the $Ca_{14}Cd_{51}$ really provide relief to the chemical pressure issues that a $CaCu_5$-type $CaCd_5$ phase would experience? Figure 7.7 presents the CP scheme calculated for the Ca-coordination environments of $Ca_{14}Cd_{51}$, along with those of $CaCd_5$ and a hypothetical Ca-Cd phase isotypic to Ca_2Ag_7 for comparison. As we saw previously, the strain inherent in a $CaCu_5$-type $CaCd_5$ phase is striking (Figure 7.7a): large negative pressures on the Ca atoms call for shorter contacts to the layers above and below, but the contraction along these interactions is prevented by positive pressures within the Cd sublattice.

Following the same structural path as the Ca-Ag system to form a Cd analog to Ca_2Ag_7 would seem to be a reasonable solution to this. In fact, CP calculations on such a structure (Figure 7.7b) show a similar form of relief around the Ca sites as was found for earlier for Ca_2Ag_7. However, a closer look at the integrated pressure values (-423 GPa for Ca in $CaCd_5$ vs. -430 GPa in Ca_2Cd_7) reveals that the smaller Ca lobe size in Ca_2Cd_7 represents more of a redistribution of the negative CP in a more isotropic fashion than a true reduction. Evidently, the larger size of Cd prevents this structure from providing adequate relief to the Ca atoms.

Moving to the $Ca_{14}Cd_{51}$ structure, with its more extensive fragmentation of the $CaCu_5$-type, leads are somewhat larger release of the Ca atoms' negative CP (Figures 7.7c-e). As in Ca_2Cd_7, the CP distributions around the Ca sites appear much more isotropic than in the $CaCu_5$ type. The magnitudes of the net pressures, on average, have also decreased from -423 to -395 GPa. The effect here, however, is uneven: the majority Ca2 and Ca3 sites achieve negative CPs as mild as -345 GPa, but the Ca1 sites in the $CaCu_5$-derived columns actually exhibit enhanced CPs of -483 GPa. These results may indicate that the

form of the columns is templated by the geometrical requirements of intercolumnar matrix, rather than vice versa.

In addition to illustrating a driving force of the formation of the phase, the CP schemes of the Ca2 and Ca3 coordination environments helps provide a foundation for the layered description used in Figures 7.6a,b to draw an analogy to the $CaCu_5$-type. In CP plots of Figures 7.7c,e we emphasize the same layers in these environments using thicker cylinders. The contacts within the layers on the whole exhibit different CP features than those between them: the intralayer contacts tend to be punctuated with positive pressure lobes, while many of those between the layers show negative CP. These layers that were originally identified in a search for connections to the $CaCu_5$ type thus have some relevance to the electronic structure of the phase.

In summary, the $Ca_{14}Cd_{51}$ structure can be seen as a more drastic response to the internal stresses of the $CaCu_5$ type than the Ca_2Ag_7 structure. In both cases, the deletion of transition metal atoms from the $CaCu_5$ type relieves negative CPs around the Ca atoms by providing to tighter Ca coordination environments. In Ca_2Ag_7 the Ca coordination number by Ag is decreased from 18 to 14, while in $Ca_{14}Cd_{51}$ gets this number gets as low as 13 (for the Ca3 site). This, of course, suits the more severe CP issues of $CaCd_5$ than those of its Ag analogue.

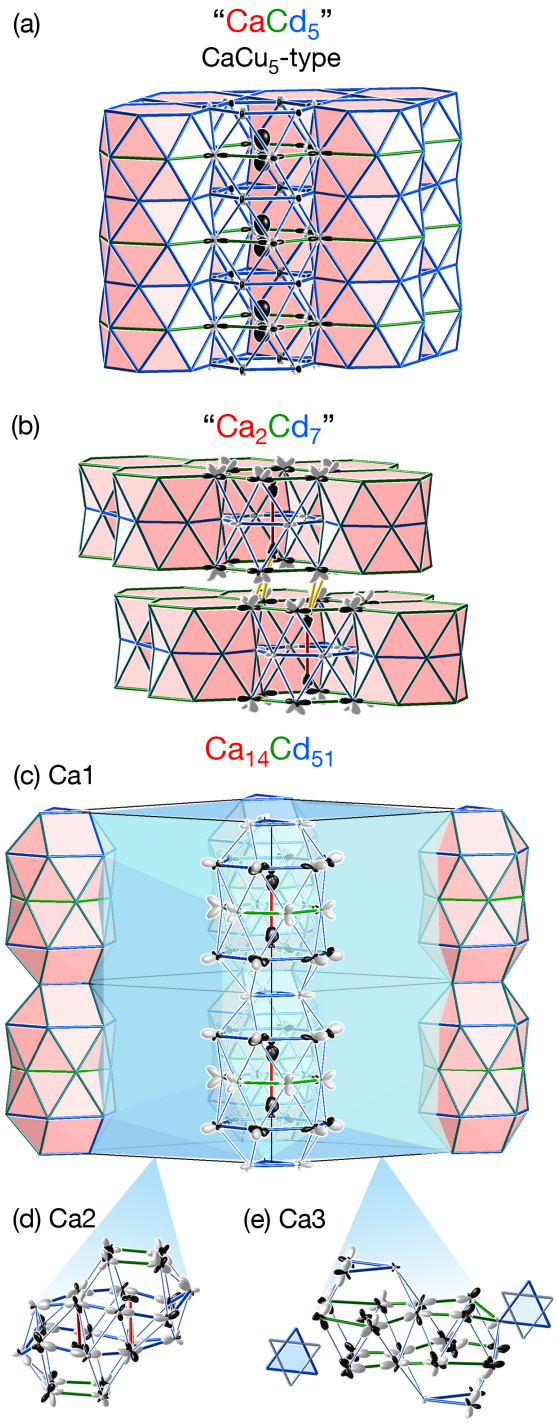

Figure 7.7. Chemical pressure in various Ca-Cd compounds. Two of these compounds represent hypothetical alternatives to the phase that forms: (a) $CaCu_5$-type $CaCd_5$ and (b) Ca_2Ag_7-type Ca_2Cd_7. The three symmetry unique calcium environments for the observed $Ca_{14}Cd_{51}$ are shown in (c-e). Pressures are plotted to scale across the figure. See text for plotting conventions.

7.6.3 The Cd-rich Path to Chemical Pressure Relief: Tsai-type Cluster Formation in $CaCd_6$

The complex structures we have considered so far all involved the use of transition metal-poor stoichiometries to tighten the coordination environments of the Ca atoms. In the Ca-Cd system, a series of phases are also present which are Cd-rich relative to a 1:5 stoichiometry: a Tsai-type icosahedral quasicrystal and two of its approximants. A look at the CP distributions in these compounds offers the potential of including quasicrystallinity as an expression of the structural plasticity of intermetallic structures.

To explore this possibility, let's focus on the simplest (and thus most amenable to electronic structure calculations) of these phases: the 1/1 Tsai-type approximant $CaCd_6$ (Figure 7.8). Its structure consists of body-centered cubic packing of spheroidal Tsai-type clusters, which are usually described in terms of concentric shells. The center of the cluster is occupied by a Cd tetrahedron (Figure 7.8a), which is orientationally disordered in the refined crystal structure (but we will lock to one specific orientation for the purpose of our calculations). This is surrounded by a Cd pentagonal dodecahedron (Figure 7.8b), which is in turn encapsulated in a Ca icosahedron (Figure 7.8c), Cd icosidodecahedron (Figure 7.8d), and finally a defect soccer-ball arrangement of Cd atoms (Figure 7.8e).

At first glance, this arrangement of atoms might appear to have little in common with the simple $CaCu_5$ type. However, if we zoom in on the Ca coordination polyhedron of $CaCd_6$, a connection begins to take shape (Figure 7.8g). The Ca sits in a pentagonal void space, defined by three staggered pentagons: one in the plane of the Ca, with the others above and below, an arrangement very similar to the double hexagonal antiprism that defines the Ca coordination environment in the $CaCu_5$ type (Figure 7.8h). In essence, the Ca's coordination in $CaCd_6$ is a pentagonal analog of that in the $CaCu_5$ type.

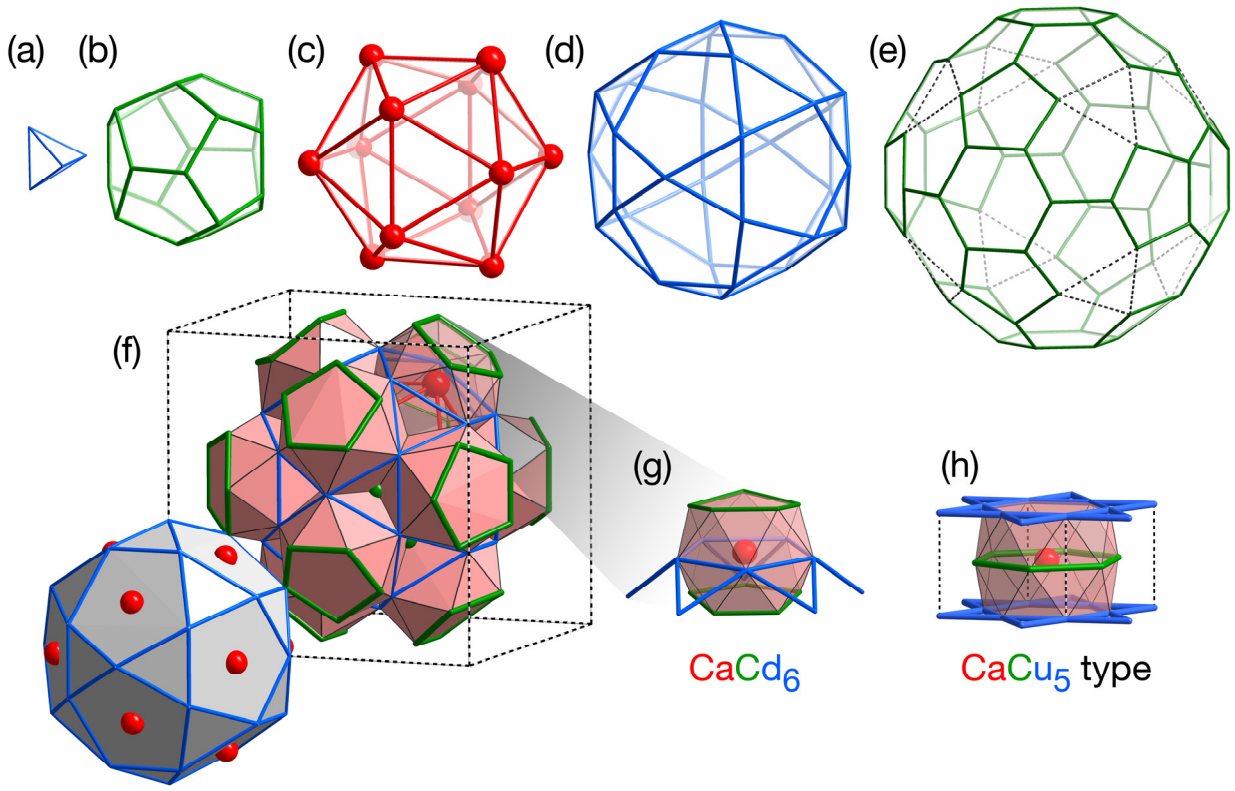

Figure 7.8. Structural interpretation of the Tsai type quasicrystalline approximant, $CaCd_6$. The Tsai cluster is comprised of nesting polyhedra: (a) the central, positionally disordered Cd tetrahedron, (b) Cd dodecahedron, (c) Ca icosahedron, (d) the Cd icosidodecahedron, and (e) defect Cd fullerene-like cage. The cluster packs in a body centered cubic fashion to form the (f) $CaCd_6$ structure. We compare the local calcium environments in (g) $CaCd_6$ and (h) $CaCu_5$-type.

The contraction from a hexagonal polyhedron to a pentagonal one would seem like an excellent means of relieving the negative CPs that would be experienced by the Ca atoms in the $CaCu_5$ type. Such is confirmed by a comparison of the CP distributions calculated for $CaCd_5$ and an ordered model of $CaCd_6$ (Figure 7.9). On moving from $CaCd_5$ to $CaCd_6$, the average Ca net negative CP shrinks significantly from -423 GPa to -380 GPa, with the distribution of pressure lobes becoming much less isotropic.

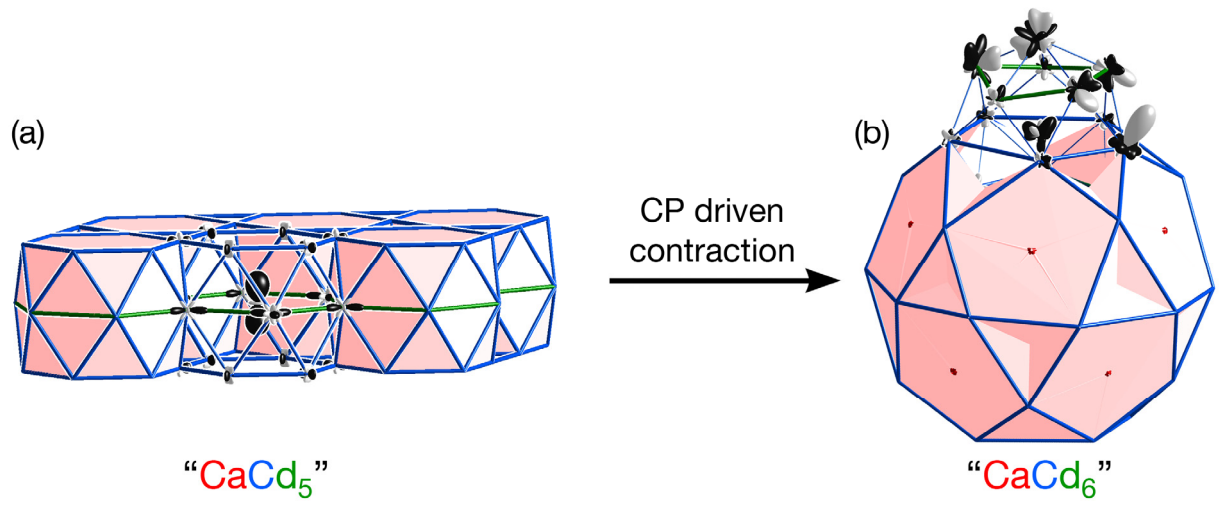

Figure 7.9. Chemical pressure plots for the chemical pressure seen in $CaCd_6$. Pressures are plotted to scale across the figure. See text for plotting conventions.

The use of pentagonal polyhedra thus soothes the Ca atoms' need for tighter coordination, but it introduces a new problem: pentagonal units are significantly more difficult to arrange periodically in space than hexagonal ones. A beautiful solution to this issue is found by the structure of $CaCd_6$, as is detailed in our earlier communication: the substitution of hexagons with pentagons is accommodated by the introduction of curvature. The shells of the Tsai-type cluster comprise curved analogues to the layers of the $CaCu_5$ type, in the same way as introducing pentagons into a graphene layer will lead to a C_{60} fullerene.

The soothing of the CPs upon adopting the $CaCd_6$ structure extends beyond the Ca atoms' immediate surroundings. Most of the Tsai-type cluster from the icosidodecahedron down toward the core exhibit only relatively subtle features. The main exception is in some of the contacts between the central tetrahedron to the next shell outwards, which may be partially relieved by moving to a model in which the orientations of these units are allowed to vary, providing a closer approximation to the true disorder.

The largely strain-free nature of the cluster interior helps us understand why this unit should be the fundamental building block of Tsai-type quasicrystals.

All this is not to say, however, that the $CaCd_6$ structure is free from chemical pressures. If we shift our attention from the contents of the Tsai-type clusters to their interactions with each other, the intense pressure lobes become apparent. The strongest of these are positive Cd-Cd CPs, which appear quite prominently at the unit cell faces where neighboring clusters meet through shared hexagons. Such CP features at the cluster interfaces hint that alternative arrangements of the clusters may be favorable, as are indeed seen in the more complex $Ca_{13}Cd_{76}$ approximant, and the $CaCd_{5.7}$ quasicrystal itself.

The observation of these positive Cd-Cd CPs away from the Ca coordination environments can also help us understand how a moving to a more Cd-rich composition relative to the $CaCu_5$-type has resulted in a decrease in the number of Ca-Cd contacts. Whereas in the earlier structures we discussed, the Ca coordination number was reduced through removing transition metal atoms, here this effect is achieved by enhancing the number of Cd-Cd contacts, which reduces the number of Ca atoms that each Cd atom touches. In the $CaCu_5$-type, the transition metals have either three or four Ca neighbors. In $CaCd_6$, the introduction of the Cd4 tetrahedron the Tsai-type cluster core, and the absence of Ca atoms associated with the hexagons of the fullerene cage lowers the average number of Ca-Cd contacts per Cd to 2.72.

7.7. Conclusions

In this Chapter, we have developed the theme of structural plasticity by combining updated results of our earlier DFT-CP studies of the Ca_2Ag_7, and $CaCd_6$ structures, with a new analysis of driving forces stabilizing the complex structure of $Ca_{14}Ag_{51}$. All three of these phases share a common origin in the presence of large negative CPs in the Ca coordination environments of the $CaCu_5$-type phase that would

normally be anticipated to form in the Ca-Ag and Ca-Cd phases at the 1:5 stoichiometry. In each case, structural variations are introduced which tighten the Ca coordination, but different approaches are taken to accomplish this. In Ca_2Ag_7 and $Ca_{14}Cd_{51}$, the $CaCu_5$-type is progressively fragmented through the deletion of Ag/Cd atoms. In $CaCd_6$, however, additional Cd atoms are incorporated to create greater independence of the Ca coordination polyhedra. The ability of the structures to choose between transition metal insertion and deletion to modulate the surroundings of the Ca atoms is represented by the two branches of the structural family tree in Figure 7.1.

Through this work, we have seen how the concept of structural plasticity can be used to draw causal relationships between a disparate collection of crystal structures. We are looking forward to further expanding this network of connections. For example, the $AuBe_5$ structure type is another common crystal structure that is adopted by compounds that combine late transition metals with an electropositive metal. We recently illustrated that its stability relative to the $CaCu_5$ type is enhanced as the electropositive metal is made. The transition from the $CaCu_5$ to $AuBe_5$ types could be added as a fixed stoichiometry branch to Figure 7.1, with the $AuBe_5$ type then serving starting point for the complex $AuBe_5$-$MgCu_2$ intergrowth structures that have been observed in compounds such as $YbCu_{4.5}$ (*mC*7448).[29,30]

Another potential use of the structural relationships revealed in this work is the design of syntheses targeting new phases. As all of the complex structures discussed here emerge from the release of negative pressures around the Ca sites in $CaCu_5$-type phases, elemental substitutions that modulate these pressures could be used to stabilize other structures. For instance, the partial replacement of Cd or Ag in the Ca-Cd and Ca-Ag systems, respectively with smaller Pd atoms would lessen the stresses in the Ca coordination environments. This in turn could lead an enhancement of the $CaCu_5$-type features in the

reaction products. An exciting avenue for future research will be to explore these expectations through new solid state syntheses.

Acknowledgements

We thank J. Engelkemier and Yiming Guo for helpful conversations contributing to this work. We also are grateful to the National Science Foundation for financial support through grant number DMR-1207409. This work utilized computer resources supported by NSF grant CHE-084494.

7.8. References

(1) Pearson, W. B. *The crystal chemistry and physics of metals and alloys*; Wiley-Interscience: New York, 1972.

(2) Villars, P.; Calvert, L. D. *Pearson's handbook of crystallographic data for intermetallic phases*; 2nd ed.; ASM International: Materials Park, OH, 1991.

(3) Shechtman, D.; Blech, I.; Gratias, D.; Cahn, J. W. *Physical Review Letters* 1984, *53*, 1951-1953.

(4) Dshemuchadse, J.; Jung, D. Y.; Steurer, W. *Acta Crystallogr. B* 2011, *67*, 269-292.

(5) Berger, R. F.; Lee, S.; Johnson, J.; Nebgen, B.; Sha, F.; Xu, J. *Chem. Eur. J.* 2008, *14*, 3908-3930.

(6) Ilyushin, G. D.; Blatov, V. A. *Russ. J. Inorg. Chem.* 2010, *55*, 1909-1918.

(7) Blatov, V. A.; Ilyushin, G. D.; Proserpio, D. M. *Inorg. Chem.* 2010, *49*, 1811-1818.

(8) Blatov, V. A.; Ilyushin, G. D.; Proserpio, D. M. *Inorg. Chem.* 2011, *50*, 5714-5724.

(9) Pankova, A. A.; Blatov, V. A.; Ilyushin, G. D.; Proserpio, D. M. *Inorg. Chem.* 2013, *52*, 13094-13107.

(10) Fredrickson, D. C.; Lee, S.; Hoffmann, R. *Angew Chem Int Edit* 2007, *46*, 1958-1976.

(11) Schmidt, J. T.; Lee, S.; Fredrickson, D. C.; Conrad, M.; Sun, J. L.; Harbrecht, B. *Chem. Eur. J.* 2007, *13*, 1394-1410.

(12) Cenzual, K.; Parthé, E.; Waterstrat, R. M. *Acta Crystallogr. C* 1986, *42*, 261-266.

(13) Yang, Q.-B.; Andersson, S.; Stenberg, L. *Acta Crystallogr. B* 1987, *43*, 14-16.

(14) Fredrickson, D. C. *J. Am. Chem. Soc.* 2012, *134*, 5991-5999.

(15) Engelkemier, J.; Berns, V. M.; Fredrickson, D. C. *J. Chem. Theory Comput.* 2013, *9*, 3170-3180.

(16) Harris, N. A.; Hadler, A. B.; Fredrickson, D. C. *Z. Anorg. Allg. Chem.* 2011, *637*, 1961-1974.

(17) Hadler, A. B.; Harris, N. A.; Fredrickson, D. C. *J. Am. Chem. Soc.* 2013, *135*, 17369-17378.

(18) Fulfer, B. W.; McAlpin, J. D.; Engelkemier, J.; McCandless, G. T.; Prestigiacomo, J.; Stadler, S.; Fredrickson, D. C.; Chan, J. Y. *Chem. Mater.* 2014, *26*, 1170-1179.

(19) Berns, V. M.; Fredrickson, D. C. *Inorg. Chem.* 2013, *52*, 12875-12877.

(20) Gonze, X.; Rignanese, G.-m.; Verstraete, M.; Beuken, J.-m.; Pouillon, Y.; Caracas, R.; Raty, J.-y.; Olevano, V.; Bruneval, F.; Reining, L.; Godby, R.; Onida, G.; Hamann, D. R.; Allan, D. C. *Z. Kristallogr.* 2005, *220*, 558-562.

(21) Gonze, X.; Amadon, B.; Anglade, P.-M.; Beuken, J.-M.; Bottin, F.; Boulanger, P.; Bruneval, F.; Caliste, D.; Caracas, R.; Côté, M.; Deutsch, T.; Genovese, L.; Ghosez, P.; Giantomassi, M.; Goedecker, S.; Hamann, D. R.; Hermet, P.; Jollet, F.; Jomard, G.; Leroux, S.; Mancini, M.; Mazevet, S.; Oliveira, M. J. T.; Onida, G.; Pouillon, Y.; Rangel, T.; Rignanese, G.-M.; Sangalli, D.; Shaltaf, R.; Torrent, M.; Verstraete, M. J.; Zerah, G.; Zwanziger, J. W. *Comput. Phys. Commun.* 2009, *180*, 2582-2615.

(22) Goedecker, S.; Teter, M.; Hutter, J. *Phys. Rev. B* 1996, *54*, 1703-1710.

(23) Hartwigsen, C.; Goedecker, S.; Hutter, J. *Phys. Rev. B* 1998, *58*, 3641-3662.

(24) Nelder, J. A.; Mead, R. *Comput J* 1965, *7*, 308-313.

(25) Bruzzone, G. *Gazz. Chim. Ital.* 1972, *102*, 234-242.

(26) Subramanian, P. R. In *Binary Alloy Phase Diagrams, 2nd Ed.*; Massalski, T. B., Ed.; ASM International: Materials Park, Ohio, 1990; Vol. 44, p 899-901.

(27) Gomez, C. P.; Lidin, S. *Angew. Chem. Int. Ed.* 2001, *40*, 4037-4039.

(28) Gómez, C. P.; Lidin, S. *Phys. Rev. B* 2003, *68*, 024203.

(29) Cerny, R.; Francois, M.; Yvon, K.; Jaccard, D.; Walker, E.; Petricek, V.; Cisarova, I.; Nissen, H.-U.; Wessicken, R. *J Phys Condens. Matter* 1996, *4485*.

(30) Gottlieb-Schönmeyer, S.; Brühne, S.; Ritter, F.; Assmus, W.; Balanetskyy, S.; Feuerbacher, M.; Weber, T.; Steurer, W. *Intermetallics* 2009, *17*, 6-10.

Chapter 8.

Atomic Size Matters

A comic book–style interpretation of some of the previous work, presented here for a more general audience.

Chemical Pressure and Its Applications to the Tsai-type Quasicrystal

– or –

Atomic Size Matters

Veronica M. Berns

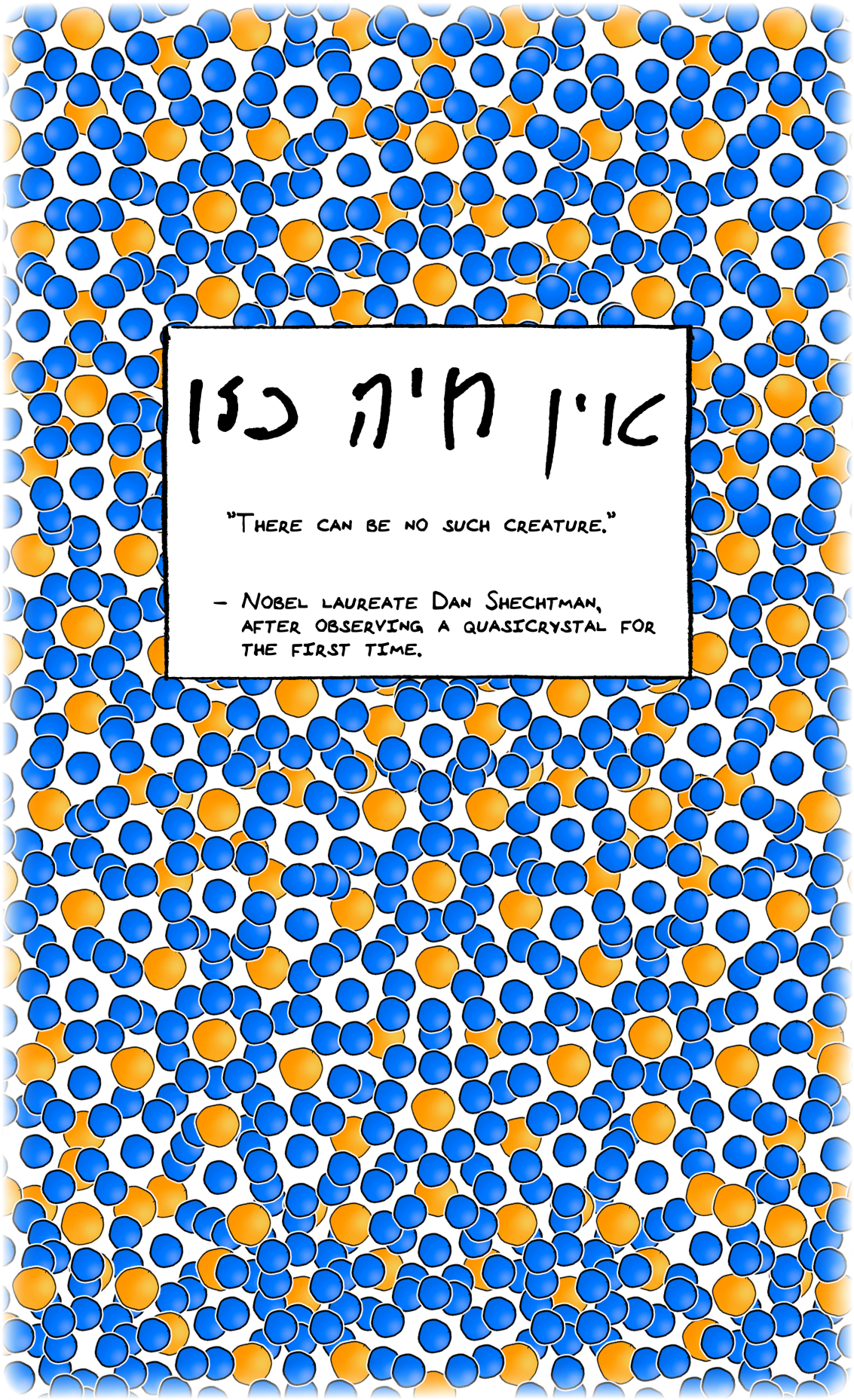
אין חיה כזו
"There can be no such creature."
– Nobel laureate Dan Shechtman, after observing a quasicrystal for the first time.

TO SCIENCE, FOR THE INSPIRATION
AND TO MY FRIENDS AND FAMILY, FOR THE MOTIVATION

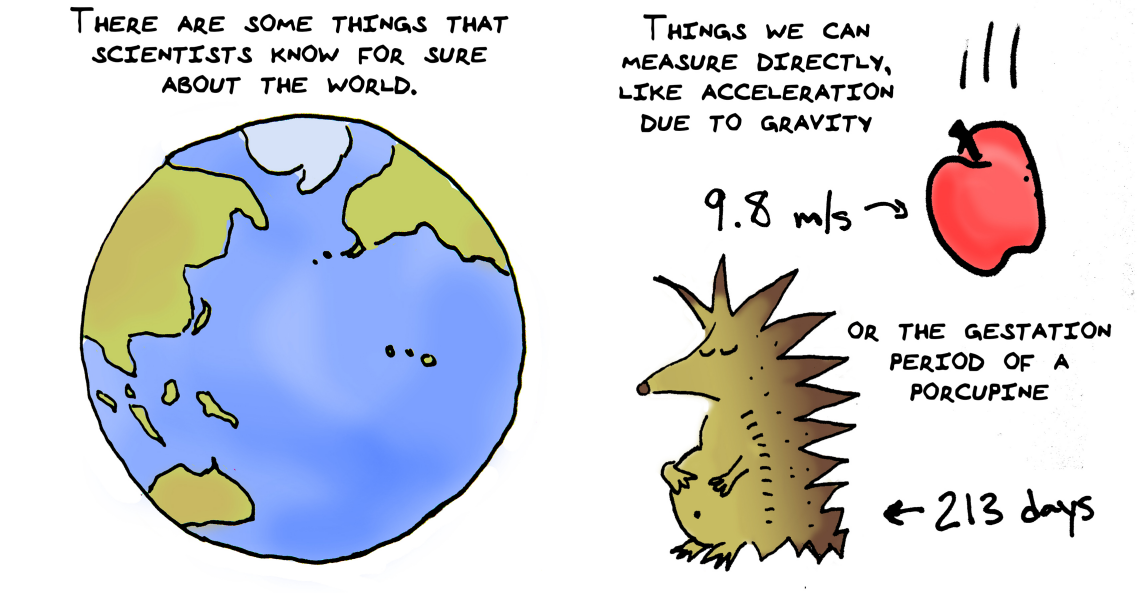
THERE ARE SOME THINGS THAT SCIENTISTS KNOW FOR SURE ABOUT THE WORLD.
THINGS WE CAN MEASURE DIRECTLY, LIKE ACCELERATION DUE TO GRAVITY
9.8 m/s²
OR THE GESTATION PERIOD OF A PORCUPINE
← 213 days


AND THERE ARE SOME THINGS WE ARE PRETTY SURE ABOUT BECAUSE OF A COMBINATION OF EVIDENCE FROM DATA AND, WELL...
...A HUNCH.
LIKE GLOBAL WARMING OR THE BIG BANG.
WE CAN NEVER BE 100 % CERTAIN, BUT MOST SCIENTISTS AGREE ON THOSE THINGS.

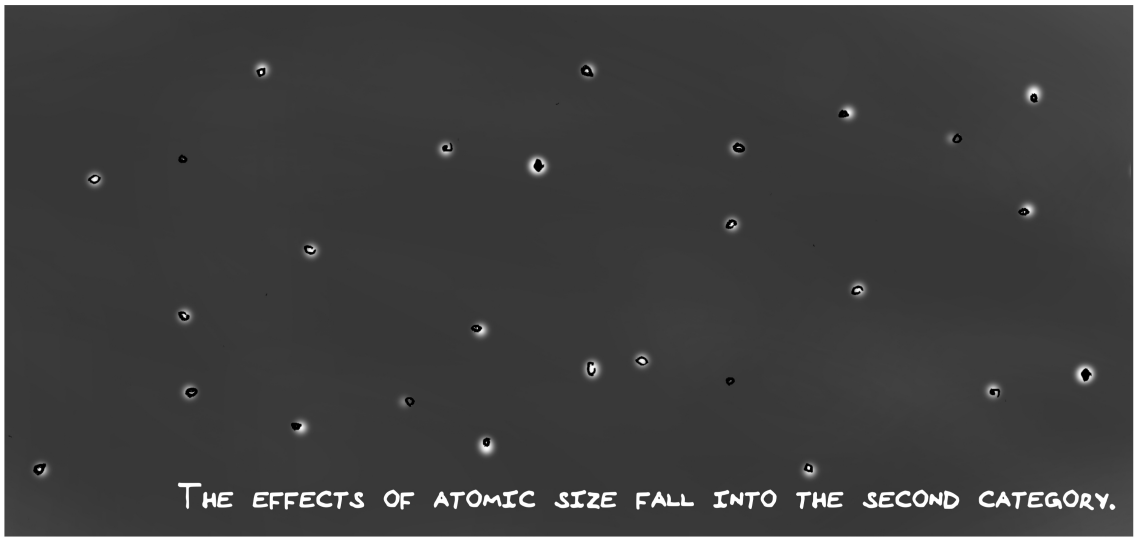
THE EFFECTS OF ATOMIC SIZE FALL INTO THE SECOND CATEGORY.

ATOMS CAN BE THOUGHT OF AS HARD SPHERES. THEY AREN'T, BUT YOU CAN THINK ABOUT THEM THAT WAY SOMETIMES, TO SIMPLIFY THINGS.

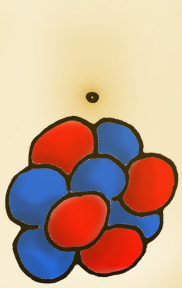

EVERYTHING IS BASICALLY A PILE OF ATOMS.

WHETHER WE CALL THAT PILE A SOLID, LIQUID, OR GAS DEPENDS ON HOW CLOSE TOGETHER THOSE ATOMS ARE AND HOW FAST THEY ARE MOVING.

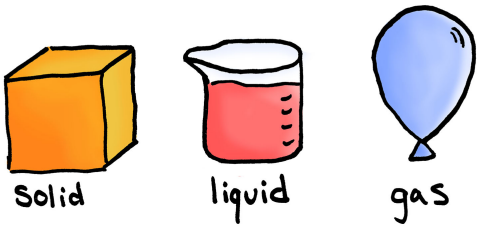

THE FAST ONES FLY APART FROM EACH OTHER. THESE ARE GASES.

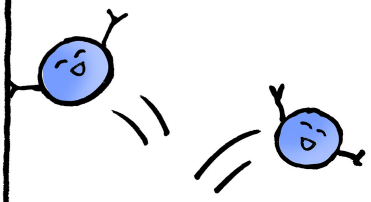

LIQUIDS' ATOMS ARE CLOSER TOGETHER AND SLOSH ABOUT IN THEIR CONTAINERS.

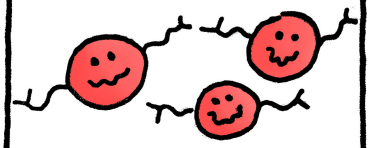

AND THEN THERE'S SOLIDS.

SOLIDS HUDDLE TOGETHER AND THE ATOMS MOVE SLOW.

SO SLOW THAT WE OFTEN ROUND DOWN TO SAY THEY AREN'T MOVING AT ALL.

SOLIDS CAN BE NEAT AND ORDERLY, OR MESSY AND UNPREDICTABLE.

MESSY HAS ITS PLACE, BUT IF YOU WANT TO LEARN ABOUT A CHEMICAL COMPOUND, OFTEN THE EASIEST WAY TO DO IT IS TO MAKE A CRYSTAL.

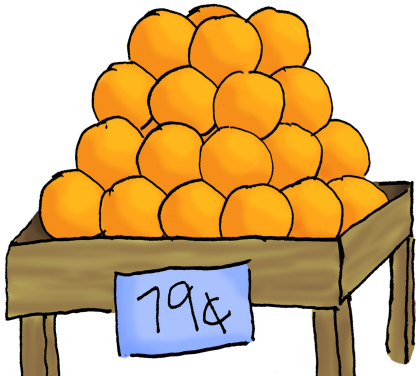

IN CRYSTALS, ATOMS PACK ORDERLY AND TIGHTLY, LIKE ORANGES IN A GROCERY STORE DISPLAY.

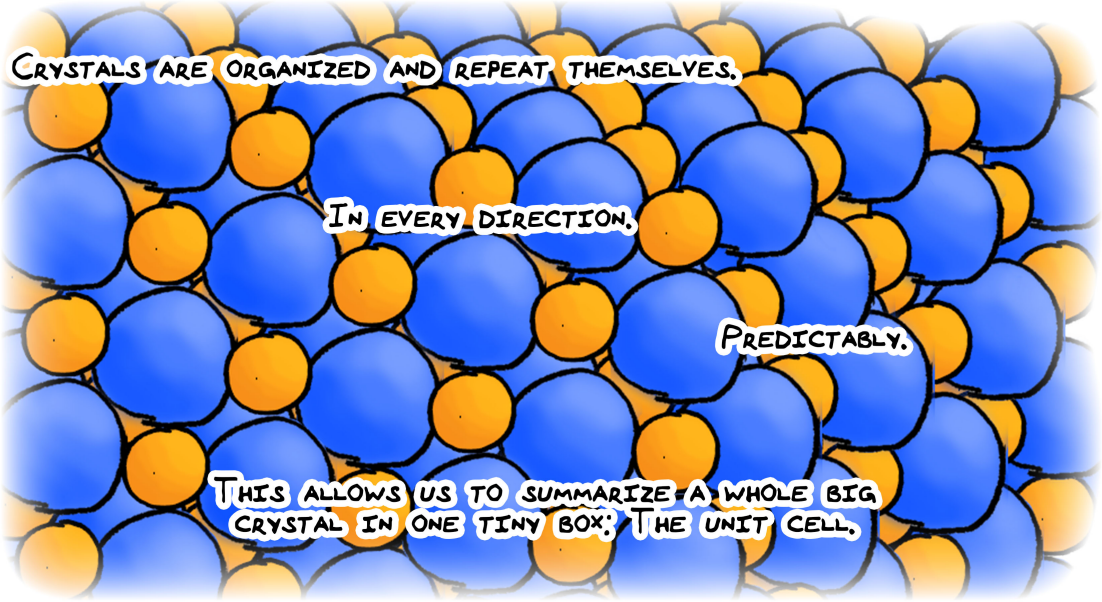

The unit cell is the smallest region that repeats itself in every direction.

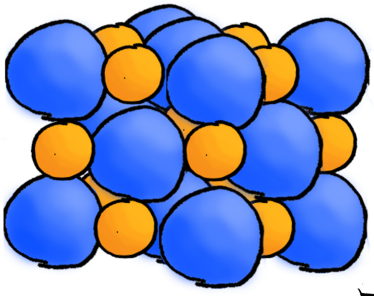

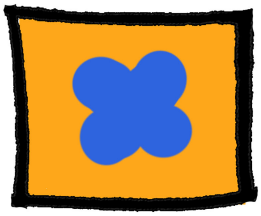

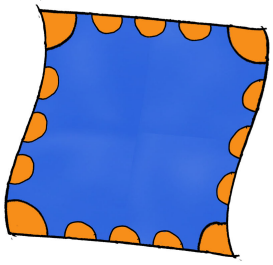

Like a decorative kitchen tile, or a patterned swatch of fabric.

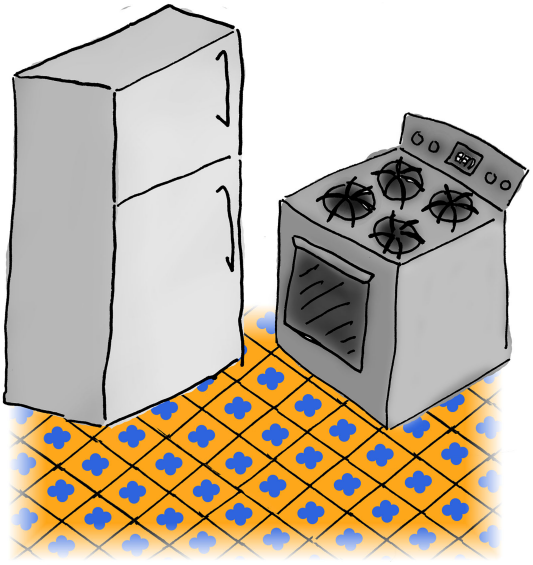

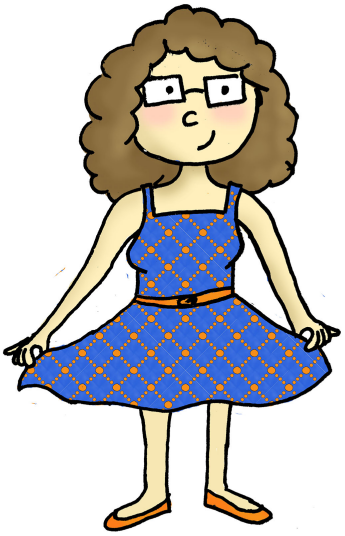

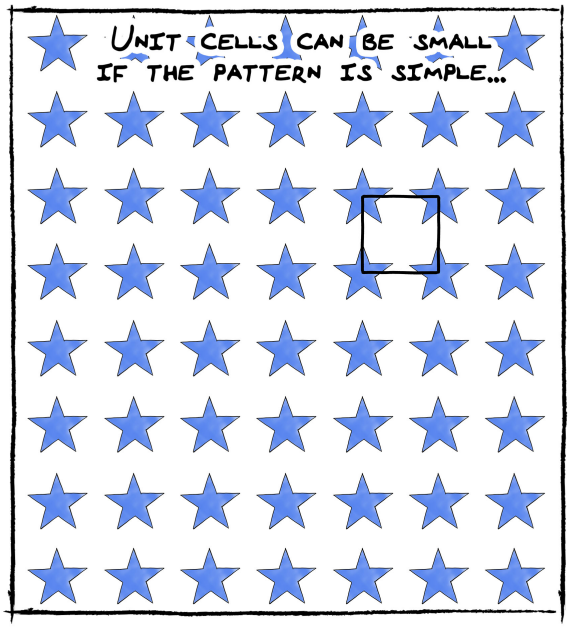

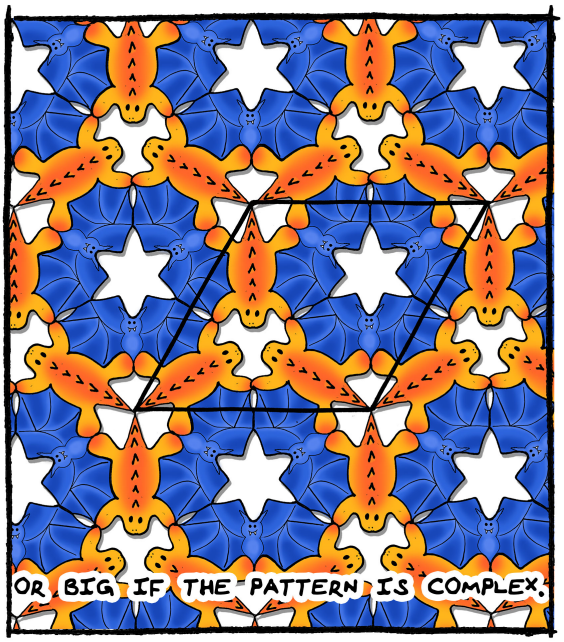

ONE FACTOR THAT CONTRIBUTES TO HOW COMPLEX OUR ATOMIC PATTERN WILL BE IS THE SIZE OF THE ATOMS. ATOMIC SIZE IS GOVERNED BY AN ELEMENT'S SPOT ON THE PERIODIC TABLE.

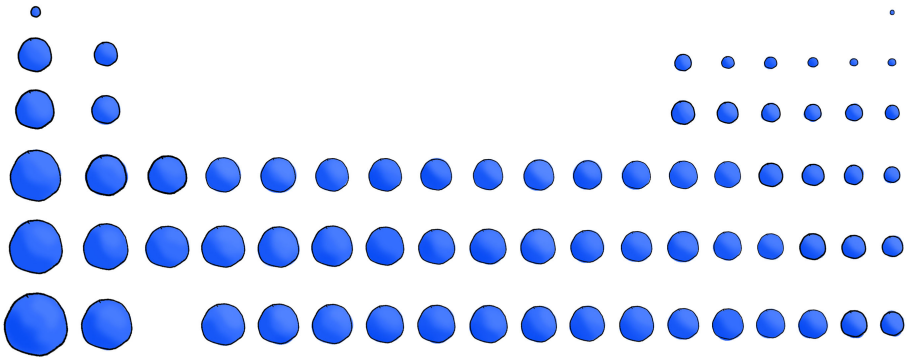

IT MAKES INTUITIVE SENSE THAT WHEN YOU HAVE DIFFERENT SIZE SPHERES PACKING TOGETHER THINGS WILL GET INTERESTING.

CONSIDER MIXING TANGERINES WITH YOUR ORANGES.

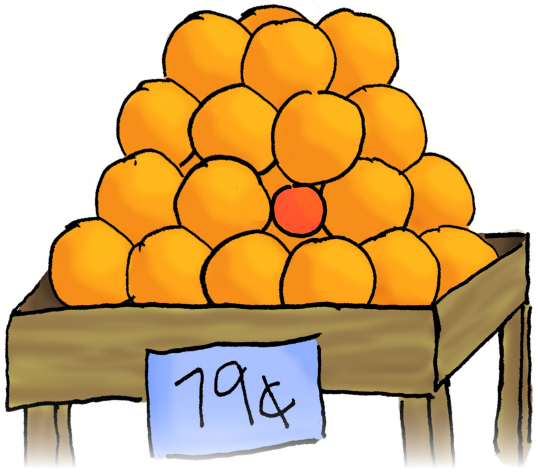

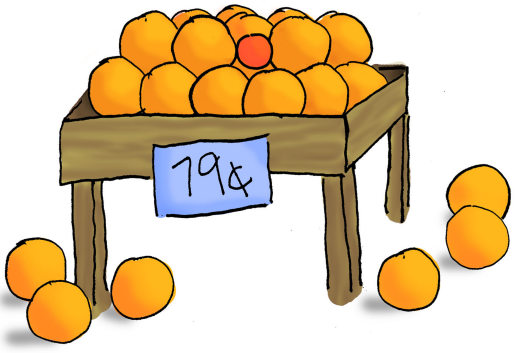

SIZE AND STRUCTURE HAVE A STRONG RELATIONSHIP, IN CITRUS AND IN SCIENCE.

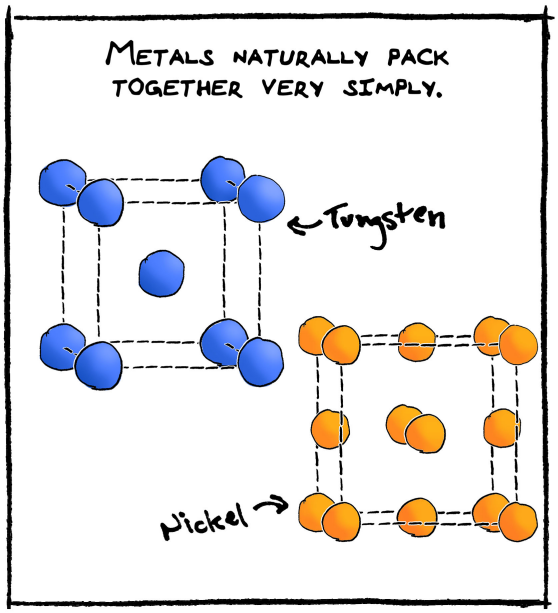
METALS NATURALLY PACK TOGETHER VERY SIMPLY.
Tungsten
Nickel

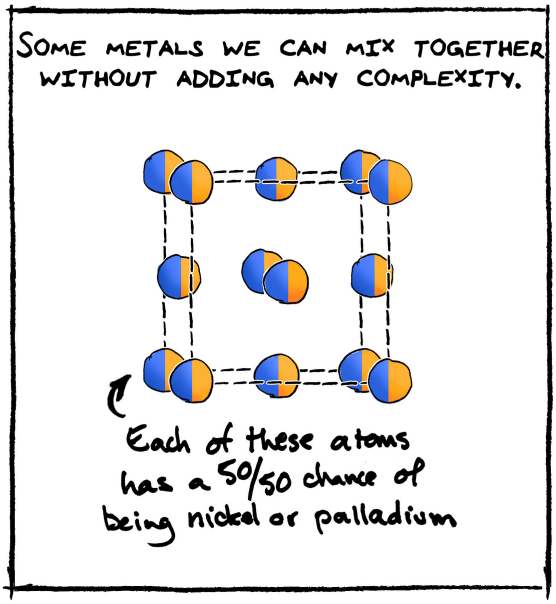
SOME METALS WE CAN MIX TOGETHER WITHOUT ADDING ANY COMPLEXITY.
Each of these atoms has a 50/50 chance of being nickel or palladium

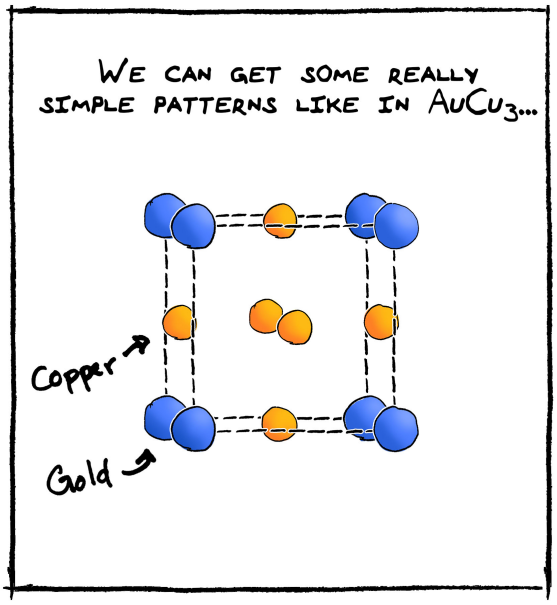
WE CAN GET SOME REALLY SIMPLE PATTERNS LIKE IN $AuCu_3$...
Copper
Gold

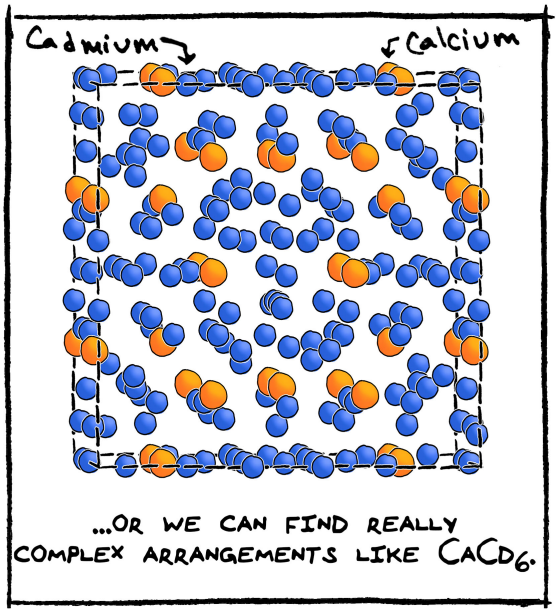
Cadmium
Calcium
...OR WE CAN FIND REALLY COMPLEX ARRANGEMENTS LIKE $CaCD_6$.

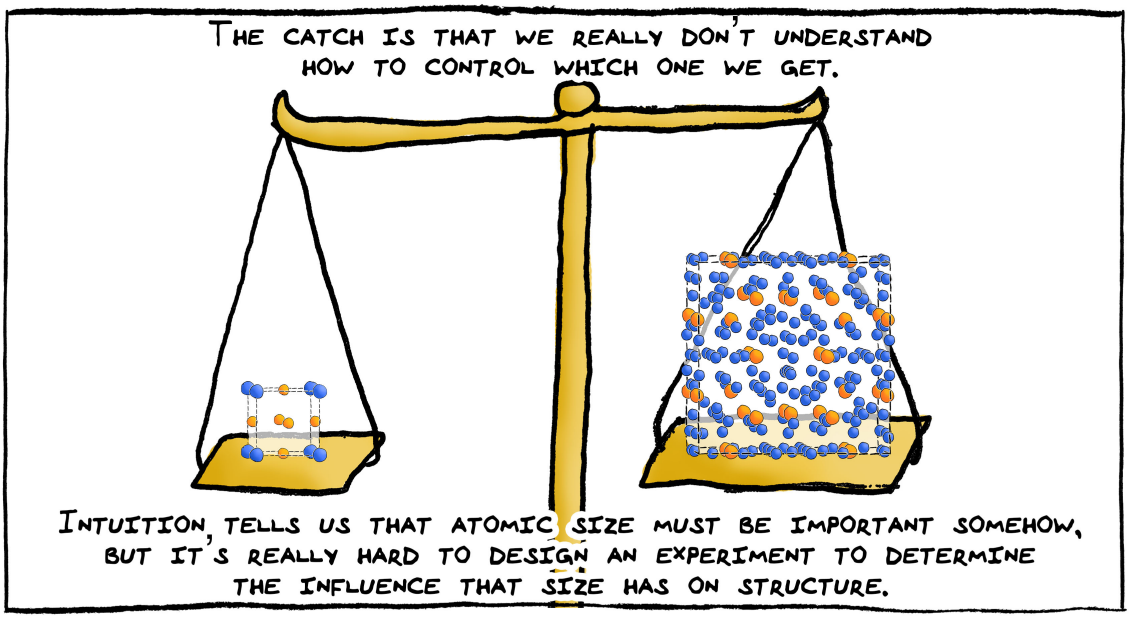
THE CATCH IS THAT WE REALLY DON'T UNDERSTAND HOW TO CONTROL WHICH ONE WE GET.
INTUITION, TELLS US THAT ATOMIC SIZE MUST BE IMPORTANT SOMEHOW, BUT IT'S REALLY HARD TO DESIGN AN EXPERIMENT TO DETERMINE THE INFLUENCE THAT SIZE HAS ON STRUCTURE.

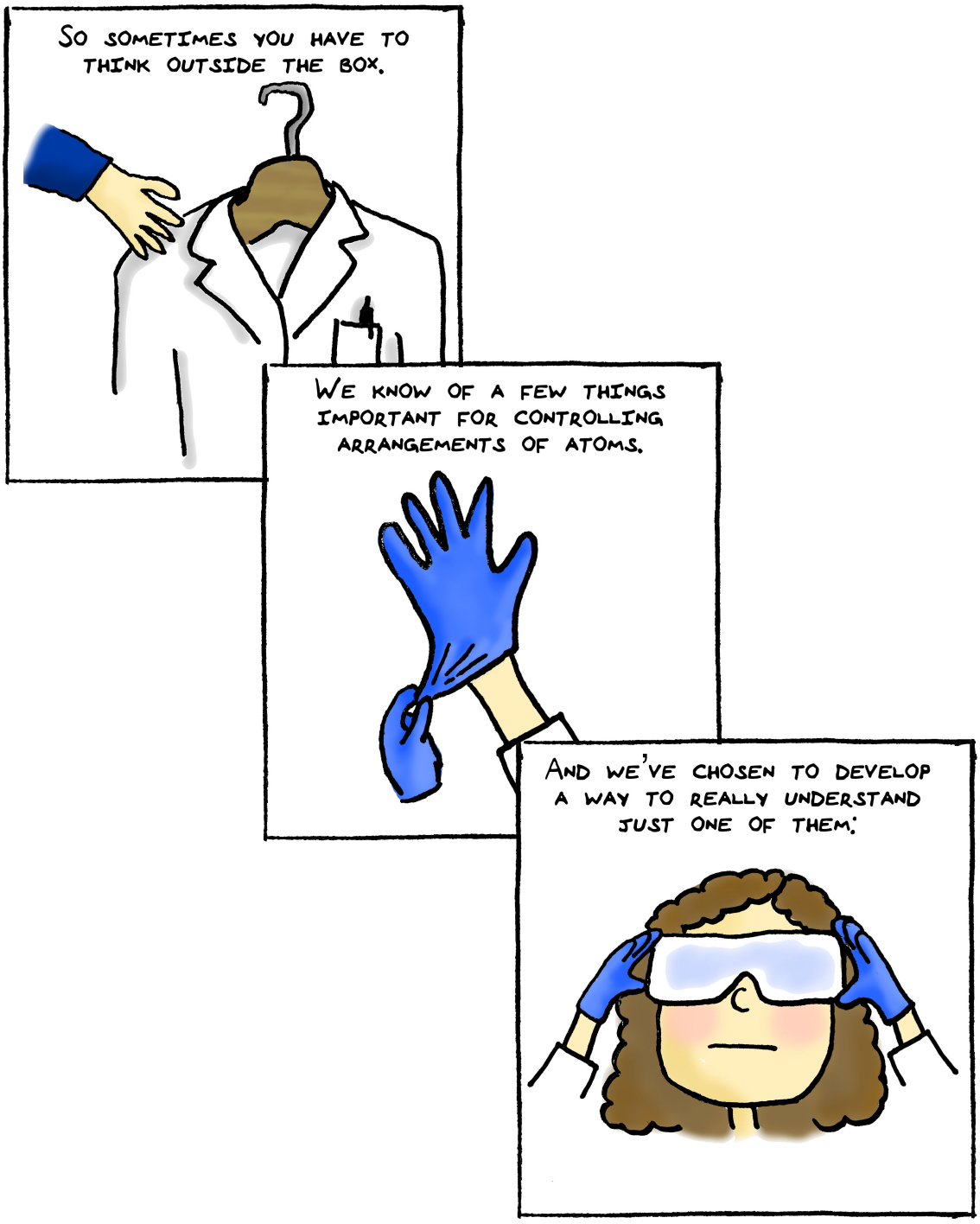
So sometimes you have to think outside the box.
We know of a few things important for controlling arrangements of atoms.
And we've chosen to develop a way to really understand just one of them:
Size.

FOR PEOPLE, WE KNOW THIS BECAUSE TAKING A NAP FEELS SO GOOD.
FOR BONDS, WE KNOW THIS BECAUSE WE
CAN CALCULATE A BONDING POTENTIAL.

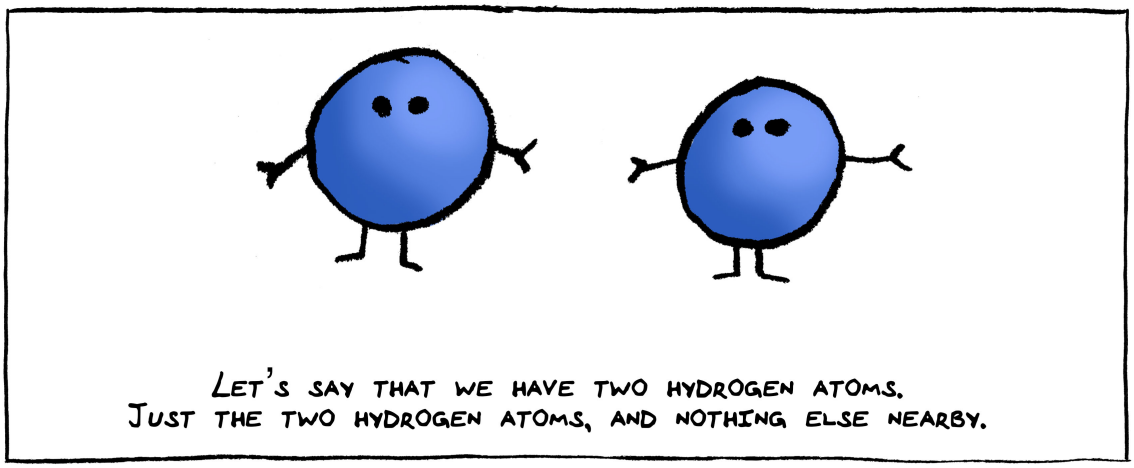

THE BONDING POTENTIAL TELLS YOU HOW MUCH THE HYDROGENS
BENEFIT FROM BEING NEAR ONE ANOTHER: FROM CHEMICALLY BONDING.

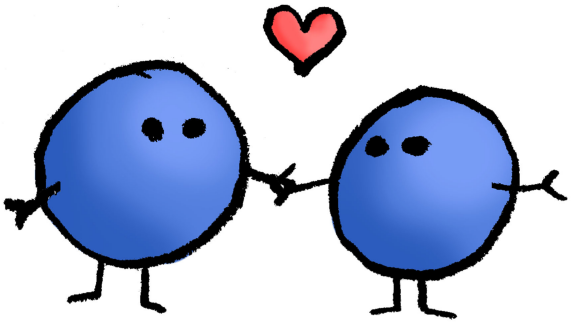

WE CAN REPRESENT THIS POTENTIAL AS A GRAPH OF ENERGY VERSUS THE DISTANCE BETWEEN THE ATOMS. AND EVERYTHING SEEKS THE LOWEST ENERGY POSSIBLE.

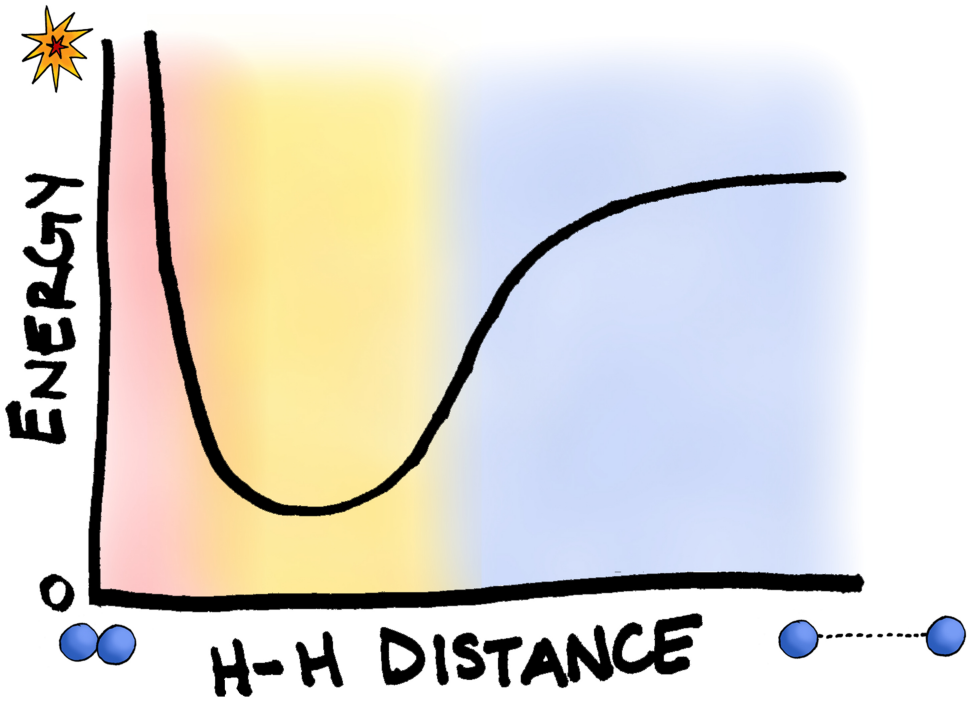

THIS GRAPH IS BEST UNDERSTOOD IN THREE PARTS:

TOO CLOSE.

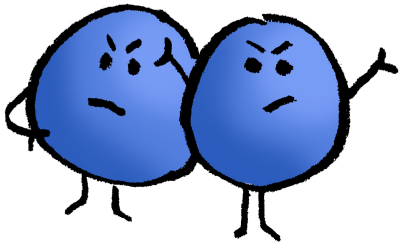

THE NUCLEI START TO FEEL EACH OTHER'S POSITIVE CHARGE TOO MUCH, AND ENERGY SKY ROCKETS.

WHAT OTHER HYDROGEN?

TOO FAR AWAY AND THE ATOMS DON'T NOTICE ONE ANOTHER

GOLDILOCKS.

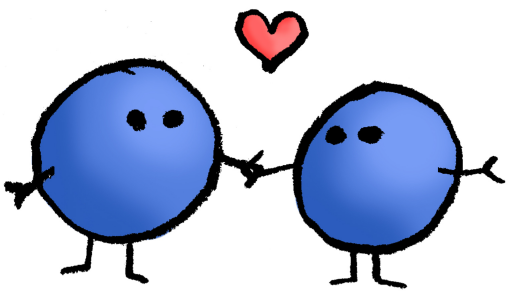

IN A RANGE OF BONDING DISTANCES, THE ENERGY PLUMMETS AS THE ATOMS FAVORABLY BOND.

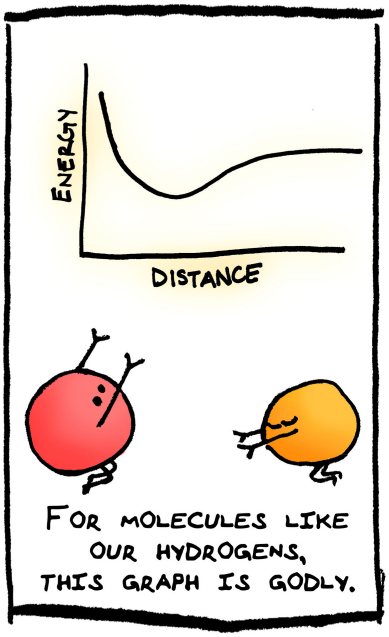
ENERGY
DISTANCE
FOR MOLECULES LIKE OUR HYDROGENS, THIS GRAPH IS GODLY.

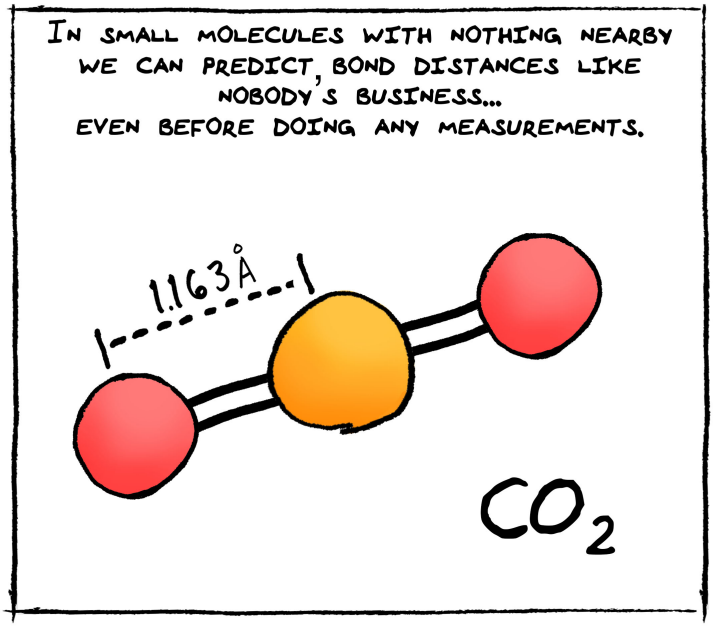
IN SMALL MOLECULES WITH NOTHING NEARBY WE CAN PREDICT BOND DISTANCES LIKE NOBODY'S BUSINESS...
EVEN BEFORE DOING ANY MEASUREMENTS.
1.163Å
CO_2

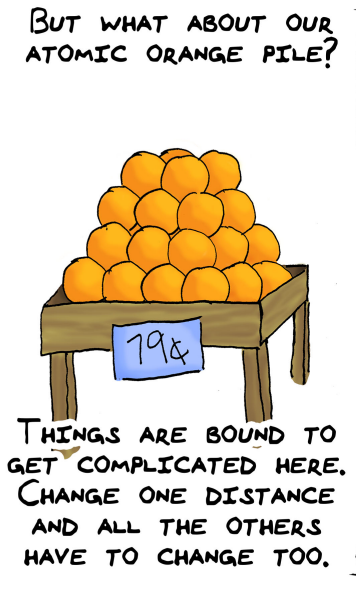
BUT WHAT ABOUT OUR ATOMIC ORANGE PILE?
79¢
THINGS ARE BOUND TO GET COMPLICATED HERE. CHANGE ONE DISTANCE AND ALL THE OTHERS HAVE TO CHANGE TOO.

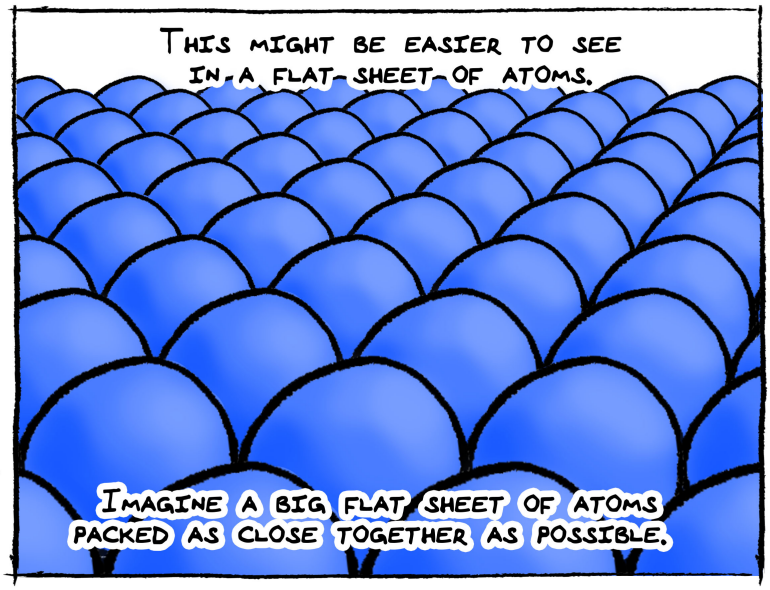
THIS MIGHT BE EASIER TO SEE IN A FLAT SHEET OF ATOMS.
IMAGINE A BIG FLAT SHEET OF ATOMS PACKED AS CLOSE TOGETHER AS POSSIBLE.

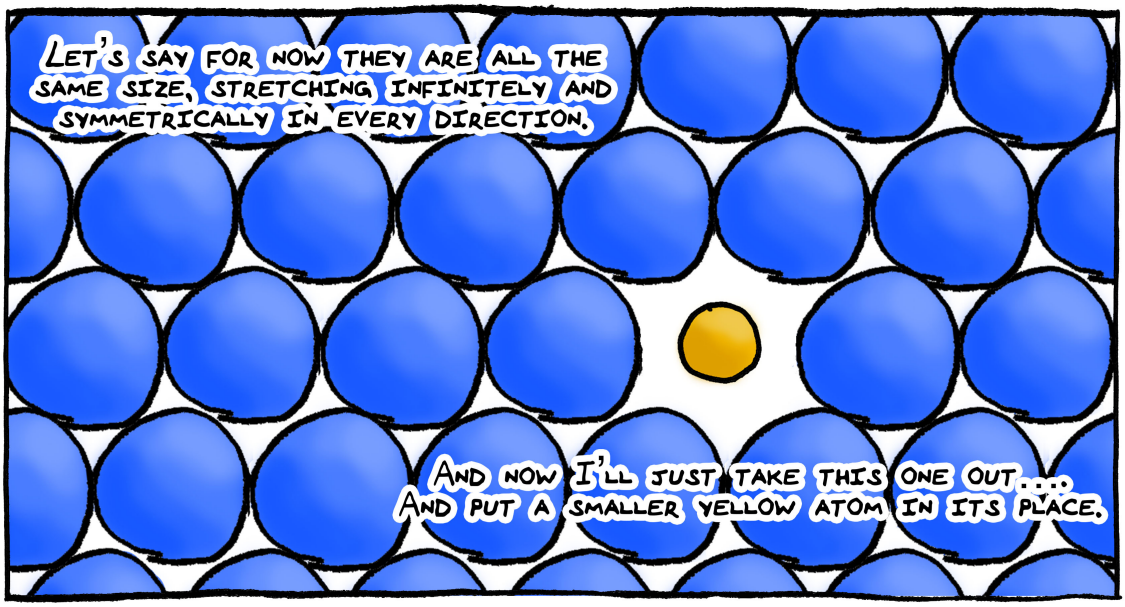
LET'S SAY FOR NOW THEY ARE ALL THE SAME SIZE, STRETCHING INFINITELY AND SYMMETRICALLY IN EVERY DIRECTION.
AND NOW I'LL JUST TAKE THIS ONE OUT... AND PUT A SMALLER YELLOW ATOM IN ITS PLACE.

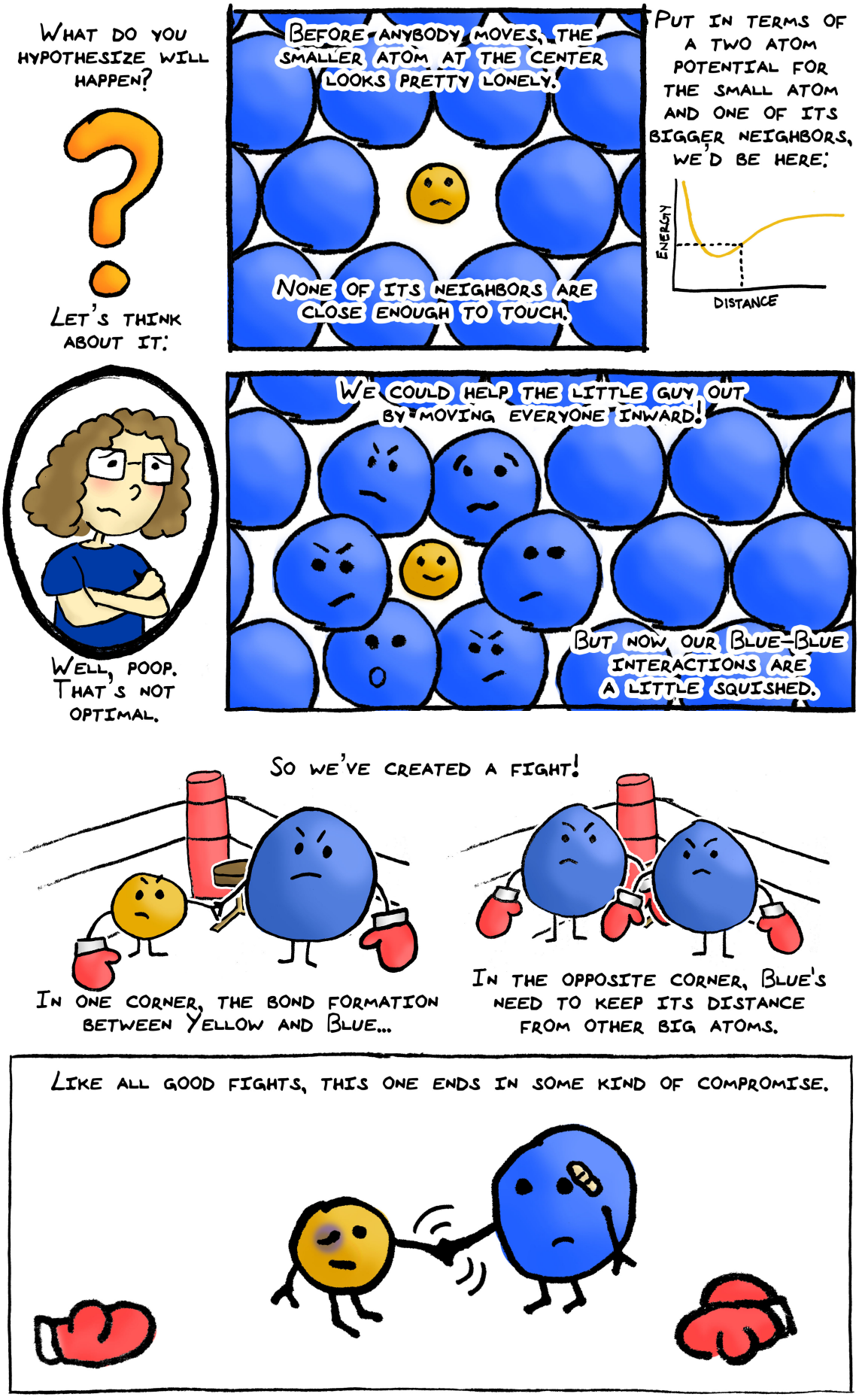
What do you hypothesize will happen?
Let's think about it:
Before anybody moves, the smaller atom at the center looks pretty lonely.
None of its neighbors are close enough to touch.
Put in terms of a two atom potential for the small atom and one of its bigger neighbors, we'd be here:
Energy
Distance
We could help the little guy out by moving everyone inward!
But now our Blue-Blue interactions are a little squished.
Well, poop. That's not optimal.
So we've created a fight!
In one corner, the bond formation between Yellow and Blue...
In the opposite corner, Blue's need to keep its distance from other big atoms.
Like all good fights, this one ends in some kind of compromise.

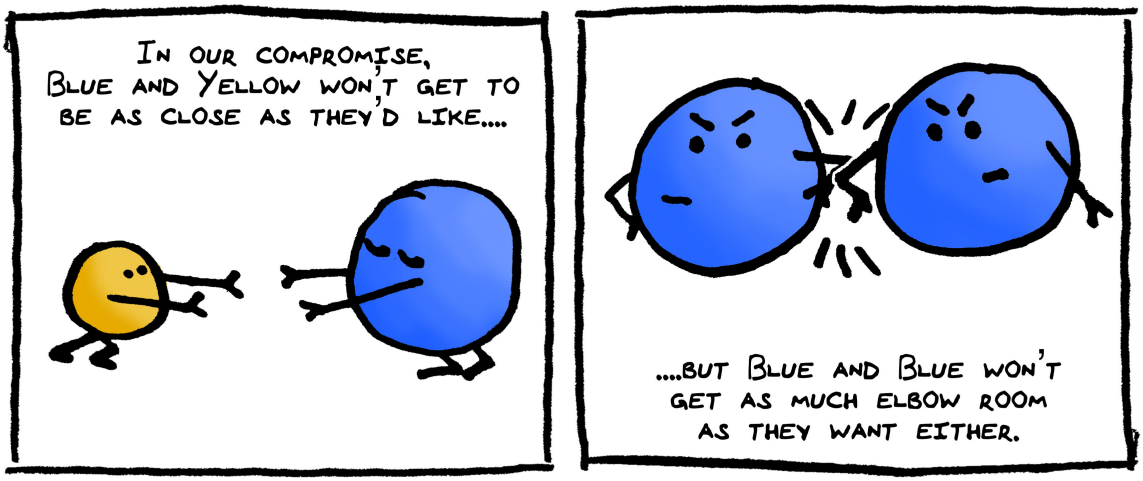

What does this compormise mean on our energy–distance graphs?

At the black line, after we move everyone inwards a little, neither curve is at its lowest point. Both interactions aren't optimal, but this is the best case scenario, energetically speaking.

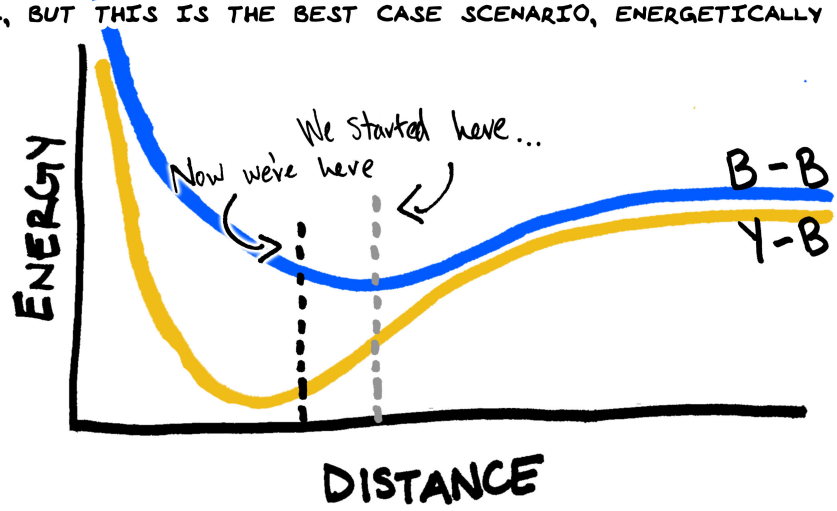

Being held at a non-optimal energy creates strain. Let's take a closer look at what it means to be strained in our example:

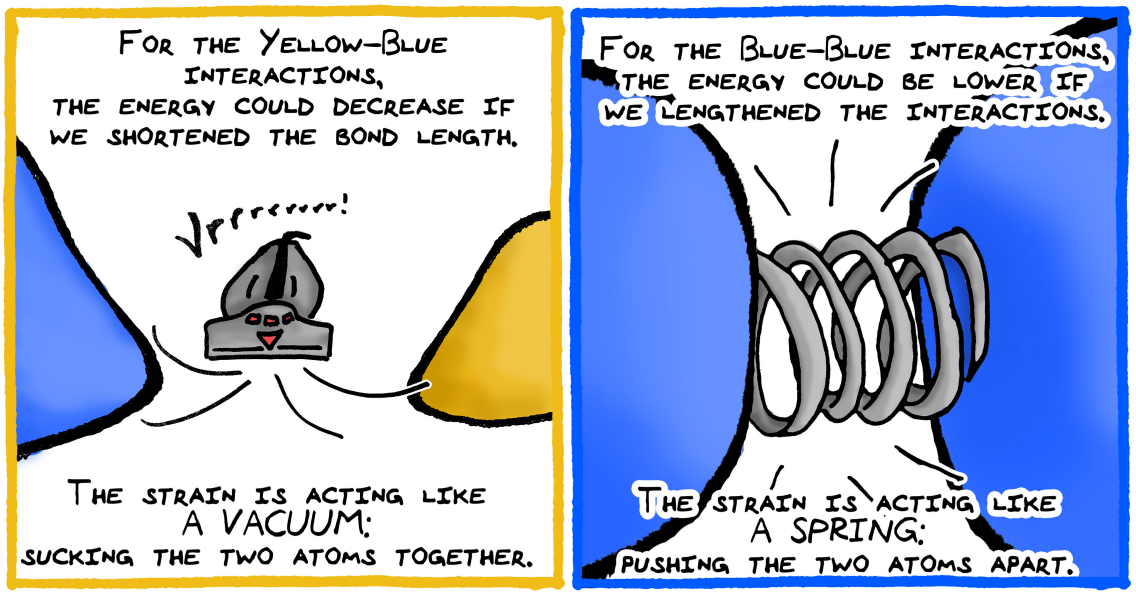

THE QUICK-AND-DIRTY WAY TO TELL IF WE'VE GOT A VACUUM OR A SPRING IS TO LOOK AT THE SLOPE OF THE LINE.

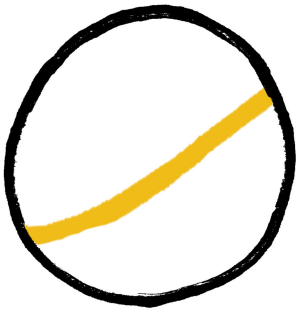

IF THE LINE TILTS THIS WAY, WE'D NEED TO SHORTEN THE BOND.

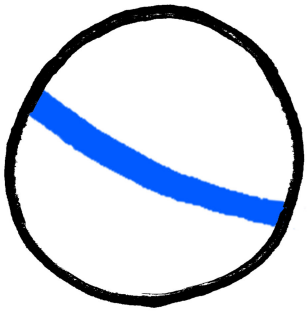

IF THE LINE TILTS THIS WAY WE'D NEED TO LENGTHEN IT.

THE SLOPE OF THE LINE TANGENT TO THE CURVE TELLS US THE SIGN OF THE STRAIN AND THE DEGREE OF TILT TELLS US HOW STRONG IT IS.

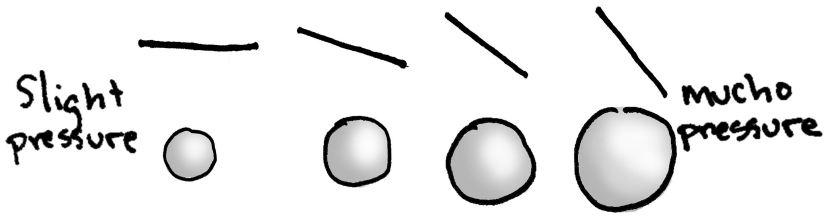

WE'VE DECIDED TO CALL THE STRAIN CHEMICAL PRESSURE, AND WE DRAW IT LIKE THIS:

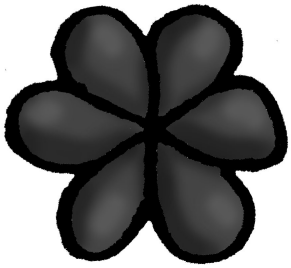

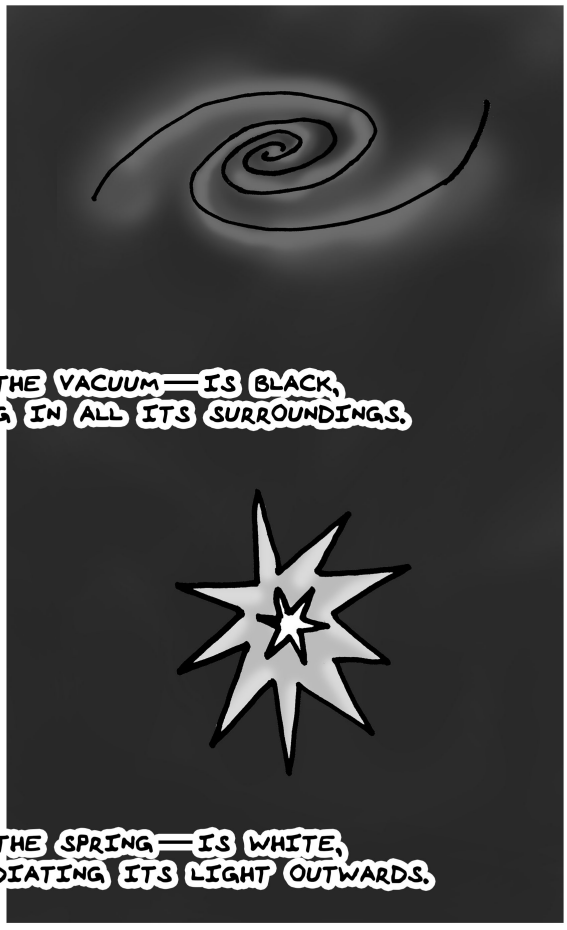

NEGATIVE PRESSURE — THE VACUUM — IS BLACK, LIKE A BLACK HOLE, SUCKING IN ALL ITS SURROUNDINGS.

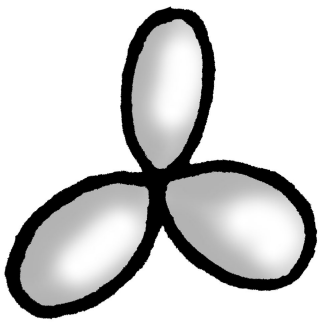

POSITIVE PRESSURE — THE SPRING — IS WHITE, LIKE A WHITE HOT STAR, RADIATING ITS LIGHT OUTWARDS.

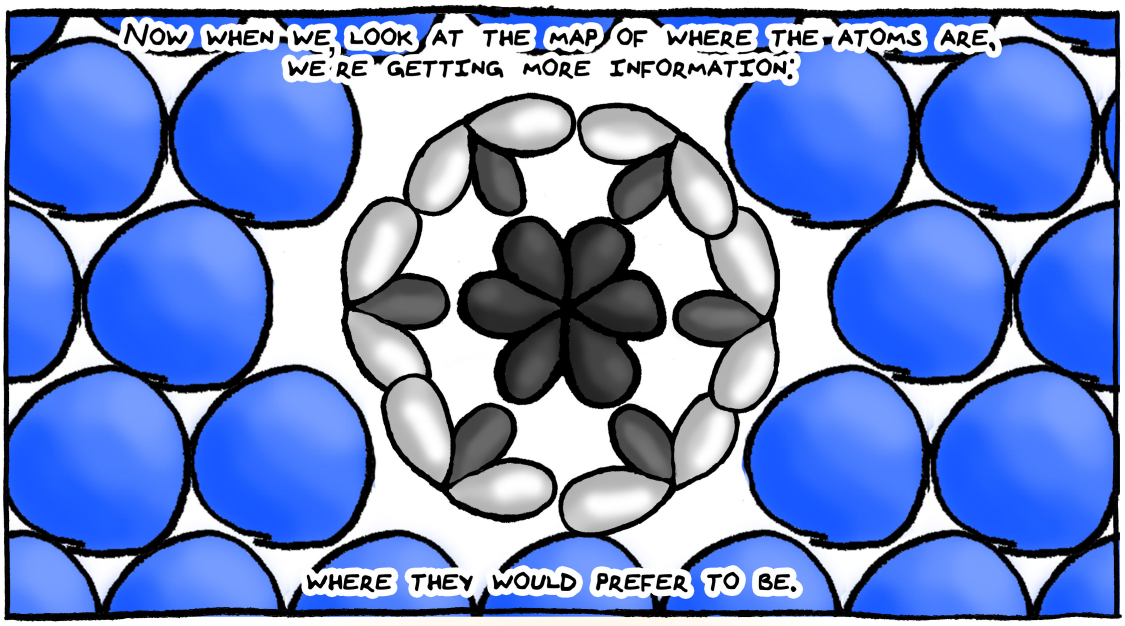

BUT WHAT ABOUT THE ORANGES? CAN WE EXTEND THIS IDEA INTO 3-D?

YES, YES WE CAN.

So much is possible with computers.

They let you watch cat videos, listen to podcasts, and fight battles with lasers in outer space.

Turns out they are pretty helpful when it comes to chemistry too.

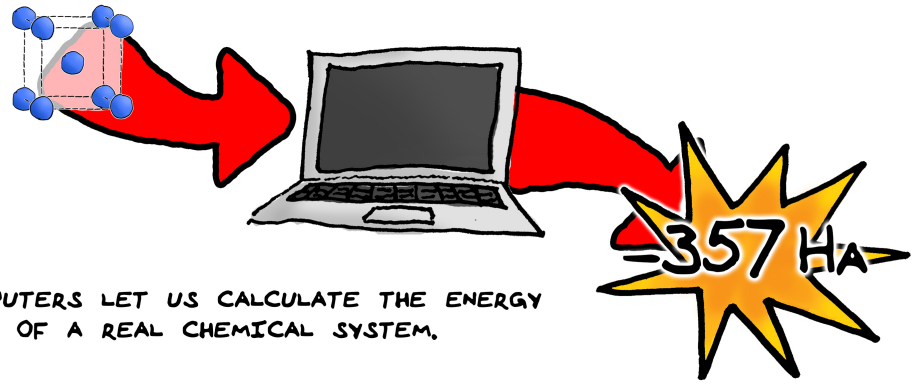

Computers let us calculate the energy of a real chemical system.

This gives us the data for our all-important energy-distance diagram...

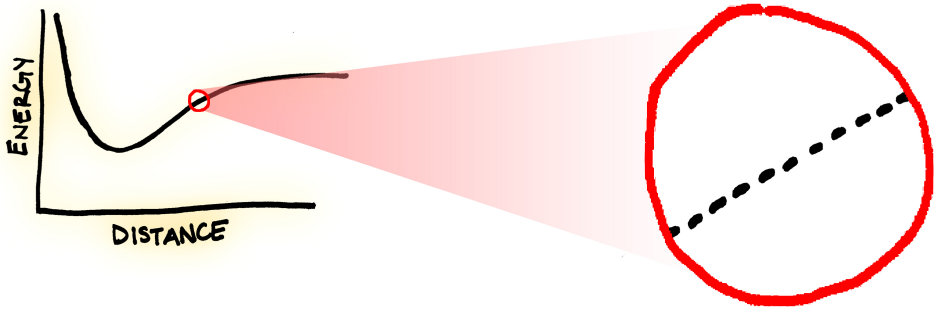

But here's the bad news:

They do it one point at a time.

EACH POINT NEEDS BETWEEN A FEW HOURS AND A FEW DAYS FOR THE CALCULATION TO FINISH.

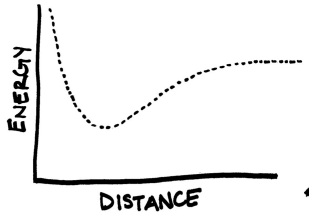

...BUT REMEMBER, WE DON'T NEED THE WHOLE CURVE.

SINCE THE SLOPE OF THE LINE TELLS US EVERYTHING WE NEED TO KNOW,

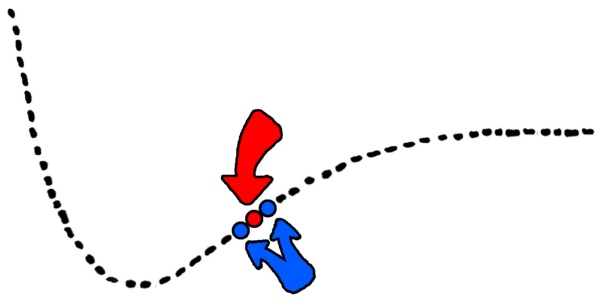

ALL THERE IS TO DO IS CALCULATE THE ENERGY AT TWO POINTS, ONE ON EITHER SIDE OF THE ONE WE CARE ABOUT.

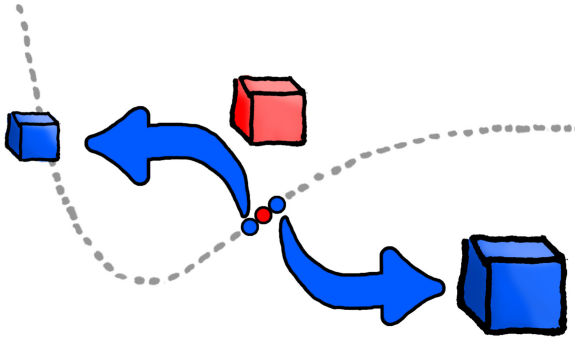

PRACTICALLY SPEAKING, THIS MEANS WE ARE GOING TO MAKE A SMALL VERSION OF THE UNIT CELL THAT ARTIFICIALLY SHORTENS EVERYTHING TO GET THE ENERGY AT POINT #1, AND THEN A BIG VERSION THAT LENGTHENS EVERYTHING TO GET THE ENERGY AT POINT #2.

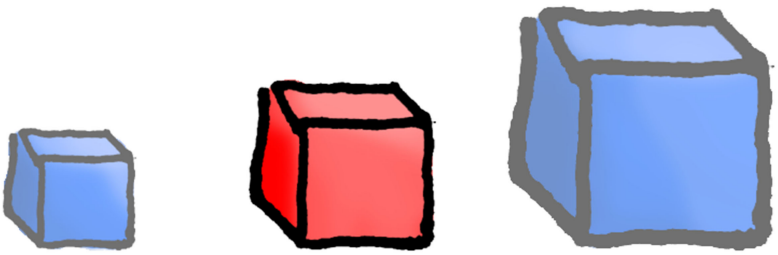

NOTE: THE SMALL VERSION AND THE BIG VERSION DON'T ACTUALLY EXIST. WE CAN ONLY MAKE THEM BECAUSE WE ARE INSIDE A COMPUTER.

Once we have the energies for Big Version and Small Version, all we need to do is draw a line and determine if our leftover tension is a vacuum or a spring.

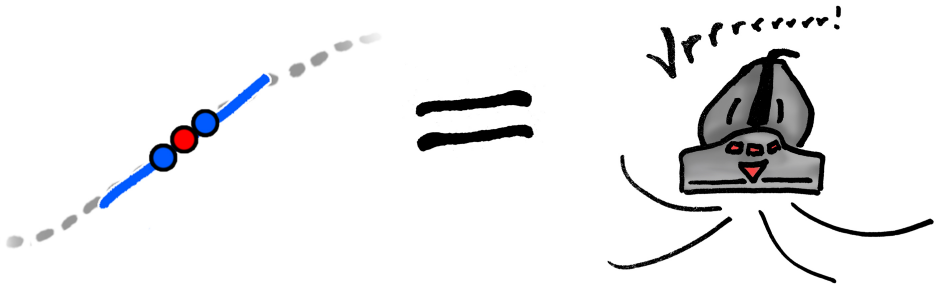

Up until this point, the 3-D seems a lot like our 2-D example. Here's the difference:

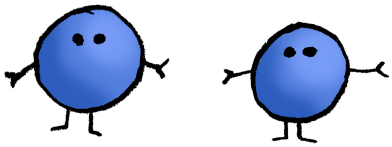

In 2-D, it was enough to look at one atom pair at a time.

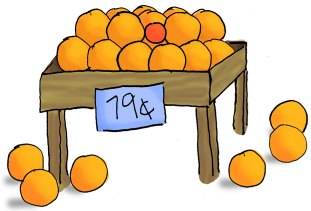

In 3-D, we anticipate that every interaction will influence all of the others, in every direction.

In 3-D, we need to make an energy – distance diagram for every point in the structure in the Big Version and the Small Version, because we can't move just one atom. Now for the good news:

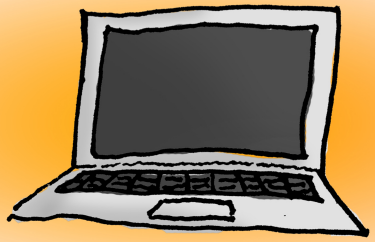

The computer gives us an energy for every point in the structure at the same time. Thanks, computer!

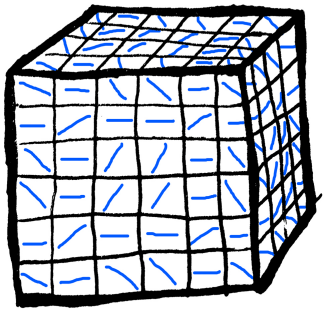

We can draw that line between Big Version Energy and Small Version Energy for every one of these points simultaneously.

And we end up with an array of vacuums and springs of varying intensities.

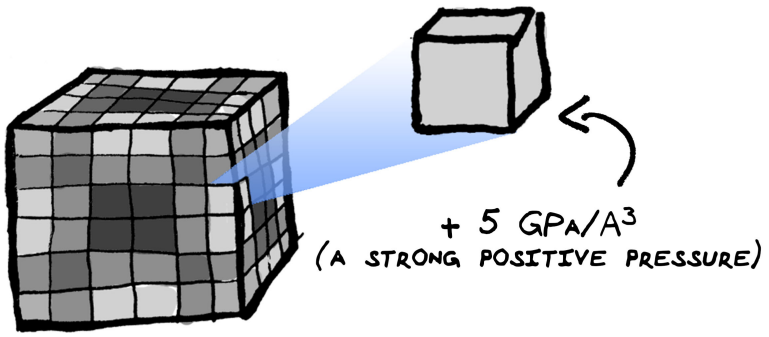

But this just gives us a map of where pressure is high and low. How can we turn this into a picture that emphasizes how the atoms might react to the pressure?

The answer requires some fancy scissors.

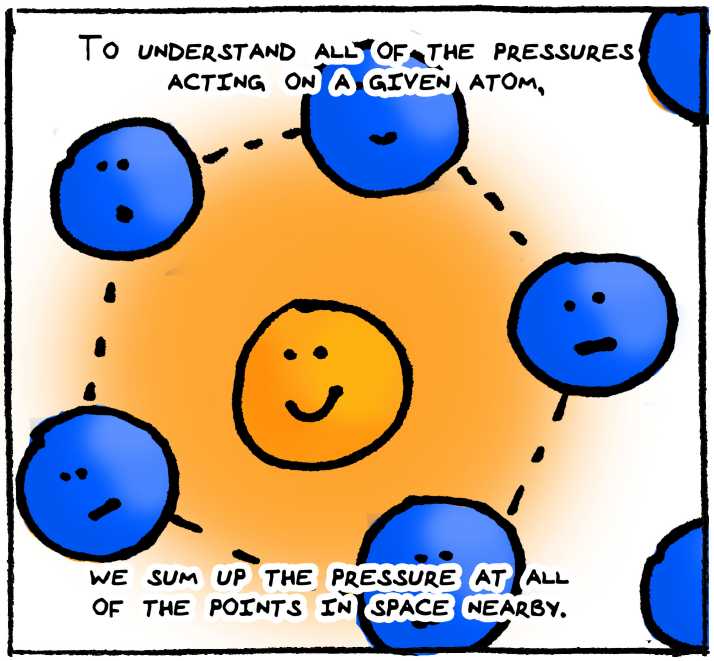

It turns out that the way we cut the map into separate atoms has to be pretty involved.

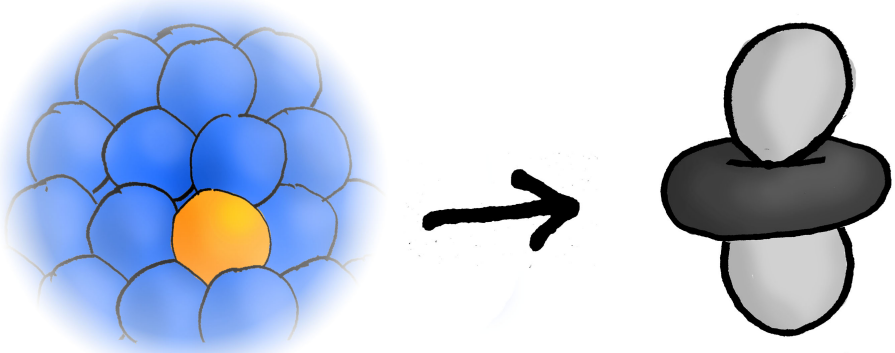

But simply put, we take all of the points within the atom's reach, turn it into an interpretable 3-D object that corresponds to the sign and intensity of the pressures in all directions.

LET'S TAKE A QUICK 2-D EXAMPLE TO SEE THE CONCEPT:

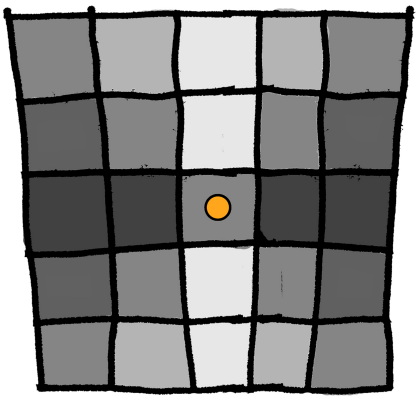

THIS MAP HAS POSITIVE PRESSURES ABOVE AND BELOW THE ATOM AT THE CENTER, BUT OFF TO THE LEFT AND RIGHT, WE SEE DARK REGIONS.

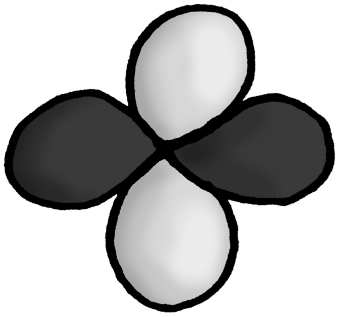

THAT MAP WOULD SUM UP TO THIS OBJECT – A CLOVER THAT ALTERNATES BLACK AND WHITE PETALS.

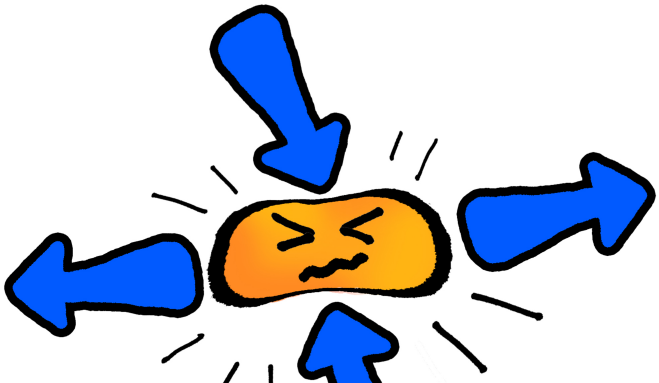

THIS CLOVER SHAPE IS INTERPRETED AS THE ATOM BEING SQUISHED VERTICALLY, BUT IT WOULD LIKE TO STRETCH IN THE HORIZONTAL DIRECTION. IF WE MOVED TO THREE DIMENSIONS, WE WOULD HAVE INFORMATION ABOUT PRESSURE ABOVE AND BELOW THE SURFACE OF THIS PAGE TOO.

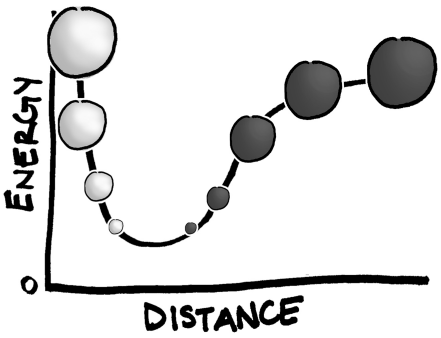

UP UNTIL THIS POINT, WE'VE LOOKED AT THE INNER WORKINGS OF CHEMICAL PRESSURE, A TOOL THAT WE CAN USE TO UNDERSTAND HOW THE SIZE OF AN ATOM CAN INFLUENCE A 3-D CRYSTAL STRUCTURE.

IT'S A PRETTY POWERFUL TOOL. WE'VE BEEN ABLE TO USE IT TO EXPLAIN THE FORMATION OF MANY COMPLEX ATOMIC ARRANGEMENTS.

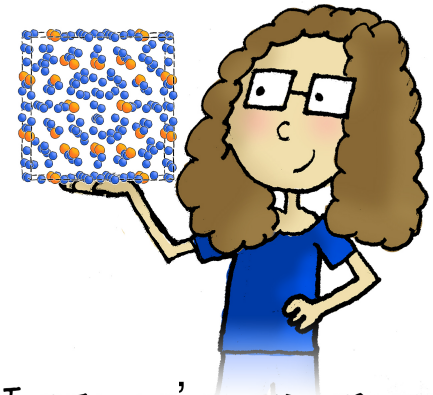

I THINK WE'RE READY TO SEE WHAT THIS PUPPY CAN DO.

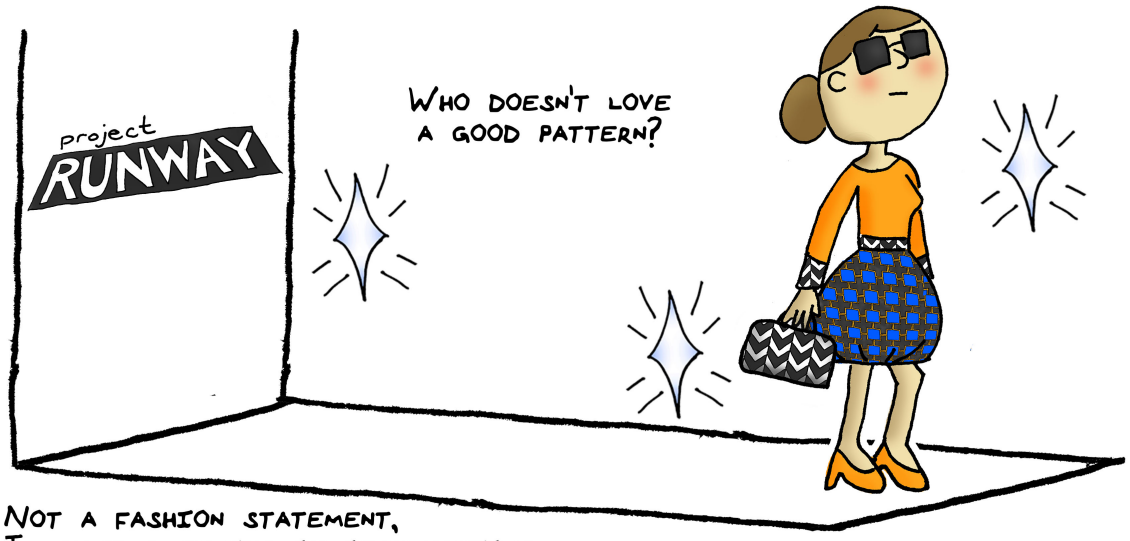

NOT A FASHION STATEMENT,
I MEANT A SERIES OF OBSERVATIONS
THAT WE THINK IS MORE THAN A COINCIDENCE.

IN THIS CASE, WE FOUND A PATTERN IN WHICH
DIFFERENT COMPOUNDS TAKE ON ONE PARTICULAR STRUCTURE:

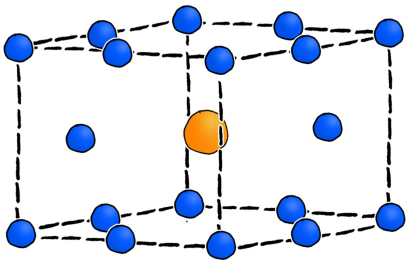

← LOTS OF INTERMETALLICS
MAKE THIS STRUCTURE TYPE.
IT'S ALL THE RAGE THIS SPRING.

WE CALL IT "THE $CaCu_5$ TYPE", WHICH DOESN'T MEAN THAT IT ABSOLUTELY HAS TO CONTAIN CALCIUM OR COPPER, IT JUST MEANS THAT THE FIRST TIME WE SAW THIS STRUCTURE, THAT'S WHAT WE HAPPENED TO BE LOOKING AT. THE ESSENCE OF THE $CaCu_5$ TYPE IS THE SPECIFIC ATOMIC POSITIONING.

THIS STRUCTURE IS MADE UP OF TWO FLAT LAYERS, AND THEY ALTERNATE:

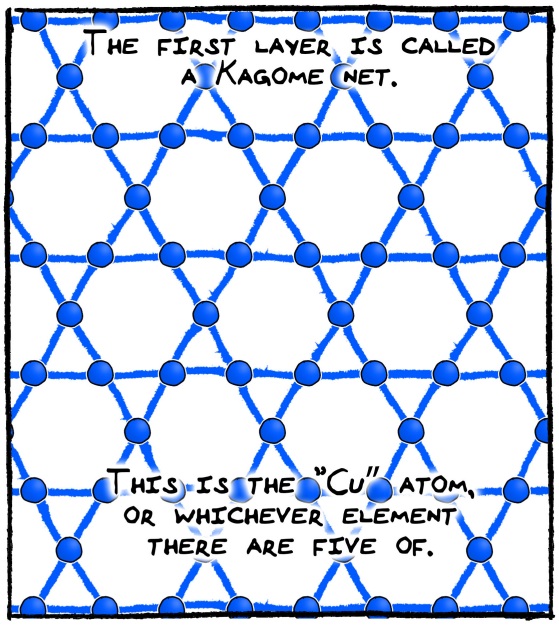

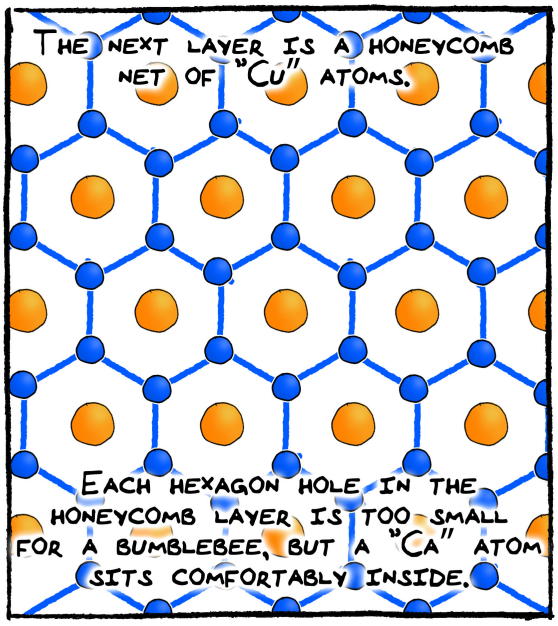

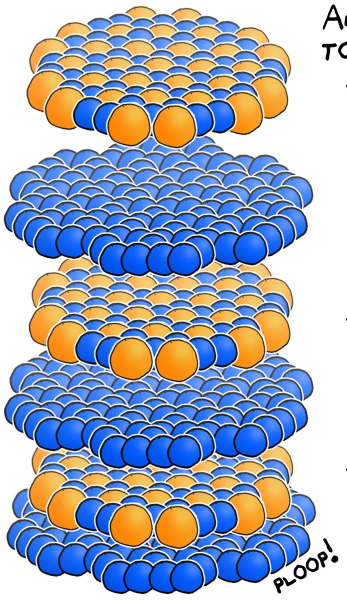

AND THE LAYERS STACK TOGETHER, ALTERNATING STUFFED HONEYCOMB,

KAGOME,

STUFFED HONEYCOMB,

KAGOME,

STUFFED HONEYCOMB,

KAGOME,

HONEYCOMB... UNTIL...INFINITY.

IF WE LOOK AT THIS FROM CA'S PERSPECTIVE, WHAT WOULD WE SEE?

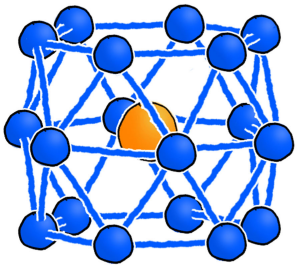

THAT ATOM GETS A NICE LITTLE BASKET TO SIT IN: HEXAGON ABOVE, HEXAGON BELOW, AND A NICE HUG FROM A HEXAGON AROUND THE CENTER TOO.

SO WHAT'S ALL THIS TALK ABOUT A PATTERN? LET'S CHECK OUT THE PERIODIC TABLE:

1 H																	2 He
3 Li	4 Be											5 B	6 C	7 N	8 O	9 F	10 Ne
11 Na	12 Mg											13 Al	14 Si	15 P	16 S	17 Cl	18 Ar
19 K	20 Ca	21 Sc	22 Ti	23 V	24 Cr	25 Mn	26 Fe	27 Co	28 Ni	29 Cu	30 Zn	31 Ga	32 Ge	33 As	34 Se	35 Br	36 Kr
37 Rb	38 Sr	39 Y	40 Zr	41 Nb	42 Mo	43 Tc	44 Ru	45 Rh	46 Pd	47 Ag	48 Cd	49 In	50 Sn	51 Sb	52 Te	53 I	54 Xe
55 Cs	56 Ba	*	72 Hf	73 Ta	74 W	75 Re	76 Os	77 Ir	78 Pt	79 Au	80 Hg	81 Tl	82 Pb	83 Bi	84 Po	85 At	86 Rn
87 Fr	88 Ra	**	104 Rf	105 Db	106 Sg	107 Bh	108 Hs	109 Mt	110 Ds	111 Rg	112 Cn	113 Uut	114 Fl	115 Uup	116 Lv	117 Uus	118 Uuo

*	57 La	58 Ce	59 Pr	60 Nd	61 Pm	62 Sm	63 Eu	64 Gd	65 Tb	66 Dy	67 Ho	68 Er	69 Tm	70 Yb	71 Lu
**	89 Ac	90 Th	91 Pa	92 U	93 Np	94 Pu	95 Am	96 Cu	97 Bk	98 Cf	99 Es	100 Fm	101 Md	102 No	103 Lr

IF WE KEEP THE CALCIUM ATOM A CALCIUM ATOM, THEN ALL OF THESE BLUE METALS STANDING IN FOR "CU" WOULD GIVE US THE $CaCu_5$ TYPE. FOR EXAMPLE, $CaNi_5$ MAKES THIS STRUCTURE, BUT $CaAg_5$ DOESN'T.

WHAT DOES THIS MEAN?

WE'RE SEEING THE VERSATILITY OF THIS STRUCTURE TYPE.

THERE'S SOMETHING ABOUT ALL FIVE OF THESE METALS THAT JUST WORKS WHEN WE COMBINE THEM WITH CALCIUM IN A 5:1 RATIO.

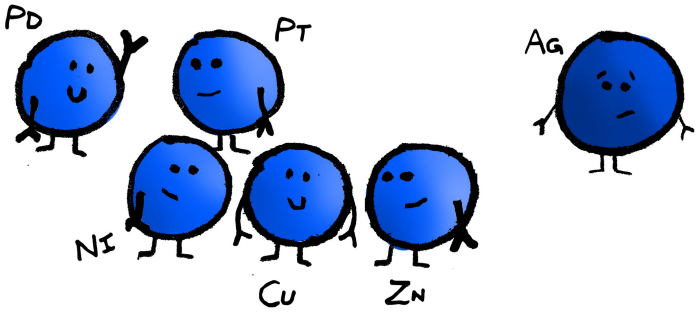

COULD THAT SOMETHING BE...SIZE?

Let's look at what a chemical pressure plot of $CaPd_5$ has to say.

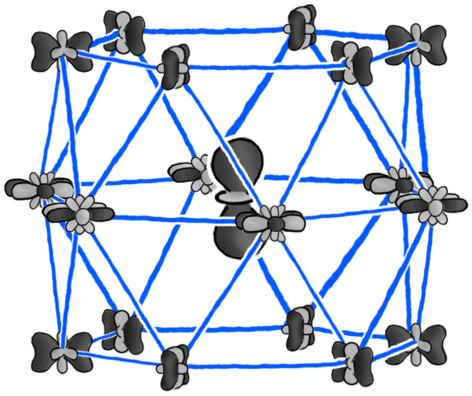

The large black peanut shape in the center implies the calcium is experiencing negative pressures, and it wants to be closer to the atoms in the Kagome nets above and below.

The pressures between Ca and the honeycomb net are positive, indicated by the white doughnut shape in the middle.

We can tell this positive pressure is not as strong as the negative pressure: The size of the lobe is proportional to the magnitude of CP.

Calcium experiences an overall negative CP.

With a black hole at the center of the basket, why doesn't it implode?

Take a close look above. The negative pressure at the center is countered by a positive pressure between the palladium atoms of different layers.

The palladium Kagome rings can't even contract around the calcium because those Pd–Pd contacts are already too close.

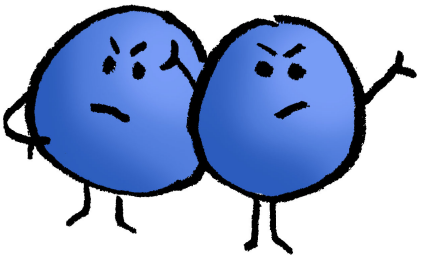

We've got another fight! But that's not a bad thing.

We know that this compound actually exists in the real world, and everything will inherently have a little bit of strain in it.

This strain is only meaningful when we compare it to the strain in similar compounds.

(This is where it gets really fun.)

KNOWING THAT THE CALCIUM ATOM IS A LITTLE TOO SMALL FOR ITS PALLADIUM BASKET,

WHAT DO YOU THINK, WOULD HAPPEN IF WE PUT LARGER ATOMS IN PLACE OF PALLADIUM?

WE ALREADY KNOW THE ATOMS MAKING UP THE CAGE ARE SQUEEZING TOGETHER AS TIGHTLY AS POSSIBLE.

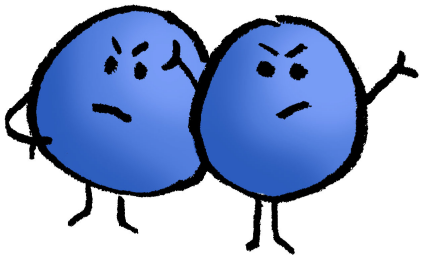

IF WE MAKE THOSE ATOMS BIGGER, WE PREDICT THAT THEY'LL BE EVEN MORE STRESSED OUT!

BUT WHAT EFFECT WILL THAT HAVE ON CALCIUM, WHICH OBVIOUSLY STAYS ITS SAME SIZE?

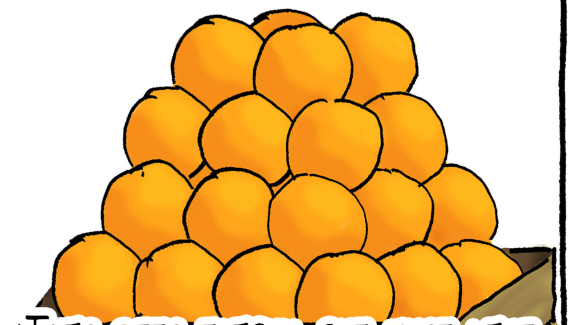

THIS GETS TRICKY, BUT JUST LIKE A STACK OF 18 ORANGES IS BIGGER THAN A STACK OF 18 TANGERINES, IF WE USE LARGER ATOMS, THE CAGE WILL BE BIGGER, MAKING FOR A BIGGER HOLE FOR CALCIUM TO SIT IN.

THEREFORE THE AMOUNT OF EMPTY SPACE BETWEEN SOMETHING LIKE A COUPLE OF BEACH BALLS IS MUCH BIGGER THAN THE EMPTY SPACES BETWEEN OUR DEAR CITRUS FRUITS.

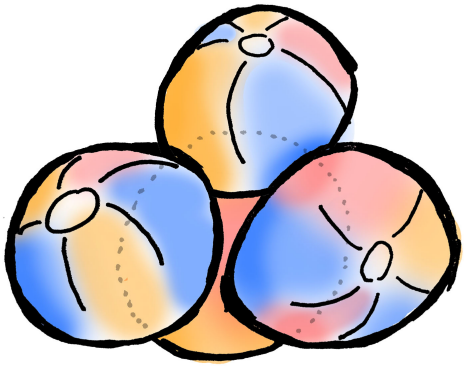

BUT WAIT!

DIDN'T WE SAY WE WANTED A SMALLER HOLE FOR OUR TINY CALCIUM ATOM TO SIT IN?

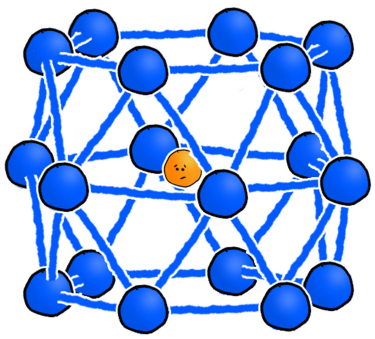

THIS BIGGER CAGE IDEA IS GOING TO RUIN EVERYTHING!

WELL, YES, A SMALLER ATOM WOULD MAKE THIS ONE SITUATION BETTER. BUT WE'RE INTERESTED IN TAKING OUR UNDERSTANDING EVEN FURTHER.

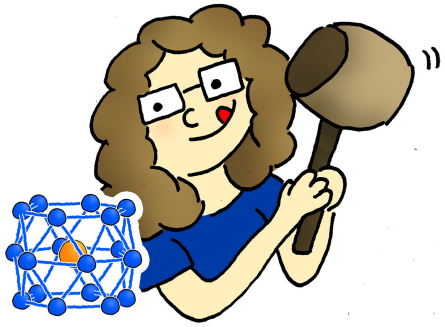

AND SOME THINGS HAVE TO BREAK BEFORE WE CAN TOTALLY UNDERSTAND THEM.

OK LET'S DO THIS, LET'S GET TO THE REAL DATA! HERE WE COMPARE THE FAMILIAR $CaPd_5$ WITH HYPOTHETICAL COMPOUNDS "$CaAg_5$" AND "$CaCd_5$".

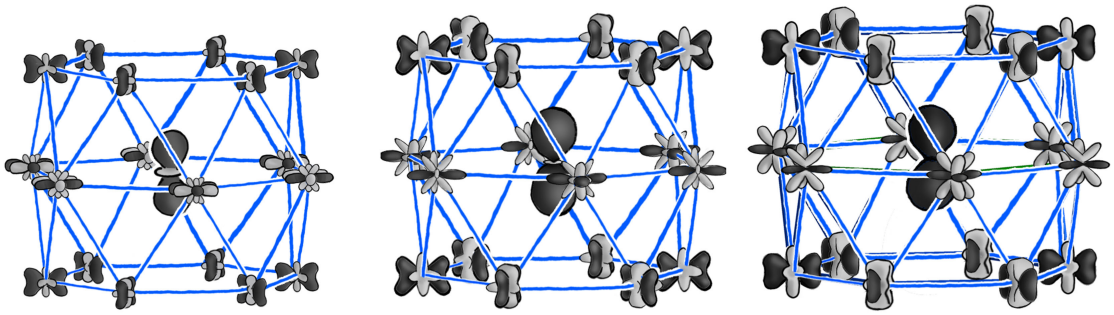

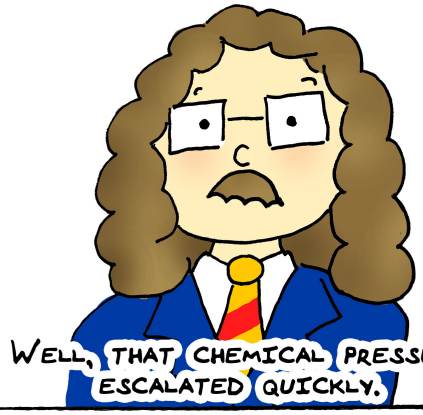

JUST LIKE WE HAD GUESSED, THE BIGGER THE TRANSITION METAL, THE MORE INTENSE THE NEGATIVE PRESSURE IS INSIDE THAT BASKET.

IN THE HYPOTHETICAL "$CaCd_5$", CALCIUM IS EXPERIENCING QUITE THE VACUUM! NO WONDER "$CaCd_5$" HAS NEVER BEEN MADE.

WHAT DO WE OBSERVE INSTEAD?

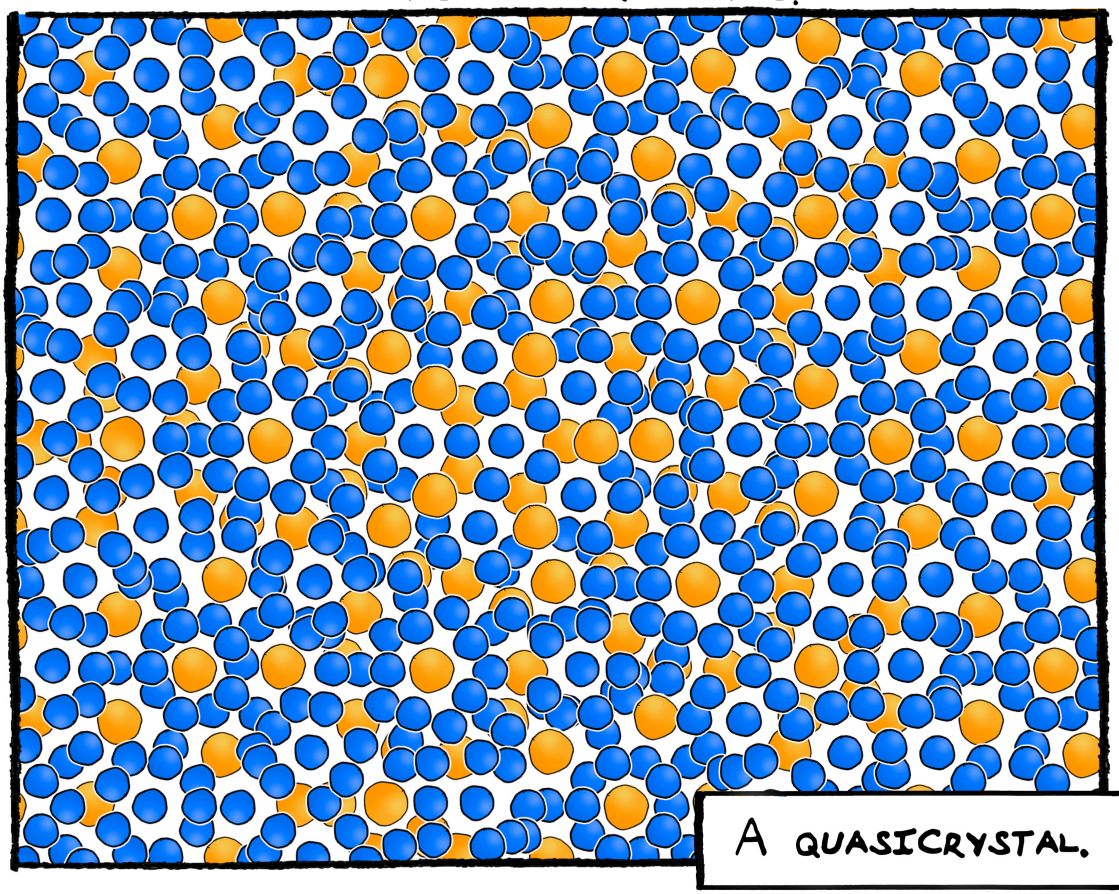

A QUASICRYSTAL.


QUASICRYSTALS ARE THE
REBELS OF THE CRYSTALLINE WORLD
THEY'RE ROTATIONALLY SYMMETRIC, BUT NOT TRANSLATIONALLY SYMMETRIC.
THEY CAN BE PERIODIC IN ONE DIRECTION, BUT NOT PERIODIC IN EVERY DIRECTION.
THEY DIFFRACT, BUT YOU HAVE TO USE MORE THAN 3 DIMENSIONS TO SOLVE THEIR STRUCTURES.
QUASICRYSTALS BREAK ALL THE RULES, AND THEY DON'T GIVE A #@$&.

STUFF THAT BREAKS RULES IS OFTEN THE MOST INTERESTING STUFF TO STUDY, BECAUSE IT LETS YOU REVISE WHAT YOU THOUGHT WAS TRUE AND GET AT WHAT'S REALLY GOING ON.

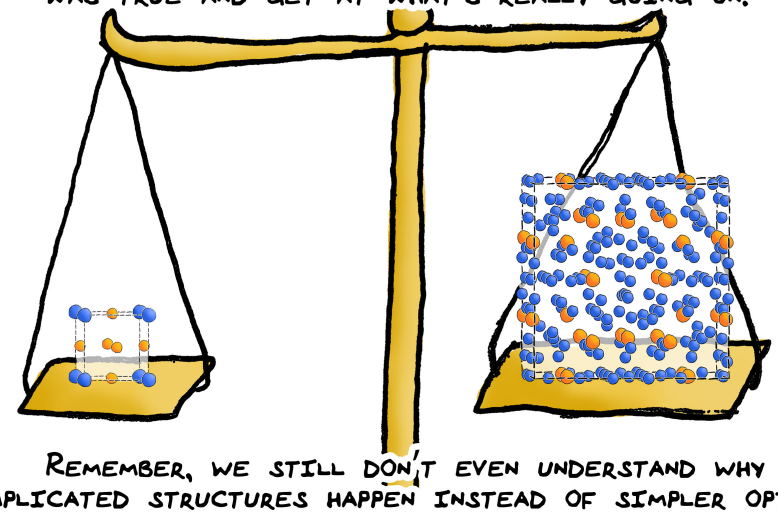

REMEMBER, WE STILL DON'T EVEN UNDERSTAND WHY COMPLICATED STRUCTURES HAPPEN INSTEAD OF SIMPLER OPTIONS.

WE WANT SOME RULES.

BUT WE'RE ONLY GOING TO GET THEM IF WE TAKE A CLOSER LOOK AT THE REBELS, THE RULEBREAKERS, THE WEIRD STUFF ON THE FRINGES OF OUR CURRENT UNDERSTANDING.

WHAT DO WE KNOW SO FAR ABOUT QUASICRYSTALS?

QUASICRYSTALS HAVE ROTATIONAL SYMMETRIES THAT ARE INCOMPATIBLE WITH TRANSLATION.

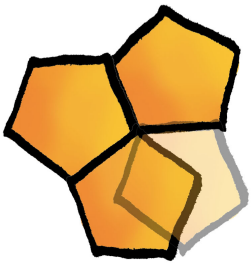

ONLY 2-, 3-, 4-, AND 6-FOLD PATTERNS CAN HAVE UNIT CELLS.

WHY CAN'T WE HAVE 5-FOLD PATTERNS?

UNLIKE HEXAGONS, SQUARES, AND TRIANGLES, YOU CAN'T COMPLETELY COVER A PLANE WITH ONLY REGULAR PENTAGONS OR OCTAGONS.

YOU'LL END UP WITH WEIRD SHAPES OF EMPTY SPACE. GRAB SOME TANGRAMS AND TRY IT.

WE'VE FOUND QUASICRYSTALS THAT HAVE 5-, 7-, 8-, 10-, EVEN 12-FOLD SYMMETRIES.

Some of them look like this

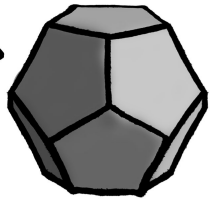

THEY DON'T HAVE UNIT CELLS, BUT THEY'VE STILL GOT SYMMETRY.

I'VE SAID IT BEFORE, BUT IT IS WORTH (AHEM) REPEATING...

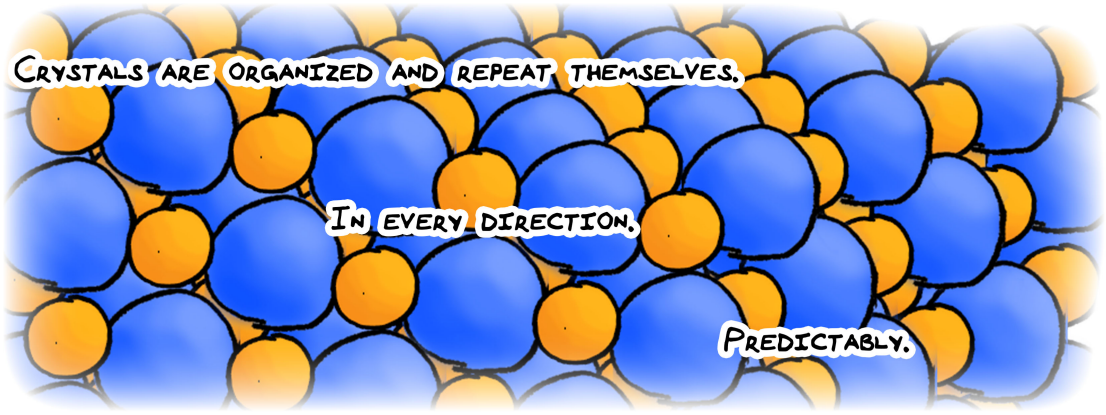

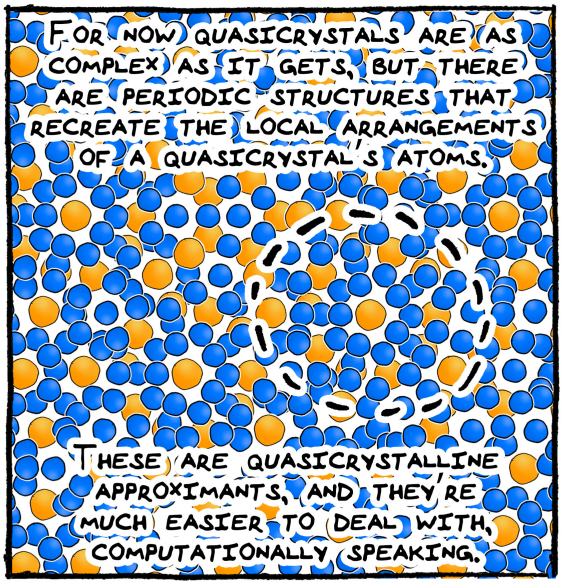

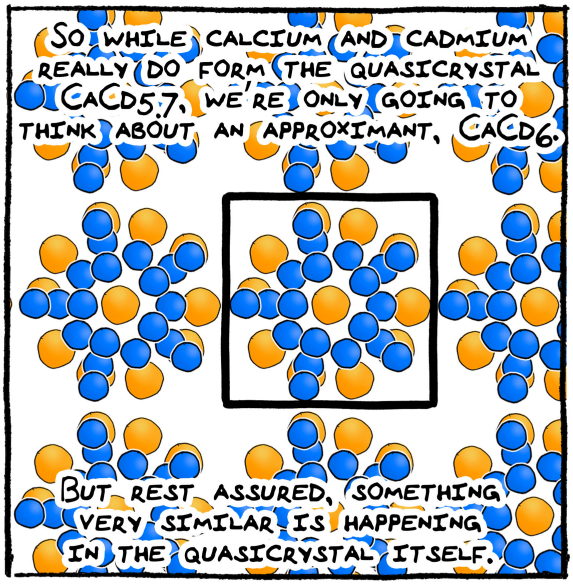

When we looked at the hypothetical $CaCd_5$ compound, we noticed that there was a vacuum in the center.

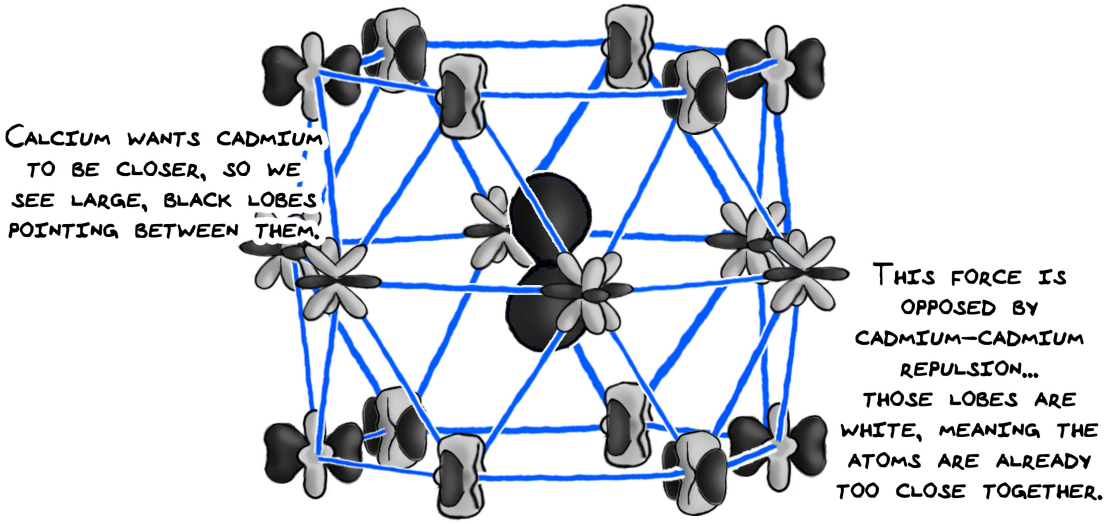

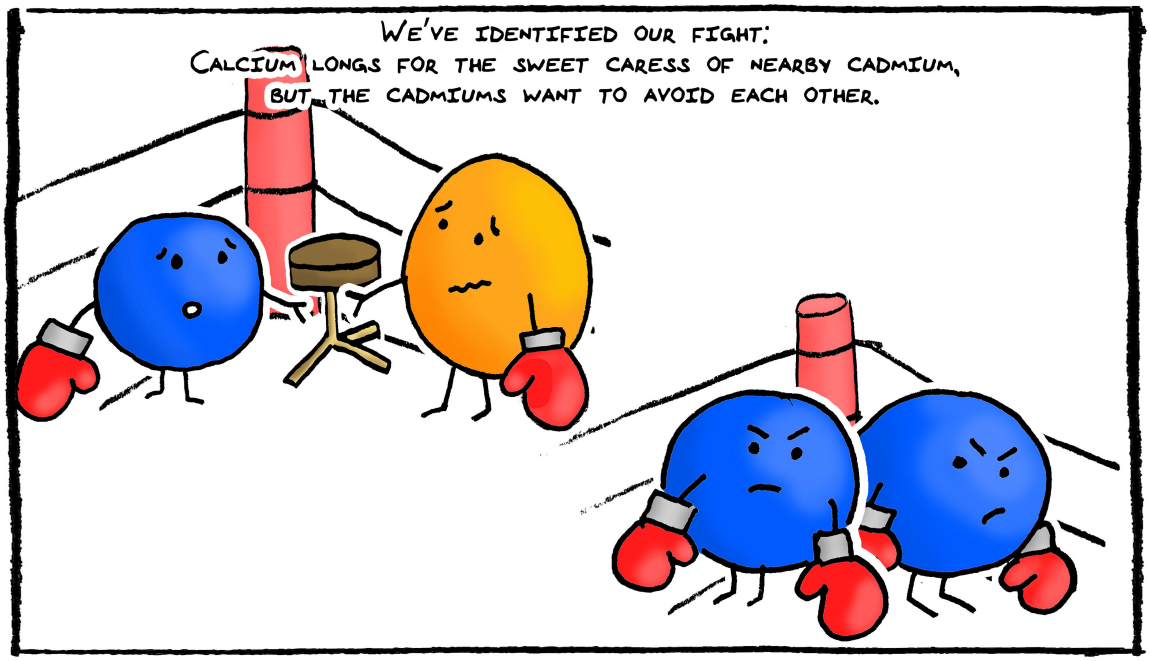

One possible way to calm everybody down is to knock out a cadmium.

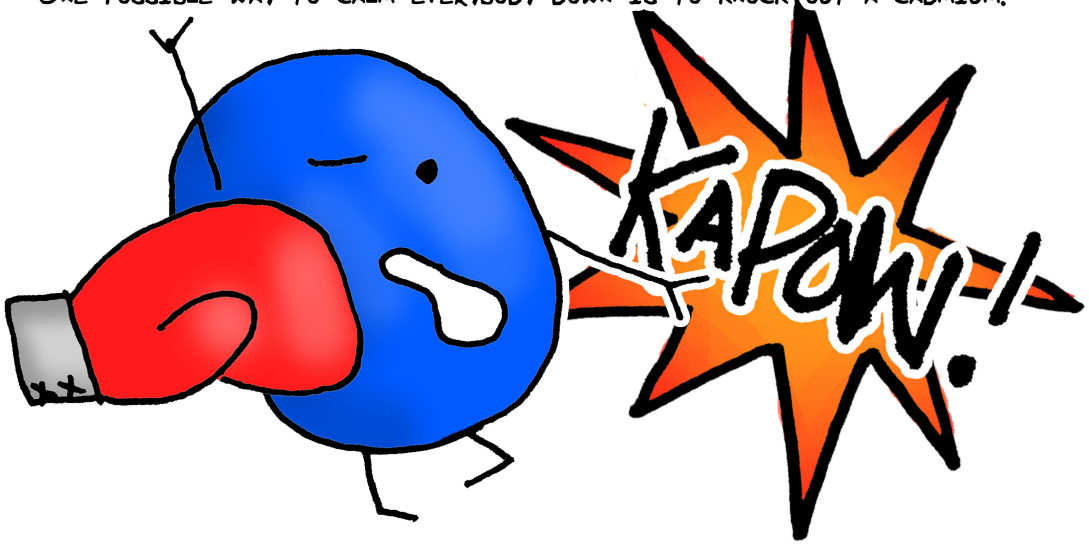

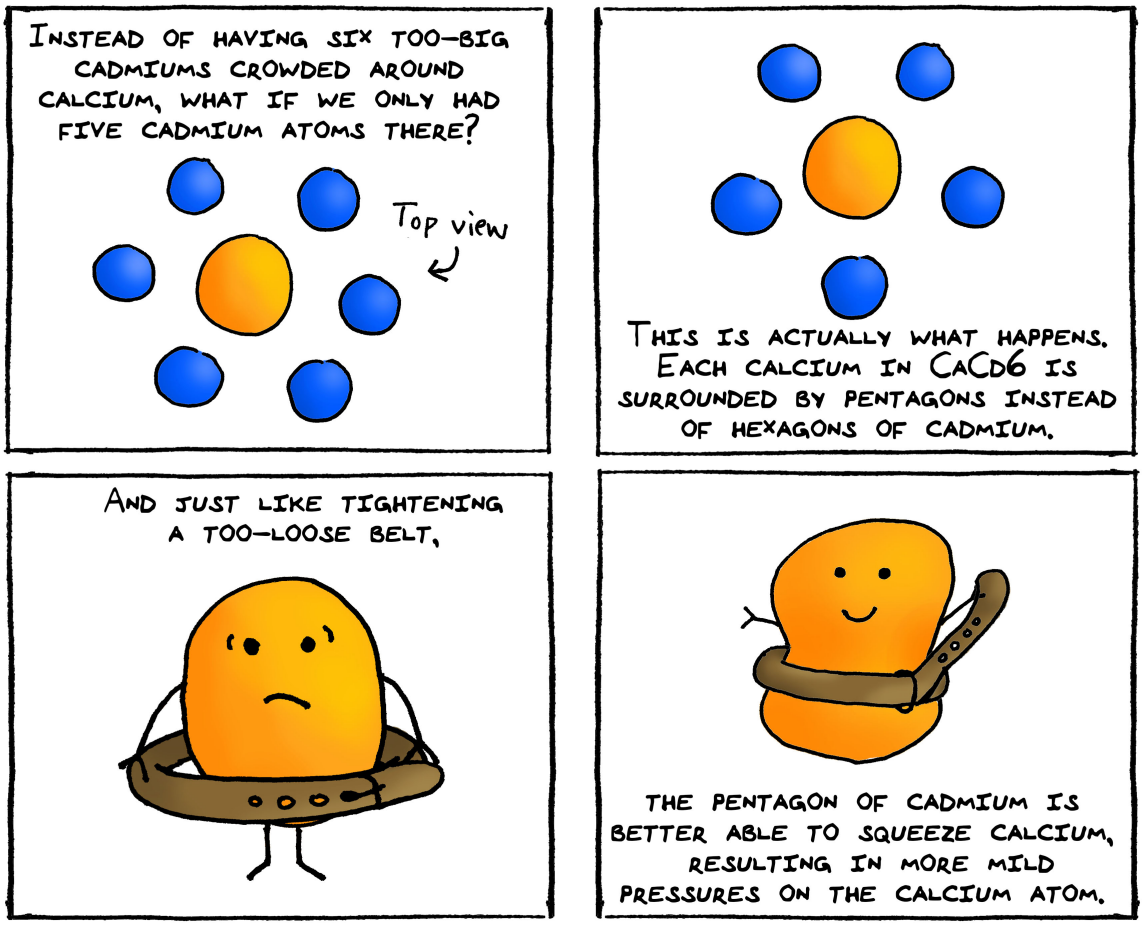

Cadmium is pretty happy with this arrangement too; there's fewer neighbors to bump into. Here's what the CP looks like:

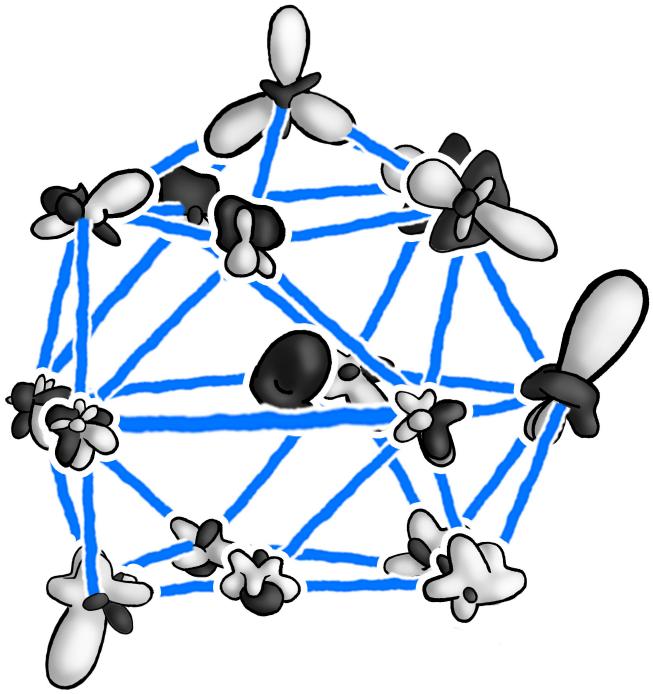

Now it's smooth sailing, right? The CP is better, Calcium has a pentagonal belt, and cadmium mostly stopped hitting itself.

We've got a problem with periodicity.
The very thing that pleases our compound upsets the periodicity of our structure!

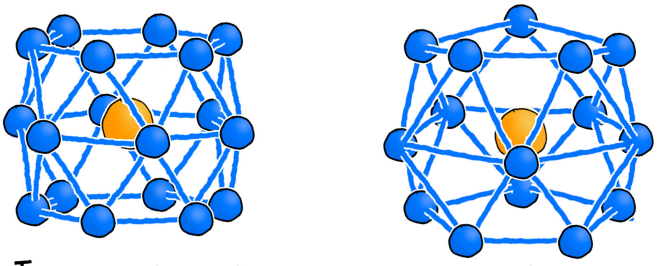

Instead of those infinite hexagonal nets,
our new compound demands infinite pentagonal nets.

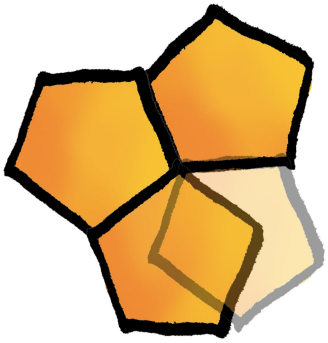

And we know that you can't have 2-D pentagonal tiles.

But we never said anything about 3-D pentagonal tiles.

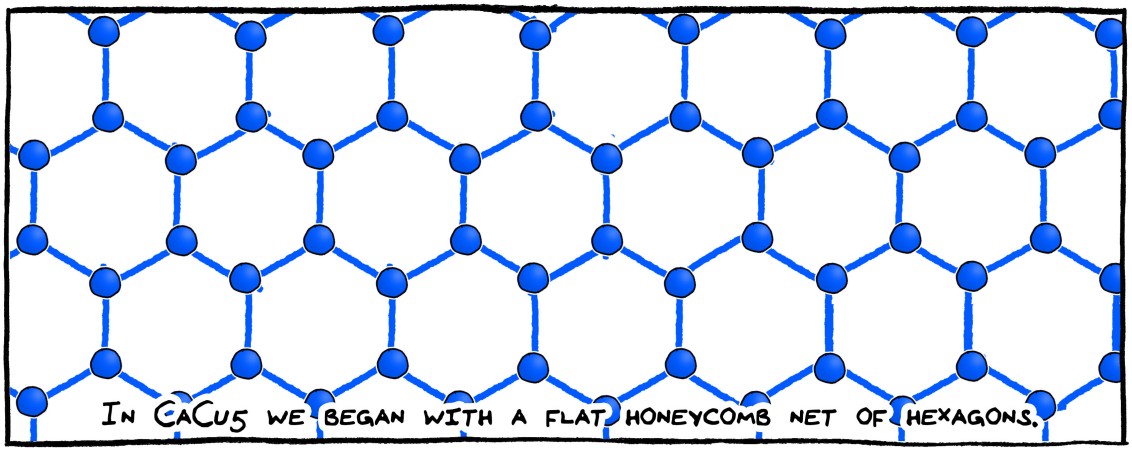

In $CaCu_5$ we began with a flat honeycomb net of hexagons.

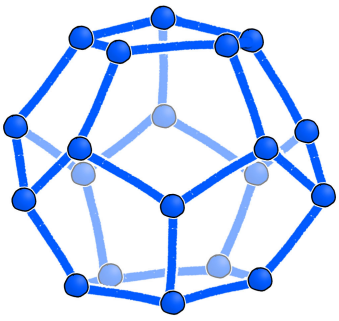

In $CaCd_6$ we'll begin with a dodecahedron:
A shape with 12 pentagonal faces.

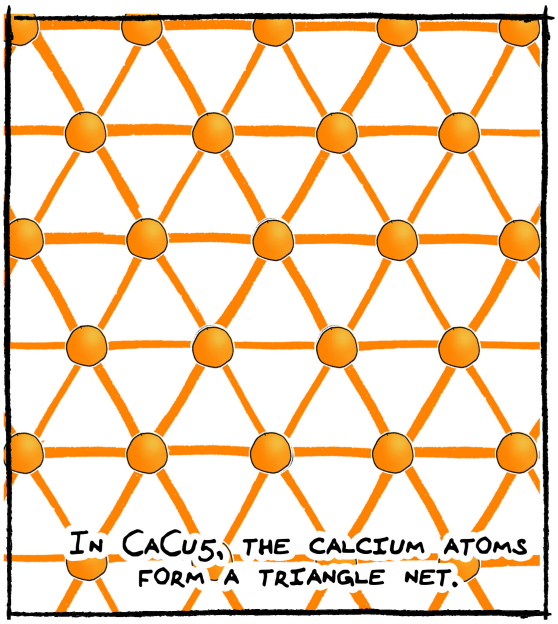

In CaCu5, the calcium atoms form a triangle net.

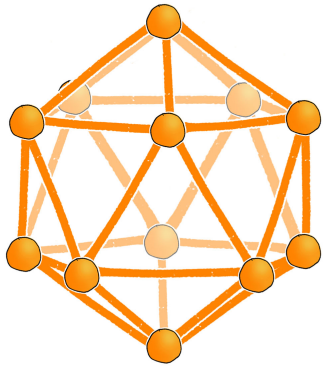

In CaCd6, calcium atoms form an icosahedron: a shape with triangle faces.

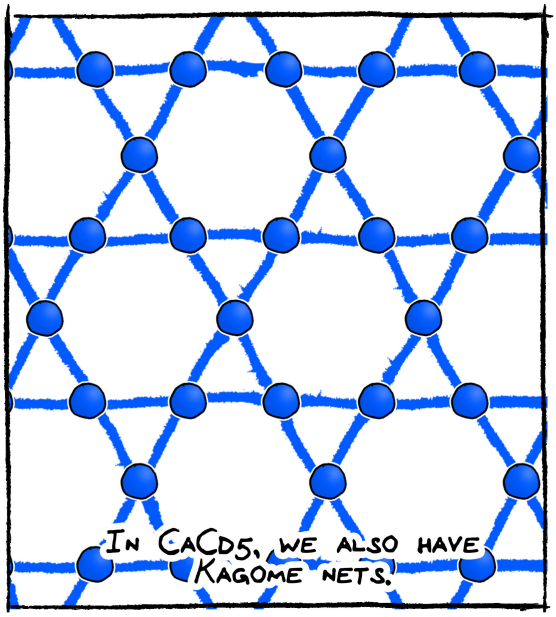

In CaCd5, we also have Kagome nets.

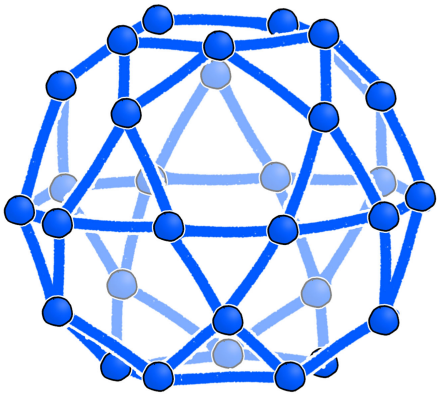

In CaCd6, we have icosidodecahedra: five-pointed stars, not six.

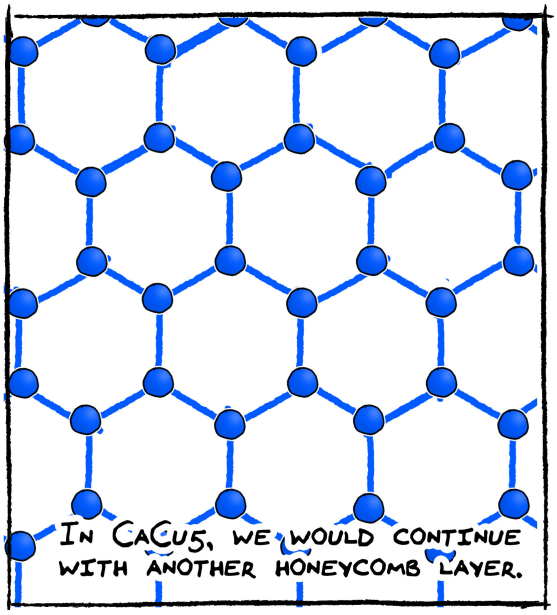

In CaCu5, we would continue with another honeycomb layer.

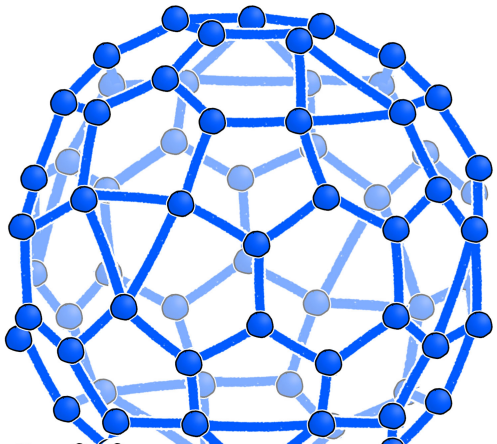

In CaCd6, we terminate our cluster with a truncated icosahedron: a solid with some faces pentagons, some hexagons.

This is our Tsai-type cluster.

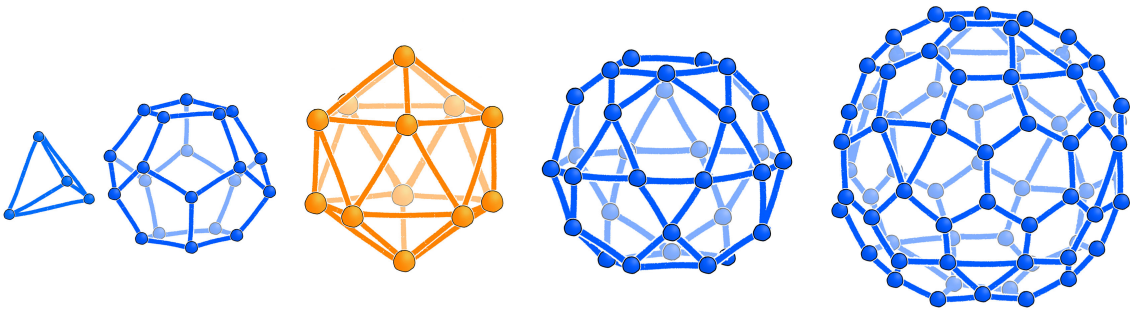

A dodecahedron inside of an icosahedron inside of
an icosidodecahedron inside of a truncated icosahedron
(with a tiny tetrahedron in the center, to fill the empty space).

We can stack infinite layers of the $CaCu_5$ type.

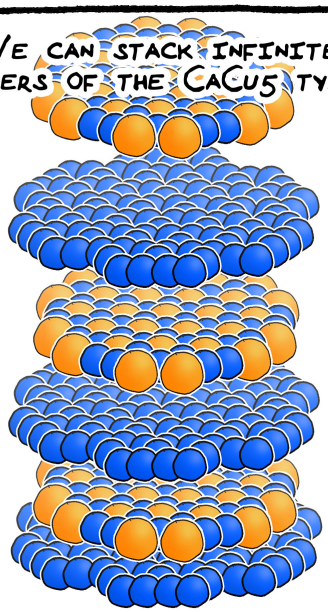

Our cluster ends here.

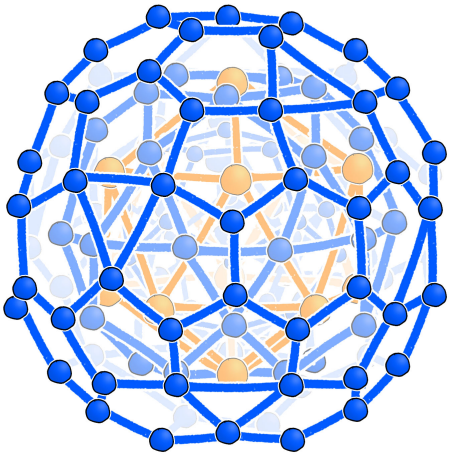

To make $CaCd_6$, we pack these clusters together periodically.

But now that we understand the pieces of the puzzle,
and why they are doing what they are doing,
and that calcium really needs those pentagons,
you can imagine an infinite array of little five-fold blocks.
You can imagine them making five-fold
patterns that never repeat themselves.

You can imagine a quasicrystal.

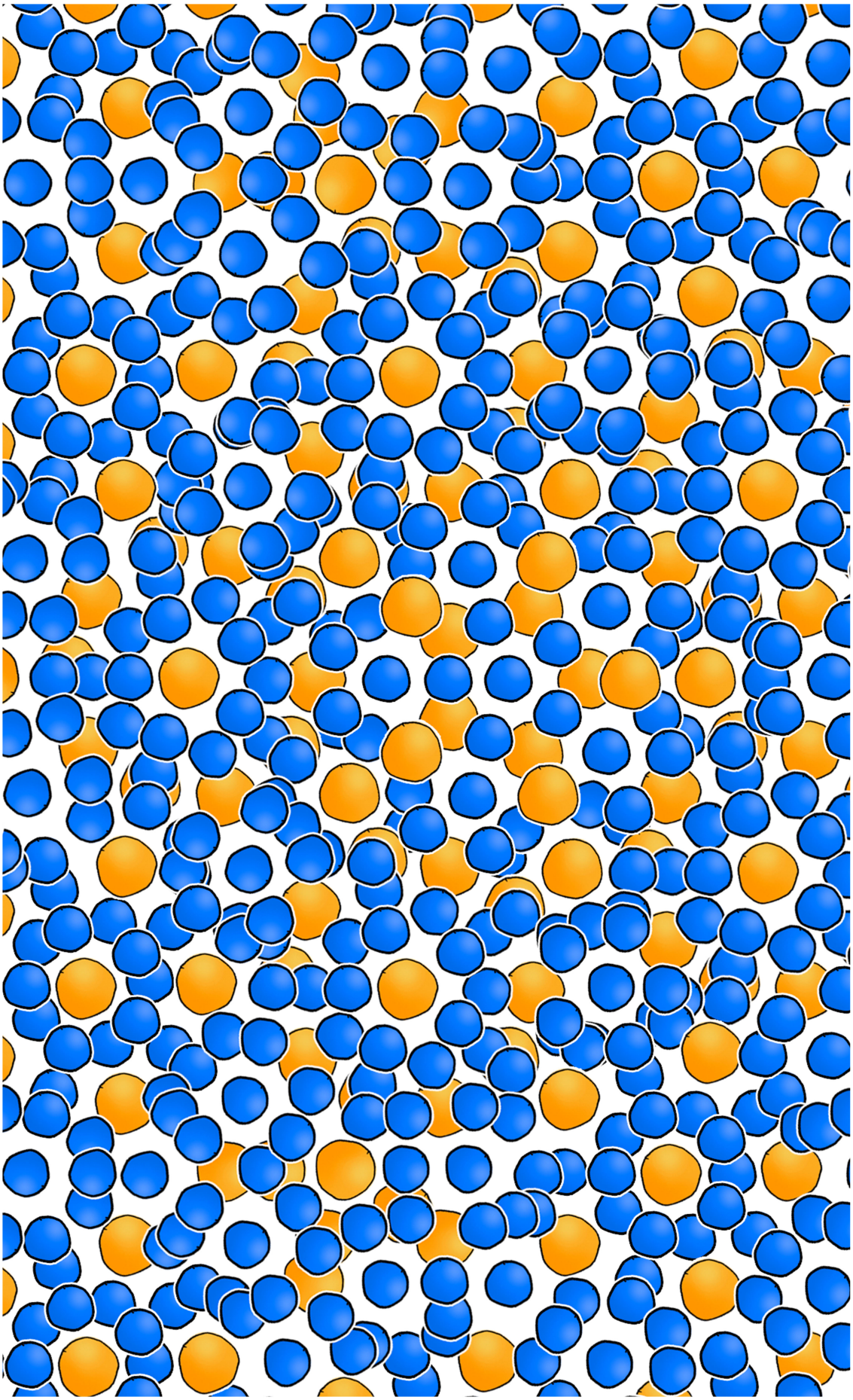

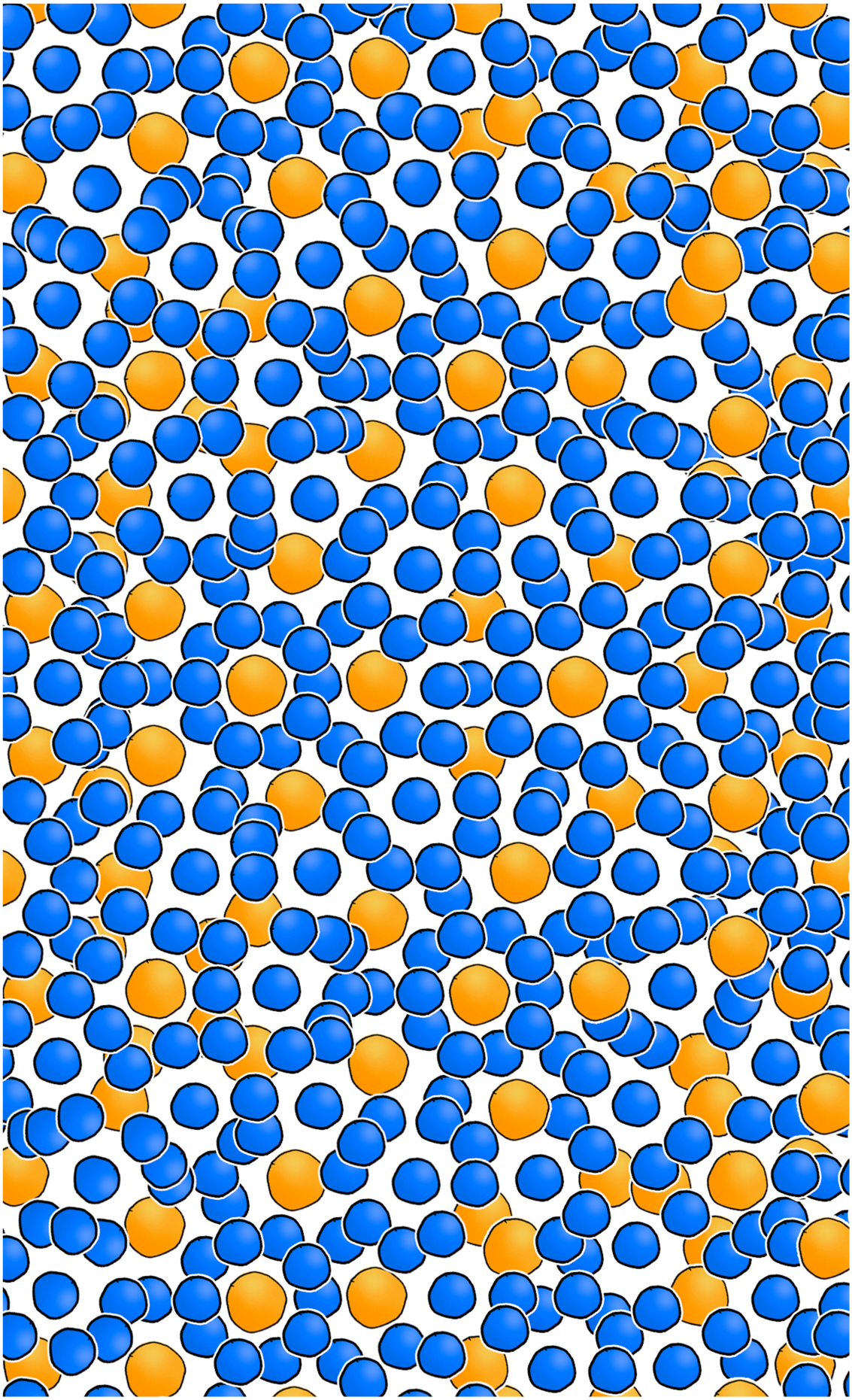

THE RELATIONSHIP OF THE SIMPLE CaCu5 TYPE TO THE COMPLEX TSAI-TYPE QUASICRYSTAL IS JUST ONE EXAMPLE OF A STRUCTURAL REMIX.

JUST LIKE A DJ CUTS UP OLD SONGS TO MAKE NEW ONES, WE CUT UP A SIMPLE STRUCTURE AND MADE A MORE COMPLICATED ONE.

WIGGY WIGGY WIGGY

SIMILAR STRUCTURAL THINGS WERE HAPPENING IN BOTH COMPOUNDS.

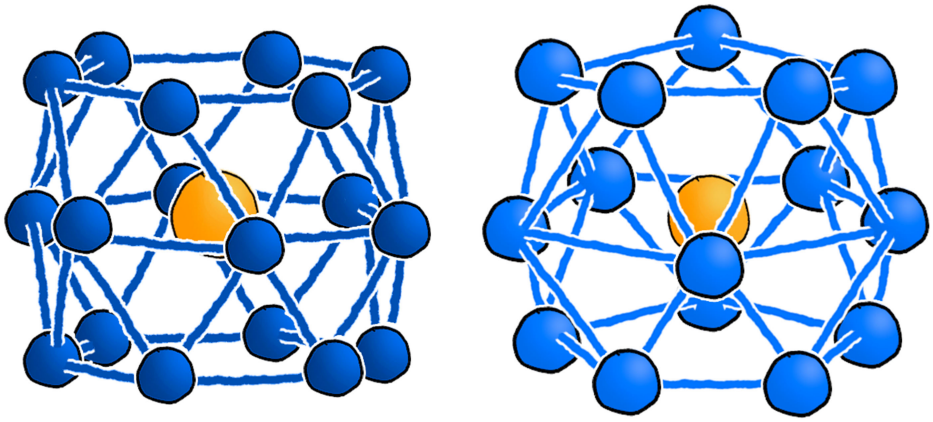

BUT WHEN YOU CHANGE THE SIZES OF THE ATOMS INVOLVED, YOU STRESS OUT THE MATERIAL, AND YOU MIGHT GET SOMETHING TOTALLY NEW.

BUT OFTEN TIMES, THERE IS A CONNECTION BETWEEN THE SIMPLE AND THE COMPLEX.

THIS HAPPENS FOR A LOT OF COMPOUNDS. WE'VE ONLY SCRATCHED THE SURFACE.

BY UNDERSTANDING THESE CONNECTIONS, WE HAVE BETTER FOOTING TO MANIPULATE A COMPOUND AND CREATE SOMETHING WE'VE NEVER SEEN BEFORE.

CA AND PD FORM THE CaCu5 TYPE. CAN YOU IMAGINE ADDING A LITTLE PALLADIUM TO OUR CALCIUM AND CADMIUM?

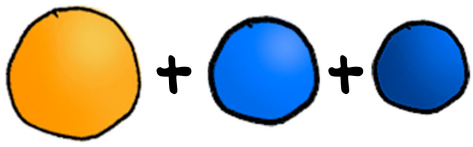

WE MIGHT GET A NEW COMPOUND! AND IT MIGHT BE A WHOLE NEW STRUCTURAL REMIX!


NOW THAT WE'VE THOUGHT A LOT ABOUT THIS TINY PIECE OF THE UNIVERSE WE LIVE IN, IT'S TIME TO TEST OUT OUR THEORIES BY TRYING TO MAKE NEW THINGS.
THERE ARE SO MANY COMPOUNDS THAT MIGHT EXIST, AND WE WON'T KNOW UNTIL WE MAKE THEM.
ISN'T IT WONDERFUL?
THERE'S SO MUCH TO DO.
SOLID STRUCTURES ARE FULL OF POSSIBILITIES.

IT'S A BEAUTIFUL WORLD
OUT THERE, MY FRIENDS.

LET'S GO EXPLORING.

Abridged and Annotated Bibliography

These are certainly not the only materials referenced throughout my work on this project, but they are perhaps the most relevant to someone wanting to learn more about the science behind this comic. I've written a short summary of each, so you know what you're getting into before you get into it.

The number of papers developing the CP method should tell you that science isn't straightforward. We've had to go through a lot of potential methods before settling on the current one. This doesn't mean previous iterations are wrong or bad, we're just trying to figure out the best way to measure something that has never been measured before. So chances are good we'll end up modifying the current method too. That's just how it goes.

Sands, Donald E. Introduction to Crystallography. Dover Publications: Mineola NY, 1975.

This was the first book I ever read about crystallography. I don't explicitly talk much about this technique in the pages of this comic, but if the structures of materials caught your attention, this is a great little book. Crystallography is how we know what materials look like on an atomic scale. Someone (not me!) discovered every one of the structures in this comic with a crystallography experiment. X-rays go in to a crystal, bounce around a little, and then diffract outwards in interpretable patterns. It's these patterns that give us very precise placement of the atoms in the crystal.

Hoffmann, Roald. Solids and Surfaces: A Chemist's View of Bonding in Extended Structures. Wiley-VCH: New York, 1988.

Ideas behind chemical bonding are all based on where electrons are, and how much energy they have. Many chemists have a good handle on "chemical bonds" in molecules, but in 3-D solids, there are a lot of electrons flying around. This book offers a beautiful explanation of the techniques behind thinking about electrons in solid materials. Additionally, Professor Hoffmann is very talented* when it comes to communicating technical material, and this book is no exception. Every chapter feels like going on a splendid little adventure with a very knowledgeable* friend.

*Severe understatements

Fredrickson, Daniel C. Electronic Packing Frustration in Complex Intermetallic Structures: The Role of Chemical Pressure in Ca_2Ag_7. Journal of the American Chemical Society. **2011**, vol. 133, pg. 10070–10073.

Coca-Cola Classic. Action Comics. Star Wars Episode IV. CSI: Las Vegas. This paper. This is the original introduction to the idea of chemical pressure, calculated with Hückel theory instead of the current method that uses Density Functional Theory (DFT). Practically speaking, all that means is that it is less accurate, but easier to use because we don't have to worry about the fancy scissors and cutting up space. This paper lays out the methods and ideas behind chemical pressure, and then applies them to a calcium-silver compound, Ca_2Ag_7.

Fredrickson, Daniel C. DFT-Chemical Pressure Analysis: Visualizing the Role of Atomic Size in Shaping the Structures of Inorganic Materials. Journal of the American Chemical Society. 2012, vol. 134, pg. 5991–5999.

A follow-up to the previous paper, this one introduces chemical pressure powered by DFT. It goes through the same example, Ca_2Ag_7. Just like the compound in this comic, Ca_2Ag_7 is based on the $CaCu_5$ type: strontium and silver form $CaCu_5$-type $SrAg_5$. Calcium is smaller than strontium, and the Ca_2Ag_7 type provides a few close Ca–Ag contacts to make up for the stresses we see in $CaCu_5$-type $CaAg_5$.

Engelkemier, J.; Berns, Veronica M.; Fredrickson, Daniel C. First-principles elucidation of atomic size effects using DFT-chemical pressure analysis: Origins of $Ca_{36}Sn_{23}$'s long-period superstructure. Journal of Chemical Theory and Computation. **2013**, vol. 9, pg. 3170–3180.

This paper tells another story about chemical pressure in a calcium-tin compound. Again, calcium isn't the right size for a simple structure, and everything is happier in a more complicated arrangement. In this case, the hypothetical simple structure has chains of tin tetrahedra with calcium in the middle, but the Ca atoms are held too close together for this compound to exist. The structure that we actually can make out of calcium and tin occasionally incorporates an octahedron that gives calcium more room. This paper also has a bunch of cool math and develops the theoretical methods behind chemical pressure, and chronicles a drastic improvement to our "fancy scissors".

Berns, Veronica M.; Fredrickson, Daniel C. Problem Solving with Pentagons: Tsai-Type Quasicrystal as a Structural Response to Chemical Pressure. Inorganic Chemistry. 2013, vol. 52, pg. 12875–12877.

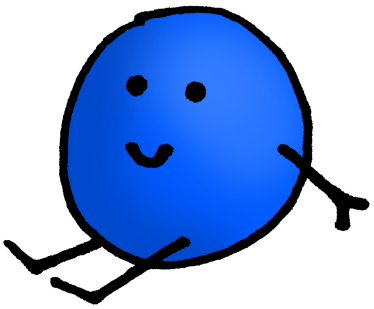

The last few pages of this comic are pretty much straight from this paper, but the paper goes into more detail. It shows the chemical pressure pictures for the hypothetical $CaCu_5$– type "$CaCd_5$" and compares them with the chemical pressures of the quasicrystal approximant $CaCd_6$. The ultimate conclusion is that the pressures on the calcium drive the transformation into a quasicrystalline approximant: the $CaCu_5$ type is based on hexagon rings, and $CaCd_6$ is based on pentagonal rings. The quasicrystallinity comes from trying to cram a bunch of pentagons together to fill space.

Berns, Veronica M.; Engelkemier, J.; Guo, Yiming; Kilduff, Brandon J.; Fredrickson, Daniel C. Progress in Visualizing Atomic Size Effects With DFT–Chemical Pressure Analysis: From Isolated Atoms to Trends in AB_5 Intermetallics. Journal of Chemical Theory and Computation. ASAP.

Occasionally we find the need to update the methodology of the chemical pressure technique. This paper brings us ever fancier scissors, but more importantly it corrects for a distortion in our chemical pressure maps that we didn't know we had. This was due to a mismatch in the grids during the calculation. Once we realized we were inadvertently distorting the grid, we fixed it. This paper shows that our old method gave us a nonsensical story for compounds in the $MgCu_2$ type, but our new method allows us to analyze these structures that were once troublesome.

Takakura, Hiroyuki; Pay Gómez, Cesar; Yamamoto, Akiji; De Boisseau, Marc; Tsai, An-Pang. Atomic Structure of the Binary Icosahedral Yb–Cd Quasicrystal. Nature Materials. 2007, vol. 6, pg. 58–63.

Tsai, An-Pang; Pay Gómez, Cesar. Quasicrystals and Approximants in Cd–M Systems and Related Alloys. In Handbook of Metal Physics. Elsevier, 2008.

We often rely on periodicity to get atomic positions out of crystallography experiments, but these guys figured out how to get a structure for a quasicrystal. The short paper from Nature Materials talks about why it was necessary to do this in 6 dimensions (the TL;DR answer is "math"), but the book chapter gives a great overview of the whole family of related compounds we've found, some of which we're able to understand with our humble 3 dimensions, like $CaCd_6$.

Shadle, Albert R. Gestation Period in the Porcupine, Erethizon dorsatum dorsatum. Journal of Mammology. 1948, vol. 29, pg. 162–164.

If you look up the gestation period of a porcupine on Wikipedia, it will say 113 days. That was the belief in 1928, based on the time between someone's observation of a lady porcupine mating with a man porcupine, and that lady-pine giving birth. But in 1948, Albert Shadle changed our understanding of porcupine gestation with a very controlled experiment. He isolated a pair of lady porcupines, and later introduced a male. After they bred, the females had no other contact with males, and it took 209 and 217 days for the porcupine babies to be born. Ideally he would have gotten more than two data points, but later studies confirmed his observations, suggesting that the estimation of 113 days was incorrect.

Thanks!

This comic book couldn't have been made without the help of so many people. Number one is Professor Danny Fredrickson, my PhD advisor and the guy who so brilliantly captains the CP ship. Of all the things I will take away from grad school, your kindness and engouragement has meant the most.

I'm beyond lucky to have had Kale Engelkemier as my coworker on the CP code. They've also helped edit this book, and been a fantastic friend for the past three years.

Yiming Guo is a brilliant scientist and an all-around great person who has with Kale written a lot of the CP programs.

To Kale, Yiming, and the rest of the Fredrickson Group- Brandon Kilduff, Vince Yannello, Anastasiya Vinokur, Katie Hilleke, Rie Fredrickson, Amelia Hadler, Arthur White, Nick Harris, Mike Sapiro, and Tim Stacey: I couldn't have dreamed up a better group of passionate and inspiring people to work with. May you jump and always go.

Ashlan Musante lent her scientific and creative mind as an editor. Josh Klemons is a bit more removed from the world of science, but he's been amazing at helping edit as well.

Another big thanks to my many draft-readers and encouragement-providers. Especially Max.

And finally, the last thank you goes to you, for jumping into this little bit of the scientific world. I set out to make something that would bring the joy and wonderment of cutting-edge science to more people, and your curiosity was the last piece of the puzzle.

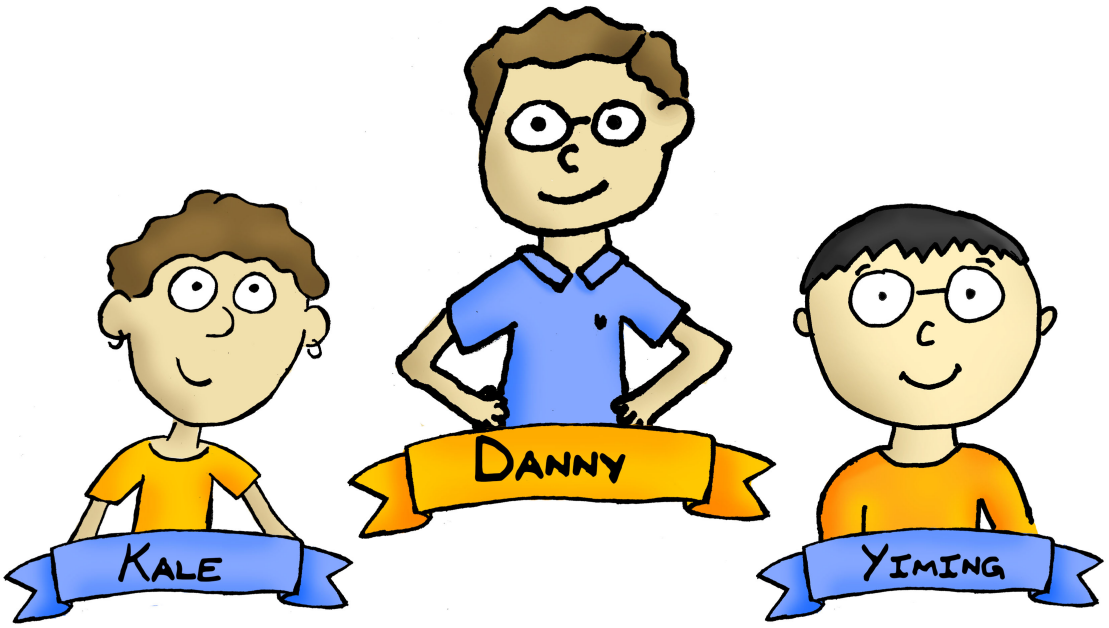

Appendix A.

Supplemental information for Chapter 3:

Unpublished crystal structures exhibiting structural plasticity

A.1 Tables of atomic coordinates and unit cells for $Mn_{24}Co_{14}Si_{14}$ and $Fe_7Mo_4Si_8$

Table A.1. Unit cell dimensions for $Mn_{24}Co_{14}Si_{14}$ and $Fe_7Mo_4Si_8$

	Space Group	*a*	*b*	*c*
$Mn_{24}Co_{14}Si_{14}$	*Pbam*	7.5464	8.9168	9.3703
$Fe_7Mo_4Si_8$	*Pnma*	12.7951	4.8251	15.3018

Table A.2. Atomic coordinates for $Mn_{24}Co_{14}Si_{14}$

Element	*x*	*y*	*z*
Co	0.50000	1.00000	0.00000
Co	0.50000	0.00000	1.00000
Co	0.50000	1.00000	1.00000
Co	0.00000	0.50000	0.00000
Co	1.00000	0.50000	0.00000
Co	0.00000	0.50000	1.00000
Co	1.00000	0.50000	1.00000
Co	0.50000	0.00000	0.00000
Co	0.40527	0.73779	0.00000
Co	0.40527	0.73779	1.00000
Co	0.59473	0.26221	0.00000
Co	0.59473	0.26221	1.00000
Co	0.90527	0.76221	0.00000
Co	0.90527	0.76221	1.00000
Co	0.09473	0.23779	0.00000
Co	0.09473	0.23779	1.00000
Co	0.34583	0.18158	0.36834
Co	0.65417	0.81842	0.36834
Co	0.84583	0.31842	0.63166
Co	0.15417	0.68158	0.63166

Co	0.65417	0.81842	0.63166
Co	0.34583	0.18158	0.63166
Co	0.15417	0.68158	0.36834
Co	0.84583	0.31842	0.36834
Mn	0.54620	0.37799	0.75038
Mn	0.95380	0.87799	0.24962
Mn	0.04620	0.12201	0.24962
Mn	0.54620	0.37799	0.24962
Mn	0.45380	0.62201	0.24962
Mn	0.04620	0.12201	0.75038
Mn	0.95380	0.87799	0.75038
Mn	0.45380	0.62201	0.75038
Mn	0.83344	0.04816	0.50000
Mn	0.16656	0.95184	0.50000
Mn	0.33344	0.45184	0.50000
Mn	0.66656	0.54816	0.50000
Mn	0.83868	0.04626	1.00000
Mn	0.16132	0.95374	0.00000
Mn	0.16132	0.95374	1.00000
Mn	0.33868	0.45374	0.00000
Mn	0.33868	0.45374	1.00000
Mn	0.66132	0.54626	0.00000
Mn	0.66132	0.54626	1.00000
Mn	0.83868	0.04626	0.00000
Mn	0.65967	0.08893	0.24812
Mn	0.34033	0.91107	0.24812
Mn	0.15967	0.41107	0.75188
Mn	0.84033	0.58893	0.75188
Mn	0.34033	0.91107	0.75188
Mn	0.65967	0.08893	0.75188
Mn	0.84033	0.58893	0.24812
Mn	0.15967	0.41107	0.24812
Si	0.50000	0.00000	0.50000
Si	0.50000	1.00000	0.50000
Si	0.00000	0.50000	0.50000
Si	1.00000	0.50000	0.50000
Si	0.59149	0.27039	0.50000
Si	0.90851	0.77039	0.50000
Si	0.09149	0.22961	0.50000
Si	0.40851	0.72961	0.50000
Si	0.34515	0.18018	0.13278
Si	0.65485	0.81982	0.13278
Si	0.84515	0.31982	0.86722
Si	0.15485	0.68018	0.86722
Si	0.65485	0.81982	0.86722
Si	0.34515	0.18018	0.86722
Si	0.15485	0.68018	0.13278
Si	0.84515	0.31982	0.13278

Table A.3. Atomic coordinates for $Fe_7Mo_4Si_8$

Element	*x*	*y*	*z*
Fe	0.68768	0.75000	0.24989
Fe	0.18768	0.75000	0.25011
Fe	0.31232	0.25000	0.75011
Fe	0.81232	0.25000	0.74989
Fe	0.93915	0.50226	0.62043
Fe	0.56085	1.00226	0.12043
Fe	0.56085	0.00226	0.12043
Fe	0.56085	0.49774	0.12043
Fe	0.43915	-0.00226	0.87957
Fe	0.93915	-0.00226	0.62043
Fe	0.93915	0.99774	0.62043
Fe	0.43915	0.50226	0.87957
Fe	0.43915	0.99774	0.87957
Fe	0.06085	0.49774	0.37957
Fe	0.06085	0.00226	0.37957
Fe	0.06085	1.00226	0.37957
Fe	0.63538	1.00525	0.67557
Fe	0.63538	0.00525	0.67557
Fe	0.86462	0.99475	0.17557
Fe	0.86462	-0.00525	0.17557
Fe	0.36462	0.50525	0.32443
Fe	0.13538	0.49475	0.82443
Fe	0.13538	1.00525	0.82443
Fe	0.36462	0.99475	0.32443
Fe	0.63538	0.49475	0.67557
Fe	0.86462	0.50525	0.17557
Fe	0.13538	0.00525	0.82443
Fe	0.36462	-0.00525	0.32443
Fe	0.86658	0.75000	0.34613
Fe	0.63342	0.25000	0.84613
Fe	0.36658	0.75000	0.15387
Fe	0.13342	0.25000	0.65387
Mo	0.24713	0.25000	0.47518
Mo	0.75287	0.75000	0.52482
Mo	0.74713	0.25000	0.02482
Mo	0.25287	0.75000	0.97518
Mo	0.93079	0.75000	0.80303
Mo	0.06921	0.25000	0.19697
Mo	0.43079	0.75000	0.69697
Mo	0.56921	0.25000	0.30303
Mo	0.86554	0.25000	0.45678
Mo	0.13446	0.75000	0.54322
Mo	0.36554	0.25000	0.04322
Mo	0.63446	0.75000	0.95678
Mo/Fe	0.87616	0.75000	0.00211
Mo/Fe	0.37616	0.75000	0.49789
Mo/Fe	0.12384	0.25000	-0.00211
Mo/Fe	0.12384	0.25000	0.99789

Mo/Fe	0.62384	0.25000	0.50211
Mo/Fe	0.87616	0.75000	1.00211
Mo/Fe	0.45172	0.25000	0.59423
Mo/Fe	0.54828	0.75000	0.40577
Mo/Fe	0.95172	0.25000	0.90577
Mo/Fe	0.04828	0.75000	0.09423
Si	0.21820	0.00415	0.12208
Si	0.21820	1.00415	0.12208
Si	0.28180	-0.00415	0.62208
Si	0.28180	0.99585	0.62208
Si	0.71820	0.49585	0.37793
Si	0.78180	0.50415	0.87792
Si	0.78180	-0.00415	0.87792
Si	0.78180	0.99585	0.87792
Si	0.71820	0.00415	0.37793
Si	0.71820	1.00415	0.37793
Si	0.28180	0.50415	0.62208
Si	0.21820	0.49585	0.12208
Si	0.00439	0.75000	0.24939
Si	1.00439	0.75000	0.24939
Si	0.49561	0.25000	0.74939
Si	0.50439	0.75000	0.25061
Si	-0.00439	0.25000	0.75061
Si	0.99561	0.25000	0.75061
Si	0.79297	0.75000	0.69218
Si	0.20703	0.25000	0.30783
Si	0.29297	0.75000	0.80782
Si	0.70703	0.25000	0.19218
Si	0.72534	0.75000	0.10192
Si	0.77466	0.25000	0.60192
Si	0.22534	0.75000	0.39808
Si	0.27466	0.25000	0.89808
Si	0.94897	0.75000	0.48296
Si	0.05103	0.25000	0.51704
Si	0.44897	0.75000	0.01704
Si	0.55103	0.25000	0.98297
Si	0.58502	0.75000	0.80285
Si	0.91498	0.25000	0.30285
Si	0.08502	0.75000	0.69715
Si	0.41498	0.25000	0.19715
Si	0.55237	0.75000	0.56371
Si	0.44763	0.25000	0.43629
Si	0.05237	0.75000	0.93629
Si	0.94763	0.25000	0.06371

Appendix B.

Supplemental information for Chapter 4:

First-principles elucidation of atomic size effects using DFT-chemical pressure analysis: Origins of $Ca_{36}Sn_{23}$'s long-period superstructure

B.1. Treatment of the $P_{remainder}$ components

One question encountered in the development of the DFT-CP analysis is to what extent each of the terms of the DFT total energy can be mapped to an energy grid. The energetic terms contributing to $P_{remainder}$ in Equation 4.4 all share the feature that they are not easily represented as an integral of an energy density over the unit cell volume. However, in principle some of these terms can be divided to some degree across a structure. Consider the E_a component of E_{total}. This component of the total energy represents the difference in the stability provided to a homogeneous electron gas by the ion cores and the simple Coulomb potentials used in the calculation of E_{Ewald}:

$$\begin{aligned} E_a &= \left(\sum_{j}^{N_{ions}} \iiint_{all\ space} V_{local_j}(\vec{r}-\vec{r}_{ion,j}) - \frac{Z_j}{|\vec{r}-\vec{r}_{ion,j}|} dV \right) \frac{N_{electrons}}{V_{cell}} \\ &= \left(\sum_{j}^{N_{ions}} \alpha_j \right) \frac{N_{electrons}}{V_{cell}} \end{aligned} \tag{B.1}$$

As is evident from the above equation, the E_a contribution can be decomposed into a sum over terms corresponding to individual ions, which could then be mapped to the positions of these ions in space. The effort required to achieve this using the ABINIT program is minimal: the a_j values for Equation S1 are given in the ABINIT output file for each pseudopotential with the label "epsatm." The atomic contributions to E_a are then obtained by multiplying the corresponding a_j values by the average electron density for the unit cell.

Similar considerations apply to $E_{nonlocal}$, which is built up from a sum of terms resulting from the differential screening of s-, p-, d- and f- type orbital character around the individual ion cores in the system. While this is difficult to represent as a continuous function in 3D space, it should certainly be possible to distribute $E_{nonlocal}$ appropriately among the atoms of the structure. A more complicated procedure is necessary here than for E_a. One begins by running a self-consistent field calculation on the structure of interest to obtain the ground state electron density and wavefunctions. Then holding fixed this electron density, the wavefunctions, and their occupancies, one goes atom by atom through the structure and calculates the total energy resulting when each ion core is placed alone in the unit cell in the midst of this electronic structure. The $E_{nonlocal}$ term listed in the output for each atom then corresponds to the contribution from that atom to the nonlocal energy for the full structure. An annotated ABINIT input file for performing this procedure is provided in Section B.2.

Once the E_a and $E_{nonlocal}$ energies are resolved into atomic contributions, this information can be incorporated in the DFT-CP analysis by distributing these atomic terms among the voxel energies ($E_{voxel,n}$'s) of Equation 4.3. Here, we follow the argument of Filippetti and Fiorentini[1] that the nonlocal energies are associated with the ion core regions, and as such can be localized to the space close to their

corresponding nuclei. For each atom, we count the voxels that occur within a fixed radius of the nuclear position, and partition the atomic E_a and $E_{nonlocal}$ equally across these voxels. The specific value of the radius should have no effect on the results of the CP analysis as long as the volume it encloses does not cross the boundaries of the atomic cells used in the integration of the CP map, at least when isotropic core component averaging is used.

In this way, the E_a and $E_{nonlocal}$ components of the DFT total energy can be moved from the $E_{remainder}$ term of Equation 4.2 into the grid of voxel energies. Their incorporation into the pressure map then occurs naturally through the differentiation of the energy grid with respect to volume (Equation 4.4). At this point, $P_{remainder}$ contains only contributions from the Ewald energy and the band occupancy smearing energy.

As the band occupancy smearing energy is not localizable to any particular points in space, it is reasonable to treat this unmapped pressure as homogenously distributed across the unit cell. E_{Ewald}, on the other hand, represents the electrostatic energy of a homogeneous electron gas surrounding an array of point charges, which involves both the total energy of all the ions interacting with the homogenous electron gas as well as a converging sum of the Coulomb repulsion between every pair of ions in an infinite crystal lattice, shown in Equation 2. The Ewald energy has the form:[2]

$$E_{Ewald} \propto \sum_{i \neq j} \frac{q_i q_j}{|r_i - r_j|} = \sum_{i \neq j} \left(\frac{q_i q_j \, erfc(\eta |r_i - r_j|)}{|r_i - r_j|} \right) + \sum_{i \neq j} \left(\frac{q_i q_j \, erf(\eta |r_i - r_j|)}{|r_i - r_j|} \right) \tag{B.2}$$

In this equation, the divergent summation over the Coulombic interactions between charges in a lattice is decomposed into a short range and long range components, which are best treated in real and reciprocal space, respectively. The parameter η determines how steeply the short range interactions are extinguished with increasing distance (r), with the distance cut-off of the short range component rough-

ly corresponding to $\eta \times r = 2.0$. Once and η value is chosen, the short range ion-ion portion of E_{Ewald} is attributed to pairs of atoms, and the corresponding pressures can be applied to the contact volumes described in the main text.

We have now described how the largest energy components contributing to $P_{remainder}$ can be resolved spatially. In what ways does such a mapping influence the results of a DFT-CP analysis? In Figure S1, we plot CP anisotropy surfaces for Ca_5Sn_3 with different combinations of $P_{remainder}$ terms included in the CP map, using the contact volume integration scheme. Two different pseudopotentials for Ca are used: the images in the left column were generated from calculations using the semicore Ca potential, while those on the right we made using the valence-only potential. E_a and $E_{nonlocal}$ energies were mapped to spheres of radius 0.3 Å around the nuclear positions, while an η value of 0.25 a_0^{-1} (corresponding to a cut-off distance of about 8 a_0 or 4.2 Å) was used for the short-range E_{Ewald} contributions.

All versions of the semicore calculations, including Figure 4.6c, show essentially identical results, regardless of which additional terms are mapped. This high correspondence can be understood in that the semicore Ca pseudopotential, which explicitly models 10 electrons as valence as compared to 2 electrons in the valence-only pseudopotential, nearly completely captures the true core-electron effects of an all-electron calculation in the vicinity of the Ca. In this case, the short-range Ewald repulsion between Ca cores is high and the $E_{nonlocal}$ and E_a corrections are small.

The invariance of the semicore Ca results to the mapping of $P_{remainder}$ terms suggests that a reliable picture of the pressures at work in the hypothetical Ca_5Sn_3 structure has been obtained. From a practical point of view, then, we can judge the value of mapping the $P_{remainder}$ terms by their ability to bring agreement between the semicore Ca picture and that obtained with the valence-only Ca pseudopotential. In

other words, the mapping the remainder terms is useful if they correct for any missing core effects from using a smoother, valence-only pseudopotential. Somewhat surprisingly, this appears to not be the case. Moving down the valence-only results from Figures B.1a, to B.1b, to B.1c, and finally to Figure 4.6c, we see that the correspondence to the semicore picture increases as fewer $P_{remainder}$ terms are mapped.

Why would this be? There are, in fact, good physical reasons why mapping the remainder terms could be problematic. The short-range E_{Ewald} pressure depends heavily on the choice of η value, which introduces a large ambiguity into the CP results. There is also an inherent ambiguity in the E_a and $E_{nonlocal}$ terms as well. While we have shown how to distribute these pressures to individual atoms, we have no way of determining their spatial directionality. Rather than arbitrarily mapping these values isotropically into the core regions, it seems more valid to treat them homogeneously across the entire unit cell.

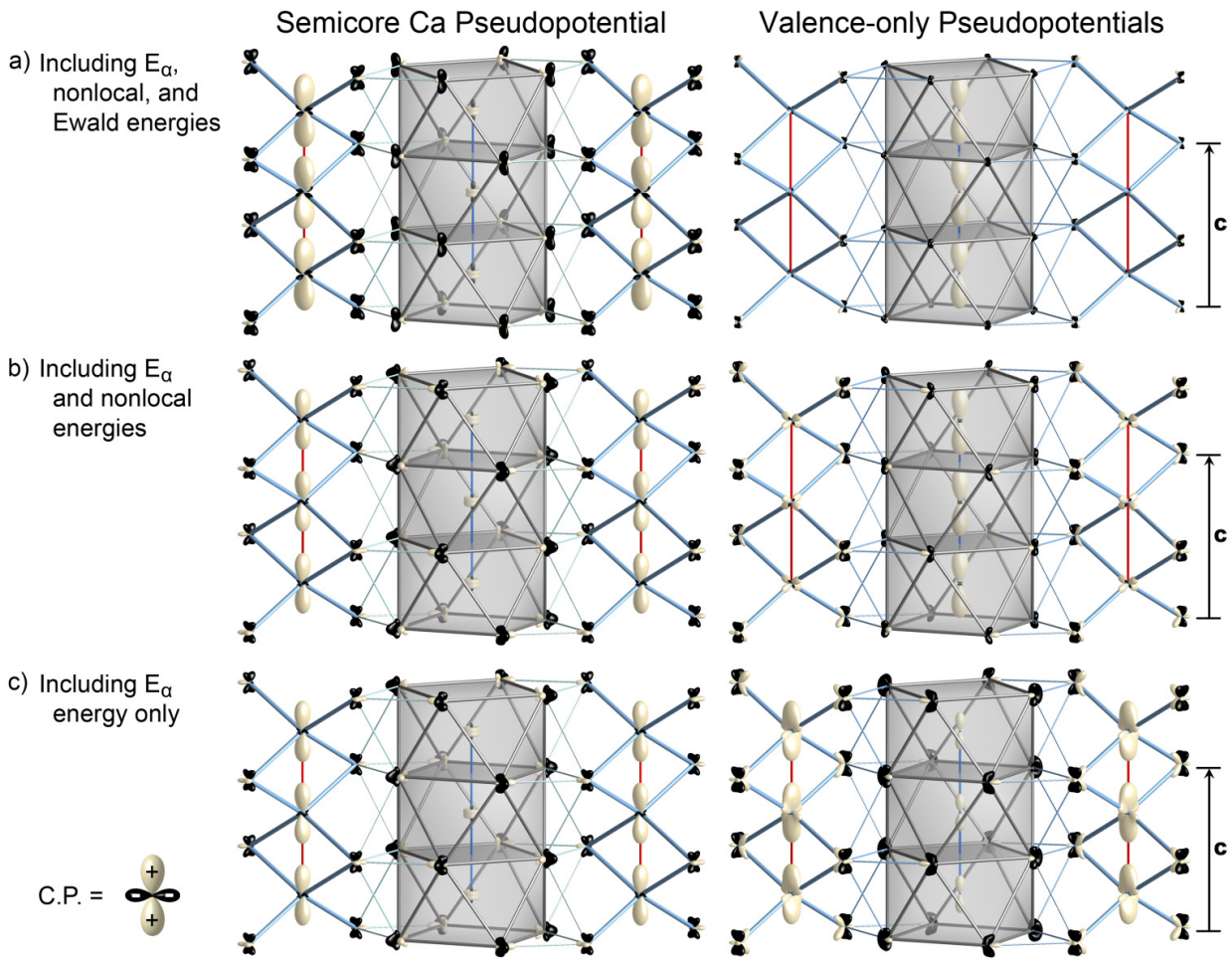

Figure B.1. The CP distribution around each atom is shown as a radial plot. See Figure 6 for details. The scale in the three semicore results is set to 150. For the valence-only plots, the scale of (a) is 1250 and the scales of (b) and (c) are both 2500.

B.2. Annotated ABINIT input file for the calculation of nonlocal energies atom by atom

```
!Ca5Sn3 first nonlocal calculation for the conventional unit cell.

!Changes for the nonlocal calculation:
natom  1              !Only one atom is placed in the cell at a time.
ndtset  32            !There is a separate calculation for each atom.
nsym  1               !The symmetry is set to P1.
ntypat  2
znucl  20      50
typat1  1             !The first 20 calculations are for Ca atoms.
typat2  1
typat3  1
typat4  1
typat5  1
typat6  1
typat7  1
typat8  1
typat9  1
typat10 1
typat11 1
typat12 1
typat13 1
typat14 1
typat15 1
typat16 1
typat17 1
typat18 1
typat19 1
typat20 1
typat21 2             !The final 12 calculations are for Sn atoms.
typat22 2
typat23 2
typat24 2
typat25 2
typat26 2
typat27 2
typat28 2
typat29 2
typat30 2
typat31 2
typat32 2
```

```
!The fractional coordinates of each atom for separate calculations:
xred1    0.5000000000    0.0000000000    0.2499999992
xred2    0.5000000000    0.0000000000    0.7499999803
xred3    0.0000000000    0.5000000000    0.7499999803
xred4    0.0000000000    0.5000000000    0.2499999992
xred5    0.4159988753    0.2844270151    0.5000000000
xred6    0.2155730038    0.9159988377    0.0000000000
xred7    0.7155730218    0.4159988753    0.5000000000
xred8    0.0840011616    0.7844270151    0.5000000000
xred9    0.5840011616    0.2844270151    0.0000000000
xred10   0.9159988377    0.2155730038    0.5000000000
xred11   0.4159988753    0.7155730218    0.0000000000
xred12   0.2155730038    0.0840011616    0.5000000000
xred13   0.7155730218    0.5840011616    0.0000000000
xred14   0.7844270151    0.9159988377    0.5000000000
xred15   0.0840011616    0.2155730038    0.0000000000
xred16   0.5840011616    0.7155730218    0.5000000000
xred17   0.7844270151    0.0840011616    0.0000000000
xred18   0.2844270151    0.5840011616    0.5000000000
xred19   0.9159988377    0.7844270151    0.0000000000
xred20   0.2844270151    0.4159988753    0.0000000000
xred21   0.5000000000    0.5000000000    0.2499999992
xred22   0.0000000000    0.0000000000    0.2499999992
xred23   0.5000000000    0.5000000000    0.7499999803
xred24   0.0000000000    0.0000000000    0.7499999803
xred25   0.3427017685    0.8427018053    0.5000000000
xred26   0.1572982504    0.3427017685    0.5000000000
xred27   0.8427018053    0.3427017685    0.0000000000
xred28   0.8427018053    0.6572982315    0.5000000000
xred29   0.3427017685    0.1572982504    0.0000000000
xred30   0.6572982315    0.1572982504    0.5000000000
xred31   0.1572982504    0.6572982315    0.0000000000
xred32   0.6572982315    0.8427018053    0.0000000000

!The total charge in the unit cell for each calculation:

charge1 -86
charge2 -86     !The first 20 calculations involve a
charge3 -86             !single Ca atom in a unit cell with
charge4 -86             !the surrounding electronic structure
charge5 -86             !arising from 20 Ca and 12 Sn atoms.
charge6 -86             !The total number of electrons is
charge7 -86             !20*2 + 12*4 = 88 electrons. The one
```

```
charge8 -86                !Ca ion has a charge of +2, which makes
charge9 -86                !the total charge in the cell -86.
charge10 -86
charge11 -86
charge12 -86
charge13 -86
charge14 -86
charge15 -86
charge16 -86
charge17 -86
charge18 -86
charge19 -86
charge20 -86
charge21 -84     !The last 12 calculations involve a
charge22 -84               !single Sn atom with a charge of +4,
charge23 -84               !making the total cell charge -84.
charge24 -84
charge25 -84
charge26 -84
charge27 -84
charge28 -84
charge29 -84
charge30 -84
charge31 -84
charge32 -84

!The charge and kpoint distribution is held fixed:
getwfk 1        !The wavefunction is read in from a
prtwf 0                    !previous calculation.
getden 1        !The electron density is read in
prtden 0                   !from a previous calculation.
nstep 0              !The wavefunctions are not updated.
kptopt 0             !The kpoints are specified explicitly
nkpt 12                    !from the previous SCF calculation.
kpt  0.1250000000   0.1250000000   0.0625000000
   0.3750000000   0.1250000000   0.0625000000
   0.3750000000   0.3750000000   0.0625000000
   0.1250000000   0.1250000000   0.1875000000
   0.3750000000   0.1250000000   0.1875000000
   0.3750000000   0.3750000000   0.1875000000
   0.1250000000   0.1250000000   0.3125000000
   0.3750000000   0.1250000000   0.3125000000
   0.3750000000   0.3750000000   0.3125000000
```

```
   0.1250000000    0.1250000000    0.4375000000
   0.3750000000    0.1250000000    0.4375000000
   0.3750000000    0.3750000000    0.4375000000
wtk 0.0625000000    0.1250000000    0.0625000000
   0.0625000000    0.1250000000    0.0625000000
   0.0625000000    0.1250000000    0.0625000000
   0.0625000000    0.1250000000    0.0625000000

!These parameters are left unchanged:

acell    1.8897261329      1.8897261329      1.8897261329  Bohr
rprim   12.1986207140      0.0000000000      0.0000000000
        0.0000000000     12.1986207140      0.0000000000
        0.0000000000      0.0000000000      5.9549405940
ecut   30.000000  Hartree
tsmear  0.0050000  Hartree
toldfe  0.0000000367493254  Hartree
occopt  3
nband   108
ngfft     120 120 60

!Changes for the second nonlocal calculation:
!getwfk 3        !The wavefunction and density are read in for
!getden 3                !the second volume of the CP calculation.
```

B.3. Optimized structures, total energies, and breakdowns of total pressures by energy terms

Table B.1. Unit cell parameters for the VASP optimized structures of Ca_5Sn_3 and $Ca_{36}Sn_{23}$

	Ca_5Sn_3	$Ca_{36}Sn_{23}$
a	12.1864342798648764	12.1519878572427977
c	5.9489916024459149	22.1713863342970328

Table B.2. Reduced coordinates for atoms in VASP optimized structure of Ca_5Sn_3

Atom type	*x*	*y*	*z*
Ca	0.5	0	0.25
Ca	0.5	0	0.75
Ca	0	0.5	0.75
Ca	0	0.5	0.25
Ca	0.415999	0.284427	0.5
Ca	0.215573	0.915999	0
Ca	0.715573	0.415999	0.5
Ca	0.084001	0.784427	0.5
Ca	0.584001	0.284427	0
Ca	0.915999	0.215573	0.5
Ca	0.415999	0.715573	0
Ca	0.215573	0.084001	0.5
Ca	0.715573	0.584001	0
Ca	0.784427	0.915999	0.5
Ca	0.084001	0.215573	0
Ca	0.584001	0.715573	0.5
Ca	0.784427	0.084001	0
Ca	0.284427	0.584001	0.5
Ca	0.915999	0.784427	0
Ca	0.284427	0.415999	0
Sn	0.5	0.5	0.25
Sn	0	0	0.25
Sn	0.5	0.5	0.75
Sn	0	0	0.75
Sn	0.342702	0.842702	0.5
Sn	0.157298	0.342702	0.5
Sn	0.842702	0.342702	0
Sn	0.842702	0.657298	0.5
Sn	0.342702	0.157298	0
Sn	0.657298	0.157298	0.5
Sn	0.157298	0.657298	0
Sn	0.657298	0.842702	0

Table B.3. Reduced coordinates for atoms in VASP optimized structure of $Ca_{36}Sn_{23}$

Atom type	*x*	*y*	*z*
Ca	0.944181	0.788422	0.908049
Ca	0.211578	0.944181	0.908049
Ca	0.055819	0.211578	0.908049
Ca	0.288422	0.444181	0.908049
Ca	0.444181	0.711578	0.091951
Ca	0.555819	0.288422	0.091951
Ca	0.288422	0.444181	0.091951
Ca	0.711578	0.555819	0.091951
Ca	0.711578	0.555819	0.908049
Ca	0.444181	0.711578	0.908049
Ca	0.555819	0.288422	0.908049
Ca	0.211578	0.944181	0.091951
Ca	0.944181	0.788422	0.091951
Ca	0.788422	0.055819	0.091951
Ca	0.788422	0.055819	0.908049
Ca	0.055819	0.211578	0.091951
Ca	0.912902	0.784767	0.631103
Ca	0.215232	0.912902	0.631103
Ca	0.087098	0.215232	0.631103
Ca	0.784767	0.087098	0.631103
Ca	0.412902	0.715232	0.368897
Ca	0.587098	0.284768	0.368897
Ca	0.284768	0.412902	0.368897
Ca	0.715232	0.587098	0.368897
Ca	0.412902	0.715232	0.631103
Ca	0.587098	0.284768	0.631103
Ca	0.215232	0.912902	0.368897
Ca	0.912902	0.784767	0.368897
Ca	0.784767	0.087098	0.368897
Ca	0.087098	0.215232	0.368897
Ca	0.284768	0.412902	0.631103
Ca	0.715232	0.587098	0.631103
Ca	0.787273	0.923357	0.760904
Ca	0.076643	0.787273	0.760904
Ca	0.212727	0.076643	0.760904
Ca	0.923357	0.212727	0.760904
Ca	0.287273	0.576643	0.239096
Ca	0.712727	0.423356	0.239096
Ca	0.423356	0.287273	0.239096
Ca	0.576643	0.712727	0.239096
Ca	0.287273	0.576643	0.760904

Ca	0.712727	0.423356	0.760904
Ca	0.076643	0.787273	0.239096
Ca	0.787273	0.923357	0.239096
Ca	0.923357	0.212727	0.239096
Ca	0.212727	0.076643	0.239096
Ca	0.423356	0.287273	0.760904
Ca	0.576643	0.712727	0.760904
Ca	0.416731	0.282083	0.5
Ca	0.217917	0.083269	0.5
Ca	0.916731	0.217917	0.5
Ca	0.583269	0.717917	0.5
Ca	0.782083	0.916731	0.5
Ca	0.083269	0.782083	0.5
Ca	0.717917	0.416731	0.5
Ca	0.282083	0.583269	0.5
Ca	0.834569	0.334569	0
Ca	0.334569	0.165431	0
Ca	0.165431	0.665431	0
Ca	0.665431	0.834569	0
Ca	0.5	0	0.872466
Ca	0.5	0	0.127534
Ca	0	0.5	0.127534
Ca	0	0.5	0.872466
Ca	0.5	0	0.721301
Ca	0.5	0	0.278699
Ca	0	0.5	0.278699
Ca	0	0.5	0.721301
Ca	0.5	0	0.571767
Ca	0	0.5	0.428233
Ca	0.5	0	0.428233
Ca	0	0.5	0.571767
Sn	0.153331	0.653331	0.638892
Sn	0.653331	0.846669	0.638892
Sn	0.846669	0.346669	0.638892
Sn	0.653331	0.846669	0.361108
Sn	0.846669	0.346669	0.361108
Sn	0.346669	0.153331	0.361108
Sn	0.153331	0.653331	0.361108
Sn	0.346669	0.153331	0.638892
Sn	0.303398	0.196602	0.869386
Sn	0.696602	0.803398	0.869386
Sn	0.696602	0.803398	0.130614
Sn	0.303398	0.196602	0.130614

Sn	0.803398	0.303398	0.869386
Sn	0.196602	0.696602	0.869386
Sn	0.196602	0.696602	0.130614
Sn	0.803398	0.303398	0.130614
Sn	0.662822	0.162822	0.783678
Sn	0.662822	0.162822	0.216322
Sn	0.837178	0.662822	0.216322
Sn	0.337178	0.837178	0.216322
Sn	0.837178	0.662822	0.783678
Sn	0.162822	0.337178	0.783678
Sn	0.162822	0.337178	0.216322
Sn	0.337178	0.837178	0.783678
Sn	0.843035	0.656965	0.5
Sn	0.343035	0.843035	0.5
Sn	0.156965	0.343035	0.5
Sn	0.656965	0.156965	0.5
Sn	0.912088	0.587912	0
Sn	0.587912	0.087912	0
Sn	0.412088	0.912088	0
Sn	0.087912	0.412088	0
Sn	0.5	0.5	0.164275
Sn	0.5	0.5	0.835725
Sn	0	0	0.835725
Sn	0	0	0.164275
Sn	0.5	0.5	0.301163
Sn	0	0	0.698837
Sn	0.5	0.5	0.698837
Sn	0	0	0.301163
Sn	0.5	0.5	0.433748
Sn	0	0	0.433748
Sn	0.5	0.5	0.566252
Sn	0	0	0.566252
Sn	0.5	0.5	0
Sn	0	0	0

Table B.4. Data on the total energies and pressure components of structures considered (in atomic units)

	Ca_5Sn_3 (valence-only Ca)	Ca_5Sn_3 (semicore Ca)	$Ca_{36}Sn_{23}$
total energy (ABINIT)	-58.757676168	-778.16450094	-221.67674155
total energy (VASP)	-4.499800907		-16.869428852
kinetic E pressure	0.0036552	0.003576	0.00354703
local psp E pressure	0.0016288	0.037223	0.00165429
Hartree E pressure	-0.000597	-0.0125	-0.00060361
exchange-correlation E pressure	-0.000832	-0.00135	-0.00083634
Ewald E pressure	-0.003587	-0.02925	-0.00361534
–kT × entropy pressure	3.99E-06	4.25E-06	0.00000386
psp core E pressure	0.0011493	0.002326	0.00117043
nonlocal psp E pressure	-0.001513	7.58E-06	-0.00141023
total pressure	-9.2E-05	3.17E-05	-0.00008991

B.4 References

(1) Filippetti, A.; Fiorentini, V. *Phys. Rev. B* **2000**, *61*, 8433.

(2) Martin, R. M. *Electronic structure : basic theory and practical methods*; 1st pbk. ed.; Cambridge University Press: Cambridge, UK ; New York, 2008.

Appendix C.

Supporting information for Chapter 5:

Problem Solving with Pentagons: the Tsai-type Quasicrystal as a Structural Response to Chemical Pressure

C.1. Detailed Technical Procedures

The DFT-Chemical Pressure analyses presented in this work were performed on structures optimized with LDA-DFT. Initial optimizations were performed using the Vienna Abinitio Simulation Package (VASP)[1,2] because of the low energy-cutoffs required for its ultrasoft pseudopotentials,[3] and were followed by ABINIT[4,5] optimizations to yield structures at the ground state geometry for the ABINIT potentials. In both programs, the optimizations were carried out in two steps: first the ionic positions were relaxed in a fixed unit cell, and then all structural parameters were released. In VASP, both steps were performed in the high-precision mode, corresponding to an energy cutoffs of 18.37 Ha for all *3d* and *5d* transition metal $CaCu_5$-type compounds, 9.139 Ha for $CaPd_5$, 8.298 Ha for $CaAg_5$, and 7.713 Ha for $CaCd_5$ and $CaCd_6$. $7 \times 7 \times 7$ Γ-centered k-point meshes were used for all optimizations.

The optimization performed in ABINIT utilized the LDA functional of Goedecker, Teter, and Hutter[6] and the Hartwigsen-Goedecker-Hutter (HGH) pseudopotentials.[7] In all calculations, the Ca semi-

core pseudopotential was used, with the exception of those used for Figure S1b, where a valence only Ca pseudopotential was employed for comparison. Transition metal pseudopotentials were selected to have a consistent valence electron sets: d^{10} electrons for Group 10 metals, $d^{10}s^1$ electrons for Group 11, and $d^{10}s^2$ electrons for Group 12. This corresponds to the HGH valence-only pseudopotentials for the nickel family and HGH semicore pseudopotentials for the other transition metals. Energy cutoffs were tested for convergence and set to 85 Ha for compounds containing 3*d* metals, and 35 Ha for the 4*d* and 5*d* metals. Calculations for all $CaCu_5$-type compounds utilized a 5 × 5 × 6 k-point mesh, shifted from the Γ point by half a grid step along *c**, as recommended by the ABINIT software.

Once the optimizations were complete, three single-point calculations were performed using ABINIT over a span of 3% about the optimal unit cell volume to prepare the electron densities, potentials, and kinetic energy densities needed for the creation of CP maps. Pseudopotentials, energy cutoffs, and k-point meshes for all $CaCu_5$-type compounds were the same as in the ABINIT optimization step. The calculation on the Tsai-type $CaCd_6$ compound utilized the same HGH pseudopotentials and energy cutoff as for $CaCd_5$, but a 3 × 3 × 3 Γ-centered k-point mesh. The voxel spacing in the CP maps were derived from the fast Fourier transform grids used in the ABINIT calculations (150 × 150 × 120 for all $CaCu_5$-type phases, 144 × 144 × 144 for the primitive cell of $CaCd_6$).

The DFT-CP software is based on two programs used to calculate the CP maps and integrate and project the CP distribution around each atom.[8,9] *CPcalc_abinit* was used to calculate the CP maps from the ABINIT single point calculations, and apply isotropic core averaging to the CP map with radii set to 85 % of the metallic radii[10] (other fractions of the metallic radii were found to yield similar results). The results presented here were shown to be qualitatively consistent across different choices of these radii.

The contact volume integration scheme of the *CPintegrate* program was used to project the CP map onto real spherical harmonics ($l \leq 5$) centered at the atomic positions.

The resulting CP schemes depended little on whether the VASP- or ABINIT-optimized coordinates were used for $CaCd_6$ and the $CaCu_5$-type compounds. In the figures of the paper, the plots for the $CaCu_5$-type phases are based on the geometries obtained from ABINIT, while those presented for $CaCd_6$ were generated using the VASP-optimized structure, and later checked against the results of the ABINIT optimization as it became available much later.

C.2. Chemical Pressure Analysis of $CaCu_5$-type $CaTM_5$ Structures for First, Second, and Third Row Transition Metals

CP anisotropy surfaces for $CaCu_5$-type $CaTM_5$ compounds are shown in Figure S1a. Of these nine compounds, five are observed to form ($CaNi_5$, $CaCu_5$, $CaZn_5$, $CaPd_5$, and $CaPt_5$), while the remaining four are hypothetical.[11] The same figure is replicated in Figure C.1b, employing calcium valence only pseudopotentials instead of the semicore Ca potential used for all other calculations. Within Figure S1a most striking, perhaps, is the similarity of each of the nine plots, with negative net pressure on the central calcium and positive pressure along the TM-TM contacts. Within each row, the trend of the *4d* metals repeats itself: increasing the TM radius from 1.24 Å in $CaNi_5$ to 1.28 Å in $CaCu_5$ intensifies the magnitude of the positive pressure between contacts on the TM sublattice. Increasing the transition metal radius to 1.34 Å in $CaZn_5$ further enlarges both the negative pressure on the central calcium and the positive pressure on the TM sublattice. Similar trends exist for $CaPt_5$ (r_{Pt} = 1.385 Å), $CaAu_5$ (r_{Au} = 1.44 Å), and $CaHg_5$ (r_{Hg} = 1.51 Å).

Comparing CP down a column, however, yields the opposite trend, where smaller radii are associated with larger pressure magnitudes. This appears to be a disconcerting result as generally a compound with higher overall pressures is expected to be more unstable. Yet in the case of these 3*d* compounds, all are observed experimentally, and all have more intense CP values than the hypothetical $CaCd_5$. An explanation for the large differences between TMs from different rows could be the large changes in localization and polarizability on moving from the 3*d* orbitals to the 4*d* and then 5*d* orbitals. For instance, compared to the nearly core-like *d* electrons of zinc, the valence *d* electrons of cadmium would be expected to much more easily adapt to volume perturbations. Ultimately this observation leads to our hesitation in making quantitative CP comparisons between the rows of the transition metal series, but in our current research we are continuing to address the issue of handling highly localized electrons in the generation of CP maps. The best comparisons of all, of course, are between different structures adopted by the same elements, e.g. $CaCd_5$ versus $CaCd_6$.

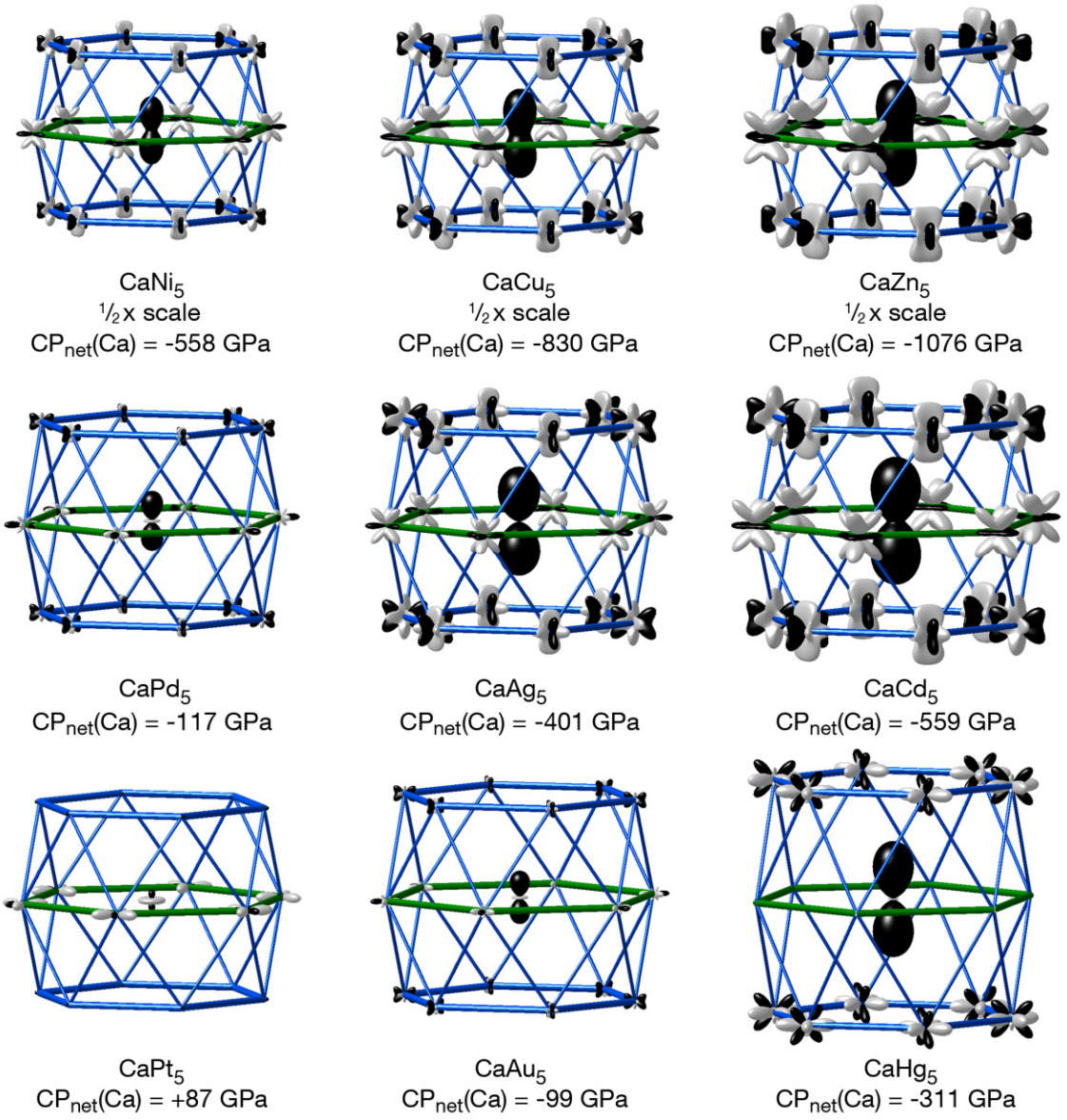

Figure C.1.1. Chemical pressure analysis for $CaCu_5$-type $CaTM_5$ compounds for 3*d*, 4*d*, and 5*d* transition metals of Groups 10-12 calculated using the HGH semicore pseudopotential for calcium. Five of these are observed compounds, while the remaining four—$CaAg_5$, $CaCd_5$, $CaAu_5$, and $CaHg_5$—are hypothetical. Trends across the *3d* and *5d* compounds are similar to those seen comparing $CaPd_5$, $CaAg_5$, and $CaCd_5$ (discussed in Figure 2 of the main text). Comparisons between rows reveal that compounds involving the first row transition metals exhibit much higher pressures than those involving their heavier congeners. This may better reflect the differences between 3*d*, 4*d*, and 5*d* electrons than differences in thermodynamic feasibility.

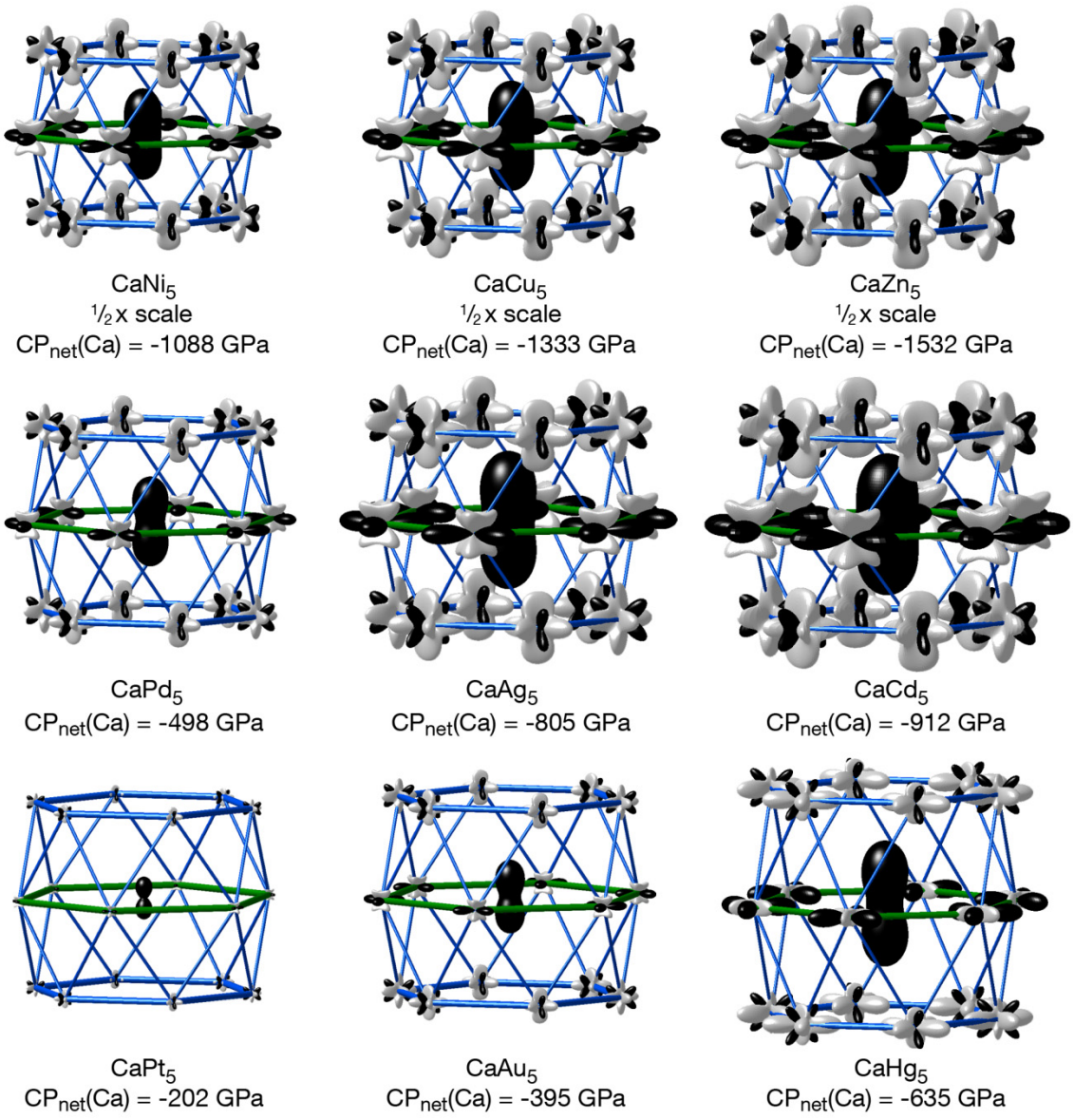

Figure C.1b. Chemical pressure analysis of nine $CaCu_5$-type $CaTM_5$ compounds using an HGH valence only pseudopotential for calcium. The previous figure illustrates a similar analysis for compounds with semicore pseudopotentials for calcium. Trends are similar in the two figures, with more isotropic negative pressures around the calcium when it is modeled with a valence-only pseudopotential.

C.3. Chemical pressure analysis of the interfaces between Tsai-type clusters

The atoms at interfaces between clusters in $CaCd_6$ experience milder chemical pressures than those in the $CaCu_5$-type alternative structure, just as with the clusters themselves. Clusters related by translation of one unit cell vector share a hexagonal face of the outer-most layer (green, Figure 5.3a). At the center of this planar ring is a Cd-Cd dumbbell of atoms from the icosidodecahedra (blue polyhedra) of the constituent clusters. We zoom-in on this shared interface in Figure C.2b. The CPs reflect mostly the expected repulsive Cd-Cd interactions, but the distances between the cadmium atoms on the dumbbells and ring are appear to be too long, resulting in black CP lobes. Outside of the disordered tetrahedron at each cluster's center, this is the only Cd-Cd interaction in the structure exhibiting negative pressure.

In Figures C.2c and d, the interface between clusters related by a (½ ½ ½) translation along the body diagonal is shown. Here, clusters interpenetrate to form a piece of the fluorite structure (Figure C.2d). While the outer Ca octahedron (red bars) is made up of three calcium atoms from each contributing cluster, 6 of the 8 atoms making up the Cd cube (blue bars) are shared between clusters in the overlapping region. A triangular face of one cluster's icosidodecahedron (blue) is shared with the other's outermost layer (green), and vise-versa. The remaining two atoms on the cube are from the inner dodecahedron (light green polyhedra). The chemical pressure distributions on these sites show the expected Ca-Cd attraction and Cd-Cd repulsion.

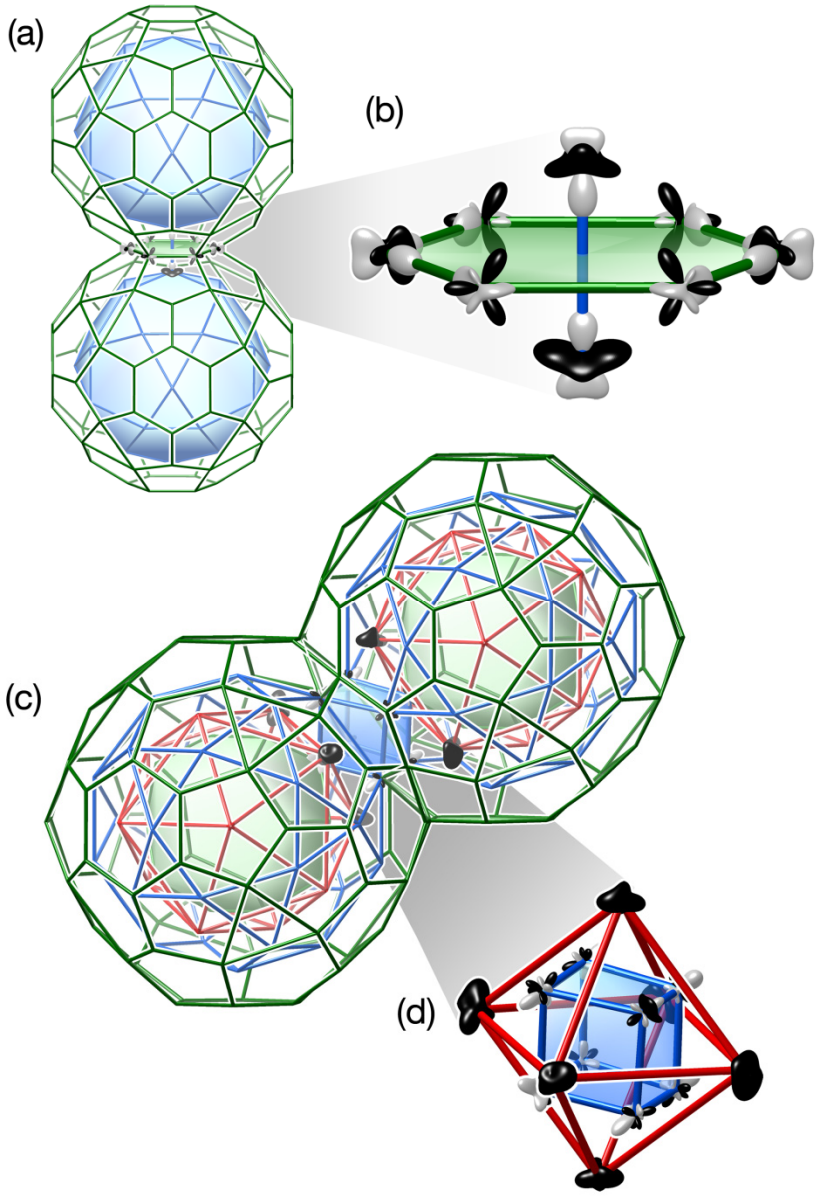

Figure C.2. The interfaces between Tsai-type clusters in $CaCd_6$ can be classified as (a) face sharing along the conventional unit cell vectors or (c) interpenetrating along the body diagonal of the unit cell. The face sharing clusters meet at the hexagonal face of each cluster's outermost layer (green). For clarity, this is highlighted in (b). The interpenetrating clusters form a piece of the fluorite structure type, highlighted in (d). The atomic CP anisotropies are represented with black and white surfaces according to plotting conventions specified in Figure 5.2 of the main text.

C.4. Optimized structural parameters and total energies for the featured compounds

Table C.1. Unit cell parameters for the VASP- and ABINIT-optimized hexagonal $CaCu_5$-type structures

	VASP-optimized cell parameters (Å)		*ABINIT-optimized cell parameters (Å)*	
	a	**c**	**a**	**c**
$CaNi_5$	4.79900963303210	3.82861647198872	4.8170111191	3.8434428996
$CaCu_5$	4.94592168597328	3.96851985724119	4.9726743200	3.9701005013
$CaZn_5$	5.20133415091003	4.11580057783162	5.2372083800	4.0891380042
$CaPd_5$	5.19464655624132	4.37413658805988	5.2452381400	4.4177836179
$CaAg_5$	5.42329541654141	4.57170632261188	5.4485355307	4.5689961513
$CaCd_5$	5.71694013733297	4.70028785946675	5.7756663887	4.6777442545
$CaPt_5$	5.29380034327244	4.36622960515773	5.3395604802	4.3989445477
$CaAu_5$	5.45954838317557	4.61208645798223	5.4823444884	4.6338144401
$CaHg_5$	5.69380980952675	5.19779257875175	5.6188638174	5.3455120203

Table C.2. Unit cell parameters for the $CaCd_6$ structure (converted to conventional cell for convenience)

	a	***b***	***c***	***α***	***β***	***γ***
VASP-optimized	15.20917 Å	15.27806 Å	15.20253 Å	90°	90°	89.9137°
ABINIT-optimized	15.2945 Å	15.3072 Å	15.2931 Å	90°	90°	90°

Table C.3.1. Atomic coordinates for VASP-optimized $CaCd_6$ structure (converted to conventional cell for convenience)

Element	***x***	***y***	***z***
Ca	0.20409	0.49988	0.31545
Ca	0.69793	0.00012	0.18868
Ca	0.31158	0.19797	0.50013
Ca	0.30207	0.99988	0.18868
Ca	0.00023	0.81083	0.29794
Ca	0.18792	0.69839	0.00051
Ca	0.31208	0.80161	0.50051
Ca	0.79591	0.50012	0.31545
Ca	0.99984	0.81229	0.69867
Ca	0.18842	0.30203	0.00013
Ca	0.49977	0.68917	0.79794
Ca	0.50016	0.68771	0.19866

Cd	0.19913	0.88117	0.65770
Cd	0.19890	0.11637	0.33944
Cd	0.84117	0.70085	0.61922
Cd	0.19907	0.88340	0.34033
Cd	0.12345	0.65534	0.20568
Cd	0.34183	0.79980	0.11829
Cd	0.15817	0.70020	0.61830
Cd	0.30110	0.38363	0.83944
Cd	0.38497	0.16029	0.30306
Cd	0.84102	0.70076	0.38408
Cd	0.87655	0.34466	0.20568
Cd	0.61503	0.83971	0.30306
Cd	0.65898	0.79924	0.88408
Cd	0.30093	0.61660	0.84033
Cd	0.30094	0.38186	0.15719
Cd	0.19906	0.11814	0.65719
Cd	0.30087	0.61883	0.15770
Cd	0.38502	0.83900	0.30295
Cd	0.15982	0.70002	0.38468
Cd	0.34018	0.79998	0.88468
Cd	0.1239	0.34422	0.20546
Cd	0.65883	0.79915	0.11922
Cd	0.61498	0.16100	0.30295
Cd	0.87610	0.65578	0.20546
Cd	0.40651	0.50009	0.73093
Cd	0.40799	0.5	0.25189
Cd	0.09201	0	0.75189
Cd	0.09349	0.99991	0.23093
Cd	0.99966	0.73635	0.09781
Cd	0.23728	0.90613	0.00366
Cd	0.75969	0.90541	0.00320
Cd	0.26272	0.59387	0.50366
Cd	0.49950	0.27553	0.41380
Cd	0.74031	0.59459	0.50320
Cd	0.00034	0.26365	0.09781
Cd	0.50050	0.72447	0.41380
Cd	0.15858	0.50008	0.09650
Cd	0.15916	0.50025	0.90356
Cd	0.59564	0.65773	0.99860
Cd	0.34084	0.99975	0.40356
Cd	0.00010	0.59489	0.34280
Cd	0.40433	0.65802	0.99888
Cd	0.09567	0.84198	0.49888
Cd	0.49979	0.09637	0.15795
Cd	0.90436	0.84227	0.49860
Cd	0.99990	0.40511	0.34280
Cd	0.50021	0.90363	0.15795
Cd	0.34142	0.99992	0.59650
Cd	0.65994	0.34039	0.33930
Cd	0.15929	0.16325	0.15944
Cd	0.84071	0.83675	0.15944

Cd	0.16123	0.83524	0.16154
Cd	0.83877	0.16476	0.16154
Cd	0.34006	0.65961	0.33930
Cd	0.33859	0.33897	0.33817
Cd	0.16141	0.16103	0.83817
Cd	0.5	0	0.31295
Cd	0.99969	0.68550	0.50006
Cd	0.50031	0.81450	0.00006
Cd	0.18442	0.99975	0.50041
Cd	0.31558	0.50025	0.00041
Cd	0	0.5	0.18388
Cd	0.49996	0.90855	0.48893
Cd	0.09329	0.50143	0.50041
Cd	0.40671	0.99857	0.00041
Cd	0	0	0.58680
Cd	0	0	0.40041
Cd	0.50004	0.09145	0.48893
Cd	0.40760	0.49611	0.43422
Cd	0.59240	0.50389	0.43422
Cd	0.00421	0.91024	0.07446
Cd	0.99579	0.08976	0.07446

Table C.3.2. Atomic coordinates for ABINIT-optimized $CaCd_6$ structure (converted to conventional cell for convenience)

Element	*x*	*y*	*z*
Ca	0.70423	0	0.81419
Ca	0.68926	0.80134	0.50055
Ca	0.5	0.69066	0.79637
Ca	0.5	0.68797	0.19958
Ca	0.19895	0.5	0.68911
Ca	0.31074	0.19866	0.50055
Ca	0.30105	0	0.18912
Ca	0.5	0.30934	0.79637
Ca	0.18926	0.69866	0.00055
Ca	0.81074	0.30134	0.00055
Ca	0.79577	0.5	0.31419
Ca	0	0.81203	0.69958
Cd	0.19909	0.88337	0.65759
Cd	0.34081	0.20102	0.88464
Cd	0.37663	0.84412	0.70545
Cd	0.11482	0.33944	0.80266
Cd	0.65919	0.79898	0.88464
Cd	0.30061	0.61593	0.84042
Cd	0.80091	0.88337	0.65759
Cd	0.69909	0.61663	0.15759

Cd	0.80091	0.11663	0.65759
Cd	0.38518	0.83944	0.30266
Cd	0.65919	0.20102	0.88464
Cd	0.69939	0.61593	0.84042
Cd	0.34081	0.79898	0.88464
Cd	0.12337	0.34412	0.20545
Cd	0.15803	0.29860	0.61896
Cd	0.61482	0.16056	0.30266
Cd	0.87663	0.65588	0.20545
Cd	0.90644	0	0.23412
Cd	0.90750	0	0.75293
Cd	0.59250	0.5	0.25293
Cd	0.59356	0.5	0.73412
Cd	0	0.73281	0.09727
Cd	0.84197	0.70140	0.61896
Cd	0.24238	0.90491	0.00325
Cd	0.25762	0.40491	0.50325
Cd	0.25762	0.59509	0.50325
Cd	0	0.77281	0.91267
Cd	0.74238	0.59509e	0.50325
Cd	0.5	0.76719e	0.59727
Cd	0	0.22719	0.91267
Cd	0.65474	0	0.59570
Cd	0.15754	0.5	0.90248
Cd	0.09579	0.15536	0.49852
Cd	0.69939	0.38407	0.84042
Cd	0.84246	0.5	0.90248
Cd	0.5	0.09549	0.84524
Cd	0.90421	0.15536	0.49852
Cd	0.09579e	0.84464	0.49852
Cd	0.5	0.09690	0.15571
Cd	0.40421	0.34464	0.99853
Cd	0.5	0.90451	0.84524
Cd	0.5	0.90310	0.15571
Cd	0.84526	0.5	0.09570
Cd	0.66050	0.33993	0.33946
Cd	0.62337	0.15588	0.70545
Cd	0.66097	0.66382	0.66055
Cd	0.33903	0.33618	0.66055
Cd	0.66097	0.33618	0.66055
Cd	0.83903	0.16382	0.16055
Cd	0.33950	0.66007	0.33946
Cd	0.33950	0.33993	0.33946
Cd	0.16050	0.16007	0.83946
Cd	0.5	0	0.30966
Cd	0	0.68791	0.49989
Cd	0	0.31209	0.49989
Cd	0.34197	0.79860	0.11896
Cd	0.18709	0	0.5
Cd	0.81292	0	0.5
Cd	0.5	0	0.68724

Cd	0	0.40702	0.98211
Cd	0.09379	0.5	0.50075
Cd	0.40621	0	0.00075
Cd	0	0	0.58934
Cd	0.5	0.5	0.90027
Cd	0	0.59298	0.98211
Cd	0.90562	0	0.93685
Cd	0.65803	0.20140	0.11896
Cd	0.09438	0	0.93685
Cd	0.5	0.40920	0.57570
Cd	0.5	0.59080	0.57570
Cd	0.80061	0.88407	0.34042
Cd	0.88518	0.66056	0.80266

Table C.4. Total energies per atom in selected VASP- and ABINIT-optimized geometries (in atomic units)

	$CaPd_5$	$CaAg_5$	$CaCd_5$	$CaCd_6$
Total free energy (ABINIT)	-30.27341961	-36.95184724	-44.51424557	-44.72989501
Total free energy (VASP)	-0.224077336	-0.134753168	-0.068562046	-0.0695630248

C.5. References

(1) Kresse, G.; Furthmüller, J. *Phys. Rev. B* **1996**, *54*, 11169.

(2) Kresse, G.; Furthmüller, J. *Comput. Mater. Sci.* **1996**, *6*, 15.

(3) Vanderbilt, D. *Phys. Rev. B* **1990**, *41*, 7892.

(4) Gonze, X.; Rignanese, G.-M.; Verstraete, M.; Beuken, J.-M.; Pouillon, Y.; Caracas, R.; Jollet, F.; Torrent, M.; Zerah, G.; Mikami, M.; Ghosez, P.; Veithen, M.; Raty, J.-Y.; Olevano, V.; Bruneval, F.; Reining, L.; Godby, R.; Onida, G.; Hamann, D. R.; Allan, D. C. *Z. Kristallogr.* **2005**, *220*, 558.

(5) Gonze, X.; Amadon, B.; Anglade, P. M.; Beuken, J. M.; Bottin, F.; Boulanger, P.; Bruneval, F.; Caliste, D.; Caracas, R.; Cote, M.; Deutsch, T.; Genovese, L.; Ghosez, P.; Giantomassi, M.; Goedecker, S.; Hamann, D. R.; Hermet, P.; Jollet, F.; Jomard, G.; Leroux, S.; Mancini, M.; Mazevet, S.; Oliveira, M. J. T.; Onida, G.; Pouillon, Y.; Rangel, T.; Rignanese, G. M.; Sangalli, D.; Shaltaf, R.; Torrent, M.; Verstraete, M. J.; Zerah, G.; Zwanziger, J. W. *Comput. Phys. Commun.* **2009**, *180*, 2582.

(6) Goedecker, S.; Teter, M.; Hutter, J. *Phys. Rev. B* **1996**, *54*, 1703.

(7) Hartwigsen, C.; Goedecker, S.; Hutter, J. *Phys. Rev. B* **1998**, *58*, 3641.

(8) Fredrickson, D. C. *J. Am. Chem. Soc.* **2012**, *134*, 5991.

(9) Engelkemier, J.; Berns, V. M.; Fredrickson, D. C. *J. Chem. Theory Comput.* **2013**, *9*, 3170.

(10) Greenwood, N.; Earnshaw, A. In *Chemistry of the Elements*; 2 ed.; Butterworth-Heinemann: Oxford, UK, 1997.

(11) *ASM Alloy Phase Diagrams Center; http://www1.asminternational.org/AsmEnterprise/APD*; Villars, P.; Okamoto, H.; Cenzual, K., Eds.; ASM International: Materials Park, OH, 2006.

Appendix D.

Supporting Information for Chapter 6:

Progress in Visualizing Atomic Size Effects with DFT-Chemical Pressure Analysis: From Isolated Atoms to Trends in AB_5 Intermetallics

D.1. Detailed Technical Procedures

The geometrical optimization of each structure was carried out in two steps: first the ionic positions were relaxed in a fixed unit cell, and then all structural parameters were released. Energy cutoffs for the planewave basis were set sufficiently high to converge the energy of formation to less than 0.5 meV/atom. Monkhorst-Pack k-point grids[1] were constructed by specifying the ngkpt input parameter or by using the prtkpt utility. Unless otherwise specified, semicore HGH potentials[2] (when available) were used for all atoms, with the exception of Pd, for which the valence-only version is most comparable to the semicore pseudopotentials of Cu, Ag and Au. Further details regarding the calculations are given in Table D.1, while the optimized structural parameters are listed in Tables D.2-D.11.

Once the optimizations were complete, three single-point calculations were performed over a span of 3% about the optimal unit cell volume to prepare the electron densities, potentials, and kinetic energy densities needed for the creation of CP maps. The voxel spacing in the CP maps were derived from the fast Fourier transform grids used in the ABINIT calculations. The DFT-CP software is based on two programs used to calculate the CP maps, as well as integrate and project the CP distribution around each

atom. *CPmap* generates the CP maps from the ABINIT single point calculations, and including the grid unwarping procedure described in the main text. The Hirshfeld-inspired integration scheme is implemented in the *CPintegrate* program, which was used to project the CP map onto real spherical harmonics ($l \leq 5$) centered at the atomic positions.

Table D.1. Computational parameters and total energies

Structure[a]	*Energy cutoff*	*Number of unique k-points*	*FFT grid*	*Total energy*
Isolated Ca (SC)	35 Ha	1	150 × 150 × 150	-36.640997 Ha
Isolated Ca (VO)	35 Ha	1	150 × 150 × 150	-0.668313 Ha
Isolated La	40 Ha	1	150 × 150 × 150	-31.592133 Ha
Isolated Cu	45 Ha	1	120 × 120 × 120	-46.910665 Ha
Isolated Pd	40 Ha	1	150 × 150 × 150	-28.799283 Ha
Isolated Cd	35 Ha	1	150 × 150 × 150	-45.998438 Ha
Isolated Au	80 Ha	1	150 × 150 × 150	-33.160002 Ha
Isolated Ga (SC)	80 Ha	1	150 × 150 × 150	-74.004191 Ha
Isolated Ga (VO)	80 Ha	1	150 × 150 × 150	-2.149122 Ha
$SrAg_5$	50 Ha	15	150 × 150 × 120	-215.769000 Ha
La_5Sn_3	40 Ha	4	108 × 108 × 108	-339.327910 Ha
Ni_3C	80 Ha	60	80 × 80 × 80	-234.948791 Ha
$NbGa_3$	50 Ha	18	75 × 75 × 75	-12.047973 Ha
$CaCu_5$ ($CaCu_5$-type)	85 Ha	15	150 × 150 × 120	-277.195271 Ha
$CaCu_5$ ($AuBe_5$-type)	85 Ha	10	150 × 150 × 150	-1108.722801 Ha
$CaAu_5$ ($CaCu_5$-type)	30 Ha	15	150 × 150 × 120	-203.316309 Ha
$CaAu_5$ ($AuBe_5$-type)	30 Ha	10	120 × 120 × 120	-813.277045 Ha

[a]"Isolated" refers to a single atom placed in the center of a 10 Å cubic unit cell. See Tables D.2 and D.3.

D.2. Structural parameters

Table D.2. Unit cell parameters for DFT-optimized structures (converted to conventional cells for convenience)

Structure	*a*	*b*	*c*	*α*	*β*	*γ*
All isolated atoms	10.00000 Å	10.00000 Å	10.00000 Å	90°	90°	90°
$SrAg_5$	5.55915 Å	5.55915 Å	4.54145 Å	90°	90°	120°
La_5Sn_3	12.59205 Å	12.59205 Å	6.17215 Å	90°	90°	90°
Ni_3C	4.49667 Å	4.49667 Å	12.71836 Å	90°	90°	120°
$NbGa_3$	3.68337 Å	3.68337 Å	8.52030 Å	90°	90°	90°
$CaCu_5$ ($CaCu_5$-type)	4.97267 Å	4.97267 Å	3.97010 Å	90°	90°	120°
$CaCu_5$ ($AuBe_5$-type)	6.88885 Å	6.88885 Å	6.88885 Å	90°	90°	90°
$CaAu_5$ ($CaCu_5$-type)	5.48234 Å	5.48234 Å	4.63381 Å	90°	90°	120°
$CaAu_5$ ($AuBe_5$-type)	7.71309 Å	7.71309 Å	7.71309 Å	90°	90°	90°

Table D.3. Atomic coordinates for all single-atom calculations

Element	*x*	*y*	*z*
Any	0.50000	0.50000	0.50000

Table D.4. Atomic coordinates for ABINIT-optimized $SrAg_5$ structure

Element	*x*	*y*	*z*
Sr	0.00000	0.00000	0.00000
Ag	0.33333	0.66667	0.00000
Ag	0.66667	0.33333	0.00000
Ag	0.50000	0.50000	0.50000
Ag	0.00000	0.50000	0.50000
Ag	0.50000	0.00000	0.50000

Table D.5. Atomic coordinates for ABINIT-optimized La_5Sn_3 structure (converted to conventional cell for convenience)

Element	*x*	*y*	*z*
La	0.08563	0.21856	0.00000
La	0.58563	0.71856	0.50000
La	0.00000	0.50000	0.25000
La	0.50000	0.00000	0.75000
La	0.78144	0.08563	0.00000
La	0.28144	0.58563	0.50000
La	0.50000	0.00000	0.25000
La	0.00000	0.50000	0.75000
La	0.91437	0.21856	0.50000

La	0.41437	0.71856	0.00000
La	0.41437	0.28144	0.50000
La	0.91437	0.78144	0.00000
La	0.28144	0.41437	0.00000
La	0.78144	0.91437	0.50000
La	0.21856	0.08563	0.50000
La	0.71856	0.58563	0.00000
La	0.71856	0.41437	0.50000
La	0.21856	0.91437	0.00000
La	0.58563	0.28144	0.00000
La	0.08563	0.78144	0.50000
Sn	0.15987	0.65987	0.00000
Sn	0.65987	0.15987	0.50000
Sn	0.00000	0.00000	0.25000
Sn	0.50000	0.50000	0.75000
Sn	0.34013	0.15987	0.00000
Sn	0.84013	0.65987	0.50000
Sn	0.34013	0.84013	0.50000
Sn	0.84013	0.34013	0.00000
Sn	0.15987	0.34013	0.50000
Sn	0.65987	0.84013	0.00000
Sn	0.00000	0.00000	0.75000
Sn	0.50000	0.50000	0.25000

Table D.6. Atomic coordinates for ABINIT-optimized $NbGa_3$ structure (converted to conventional cell for convenience)

Element	*x*	*y*	*z*
Nb	0.00000	0.00000	0.00000
Nb	0.50000	0.50000	0.50000
Ga	0.00000	0.00000	0.50000
Ga	0.50000	0.50000	0.00000
Ga	0.00000	0.50000	0.25000
Ga	0.50000	0.00000	0.75000
Ga	0.50000	0.00000	0.25000
Ga	0.00000	0.50000	0.75000

Table D.7. Atomic coordinates for VASP-optimized Ni_3C structure (converted to conventional cell for convenience)

Element	*x*	*y*	*z*
Ni	0.33333	0.00000	0.25000
Ni	0.66667	0.00000	0.75000
Ni	0.00000	0.33333	0.25000
Ni	0.00000	0.66667	0.75000
Ni	0.66667	0.66667	0.25000
Ni	0.33333	0.33333	0.75000
Ni	0.00000	0.33333	0.08333
Ni	0.33333	0.33333	0.58333
Ni	0.66667	0.66667	0.41667
Ni	0.66667	0.00000	0.58333
Ni	0.33333	0.00000	0.41667
Ni	0.00000	0.66667	0.58333
Ni	0.66667	0.66667	0.08333
Ni	0.00000	0.66667	0.91667
Ni	0.33333	0.00000	0.08333
Ni	0.33333	0.33333	0.91667
Ni	0.00000	0.33333	0.41667
Ni	0.66667	0.00000	0.91667
C	0.00000	0.00000	0.00000
C	0.00000	0.00000	0.50000
C	0.66667	0.33333	0.33333
C	0.66667	0.33333	0.83333
C	0.33333	0.66667	0.66667
C	0.33333	0.66667	0.16667

Table D.8. Atomic coordinates for ABINIT-optimized $CaCu_5$ structure ($CaCu_5$-type)

Element	*x*	*y*	*z*
Ca	0.00000	0.00000	0.00000
Cu	0.33333	0.66667	0.00000
Cu	0.66667	0.33333	0.00000
Cu	0.50000	0.50000	0.50000
Cu	0.00000	0.50000	0.50000
Cu	0.50000	0.00000	0.50000

Table D.9. Atomic coordinates for ABINIT-optimized $CaCu_5$ structure ($AuBe_5$-type)

Element	*x*	*y*	*z*
Ca	0.00000	0.00000	0.00000
Ca	0.50000	0.50000	0.00000
Ca	0.00000	0.50000	0.50000
Ca	0.50000	0.00000	0.50000
Cu	0.25000	0.25000	0.25000
Cu	0.62500	0.62500	0.62500
Cu	0.75000	0.75000	0.25000
Cu	0.37500	0.37500	0.62500
Cu	0.75000	0.25000	0.75000
Cu	0.37500	0.62500	0.37500
Cu	0.25000	0.75000	0.75000
Cu	0.62500	0.37500	0.37500
Cu	0.12500	0.12500	0.62500
Cu	0.87500	0.87500	0.62500
Cu	0.87500	0.12500	0.37500
Cu	0.12500	0.87500	0.37500
Cu	0.62500	0.12500	0.12500
Cu	0.37500	0.87500	0.12500
Cu	0.37500	0.12500	0.87500
Cu	0.62500	0.87500	0.87500
Cu	0.12500	0.62500	0.12500
Cu	0.87500	0.37500	0.12500
Cu	0.87500	0.62500	0.87500
Cu	0.12500	0.37500	0.87500

Table D.10. Atomic coordinates for ABINIT-optimized $CaAu_5$ structure ($CaCu_5$-type)

Element	*x*	*y*	*z*
Ca	0.00000	0.00000	0.00000
Au	0.33333	0.66667	0.00000
Au	0.66667	0.33333	0.00000
Au	0.50000	0.50000	0.50000
Au	0.00000	0.50000	0.50000
Au	0.50000	0.00000	0.50000

Table D.11. Atomic coordinates for ABINIT-optimized $CaAu_5$ structure ($AuBe_5$-type)

Element	*x*	*y*	*z*
Ca	0.00000	0.00000	0.00000
Ca	0.50000	0.50000	0.00000
Ca	0.00000	0.50000	0.50000
Ca	0.50000	0.00000	0.50000
Au	0.25000	0.25000	0.25000
Au	0.62500	0.62500	0.62500
Au	0.75000	0.75000	0.25000
Au	0.37500	0.37500	0.62500
Au	0.75000	0.25000	0.75000
Au	0.37500	0.62500	0.37500
Au	0.25000	0.75000	0.75000
Au	0.62500	0.37500	0.37500
Au	0.12500	0.12500	0.62500
Au	0.87500	0.87500	0.62500
Au	0.87500	0.12500	0.37500
Au	0.12500	0.87500	0.37500
Au	0.62500	0.12500	0.12500
Au	0.37500	0.87500	0.12500
Au	0.37500	0.12500	0.87500
Au	0.62500	0.87500	0.87500
Au	0.12500	0.62500	0.12500
Au	0.87500	0.37500	0.12500
Au	0.87500	0.62500	0.87500
Au	0.12500	0.37500	0.87500

D.3. Discussion of the prevalence of highly positive CP features in the atomic core regions that are oriented between internuclear vectors, rather than along them

In Figure 6.4f of the main text, strong chemical pressure features are observed in the core regions of the Ca atoms. The directionality of these features would suggest that they arise from interatomic interactions, but they are awkwardly oriented along the boundaries between contact volumes. This is in fact a specific example of an interesting trend that we have observed for a variety of phases, which we will now explore. In Figure D.1, we show isosurfaces of the CP maps generated for a series of structures, with the isosurface level set to a sufficiently high level that only the most intense, positive pressure features are visible. For all of the structures shown, the isosurfaces reveal lobes that are directed into interstitial spaces rather than along the interatomic contacts.

For $CaPd_2$ (Figure D.1a), the tetrapod of white pressure isosurfaces around each calcium atom point not to the nearest calcium neighbor, but to the centers of the triangular faces of the surrounding Pd truncated tetrahedron. This is echoed in Figure S1b, where similar four-pronged pressures on the elemental silicon point into the interstices. On $CrGa_4$ in the $PtHg_4$ type[3,4] (Figure D.1c), the octahedral arrangement of lobes around the Cr atoms appears to suggest positive pressures along Cr-Cr contacts, but the 5.5 Å bond length suggests this is quite far from a too-close contact ($2 \times d_{Cr} = 2 \times 1.28 = 2.56$ Å). Finally, the niobium atom in $NbGa_3$[5] (Figure D.1d) exhibits these pressure features oriented toward the top and bottom square faces of a cuboctahedron of gallium atoms. These features point out of the *ab* plane of the Nb atom, in which the closest Nb-Ga contacts occur (2.65 Å vs 2.86 Å for out-of-plane contacts). What is the source of these features of the chemical pressure maps?

A straightforward approach to investigating the origins of these features is to plot the contributions to the CP maps from specific terms in the total energy. For simplicity, we will pursue this

approach here with just for elemental silicon, though the same could be carried out for all of the structures depicted in Figure 6.1.

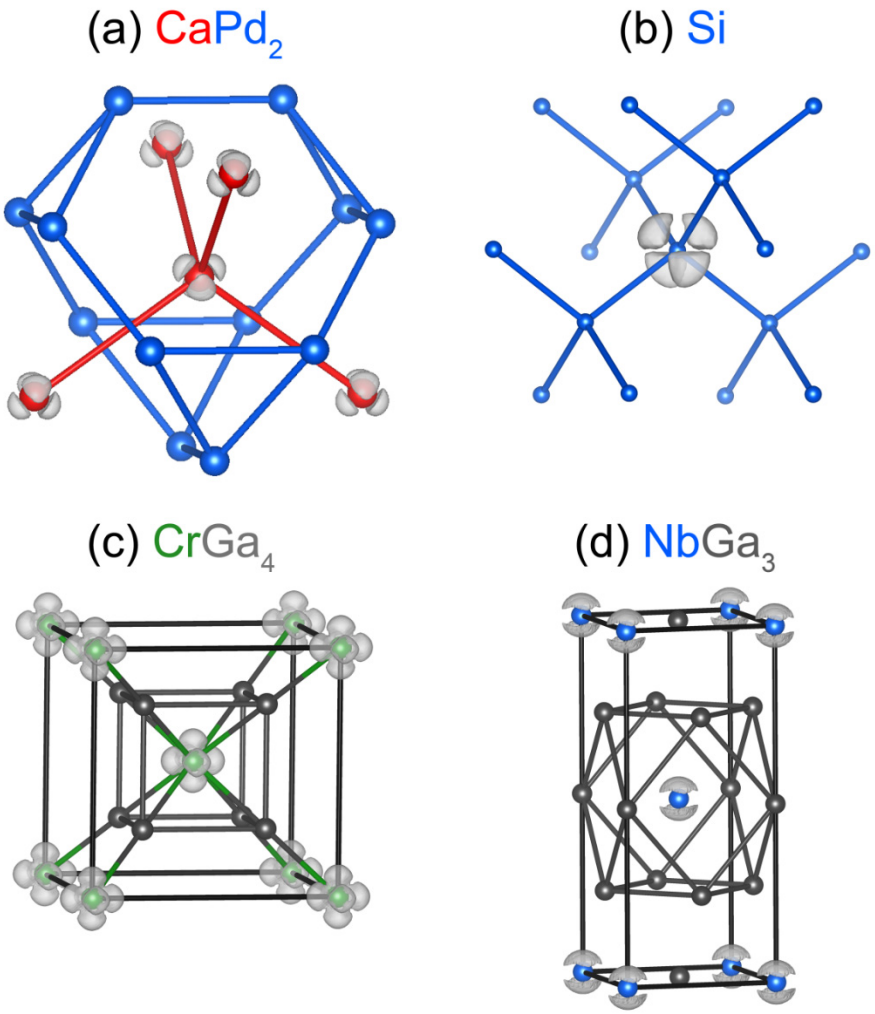

Figure D.1. Positive chemical pressure is shown for a series of solid state structures. (a) $CaPd_2$ in the $MgCu_2$-type Laves phase at an isosurface value of 0.075 a.u. This is a 3-dimensional plot of the strongest positive features seen in Figure 4f of the main text. These positive pressure features point not between atomic contacts, but rather to the void spaces in the structure. The same trend can be seen for (b) elemental Si, plotted at an isosurface value of 0.022 a.u., (c) $CrGa_4$ in the $PtHg_4$ type, plotted at 0.083, and (d) $NbGa_3$ in the $TiAl_3$ type, plotted at 0.085.

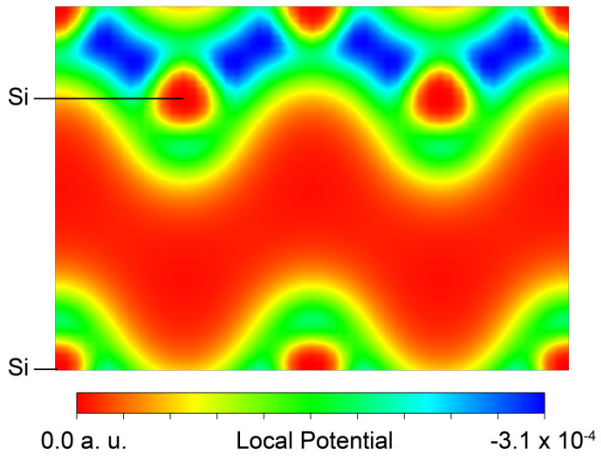

Figure D.2. The difference between the local potential surfaces of elemental silicon from the expanded unit cell volume to the contracted unit cell volume, corrected for distortion using CPmap. The (110) plane of the structure is depicted to capture the interatomic interactions.

After examining separately each energetic contribution to the chemical pressure, we found that the major contribution to these positive pressure features was the local potential component of the total energy. In Figure D.2, we see the difference in the local potential on going from a slightly expanded structure to a slightly contracted one. This is akin to computing only the local potential component of the chemical pressure, without multiplying by the electron density and dividing by the change in volume.

We note first that this function is non-positive over the entire unit cell. This implies that the potential becomes universally more negative as the cell contracts, with nearly zero change far from the nuclei. The largest changes are, in fact, between silicon atoms, implying a drastic deepening of the potential on contraction of the unit cell, as is expected for a model of overlapping potential wells. As the atoms are forced closer together, the overlap of the potentials increases, and electrons in the middle ground experience a stronger interaction with both nuclei. This strongly negative component lies directly

in line with interatomic contact. When calculating the chemical pressure, the local component depicted in Figure D.2 provides a severe negative component between atoms, which counteracts the strong positive features normally present in the core of the atom. The positive core features remain unopposed in the other directions around an atomic center, with the net result being the appearance of relatively intense positive pressure features appearing in the core regions away from the interatomic vectors for strong interactions.

Figure D.3 shows the integrated results for the chemical pressure calculation on elemental silicon. Si-Si contacts are nearly optimal, with only small white lobes pointing between them. No longer do we see the high positive pressures observed in Figure S1b; in their place are negative lobes, pointing to interstitial voids within the diamond framework, better reflecting our chemical intuition of this structure.

The integration step correctly disperses the strongly positive features (as seen in Figure 6.4f of the main text), resulting in interatomic pressures that well-represent the full interaction.

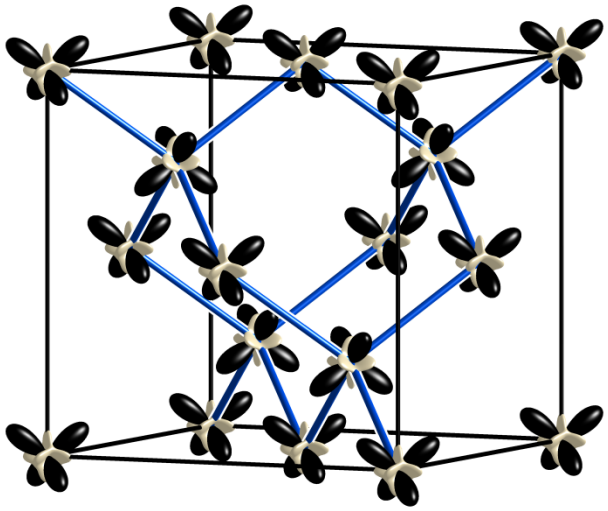

Figure D.3. The DFT-CP anisotropies calculated for elemental silicon. Pressures are near optimal between silicon atoms, as expected. Negative pressure features point towards void spaces in the structure.

D.4. Voxel volume calculation in distorted grid

Since the grid unwarping procedure leads to shifts of grid points relative to a uniform grid, the volume associated with each voxel is no longer constant. The calculation of the corrected voxel volumes is important for subsequent integration over the grids, but the computational cost for an exact calculation of voxel volumes can be prohibitive. Here we present the approximate calculation adopted in the *CPmap* program and demonstrate that it gives satisfyingly accurate results for small distortions of the grid.

In the following discussion, we use $(\boldsymbol{p},\boldsymbol{q},\boldsymbol{r}) \equiv (\boldsymbol{p}\times\boldsymbol{q})\cdot\boldsymbol{r} \equiv \begin{vmatrix} p_x & p_y & p_z \\ q_x & q_y & q_z \\ r_x & r_y & r_z \end{vmatrix}$ to denote the triple product of three-dimensional vectors $\boldsymbol{p},\boldsymbol{q},\boldsymbol{r}$.

For an undistorted grid, each voxel takes the shape of a parallelepiped, so its volume is simply given by

$$V_{voxel} = (\boldsymbol{a}_{voxel}, \boldsymbol{b}_{voxel}, \boldsymbol{c}_{voxel})$$

where $\boldsymbol{a}_{voxel}, \boldsymbol{b}_{voxel}, \boldsymbol{c}_{voxel}$ are the three edge vectors of the undistorted voxel parallelepiped. Here we take voxel 000 to be the voxel of interest, where 000 is its index $n_x n_y n_z$ in the voxel grid. If we consider the coordinates of its six direct neighbors, it can be seen that

$$r_{100} - r_{\bar{1}00} = 2\boldsymbol{a}_{voxel}, r_{010} - r_{0\bar{1}0} = 2\boldsymbol{b}_{voxel}, r_{001} - r_{00\bar{1}} = 2\boldsymbol{c}_{voxel}$$

So we can write its voxel volume as an expression of the coordinates of its neighbors:

$$V_{000} = (\boldsymbol{a}_{voxel}, \boldsymbol{b}_{voxel}, \boldsymbol{c}_{voxel}) = \frac{1}{8}(2\boldsymbol{a}_{voxel}, 2\boldsymbol{b}_{voxel}, 2\boldsymbol{c}_{voxel})$$

$$= \frac{1}{8}(\boldsymbol{r}_{100} - \boldsymbol{r}_{\bar{1}00}, \boldsymbol{r}_{010} - \boldsymbol{r}_{0\bar{1}0}, \boldsymbol{r}_{001} - \boldsymbol{r}_{00\bar{1}}) \tag{D.1}$$

As will be shown in the discussion below, Eq. D.1 can also be applied to approximately to the distorted grid. We will see that this equation captures the essential effect of distortion of neighboring voxels on a voxel's volume, and also preserves (to first order) the sum of all voxel volumes as equal to the total unit cell volume.

Lemma. For a change in the position of any of the six direct neighbor voxels to 000, the first order change to V_{000} (as defined by Eq. D.1) will be $\frac{1}{2}\Delta k \cdot V_{voxel}$, where Δk is the perturbation along the corresponding voxel edge vector away from 000. The other components of the displacement have only higher order effects.

Proof. In a distorted grid, any voxel may experience a perturbation $\Delta \boldsymbol{r}_{n_x n_y n_z}$, so we have

$$V'_{000} = \frac{1}{8}\big((r_{100} - r_{\bar{1}00}) + (\Delta r_{100} - \Delta r_{\bar{1}00}), (r_{010} - r_{0\bar{1}0}) + (\Delta r_{010} - \Delta r_{0\bar{1}0}), (r_{001} - r_{00\bar{1}}) + (\Delta r_{001} - \Delta r_{00\bar{1}})\big)$$

$$= \frac{1}{8}\big(2\boldsymbol{a}_{voxel} + (\Delta r_{100} - \Delta r_{\bar{1}00}), 2\boldsymbol{b}_{voxel} + (\Delta r_{010} - \Delta r_{0\bar{1}0}), 2\boldsymbol{c}_{voxel} + (\Delta r_{001} - \Delta r_{00\bar{1}})\big) \tag{D.2}$$

Since the triple product is linear with respect to each variable, an expansion of Eq. D.2 gives

$$\Delta V_{000} = V'_{000} - V_{000}$$

$$= \frac{1}{8}[(\Delta r_{100} - \Delta r_{\bar{1}00}, 2\boldsymbol{b}_{voxel}, 2\boldsymbol{c}_{voxel}) + (2\boldsymbol{b}_{voxel}, \Delta r_{010} - \Delta r_{0\bar{1}0}, 2\boldsymbol{c}_{voxel}) + (2\boldsymbol{a}_{voxel}, 2\boldsymbol{b}_{voxel}, \Delta r_{001} - \Delta r_{00\bar{1}})]$$

$$+ 2^{nd} \textit{and higher order terms}$$

$$= \frac{1}{8}[(\Delta r_{100}, 2\boldsymbol{b}_{voxel}, 2\boldsymbol{c}_{voxel}) + (2\boldsymbol{b}_{voxel}, \Delta r_{010}, 2\boldsymbol{c}_{voxel}) + (2\boldsymbol{a}_{voxel}, 2\boldsymbol{b}_{voxel}, \Delta r_{001})]$$

$$- \frac{1}{8}[(\Delta r_{\bar{1}00}, 2\boldsymbol{b}_{voxel}, 2\boldsymbol{c}_{voxel}) + (2\boldsymbol{b}_{voxel}, \Delta r_{0\bar{1}0}, 2\boldsymbol{c}_{voxel}) + (2\boldsymbol{a}_{voxel}, 2\boldsymbol{b}_{voxel}, \Delta r_{00\bar{1}})]$$

$$+ 2^{nd} \textit{and higher order terms} \tag{D.3}$$

Here we focus only on the $\Delta \boldsymbol{r}_{100}$ term, since the other five terms can be treated with a similar approach. If we rewrite $\Delta \boldsymbol{r}_{100}$ as a linear combination of the three voxel edge vectors, i.e.

$$\Delta \boldsymbol{r}_{100} = \Delta k_{100a} \boldsymbol{a}_{voxel} + \Delta k_{100b} \boldsymbol{b}_{voxel} + \Delta k_{100c} \boldsymbol{c}_{voxel}$$

the term becomes

$$\frac{1}{8}(\Delta \boldsymbol{r}_{100}, 2\boldsymbol{b}_{voxel}, 2\boldsymbol{c}_{voxel}) = \frac{1}{8}(\Delta k_{100a} \boldsymbol{a}_{voxel} + \Delta k_{100b} \boldsymbol{b}_{voxel} + \Delta k_{100c} \boldsymbol{c}_{voxel}, 2\boldsymbol{b}_{voxel}, 2\boldsymbol{c}_{voxel})$$

$$= \frac{1}{8}(\Delta k_{100a} \boldsymbol{a}_{voxel}, 2\boldsymbol{b}_{voxel}, 2\boldsymbol{c}_{voxel}) = \frac{1}{2} \Delta k_{100a} \cdot V_{voxel}$$

That is, for voxel 100, only a perturbation along the $\boldsymbol{a}_{voxel}$ direction has a first order effect on the voxel volume of $\frac{1}{2} \Delta k_{100a} \cdot V_{voxel}$, while perturbation along $\boldsymbol{b}_{voxel}$ and $\boldsymbol{c}_{voxel}$ has no effect (it only introduces a shearing of the parallelepiped, which does not affect its volume). ■

Proposition. The change in total volume of all voxels as calculated using Eq. S1 in a distorted grid is second order with respect to the distortion.

Proof. We will still focus our discussion on voxel 100. Following from the lemma above, we only need to consider a movement along the $\boldsymbol{a}_{voxel}$ direction. Such a perturbation will change the volume of voxel

000 by $\frac{1}{2}\Delta k_{100a} \cdot V_{voxel}$, but it also changes the volume of voxel 200 by $-\frac{1}{2}\Delta k_{100a} \cdot V_{voxel}$. Therefore the first order perturbations cancel out, so we are left with only the higher order terms in Eq. D.3. It so follows that

$$\sum_{n_x,n_y,n_z} \Delta V_{n_x n_y n_z} = O(|\,\Delta \boldsymbol{r}_{n_x n_y n_z}\,|^2)$$

i.e. the change in total volume of all voxels in the unit cell is second order with respect to the distortion.

■

In all calculations carried out in this Article, the volumes of the voxels in the distorted grid add up to the unit cell volume within 0.00001 Å^3. This threshold can be adjusted in the source code if testing to higher precision is desired.

D.5. References

(1) Monkhorst, H.; Pack, J. *Phys. Rev. B* **1976**, *13*, 5188-5192.

(2) Hartwigsen, C.; Goedecker, S.; Hutter, J. *Phys. Rev. B* **1998**, *58*, 3641-3662.

(3) Meissner, H.-G.; Schubert, K. *Z. Metallkd.* **1965**, *56*, 523-530.

(4) Häussermann, U.; Viklund, P.; Boström, M.; Norrestam, R.; Simak, S. *Phys. Rev. B* **2001**, *63*.

(5) Baron, V. V.; Myzenkova, L. F.; Savitskii, E. M.; Gladyshevskii, E. I. *Zh. Neorg. Khim.* **1964**, *9*, 2170-2173.

Appendix E.

Supplemental information for Chapter 7:

Structural plasticity of the $CaCu_5$-type in Ca-TM systems: Paths for dimensionality reduction under chemical pressure

E.1. Tables of ABINIT optimized geometries

Table E.1. ABINIT-optimized unit cell parameters

	a	*b*	*c*	*α*	*β*	*γ*
$CaPd_5$	5.2452	5.2452	4.4178	90	90	120
$CaAg_5$	5.4485	5.4485	4.5690	90	90	120
$CaCd_5$	5.7757	5.7757	4.6777	90	90	120
Ca_2Ag_7[a]	5.3725	5.3725	13.7402	90	90	119.4681
Ca_2Cd_7[a]	5.6345	5.6345	14.3671	90	90	119.0638
$Ca_{14}Cd_{51}$	13.1251	13.1251	9.4584	90	90	120
$CaCd_6$[b]	15.2945	15.3072	15.2931	90	90	90

[a] Primitive cell setting, [b]Converted to conventional cell from the primitive setting

Table E.2. Atomic coordinates for all ABINIT-optimized $CaCu_5$-type compounds: $CaPd_5$, $CaAg_5$, $CaCd_5$

Element	*x*	*y*	*z*
Ca	0.00000	0.00000	0.00000
Pd/Ag/Cd	0.33333	0.66667	0.00000
Pd/Ag/Cd	0.66667	0.33333	0.00000
Pd/Ag/Cd	0.50000	0.50000	0.50000
Pd/Ag/Cd	0.00000	0.50000	0.50000
Pd/Ag/Cd	0.50000	0.00000	0.50000

Table E.3. Atomic coordinates for ABINIT-optimized Yb_2Ag_7-type compound, Ca_2Ag_7

Element	*x*	*y*	*z*
Ag	0.82874	0.82874	0.25000
Ag	0.00623	0.33527	0.92367
Ag	0.33527	0.00623	0.92367
Ag	0.66473	0.99377	0.42367
Ag	0.00623	0.33527	0.57633
Ag	0.99377	0.66473	0.07633
Ag	0.32910	0.82666	0.25000
Ag	0.66473	0.99377	0.07633
Ag	0.17126	0.17126	0.75000
Ag	0.67090	0.17334	0.75000
Ag	0.33527	0.00623	0.57633
Ag	0.82666	0.32910	0.25000
Ag	0.99377	0.66473	0.42367
Ag	0.17334	0.67090	0.75000
Ca	0.32202	0.32202	0.11456
Ca	0.67798	0.67798	0.61456
Ca	0.32202	0.32202	0.38544
Ca	0.67798	0.67798	0.88544

Table E.4. Atomic coordinates for ABINIT-optimized, hypothetical Yb_2Ag_7-type compound, Ca_2Cd_7

Element	*x*	*y*	*z*
Ca	0.33026	0.33026	0.11943
Ca	0.66974	0.66974	0.61943
Ca	0.33026	0.33026	0.38057
Ca	0.66974	0.66974	0.88057
Cd	0.83026	0.83026	0.25000
Cd	0.01392	0.33411	0.92605
Cd	0.33411	0.01392	0.92605
Cd	0.66589	0.98608	0.42605
Cd	0.01392	0.33411	0.57394
Cd	0.98608	0.66589	0.07394
Cd	0.32928	0.83020	0.25000
Cd	0.66589	0.98608	0.07394
Cd	0.16974	0.16974	0.75000
Cd	0.67072	0.16980	0.75000
Cd	0.33411	0.01392	0.57394
Cd	0.83020	0.32928	0.25000
Cd	0.98608	0.66589	0.42605
Cd	0.16980	0.67072	0.75000

Table E.5. Atomic coordinates for ABINIT-optimized $Gd_{14}Ag_{51}$-type compound, $Ca_{14}Cd_{51}$

Element	*x*	*y*	*z*
Ca	0.00000	0.00000	0.69844
Ca	0.66779	0.12860	0.50000
Ca	0.53558	0.66321	0.50000
Ca	0.87140	0.53918	0.50000
Ca	0.33679	0.87238	0.50000
Ca	0.46082	0.33221	0.50000
Ca	0.00000	0.00000	0.30156
Ca	0.26477	0.38098	0.00000
Ca	0.87939	0.27991	0.00000
Ca	0.61902	0.88379	0.00000
Ca	0.72009	0.59949	0.00000
Ca	0.11621	0.73523	0.00000
Ca	0.40051	0.12061	0.00000
Ca	0.12762	0.46442	0.50000
Cd	0.66669	0.33331	0.00000
Cd	0.76343	0.93561	0.50000
Cd	0.82544	0.76044	0.50000
Cd	0.06439	0.82788	0.50000
Cd	0.26587	0.19324	0.23148
Cd	0.06842	0.26831	0.23510
Cd	0.80676	0.07263	0.23148
Cd	0.73169	0.80011	0.23510
Cd	0.92737	0.73413	0.23148
Cd	0.19989	0.93158	0.23510
Cd	0.73169	0.80011	0.76490
Cd	0.33331	0.66669	0.00000
Cd	0.92737	0.73413	0.76853
Cd	0.19989	0.93158	0.76490
Cd	0.26587	0.19324	0.76853
Cd	0.06842	0.26831	0.76490
Cd	0.80676	0.07263	0.76853
Cd	0.11212	0.49554	0.15359
Cd	0.62073	0.11078	0.15423
Cd	0.50446	0.61658	0.15359
Cd	0.88922	0.50989	0.15423
Cd	0.38342	0.88788	0.15359
Cd	0.66669	0.33331	0.30940
Cd	0.49011	0.37927	0.15423
Cd	0.88922	0.50989	0.84577
Cd	0.38342	0.88788	0.84641
Cd	0.49011	0.37927	0.84577
Cd	0.11212	0.49554	0.84641
Cd	0.62073	0.11078	0.84577
Cd	0.50446	0.61658	0.84641
Cd	0.44495	0.11572	0.33434
Cd	0.32355	0.43994	0.33190
Cd	0.88428	0.32922	0.33434
Cd	0.66669	0.33331	0.69060

Cd	0.56006	0.88361	0.33190
Cd	0.67078	0.55505	0.33434
Cd	0.11639	0.67645	0.33190
Cd	0.56006	0.88361	0.66810
Cd	0.67078	0.55505	0.66566
Cd	0.11639	0.67645	0.66810
Cd	0.44495	0.11572	0.66566
Cd	0.32355	0.43994	0.66810
Cd	0.88428	0.32922	0.66566
Cd	0.89404	0.86444	0.00000
Cd	0.33331	0.66669	0.68821
Cd	0.13556	0.02954	0.00000
Cd	0.97046	0.10596	0.00000
Cd	0.33331	0.66669	0.31179
Cd	0.23956	0.06506	0.50000
Cd	0.17212	0.23657	0.50000
Cd	0.93494	0.17456	0.50000

Table E.6. Atomic coordinates for ABINIT-optimized $CaCd_6$ (converted to conventional cell)

Element	*x*	*y*	*z*
Ca	0.70422	0.00000	0.81419
Ca	0.20422	0.50000	0.31419
Ca	0.68927	0.80133	0.50055
Ca	0.18927	0.30133	0.00055
Ca	0.50000	0.69067	0.79637
Ca	0.00000	0.19067	0.29637
Ca	0.50000	0.68799	0.19958
Ca	0.00000	0.18799	0.69958
Ca	0.19897	0.50000	0.68912
Ca	0.69897	0.00000	0.18912
Ca	0.31073	0.19867	0.50055
Ca	0.81073	0.69867	0.00055
Ca	0.30103	0.00000	0.18912
Ca	0.80103	0.50000	0.68912
Ca	0.50000	0.30933	0.79637
Ca	0.00000	0.80933	0.29637
Ca	0.18927	0.69867	0.00055
Ca	0.68927	0.19867	0.50055
Ca	0.81073	0.30133	0.00055
Ca	0.31073	0.80133	0.50055
Ca	0.79578	0.50000	0.31419
Ca	0.29578	0.00000	0.81419
Ca	0.00000	0.81201	0.69958
Ca	0.50000	0.31201	0.19958
Cd	0.69910	0.38336	0.15759
Cd	0.19910	0.88336	0.65760

Cd	0.34082	0.20105	0.88464
Cd	0.84082	0.70105	0.38464
Cd	0.37665	0.84412	0.70545
Cd	0.87665	0.34412	0.20545
Cd	0.11481	0.33942	0.80266
Cd	0.61481	0.83942	0.30266
Cd	0.65918	0.79895	0.88464
Cd	0.15918	0.29895	0.38464
Cd	0.30060	0.61591	0.84042
Cd	0.80060	0.11591	0.34042
Cd	0.80090	0.88336	0.65760
Cd	0.30090	0.38336	0.15759
Cd	0.69910	0.61664	0.15759
Cd	0.19910	0.11664	0.65760
Cd	0.80090	0.11664	0.65760
Cd	0.30090	0.61664	0.15759
Cd	0.38519	0.83942	0.30266
Cd	0.88519	0.33942	0.80266
Cd	0.65918	0.20105	0.88464
Cd	0.15918	0.70105	0.38464
Cd	0.69940	0.61591	0.84042
Cd	0.19940	0.11591	0.34042
Cd	0.34082	0.79895	0.88464
Cd	0.84082	0.29895	0.38464
Cd	0.12335	0.34412	0.20545
Cd	0.62335	0.84412	0.70545
Cd	0.15802	0.29858	0.61896
Cd	0.65802	0.79858	0.11896
Cd	0.61481	0.16058	0.30266
Cd	0.11481	0.66058	0.80266
Cd	0.87665	0.65588	0.20545
Cd	0.37665	0.15588	0.70545
Cd	0.90643	0.00000	0.23412
Cd	0.40643	0.50000	0.73412
Cd	0.90753	0.00000	0.75293
Cd	0.40753	0.50000	0.25293
Cd	0.59247	0.50000	0.25293
Cd	0.09247	0.00000	0.75293
Cd	0.59357	0.50000	0.73412
Cd	0.09357	0.00000	0.23412
Cd	0.00000	0.73279	0.09727
Cd	0.50000	0.23279	0.59727
Cd	0.84198	0.70142	0.61896
Cd	0.34198	0.20142	0.11896
Cd	0.24237	0.90491	0.00325
Cd	0.74237	0.40491	0.50325
Cd	0.25763	0.40491	0.50325
Cd	0.75763	0.90491	0.00325
Cd	0.25763	0.59509	0.50325
Cd	0.75763	0.09509	0.00325
Cd	0.00000	0.77283	0.91267

Cd	0.50000	0.27283	0.41267
Cd	0.74237	0.59509	0.50325
Cd	0.24237	0.09509	0.00325
Cd	0.50000	0.76721	0.59727
Cd	0.00000	0.26721	0.09727
Cd	0.00000	0.22717	0.91267
Cd	0.50000	0.72717	0.41267
Cd	0.65472	0.00000	0.59570
Cd	0.15472	0.50000	0.09570
Cd	0.15753	0.50000	0.90248
Cd	0.65753	0.00000	0.40248
Cd	0.09576	0.15533	0.49853
Cd	0.59576	0.65533	0.99853
Cd	0.69940	0.38409	0.84042
Cd	0.19940	0.88409	0.34042
Cd	0.84247	0.50000	0.90248
Cd	0.34247	0.00000	0.40248
Cd	0.50000	0.09546	0.84524
Cd	0.00000	0.59546	0.34524
Cd	0.90424	0.15533	0.49853
Cd	0.40424	0.65533	0.99853
Cd	0.09576	0.84467	0.49853
Cd	0.59576	0.34467	0.99853
Cd	0.50000	0.09692	0.15571
Cd	0.00000	0.59692	0.65571
Cd	0.40424	0.34467	0.99853
Cd	0.90424	0.84467	0.49853
Cd	0.50000	0.90454	0.84524
Cd	0.00000	0.40454	0.34524
Cd	0.50000	0.90308	0.15571
Cd	0.00000	0.40308	0.65571
Cd	0.84528	0.50000	0.09570
Cd	0.34528	0.00000	0.59570
Cd	0.66052	0.33990	0.33946
Cd	0.16052	0.83990	0.83946
Cd	0.62335	0.15588	0.70545
Cd	0.12335	0.65588	0.20545
Cd	0.66095	0.66382	0.66055
Cd	0.16095	0.16382	0.16055
Cd	0.33905	0.33618	0.66055
Cd	0.83905	0.83618	0.16055
Cd	0.66095	0.33618	0.66055
Cd	0.16095	0.83618	0.16055
Cd	0.83905	0.16382	0.16055
Cd	0.33905	0.66382	0.66055
Cd	0.33948	0.66010	0.33946
Cd	0.83948	0.16010	0.83946
Cd	0.33948	0.33990	0.33946
Cd	0.83948	0.83990	0.83946
Cd	0.16052	0.16010	0.83946
Cd	0.66052	0.66010	0.33946

Cd	0.50000	0.00000	0.30966
Cd	0.00000	0.50000	0.80966
Cd	0.00000	0.68793	0.49989
Cd	0.50000	0.18793	0.99989
Cd	0.00000	0.31207	0.49989
Cd	0.50000	0.81207	0.99989
Cd	0.34198	0.79858	0.11896
Cd	0.84198	0.29858	0.61896
Cd	0.18707	0.00000	0.50000
Cd	0.68707	0.50000	0.00000
Cd	0.81293	0.00000	0.50000
Cd	0.31293	0.50000	0.00000
Cd	0.50000	0.00000	0.68724
Cd	0.00000	0.50000	0.18724
Cd	0.00000	0.40704	0.98211
Cd	0.50000	0.90704	0.48210
Cd	0.09381	0.50000	0.50075
Cd	0.59381	0.00000	0.00075
Cd	0.40619	0.00000	0.00075
Cd	0.90619	0.50000	0.50075
Cd	0.00000	0.00000	0.58934
Cd	0.50000	0.50000	0.08934
Cd	0.50000	0.50000	0.90027
Cd	0.00000	0.00000	0.40027
Cd	0.00000	0.59296	0.98211
Cd	0.50000	0.09296	0.48210
Cd	0.90564	0.00000	0.93685
Cd	0.40564	0.50000	0.43685
Cd	0.65802	0.20142	0.11896
Cd	0.15802	0.70142	0.61896
Cd	0.09436	0.00000	0.93685
Cd	0.59436	0.50000	0.43685
Cd	0.50000	0.40918	0.57570
Cd	0.00000	0.90918	0.07570
Cd	0.50000	0.59082	0.57570
Cd	0.00000	0.09082	0.07570
Cd	0.80060	0.88409	0.34042
Cd	0.30060	0.38409	0.84042
Cd	0.88519	0.66058	0.80266
Cd	0.38519	0.16058	0.30266

E.2. Table of computational parameters for each calculation

Table E.7. Table of k-point grids, energy cutoffs, total energies and other computational details for all ABINIT calculations

	k-point grid	*k-point shift*	*Number of k points*	*Energy cutoff (Ha)*	*FFT grid*	*Total energy (Ha)*
$CaPd_5$	5x5x6	(0 0 ½)	15	45	150x150x120	-181.64202219
$CaAg_5$	5x5x6	(0 0 ½)	15	40	150x150x120	-221.71118496
$CaCd_5$	5x5x6	(0 0 ½)	15	40	150x150x120	-267.08583986
Ca_2Ag_7	9x9x5	(½ ½ ½)	75	45	120x120x300	-664.95297736
Ca_2Cd_7		(½ ½ ½)	9	40	150x150x120	-791.93885078
$Ca_{14}Cd_{51}$	3x3x4	(0 0 0)	9	40	120x120x90	-286.41355912
$CaCd_6$	3x3x3	(0 0 0)	8	35	150x150x150	-375.73116806

E.3. Further structural details on $Ca_{14}Cd_{51}$'s intercolumn matrix

The connections between the $CaCu_5$ type and $Ca_{14}Cd_{51}$'s columns of Ca1 are readily apparent, owing to similar hexagonal rings as those seen in $CaCu_5$, and a simple stacking pattern along the c axis. The remainder of the structure can also be interpreted as relating to the $CaCu_5$ type, albeit through distorted 7-, 5-, 4- and 3- membered rings. The Ca2 and Ca3 polyhedra shown first in Figure 7.6 reveal the relation to $CaCu_5$, but as the Ca-centered polyhedra of the intercolumn matrix are much more complex, we provide here a few additional figures to aid in the understanding of how these edge- and face-sharing polyhedra assemble to create the intercolumn matrix. Figure E.1 illustrates how the symmetry equivalent polyhedra interlock to form continuous layers in the **a**-**b** plane, while Figure E.2 details the stacking of Ca2- and Ca3-based layers along the **c**-direction.

To begin, we will look at the two types of layers of polyhedra that alternate in the **c**-direction to make up the intercolumn matrix. Each Ca2 and Ca3 polyhedron can be viewed as a dimerized piece of the

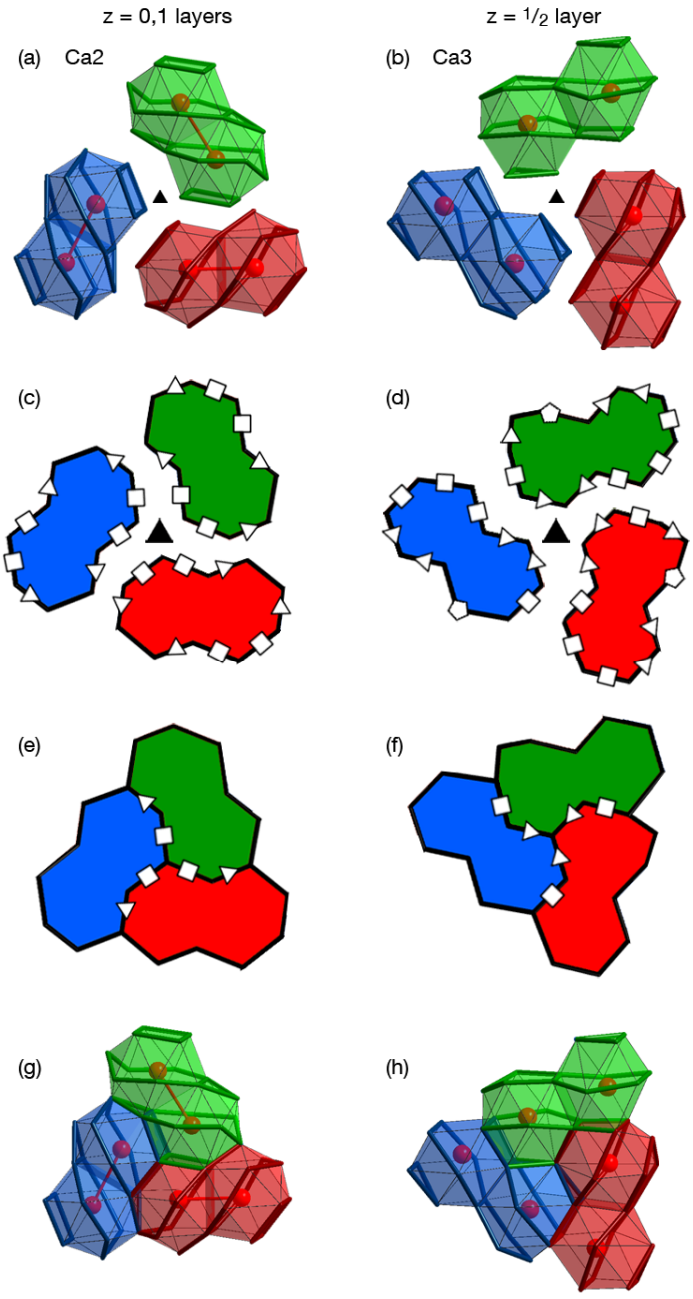

Figure E.1. The assembly of the face-sharing calcium-centered polyhedra of $Ca_{14}Cd_{51}$'s intercolumn martrix. Three symmetry equivalent (a) Ca2- or (b) Ca3-centered polyhedra are related by a three-fold axis. The three different orientations of the dimers are shown in green, red and blue. The images in (a) and (b) are shown abstracted as (c) and (d) to better understand the way these polyhedra share faces. White 2-dimensional triangles, squares, and pentagons indicate the orientation and shape of each face. These align to fit together—shown schematically in (e) and (f) and in the atomic picture in (g) and (h)—to form two types of continuous layers (see Figure 7.6).

$CaCu_5$ type, and within a given layer, the polyhedra are related by a three-fold axis, as detailed in Chapter 7. In Figure E.1a and b, we see these polyhedra color coded by relative orientation. From these two images, we can begin to see how these polyhedra may assemble together, with each bulbous end nestling into the crook of the next dimer. Figure E.1c and d represent direct abstractions of the images in a and b, with white polygons emphasizing the shape and orientation of each face. Here we see the beauty of this three-fold relationship; squares and triangles align with the same orientation, allowing the three dimers of a given layer to snap together and share the faces indicated by the polygons in Figure E.1e and f. We return to an atomic picture for each trifold cluster in Figure E.1g and h, carefully noting the face-sharing interfaces between dimers in each.

As mentioned in Chapter 7, the two clusters share edges to stack directly on top of one another, leaving some interstitial polyhedra in pockets between the layers. We can understand these empty spaces in Figure E.2. Here we see the creation of a distorted tetrahedron as we fuse together one dimer of the Ca2-type layer with one of the Ca3-type. The yellow and blue lines in Figure E.2a emphasize those edges

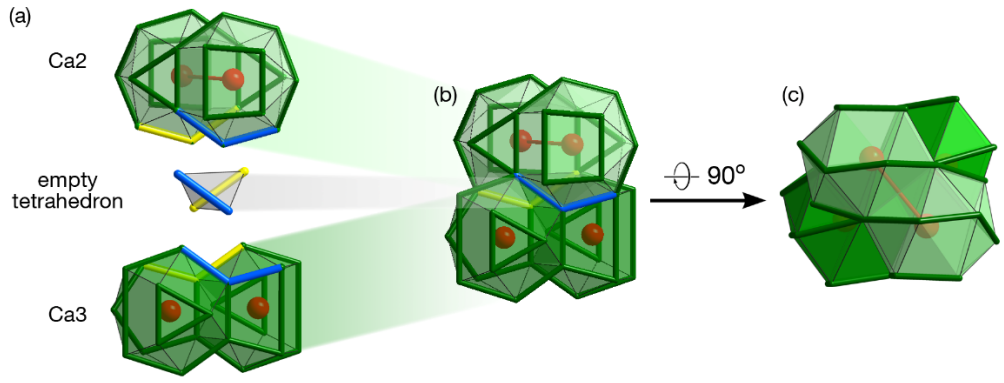

Figure E.2. The stacking of edge-sharing Ca-centered polyhedra along the c-axis. Polyhedra stack in (a) alternating layers of Ca2 and Ca3, isolating an empty distorted tetrahedron in the center. Shared edges are highlighted in blue and yellow, and are also shown in the fused polyhedra in (b). A view down the **c**-axis is provided in (c).

which become shared in the joined picture. Rotating this dimer 90 ° to look down the **c**-axis shows that these columns of distorted $CaCu_5$ fragments preserve their orientation over the length of the structure.

E.4. Supplemental information on the chemical pressures in the Tsai-type approximant, $CaCd_6$

E.4.1. The disordered tetrahedral centering each Tsai-type cluster

One prominent feature of the crystallographic solution to the structure of $CaCd_6$ is the distorted tetrahedron that centers each Tsai-type cluster, modeled in the literature as three separate tetrahedra with one-third occupations.[1] In our computational model of this system, we lowered the symmetry and locked the orientation to a single fully occupied tetrahedron. This reasonably allows us to look at this structure, but we must keep in mind the assumptions behind our approximation, as they are directly contradicted by the experimental evidence.

As it turns out, the chemical pressure on the computationally ordered tetrahedral sites reveals a potential motivation for the observed disorder. We can see this in Figure E.3, where we have an image of the computationally ordered tetrahedron inside the dodecahedron—the beginning of our Tsai-type cluster—juxtaposed with the hypothetical $CaCd_5$ model plotted to the same scale. The strong positive pressures appearing on the top two atoms of the cadmium tetrahedron exceed the magnitude of any pressures in our hypothetical $CaCd_5$. While the lower two atoms of the tetrahedron fit nicely above two pentagonal holes in the dodecahedron, this orientation forces the upper atoms to align linearly with two atoms of the dodecahedron. Unsurprisingly, we see the strong positive pressure along the linear arrangement, and relatively weak pressures around the other half of the tetrahedron. The disordering

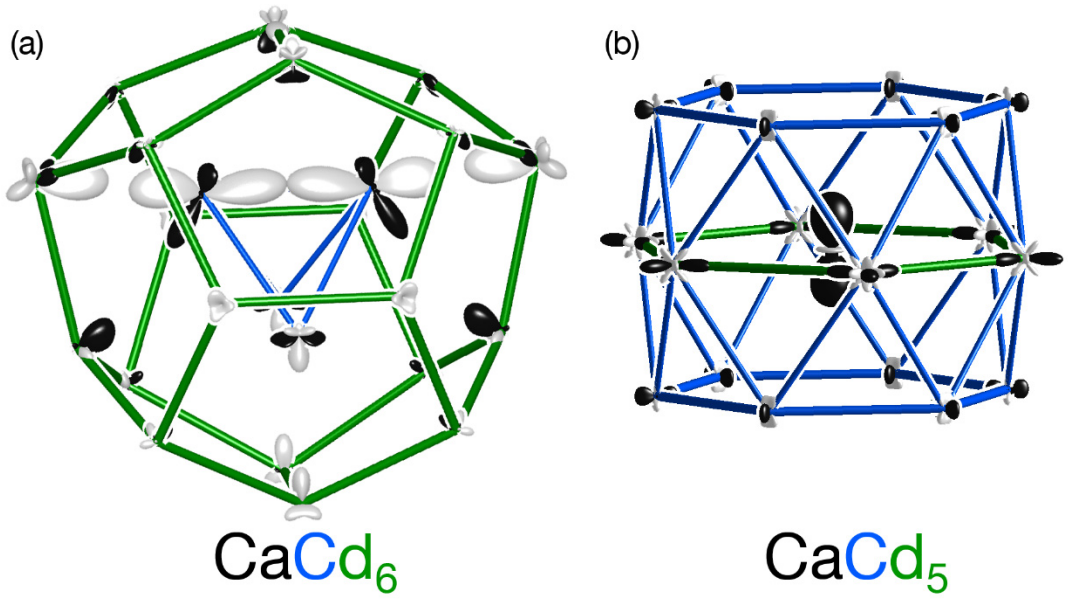

Figure E.3. The chemical pressure in (a) a fragment of 1/1 Tsai-type approximant $CaCd_6$ containing the central tetrahedron and its surrounding dodecahedron, and (b) the hypothetical $CaCu_5$-type $CaCd_5$. The central tetrahedron of the $CaCd_6$ type is crystallographically observed as disordered over three positions, but the computational model lowers the symmetry and defines one orientation for all tetrahedra in the structure.

observed in the crystal structure may relieve a systematic strain, distributing the inevitable strong positive pressures along different orientations and dispersing the overall effects isotropically across the entire crystal.

E.4.2. The interfaces between Tsai-type clusters

In our discussion of the chemical pressure analysis of $CaCd_6$ (Section 7.6.3), we briefly mention the strong positive pressures occurring between distinct Tsai-type clusters. The body-centered cubic arrangement of clusters creates two types of cluster interfaces: those along the unit cell vectors, and those

along the body diagonal of the unit cell. These interactions certainly merit a detailed discussion, as the chemical pressures in each calcium environment are observed to be strongest towards the outside of the cluster.

Along the diagonal, the clusters interpenetrate to incorporate three atoms of one icosidodecahedron as part of the neighboring cluster's outermost shell. With the addition of neighboring calcium and a cadmium atom from each dodecagon, this creates a piece of the fluorite type at this interface: a slightly distorted cadmium cube in a calcium octahedron. In Figure E.4, we see that the chemical pressures at this

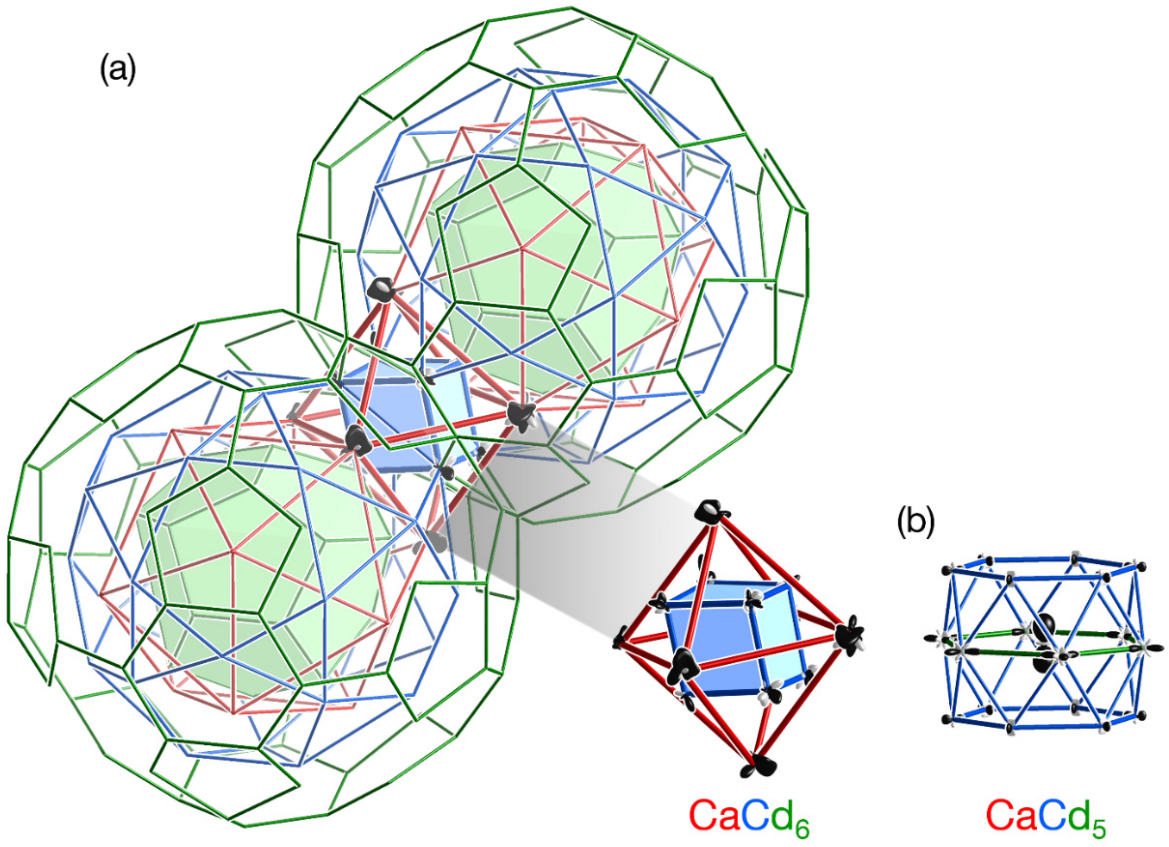

Figure E.4. The interface between two Tsai-type clusters along the body diagonal of the unit cell. Along this direction, the two clusters interpenetrate, creating a piece of the fluorite type. Chemical pressure plots are shown to scale to compare the pressures at (a) this fluorite-like fragment with (b) the hypothetical $CaCu_5$-type $CaCd_5$. Plotting conventions can be found in the text of Chapter 7.

interface are relatively subdued compared to the hypothetical $CaCd_5$, and reflect the general trend of slightly repulsive Cd-Cd contacts, and attractive Ca-Cd contacts.

The second interface between the Tsai-type clusters appears to be less pacified. Here, two Tsai-type clusters meet at a shared hexagonal face of the outermost shells, shown in Figure E.5a. Above and below this hexagon, there is a close Cd-Cd contact, formed by two atoms from the clusters' icosadodecahedra. Most apparently in the enlarged section in Figure E.5b, we see strong positive pressures between most of these Cd-Cd contacts at this interface, with the exception of those between the hexagon and the two out of plane atoms.

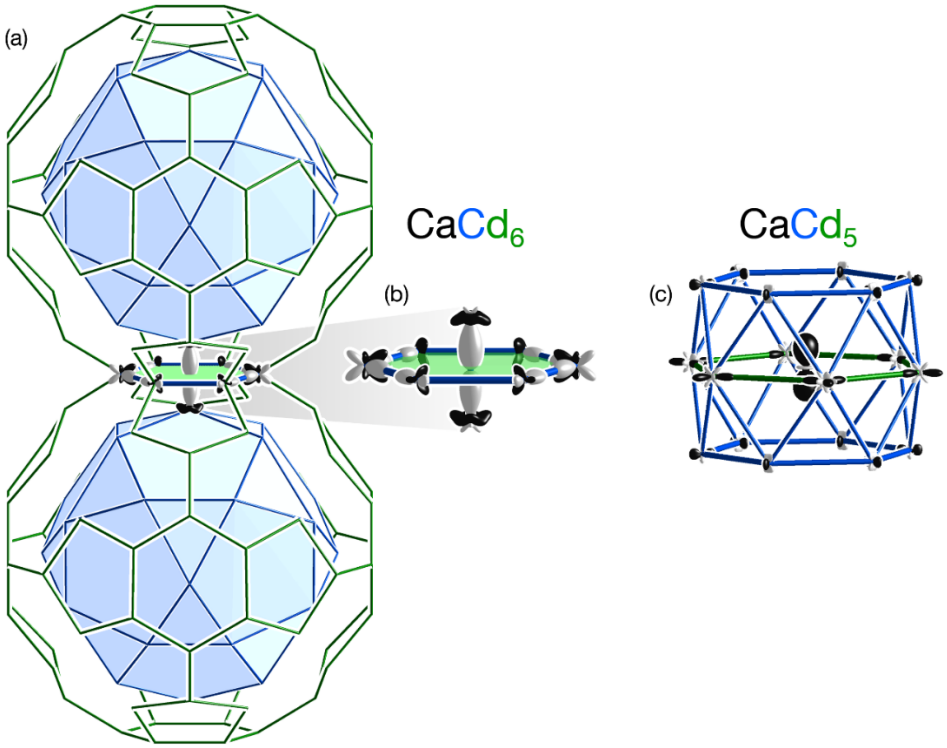

Figure E.5. Chemical pressure at the interface between clusters related by translation along a unit cell vector. (a) The two facing clusters share a hexagonal face of their outermost Cd layers. Two Cd atoms of the clusters' icosadodecahedra form a 2.89 Å contact across the hexagonal face. Chemical pressure plots are shown for (b) the hexagon and its close contacts, and (c) the hypothetical $CaCu_5$-type $CaCd_5$. Chemical pressure plotting conventions can be found in the text of Chapter 7.

E.5. References

(1) Bruzzone, G. *Gazzetta Chim. Ital.* **1972**, *102*, 234–242.